UNIVERSITY OF CALIFORNIA, SAN DIEGO

# Nacre in Abalone Shell: Organic and Inorganic Components and their effects to the Formation and Mechanical Properties

A Dissertation submitted in partial satisfaction of the requirements for the degree of

Doctor of Philosophy

in

Materials Science and Engineering

by

Maria Isabel López

Committee in Charge:

Professor Marc André Meyers, Chair
Professor David Benson
Professor Renkun Chen
Professor Joanna McKittrick
Professor Jan B. Talbot

2014

The Dissertation of Maria Isabel Lopez is approved and it is acceptable in quality and form for publication on microfilm and electronically:

Chair

University of California, San Diego

2014

# DEDICATION

*As Roald Dahl once wrote:*

*"It's a funny thing about mothers and fathers. Even when their own child is the most disgusting little blister you could ever imagine, they still think that he or she is wonderful."*

*This work is dedicated to my parents for no one will ever love me as they do.*

…

*"A mis padres por ser el pilar fundamental en todo lo que soy, en toda mi educación, tanto académica, como de la vida, por su incondicional apoyo y amor perfectamente mantenido a través del tiempo.*

*Todos mis logros han sido posibles gracias a ellos.*

EPIGRAPH

*“That's the nature of research - you don't know what in hell you're doing.”*

*--Harold "Doc" Edgerton*

TABLE OF CONTENTS

LIST OF FIGURES

LIST OF TABLES

# ACKNOWLEDGEMENTS

This work would have not been possible without financial support; I thank the Ford Foundation for giving me the opportunity to advance in my education. I would like to thank all members of the Marc Meyers' and Joanna McKittrick's research group for their daily help. In addition I would like to express gratitude to all past colleagues and mentors, in particular Prof. Lawrence E. Murr, Erika Esquivel, Fabiola Lopez and my close friend Sara Gaytan, who taught me science can be fun. Also, I would like to thank Po-Yu Chen who largely contributed to this work in content, mentorship, and friendship. Additionally, very special thanks to my good friend Jorge Muñoz who facilitated my job search. My friends and family, specifically my brother, Erika Fierro, Ryan Cary, Carlos Ruestes, Tane Remington, Andrew Marquez, and Sergio Robles, are also greatly acknowledged. They impacted my life greatly and at different times in my career have provided motivation, patience, and support.

I would also like to thank Prof. Jenq-Gong Duh and his research group for facilitating my participation in the EAPSI program. Researchers and technicians at Calit2, SIO, and NCMIR facilities at UCSD are also greatly acknowledged. I would like to give a special thanks to Prof. Joanna McKittrick for her support, mentorship, and encouragement. Prof. Marc A. Meyers, who provided extensive mentorship and support over the last years; they will always be acknowledged as a major impact in my research and schooling.

At last, I would like to thank to my devoted parents, who represent the single greatest influence on my life. They have always provided the best guidance and

unconditional love and support. They not only symbolize where I am coming from, but also what I want to be. I love you guys.

Chapter 4, in part is a reprint of the material as it appears in Materials Science and Engineering C, vol 31: 238-245, 2010. Lopez, Maria Isabel; Chen, Po-Yu; McKittrick, Joanna; Meyers, Marc Andre, 2010. The dissertation author was the primary investigator and author of this paper.

In addition, chapter 4, in part is a reprint of the material as it appears in Advances in Bioceramics and Biotechnologies II, Ed. J. McKittrick and R. Narayan, Ceram. Trans., 247, 37-46, Wiley & Sons, Hoboken, NJ, 2014. Lopez, Maria Isabel; Chen, Po-Yu; McKittrick, Joanna; Meyers, Marc Andre, 2014. The dissertation author was the primary investigator and author of this paper.

Additionally, chapter 4, in part is a reprint of the material as it appears in ActaBiomaterialia, vol. 10 (5): 2056-2064, 2014. Lopez, Maria Isabel; Meza-Martinez, Pedro Emilio; Meyers, Marc Andre, 2014. The dissertation author was the primary investigator and author of this paper.

Chapter 4, in part, has been submitted for publication of the material as it may appear in ActaBiomaterialia, 2014. Lopez, Maria Isabel and Meyers, Marc Andre, 2014. The dissertation author was the primary investigator and author of this paper.

## VITA

| | |
|---|---|
| 2005-2009 | Research Assistant, Metallurgy and Materials Engineering Department, The University of Texas at El Paso |
| 2009 | Bachelor of Science, The University of Texas at El Paso |
| 2009-2012 | Research Assistant, Materials Science and Engineering Program, University of California, San Diego |
| 2009 | AGEP Fellow |
| 2010 | Ford Foundation Fellow |
| 2011 | Master of Science, University of California, San Diego |
| 2014 | Doctor of Philosophy, University of California, San Diego |

## PUBLICATIONS

"Organic Interlayers, Mesolayers, and Mineral Nanobridges: Contribution to Strength in Nacre," **M.I. Lopez**, P.E. Meza, M. A. Meyers, Acta Biomaterialia (accepted, 2013)

"Toward a better understanding of mineral microstructure in bony tissues," Bioinspired, Biomimetic and Nanobiomaterials," P.-Y. Chen, E.E. Novitskaya, **M.I. Lopez**, Chang-Yu Sun, J. McKittrick, Bioinspired, Biomimetic and Nanobiomaterials (accepted, 2013)

"Predation vs. Protection: Fish teeth and scales evaluated by nanoindentation," P.-Y. Chen, J. Schirer, A. Simpson. R. Nay. Y.-S. Lin. W. Yang, **M.I. Lopez**, J. Li, E.A. Olevsky, M.A. Meyers, J Mater. Res. (accepted 2012).

"The Growth of Nacre in Abalone: Seasonal and Feeding Effects on theProcess of Mineral Formation", **M.I. Lopez**, M.S. Thesis, 2011

"Biological materials: A materials science approach", M.A. Meyers, P.-Y. Chen, **M. I. Lopez**, Y. Seki, A. Y. M. Lin, Journal of the Mechanical Behavior of Biomedical Materials, 2010

"Growth of Nacre in Abalone: Seasonal and Feeding Effects", **M. I. Lopez**, P.Y. Chen, J. McKittrick, and M.A. Meyers, Materials Science and Engineering C, 2010

"Next-generation biomedical implants using additive manufacturing of complex, cellular and functional mesh arrays", L. E. Murr, S. M. Gaytan, F. Medina, H. Lopez, E.

Martinez, B. I. Machado, D. H. Hernandez, L. Martinez, **M. I. Lopez**, R. B. Wicker and J. Bracke, 2010, Phil. Trans. R. Soc. A, vol. 368 pp.1999-2032.
"Materials characterization of bizarre and catastrophic 'burst' failure in metal by 'Hutchison Effect'", L. E. Murr*, S. M. Gaytan and **M. I. Lopez**, 2010, MRI journal, vol. 13 pp. 425-430. 2010

"Metallographic characterization of additive-layered manufactured products by electron beam melting of Ti-6Al-4V-powder", L.E. Murr, S.M. Gaytan, **M. I. Lopez**, E. Martinez, F. Medina, R.B. Wicker, Practical Metallography, Vol. 46, Pp. 442-453, 2009

"The synthesis and hydrogen storage properties of a MgH(2) incorporated carbon aerogel scaffold.", with S. Zhang, A.F. gross, S.L. Van Atta, **M. Lopez**, P. Liu, C.C. Ahn, J.J. Vajo, C.M. Jensen, Nanotechnology. 2009 vol. 20.

"Characterization of 3-phase (ternary-like) n-type and p-type thermoelectric materials fabricated by explosive (shock-wave) consolidation", with V.B. Munoz, L.E. Murr, D. Nemir, R. Lourenich, E. Rubio, E.Y. Martinez, S.M. Gaytan, and **M. I. Lopez**, Materials Characterization, 2008, vol. 59 pp. 1258-1272.

"Metallurgical and Acoustical Characterization of a Hydroformed, 304 Stainless Steel, Caribbean-style Musical Pan", with S. M. Gaytan, **M. I. Lopez**, D. E. Bujanda, E. Martinez, G. Whitmyre, and H. Price, Materials Characterization, 2008, vol.59 pp. 321-328.

"Dynamic Deformation and Adiabatic Shear Microstructures Associated with Ballistic Plug Formation and Fracture in Ti-6Al-4V Targets", with F. Martinez, A. Ramirez, **M.I. Lopez**, S. M. Gaytan, and B. E. Schuster, Materials Science and Engineering A, 2007, vol. 454A, pp. 581-589.

"Fabrication of and aluminum, Caribbean-style, musical pan: Metallurgical and Acoustical Characterization", with E. V. Esquivel, S. C. Lawrie, **M. I. Lopez**, S. L. Lair, K. F. Soto, S. M. Gayton, D. Bujanda, R. G. Kerns, P. A. Guerrero, J. A. Flores, Materials Characterization, 2006, vol. 57, pp. 232-243.

"Adiabatic Shear Bands Associated with Plug Formation and Penetration in Ti-6Al-4V Targets: Formation, Structure, and Performance: A Preliminary Study", with F. Martinez, E. V. Esquivel, **M. I. Lopez**, S. M. Gaytan, D. A. Lopez, A. Ramirez, D. A. Ramirez, P. A. Guerrero, C. Pizana, I. Anchondo, B. E. Schuster, and M. Fermin-Coker, Proc. Of Sessions & Symposia (S. Howard, et al. eds.) TMS publication, 2006, pp. 137-142 (CD).

"TEM Observations of a 30 Million Year Old Mountain Leather Nanofiber Mineral Composite", with E. V. Esquivel, **M. I. Lopez**, P. C. Goodell, Materials Characterization, 2005, vol. 54, pp. 458-465.

## FIELD OF STUDY

Major: Materials Science and Engineering with an emphasis on the study of biological materials.

ABSTRACT OF THE DISSERTATION

Nacre in Abalone Shell: Organic and Inorganic Components and their Effects to the Formation and Mechanical Properties

by

Maria Isabel López Fierro

Doctor of Philosophy in Materials Science and Engineering

University of California, San Diego, 2014

Professor Marc Andre Meyers, Chair

Abalone nacre is a natural composite that exhibits exceptional mechanical properties due to its organization that extends to various levels of hierarchy. Most of the toughness has been attributed by nacre's third level of hierarchy which entitles a brick

and mortar structure consisting of the $CaCO_3$ tiles and organic interlayers. However, there are other important components that are vital to the structure and strength of red abalone nacre. The process of formation of red abalone (*Haliotis rufescens*) nacre following periods of growth interruption, taking into consideration important environmental factors (access to food and temperature) and to employ high-magnification characterization techniques (scanning electron microscopy and transmission electron microscopy) to better understand how the soft tissue (e.g. epithelium and organic membrane) influences the mechanism of growth.

The structure-property relationship of red abalone (*Haliotis rufescens*) nacre, focusing in the individual constituents (isolated mineral and isolated organic component) and comparing that to the integrated structure. Mechanical tests such as, tensile tests, microscratch, and nanoindentation is performed on the isolated organic constituent and the isolated mineral of red abalone shell. Specimens are characterized by SEM to verify the toughening and deformation mechanisms. Results obtained from the isolated mineral validate the importance of the organic constituent as the mechanical properties decline greatly as the organic component is removed. This approach forms a general picture of the mechanical response of the organic interlayers and growth bands and their effect on the toughness of the abalone nacre.

These results are significant to understand the important characteristics of abalone nacre, such as the structure and mechanical properties, and an attempt to aid in improving the latest attempts to produce novel nacre-inspired materials.

# CHAPTER 1

## INTRODUCTION AND OBJECTIVES

Materials science is one of the oldest forms of applied science and engineering. Materials have throughout history defined eras in time, for example the three-age system of archeology is divided by the 'Stone age', 'Bronze age', and 'Iron age'. The field first had a place in modern science as a derivative of Metallurgy, as ceramics and polymers expanded the field. Materials science and engineering was then considered an interdisciplinary field that incorporated elements of chemistry and applied physics. However, at the beginning of the 20$^{th}$ century the traditional paradigm of materials science changed as biological systems became considered as 'structures'. In 1917 "On growth and Form" by D'Arcy W. Thompson [1], which is now considered one of the classical works in the field, was published. This then opened up the field of Materials Science in a new direction, incorporating Biology as one of the main constituents of Materials science (Figure 1.1).

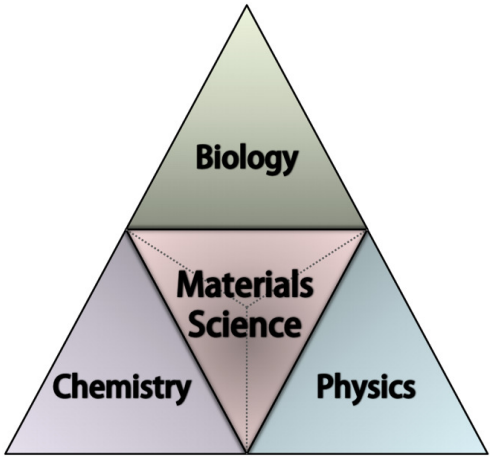


**Figure 1.1:** Schematic representation of contributing scientific fields

In science and technology there is always a need for refining and improvements. Nature can provide excellent solutions to many of these difficulties. Biological organisms are improved and refined by natural selection. Only the most successful structural forms have survived and unveiling the secrets of their survival can reveal amazing design characteristics. 'Biomimicry', or 'Biomimetics', is now a 'hot topic' pushing forward the idea of imitating life. In the context of materials science and engineering it has introduced the idea of understanding the property and structure relationship of biological materials in hopes of developing novel means of designing and processing materials. After the pioneering study by Thompson [1] it was followed by many others including Vincent [2] and Currey [3].

This subdivision of materials science and engineering is now known as "Biological Materials Science" and composed by three different fields, including:

- Biological materials: The study of natural materials.
- Bioinspired/ biomimicked materials: Creation and designing of materials by imitating natural structures.
- Biomaterials: The study and creation of synthetic materials for the purpose of biomedical applications.

These subareas are at many times mutually dependent and interconnected.

Particularly in the study of biological materials a deep understanding of biology is vital. Animal lifestyle, anatomy, and physiology at all times affect the structure and properties of their individual components. For the majority of the cases, biological materials can be divided into two categories: organic constituents and biominerals, a list of these can seen in table 1.1.

Organic constituents are associated with polymers in engineering, as they are able to deform and are able to extend in tensional loading. Biominerals are analogous to ceramics, where they can sustain loads resisting primarily in compression. A combination of both constituents is always beneficial as the biopolymer contributes in toughness and ductility, while the mineral adds stiffness and strength. Thus, in many cases biological materials are composites to advantageously encompass a combination of these properties.

**Table 1.1:** Principal components of biological materials.

| Table 1.1 Principal Components of biological materials | |
|---|---|
| Minerals: Hard Component | Biopolymers: Soft Component |
| Calcium Carbonate ($CaCO_3$) | Collagen |
| Calcium Phosphate (hydroxyapatite, $Ca_{10}(PO_4)_6(OH)_2$ | Keratin |
| Silica ($SiO_2$) | Chitin |
| Magnetite ($Fe_3O_4$) | Elastin |
| Copper Oxide | Cellulose |
| | Resilin and Abductin |

These biopolymers and minerals are independently quite weak. As an example, one can consider calcium carbonate to be quite brittle. However, when combined as a composite in a hierarchical ordered structure the mechanical properties are improved greatly. Such as in the case of the abalone shell, where calcium carbonate exists in combination with a biopolymer, making the shell a tough material. These refined, highly ordered, self-assembled structures can enhance their mechanical properties, such as

increasing their strength, by orders of magnitude [2, 4]. To date, many produced synthetic materials have not yet reached the excellent mechanical properties exhibited by biological systems [3, 5].

These biological systems are subject to complex constraints that exhibit specific characteristics presented in the hexagon shown in Figure 1.2 [6]. Biological materials are unique in their conception, design, and structure. The six components are self assembly, hierarchy of structure, functionality, ambient temperature and pressure processing, evolution/environmental constraints, and the importance of hydration to its structure and properties. These unique characteristics distinguish them from synthetic counterparts. The six components are presented below:

- The structures are assembled from the bottom-up, rather than from the top-down. This is a necessity of the growth process, since there is no availability of an overriding scaffold. This characteristic is called ‘self-assembly’.
- The structures can re-generate and/or ‘self-heal’
- Evolution, environmental constraints, and the limited availability of materials dictate the morphology and properties. The principal elements available are oxygen, nitrogen, hydrogen, calcium, phosphorous, silicon, sulfur, and carbon. The most useful synthetic metals (iron, aluminum, copper) are virtually absent and are only present in minute quantities and highly specialized applications. The processing of these elements requires high temperature processes not available in natural organisms.
- The properties are highly dependent on the level of water in the structure.

- For the most part the synthesis of biological materials is conducted in an aqueous environment at ambient temperature and pressure of 1 atm.
- Many components serve more than one purpose, a characteristic refined by over a billion years of evolution. Thus, the structures are called “multifunctional’.
- The structures are hierarchical, i.e., they have different scale levels conferring distinct properties. Biological systems are organized based on composition and structure, exhibiting a hierarchical organization from the nano, micro, to the macro (structural) level.

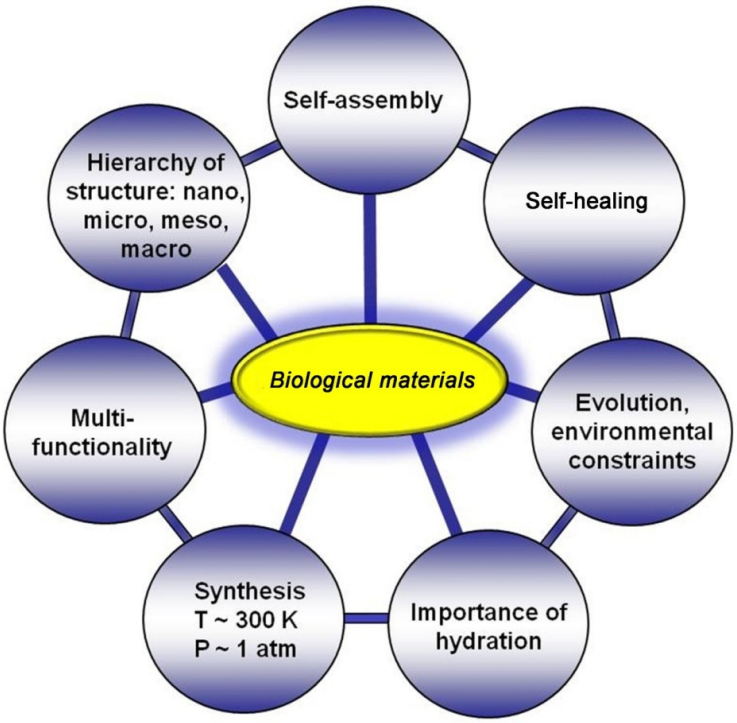


**Figure 1.2:** Characteristic constraints/components in the study of biological systems. (Modified from Meyers et al. 2010 [6])

The outstanding mechanical properties of shells and the precise mechanisms by which they form is a topic of interest in biological materials, biomimetics, and

biomineralization[7-9][10-25]. Deciphering the procedure by which nacreous shells are formed and what specifically gives them the superb properties could lead to new and better synthetic materials [10-13, 26].

Mollusk shells have been intensively studied as biomineralization models [27]. The majority of shells are comprised of calcium carbonate in a calcitic and nacreous arrangement in which the microstructures exhibit a vast range of features. There are up to at least 10 different existing morphologies in shells (bivalve) [28], including: simple prismatic, aragonite prismatic, nacreous, foliated, composite prismatic, crossed lamellar structure, complex crossed lamellar or homogeneous structure. However, from all these different structures, the nacreous platelet arrangement found in abalone shell (*Haliotis*) is the most studied. The nacreous arrangement is associated with its excellent mechanical properties. Biomimetic strategies have been proposed to produce new layered composites resembling the structure of nacre. There have been recent successes in synthesizing a ceramic/polymer composite with outstanding toughness inspired by the structure of nacre in the abalone shell [29-32].

In regards to nacre, both: the formation and the structure-property relationship is of interest. The growth and formation of nacre has been previously studied by many [6, 10, 14, 16-19, 23-25, 33-46]. Although the subject is not fully understood, results in abalone nacre show that aragonite crystals first radiate from nucleation sites forming a spherulitic pattern, then, columnar aragonite crystals form preferentially in the *c*-direction (perpendicular to the growth surface). This morphology is then replaced by the aragonite tile pattern.

Moreover, the role of the organic layer in the growth of the abalone nacre has been studied by Belcher et al. [16, 40], Zaremba et al. [19], Sarikaya et al. [10, 41, 47] Lin et al. [24, 38], Meyers et al. [23, 48], and Bezares et al. [44, 45], which has led to proposed mechanisms of growth.

However, there is still a lack of understanding of factors that affect the development of these transient phases. Environmental changes, such as changes in the feeding patterns may limit the source of ions for mineral formation in the abalone shell. In addition temperature of the sea water might also alter the animal's behavior that may affect the nucleation rate and growth rate of the transitory phases of calcium carbonate. It is also known of the involvement of the mantle and epithelial cell layer to form the intricate structure of the growing front of the shell. By its mantle, the animal can closely control the rate and even the morphology of the structure. For example, calcium radioisotopes movement studies on the oyster *Crassostrea virginica* show that movement of the $^{45}Ca$ out of the mantle correlated with the amount of $^{45}Ca$ deposited on the shell growth front. Additional mollusk ion transport studies on the isolated mantle indicate ion movements from the mantle to the shell, while other studies suggest that $Ca^{2+}$ transport occurs by diffusion through this mantle (Simkiss 1989).

Furthermore, the structure-property relationship in abalone nacre has been intensively studied [6, 19-25, 28, 33, 38, 41, 48-59]. In brief, the nacreous structure of the gastropods has the highest strength and toughness of any shells; being composed of parallel layers of tiles. This arrangement diminishes crack propagation as the crack has to travel along the organic layers creating a tortuous path, and accordingly the toughness

and the work of fracture are enhanced. The structure is anisotropic (given to the formation) which results in an orientation dependence of the mechanical properties. Additionally, there are noteworthy efforts to computationally model [58-64] the mechanical behavior of the shells, especially the interface features. This past work has lead to the main conclusion that the structure is hierarchical, and thus, different toughening mechanisms function at different levels suggesting the importance of understanding the mechanical properties at each level.

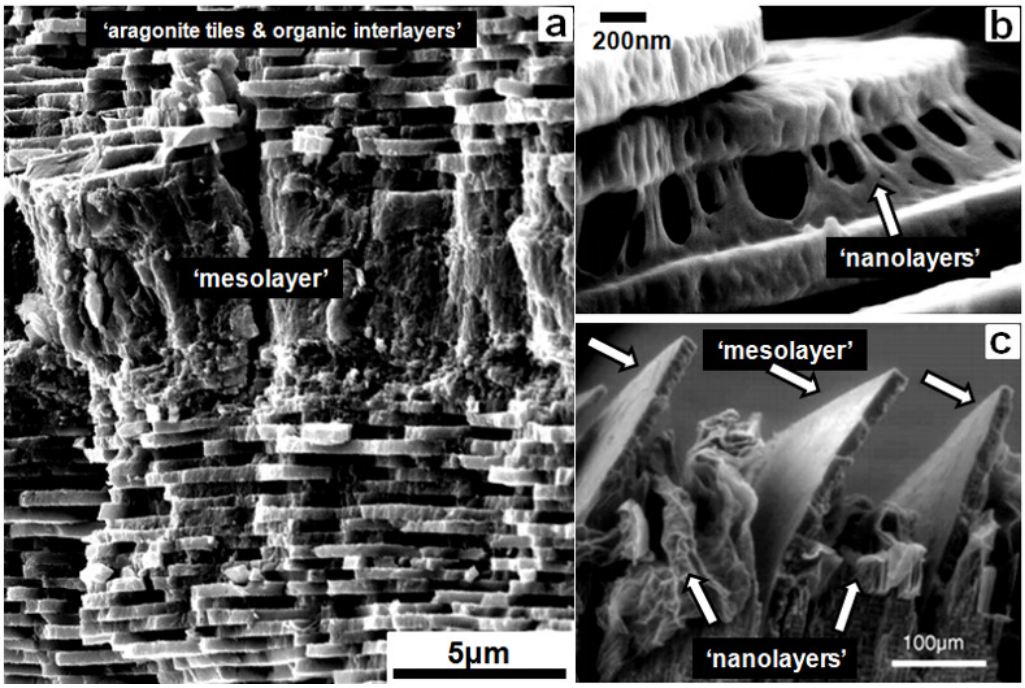


**Figure 1.3:** a) Red abalone nacre showing the brick and mortar architecture separated by a mesolayer, or growth band. b) Partially demineralized nacre exposing the tent-like organic membrane. c) Mesolayers within a partially demineralized nacreous structure consisting of a thick layer of organic material with an embedment of minerals (Note collapsed nanolayers) (Figure 'c' adapted from: Lin [65]).

This study intends to further investigate both:

1. The process of formation of red abalone (*Haliotis rufescens*) nacre following periods of growth interruption, taking into consideration important environmental factors (access to food and temperature) and to employ high-magnification characterization techniques (Scanning electron microscopy, Transmission electron microscopy, and Atomic Force microscopy) to better understand how the soft tissue (e.g. epithelium and organic membrane) influences the mechanism of growth.
2. The structure-property relationship of red abalone (*Haliotis rufescens*) nacre, focusing in the individual constituents (isolated mineral and isolated organic component) and comparing that to the integrated structure (Figure 1.3a) in hopes of determining the contributions of different hierarchical levels and components.

These results are significant to understand the important characteristics of abalone nacre, such as the structure and mechanical properties, and an aid in improving the latest attempts to produce novel nacre-inspired materials.

# CHAPTER 2

# BACKGROUND

A combined background of previous, relevant, and fundamental works will be described in this chapter in attempt of providing basic information pertaining to this study. The background will be divided into three sections:

1. The structure of abalone shell and abalone nacre.
2. Basic Biomineralization concepts, a brief overview of Biomineralization of calcium carbonate, and past studies on the formation and growth of abalone nacre.
3. The mechanical properties and relationship to the structure of abalone nacre.

These topics will expectantly cover the most relevant information pertaining to the present study and will permit a better understanding of the latest results.

## 2.1 Structure of Abalone Shell and Abalone Nacre

### *2.1.1 Structure of Abalone Shell*

The abalone shell acts for the most part as a protection method against predators. It surrounds the animal's body limiting the exposed area while the uncovered area is mainly in contact with other surfaces, such as rocks. Figure 2.1 is a schematic showing the shell is composed of two distinct layers: an outer calcite (Figure 2.2 a,b) and an inner nacreous layer (orthorhombic aragonite) (Figure 2.2 c,d). The outer layer (calcite) is hard

and brittle, and the inner layer (nacre) exhibits toughness. Although the outer calcitic layer has also been a topic of research, for example work reported by Schneider et al. [66], the inner nacreous layer has been the mayor topic of interest as it is accredited with the mayor component to affect the mechanical response of the shell.

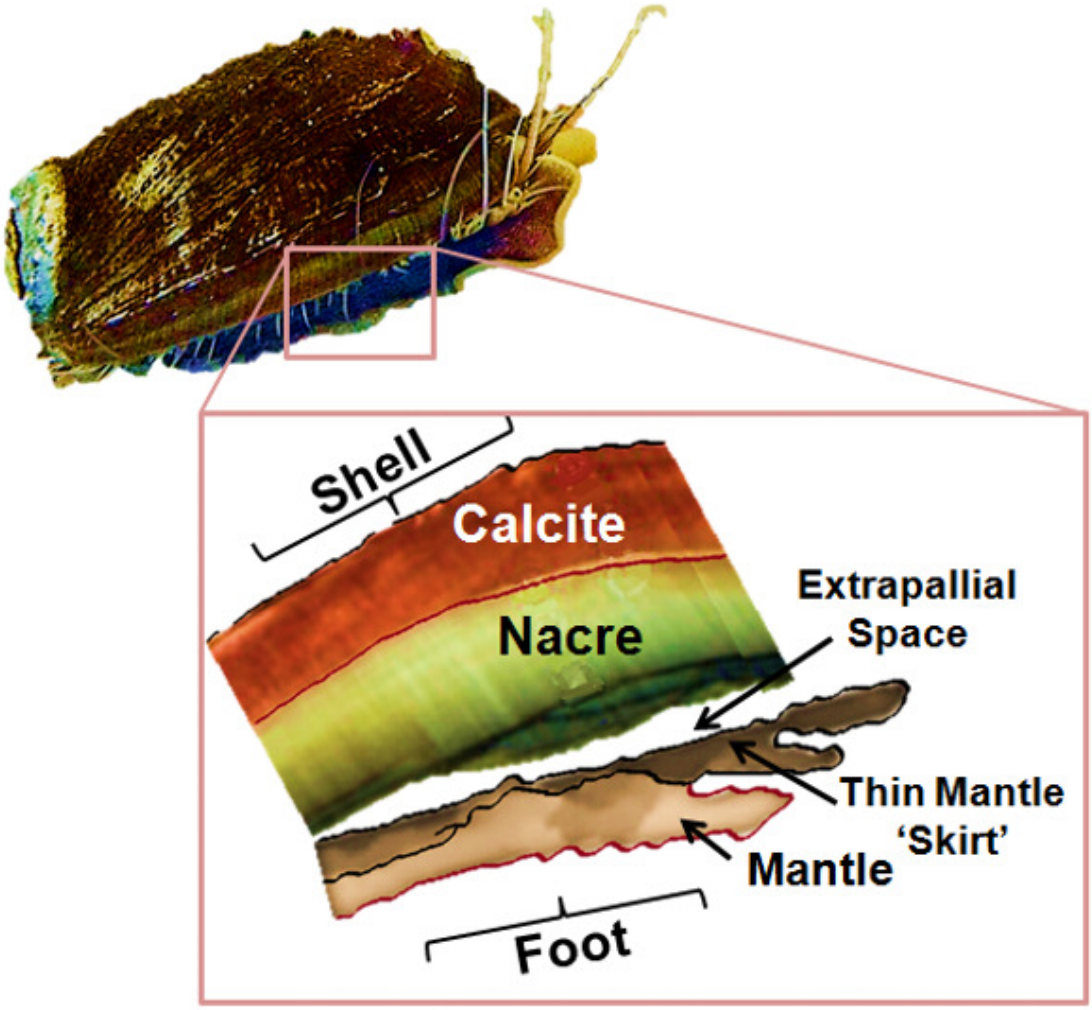


**Figure 2.1:** Structure of typical mollusk shell.

Other anatomical components of the animal are of extreme importance. For example it is noteworthy that the growing surface of the shell is in direct contact with the

mantle. The contact area between the mantle and shell surface is called the 'extrapallaial space'. Figure 2.3 shows images showing this thin mantle and some exposed surface of the shell. This thin mantle (epithelium) encounters the foot directly and is responsible for the formation of the shell. Then epipodium, a sensory area which has tentacles, circles the foot and lies underneath the mantle.

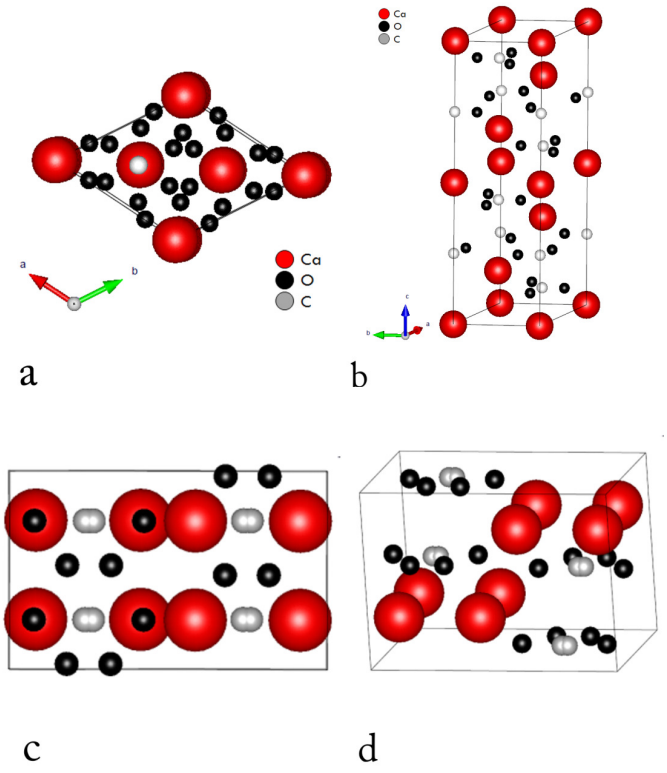


**Figure 2.2:** Comparison of the calcite and aragonite unit cells. (a) top view of calcite, (b) tridimensional view of calcite unit cell, (c) top view of aragonite, (d) tridimensional view of aragonite unit cell. Note that the large spheres depict the calcium ions, the small darker spheres depict the oxygen ions, and the smaller lighter spheres show the carbon ions.

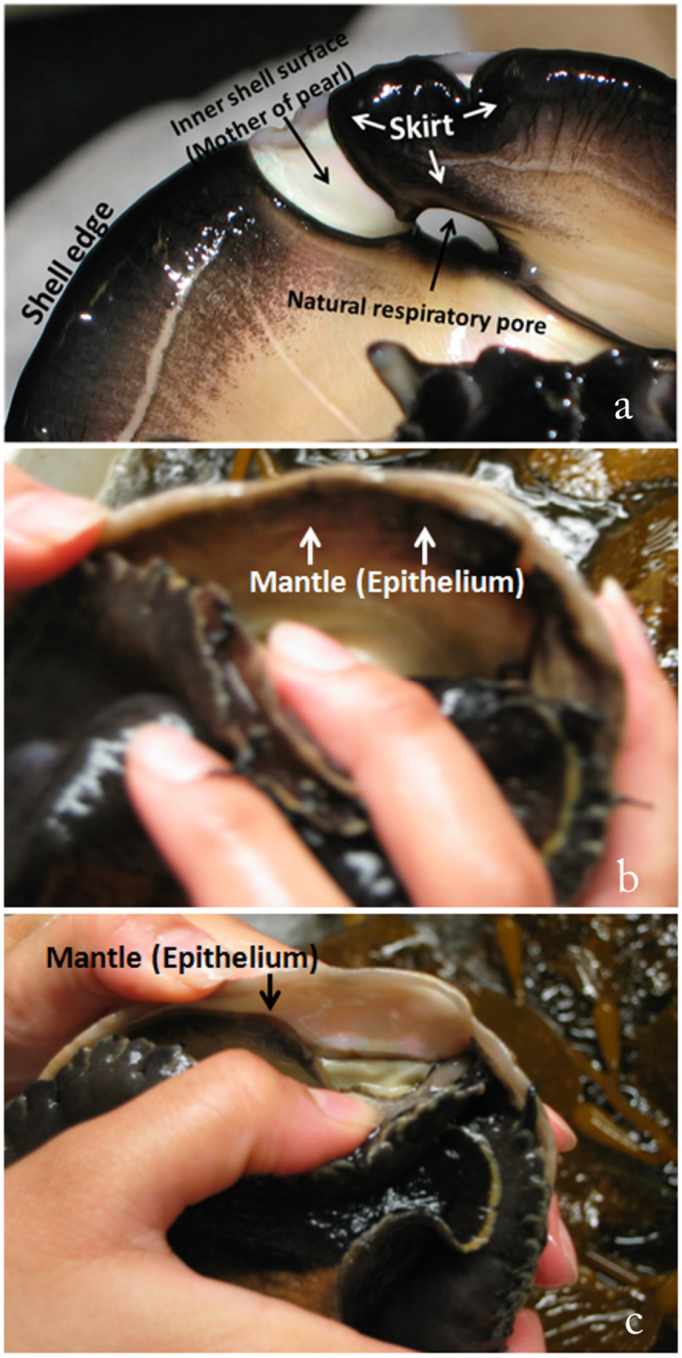


**Figure 2.3:** Abalone mantle pushed back revealing epithelium.

The abalone shell exhibits, as many other biological materials, various important levels of organization ranging from the macro-structure to the nano-level.

In total, there have been five different levels identified (Figure 2.4):

- Level I is the molecular structure of the chitin fibers that are the structural component of the intertile organic layers and of the atomic crystalline structure of the aragonite.
- Level II is composed of the mineral bridges between tiles, with a diameter of 20-60 nm; it also comprises the sandwich structure of the organic intertile layer, with a core consisting of a random dispersion of chitin fibrils and a thickness equal to the length of the mineral bridges (~20 nm). The tiles may also be comprised by nanosize islands.
- Level III are the well recognized hexagonal tiles, with lateral dimensions of 8-10 μm and thickness of 0.5 μm.
- Level IV are the mesolayers, which are formed by seasonal fluctuations and are characterized by a thick organic layer (thickness ~200 μm) separating tile assemblages with approximately 0.1 -0.3 mm.
- Level V is the entire structure that, because of its architecture (dome shape, thickness distribution, etc) is optimized for strength and toughness.

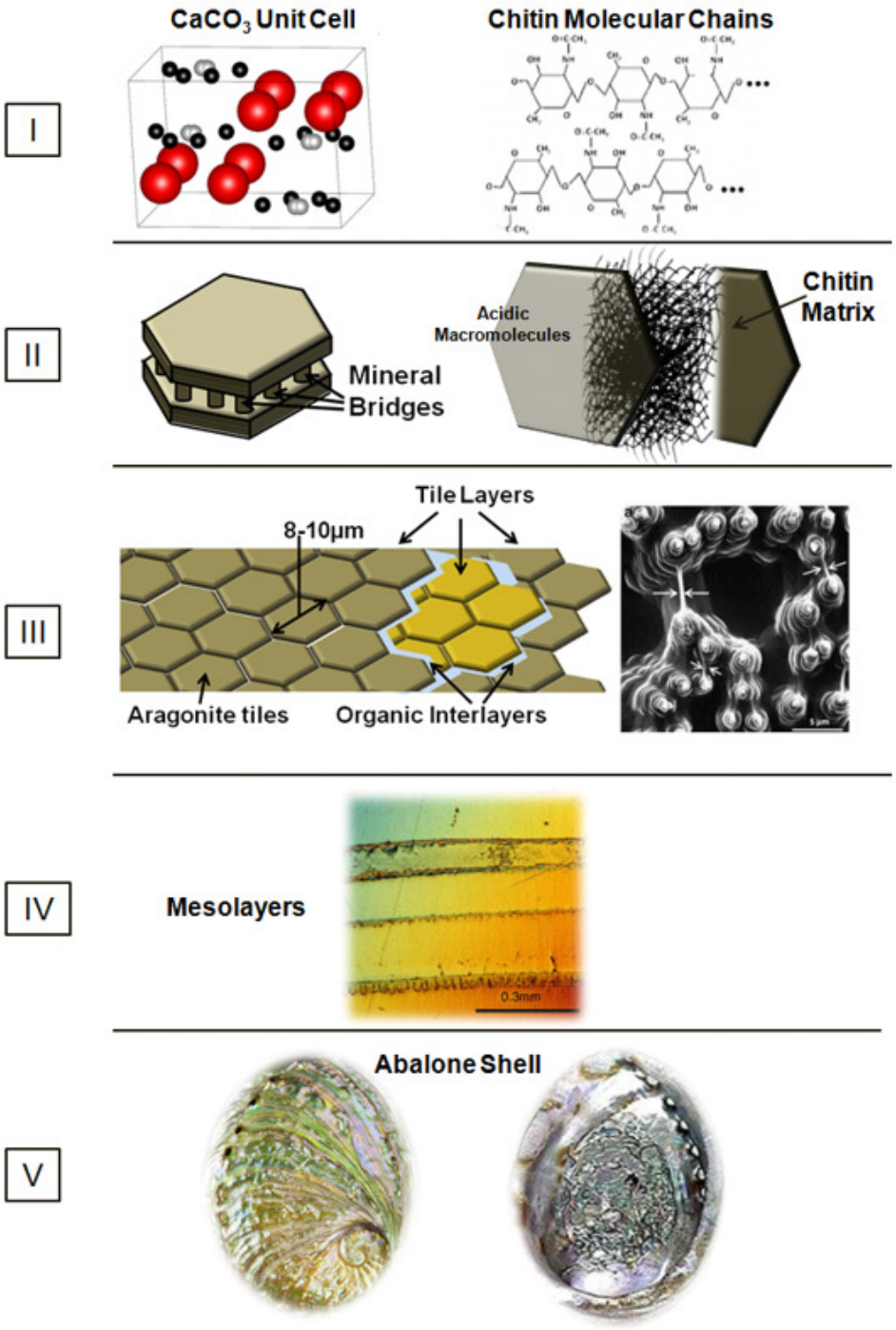


**Figure 2.4:** Hierarchical structure (5 levels) of the abalone nacre from nano-, micro-, to meso- to structural length scales. (adapted from: Meyers et al. [6])

*2.1.2 Structure of Abalone Nacre*

The mechanical and structural study of this investigation will focus mainly on the nacreous level (isolating the components when possible to observe their individual response and impact) of the shell with particular focus on: the brick and mortar portion (level III), the mineral bridges and organic intertile layers (level II), and mesolayers (level IV).

Foremost, the inner nacreous layer (level III) is a mineral/ organic composite (95 wt% calcium carbonate, 5 wt% organic material) made up of nanoscale tiles of aragonite (a $CaCO_3$ polymorph) separated by an intertile matrix of organic biopolymers, described as "brick-and mortar" structure [10, 38, 51, 64, 67, 68].

The tiles are 0.4-0.5 µm thick and 8-10 µm wide and the intertile layer is approximately 20 to 50 nm thick (Figure 2.5). This highly ordered structure results in outstanding mechanical properties [14, 17, 19, 25, 33, 34, 38, 48, 50, 51, 69-74].

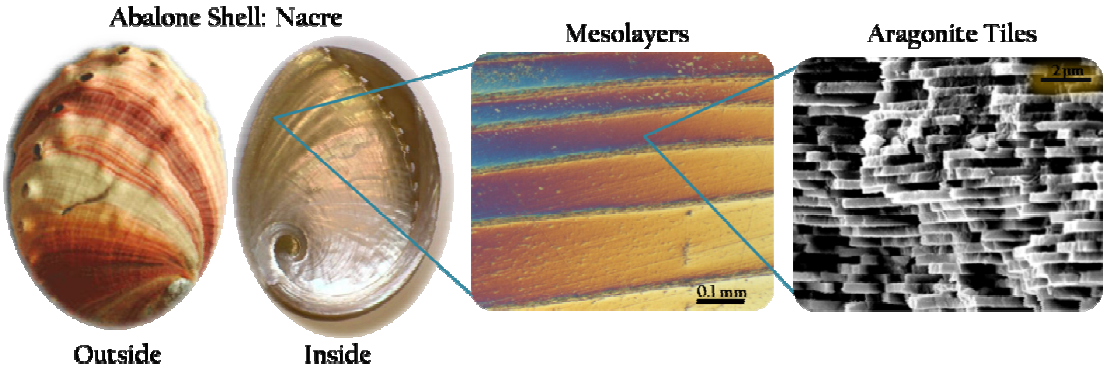


**Figure 2.5:** The levels of structural hierarchy in nacre; macro scale mesolayers, 10µm by 0.5 µm aragonite tiles, the nanostructure defined within the interface between tiles.

The organic interlayer in nacre has been subject of various structural and mechanical investigations [25, 44, 45, 48, 75-77]. This organic matrix consists of β-chitin fibrils having a diameter of ~20nm surrounded by acidic macromolecules that attach themselves to the top and bottom surface of the tiles [41, 78] (Figure 2.6). The organic interlayer appears to be periodically deposited (every ~0.5µm) by the epithelial layer of the animal allowing mineral ion transport through existing holes that have an approximate diameter of 20-60nm. Due to the permeability of the membrane to the $Ca^{2+}$ and $CO_2^{-3}$ ions flow through the holes the and lateral growth can restart and continue on to a next level of tiles allowing continuous growth between the mineral layers by the formation of mineral nano-bridges [14, 48].

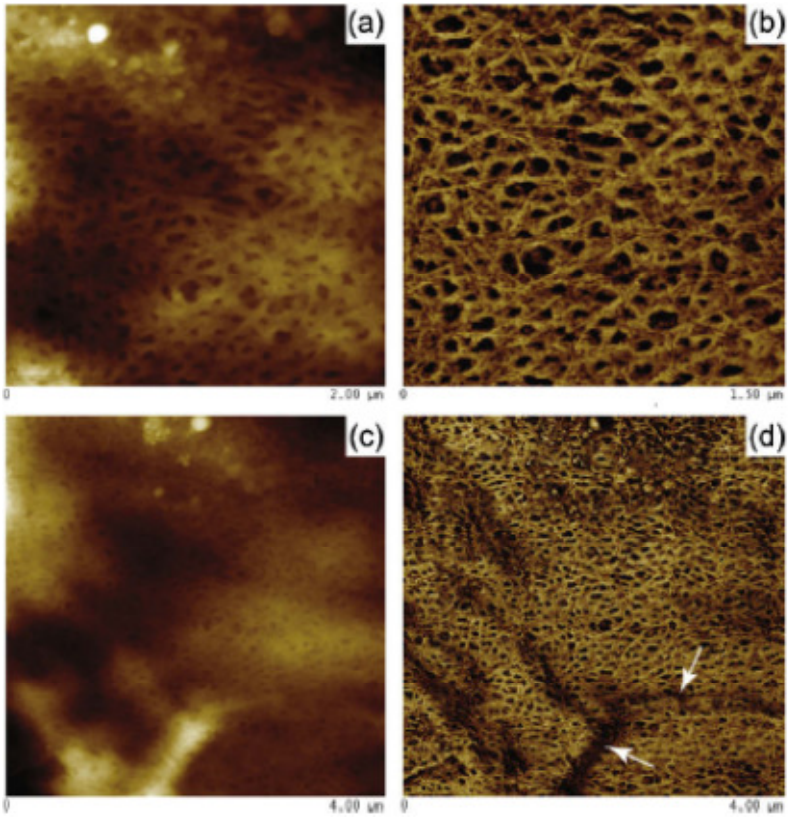


**Figure 2.6:** AFM topographical and phase images of demineralized framework. (a–d) Biopolymer layers partially digested with trypsin and proteinase K. (a and b) Scan

confined to a single tile imprint whereas (c and d) are from a scan spanning multiple tile imprints. White arrows indicate tile boundaries. (source: Bezares et al. [45])

The tiles are interconnected via mineral nano-bridges (level II) that form through the existing holes of the intertile organic matrix [14, 48, 79] (Figure 2.7). These mineral nano-bridges and nano-asperities are indeed considered to have an important role to the formation of the microstructure and the overall mechanical properties and have been studied and observed by many [20, 24, 25, 42, 64, 80-83]. These bridges, having a diameter of approximately 50 nm, have a tensile strength not determined by the critical crack size, but by the theoretical strength. Their number is such that the tensile strength of the tiles (parallel to the tile/shell surface plane) is optimized for the tile thickness of 0.5 μm, as shown by Lin and Meyers [38].

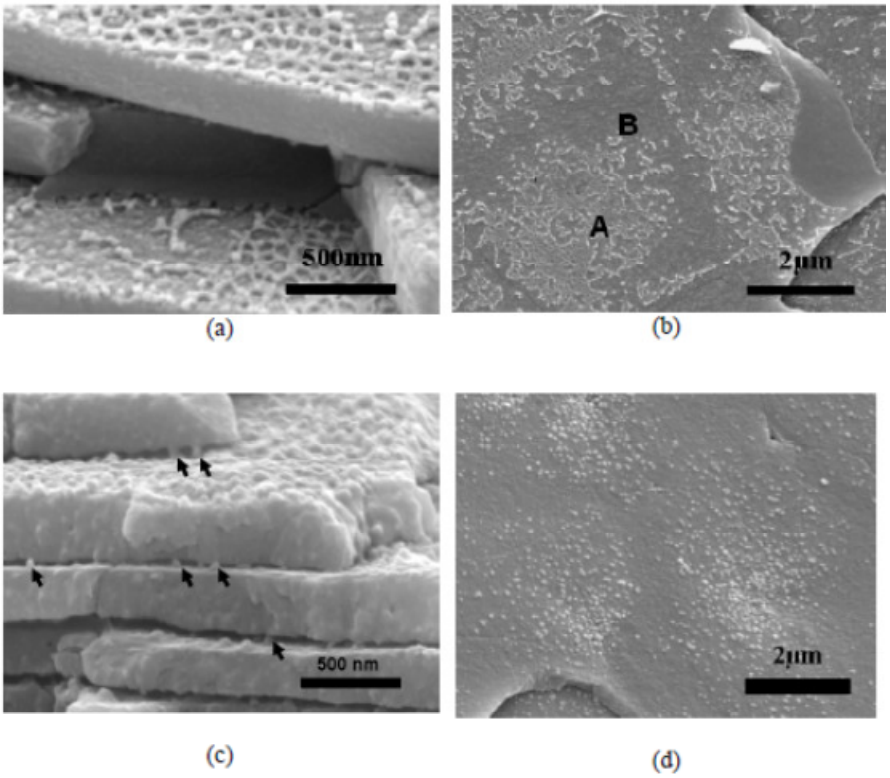


**Figure 2.7:** (a) Interface between tiles (before deproteination) with organic matrix surrounding mineral bridges; (b) tile surface (before deproteination) with regions where organic matrix "A" remains; (c) mineral bridges (marked by arrows) between aragonite tiles after 9 hours of hydrazine deproteination; (d) asperities, many of which are remnants of mineral bridges, concentrated at the center of a aragonite tile after 9 hours of hydrazine deproteination. (source: Lin [65]).

In addition, the mineral tiles' internal structure is a debatable subject. The mineral (nacre) tiles show as single crystalline tablets that contain an organic intracrystalline matrix. For example, Rousseau et al. [82] performed TEM dark field and AFM imaging of the tiles present in oyster Pinctada maxima (Figure 2.8) which confirmed a continous intracrystalline matrix surrounding the mineral 'nanograins' or 'nanoparticles' that make up the individual tiles. In other words, in a nacre tile the mineral diffracts as a single crystal but is made up of a continuous organic matrix

(intracrystalline organic matrix) which breaks the mineral up into coherent nanograins (~45 nm mean size, flat-on) which share the same crystallographic orientation. These have not been the only observations that suggest the idea of the mineral tiles containing an organic matrix, in addition Oaki and Imai [84] found similar results in the pearl oyster Pintada fucata and Watabe [85] offered similar evidence of an organic component existence within the mineral tiles.

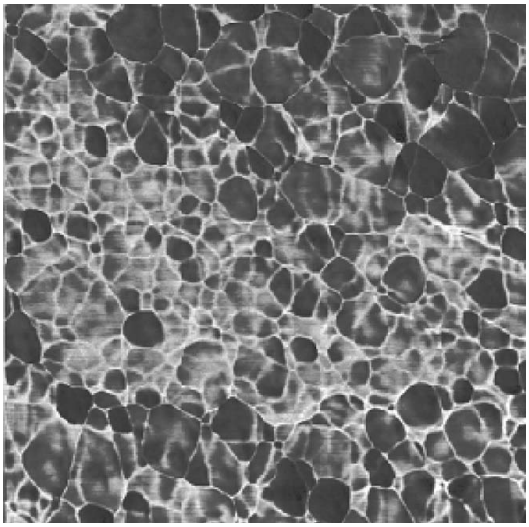

**Figure 2.8:** AFM picture in phase contrast showing the foam-like structure of the intracrystalline organic matrix. The aragonite component inside individual tablets is embedded in a crystallographically oriented foam-like structure of intra-crystalline organic materials in which the mean size of individual aragonite domains is around 50 nm. (*source:* Rousseau et al. [82])

Furthermore, the nacreous portion is composed of mesolayers (level IV) which vary in thickness (on average ~0.3 mm thick) and are composed of organic layers embedded with calcium carbonate mineral [20, 23, 25, 38, 51]. These mesolayers are thought to be the result of seasonal growth patterns (Figure 2.9) when the growth rate of the shell is reduced. Until recently, these mesolayers have for the most part been

disregarded and its effect on the mechanical properties of the nacre has not been accounted for. Previous mechanical investigations will be reviewed in section 2.3 of this chapter.

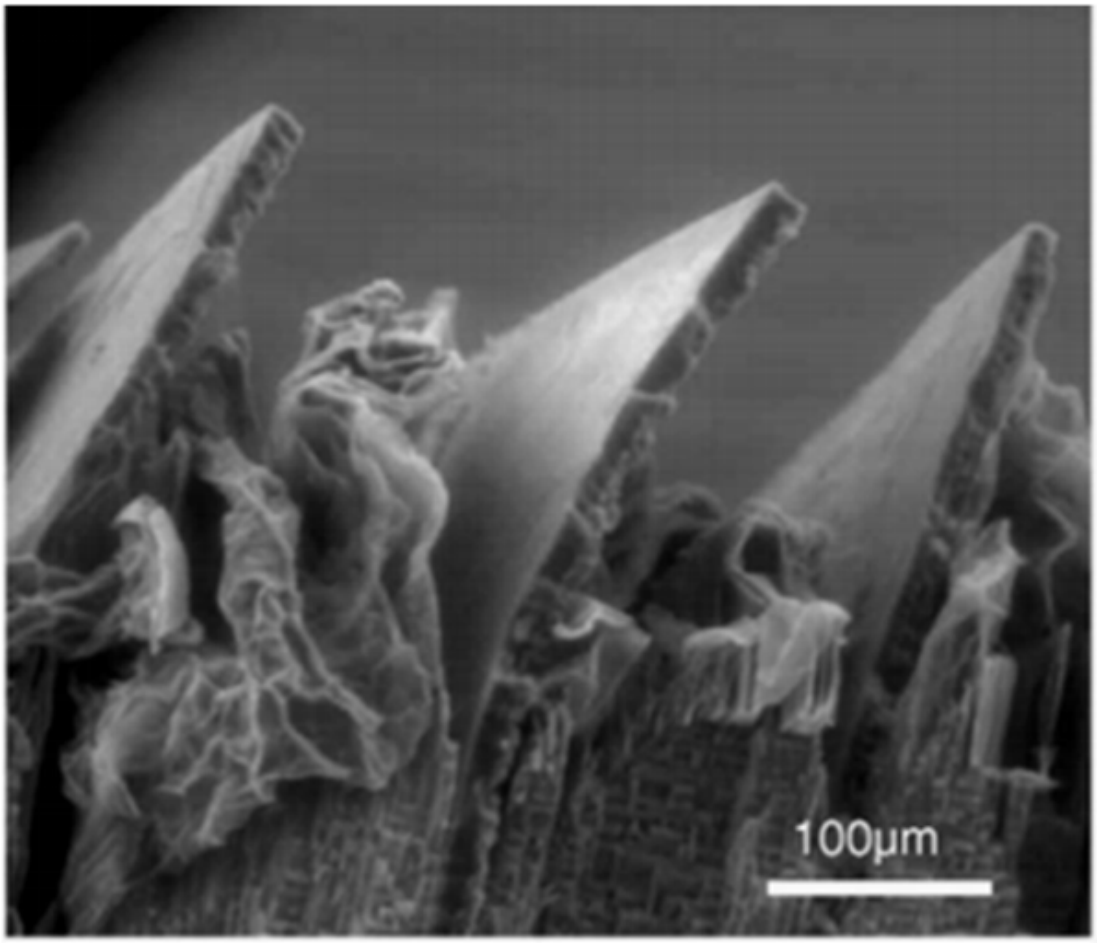


**Figure 2.9:** Mesolayers within a partially demineralized nacreous structure consisting of a thick layer of organic material with an embedment of minerals (Note collapsed nanolayers) (source: Lin [65]).

## 2.2 Biomineralization, Calcium Carbonate, and the Growth of Nacre

### *2.2.1 Biomineralization*

Biomineralization is the process by which living form and influence the precipitation of minerals. Although there is not a single or a 'grand' mechanism that covers all biomineralization processes, all biomineralization requires a combination of effort from cells (the process can be extracellular or intracellular) to produce organic and inorganic molecules to combine in structural ways and form a unique material. Biomineralization is nature's way of providing organisms with a strong building material while being 'cheap' energy wise. Biominerals are created and maintained during life and upon death sometimes retain some of the original characteristics.

Biomineralization begins with an amorphous mineral phase in where the main processes consist of nucleation and crystal growth. These processes depend on the level of supersaturation of the medium and the molecular interactions between the biomineral and organic macromolecules [7]. The organic matrix plays the most important role in Biomineralization.

The level of fluid saturation is extremely important in biomineralization as crystals only form from solutions with relevant ions if the concentration exceeds the solubility product constant. The solubility product constant is the thermodynamic product of all the activities of the ions in a solution in equilibrium with a pure solid. It is defined as:

$$K_{sp} = [C^+]^{f_C^+}[A^-]^{f_A^-} \tag{2.1}$$

Where $K_{sp}$ is the solubility product constant, $[C^+]$ and $[A^-]$ are the ion concentrations, and $f_c^+$ and $f_A^-$ are the square of mean activity coefficient of ions. Therefore, if the concentration of only one type of ion is increased crystallization might occur. This solubility product constant is specific for particular arrangement of ions; for example for calcite $K_{sp}$= 4.7 x $10^{-9}$ $Kmol^2$ $m^{-3}$, while for aragonite $K_{sp}$= 6.9x$10^{-9}$ $Kmol^2m^{-3}$ making aragonite a less stable polymorph, however, in seawater magnesium ions interfere with the crystallization process which leads the favoring of aragonite. Additionally, the number of nuclei formed within a volume is a function of the level of saturation. Below a saturation level 'S*' the nucleation rate is low (Figure 2.10). At a range where nucleation is possible the solution is known as metastable. Above 'S*' (or by seeding) the rate of nucleation is increased.

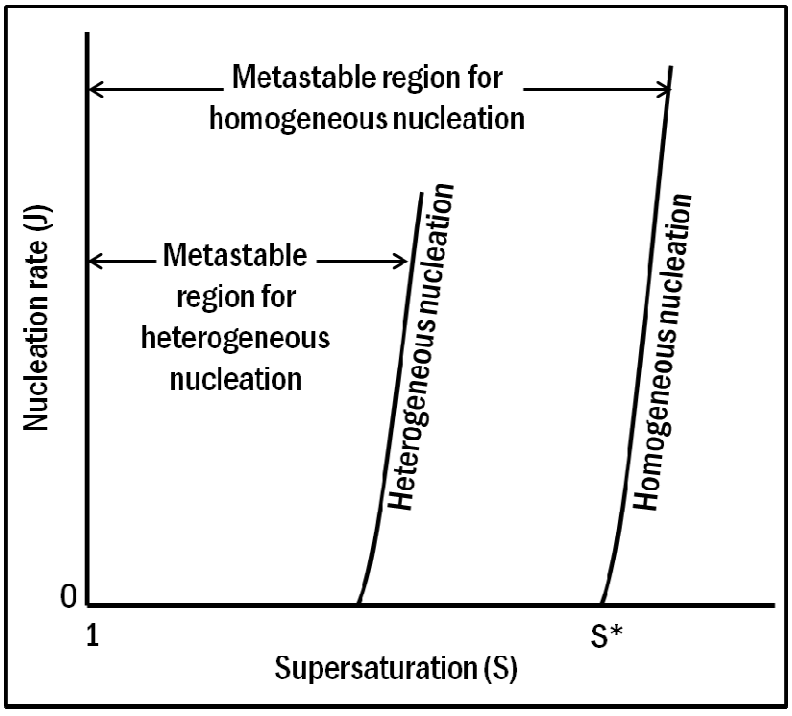


**Figure 2.10:** Super saturation levels effect on nucleation rate(adapted from Garside et al. [86]).

Supersaturation occurs when the pressure in the newly formed solid, $P_s$, is less than the pressure of the liquid, $P_L$. This causes a change in free energy per unit volume between the liquid and the new solid phase. This change in free energy is balanced by the energy gain of creating a new volume, and the energy cost due to creation of a new interface. In other words, for a stable crystal nucleus to be attained, the expenditure of the interfacial energy $\Delta G_i$ has to be balanced by the energy released in the formation of bonds in the aggregate $\Delta G_{vol}$. This occurs at the maximum $\Delta G$ (when $\frac{dG}{dr} = 0$) (Figure 2.11) given that:

$$\Delta G = \Delta G_i + \Delta G_{vol} \tag{2.2}$$

Where $\Delta G_i$ is the energy loss due to surface tension and $\Delta G_{vol}$ is the negative free energy released by the bond formation. The energy loss due to surface energy, $\Delta G_i$, is defined as:

$$\Delta G_i = aL^2\sigma \tag{2.3}$$

Where a is a shape parameter, L is the crystal length, and σ is the energy per unit area (surface energy). The negative free energy released by the bond formation, $\Delta G_{vol}$ is defined as:

$$\Delta G_{vol} = bL^3\Delta G_v \tag{2.4}$$

Where b is a shape parameter and $\Delta G_v$ is the energy per unit volume. The surface energy dominates when the average nuclei radius is less than the critical radius and the

volumetric energy dominates when the average nuclei radius is greater than the critical radius.

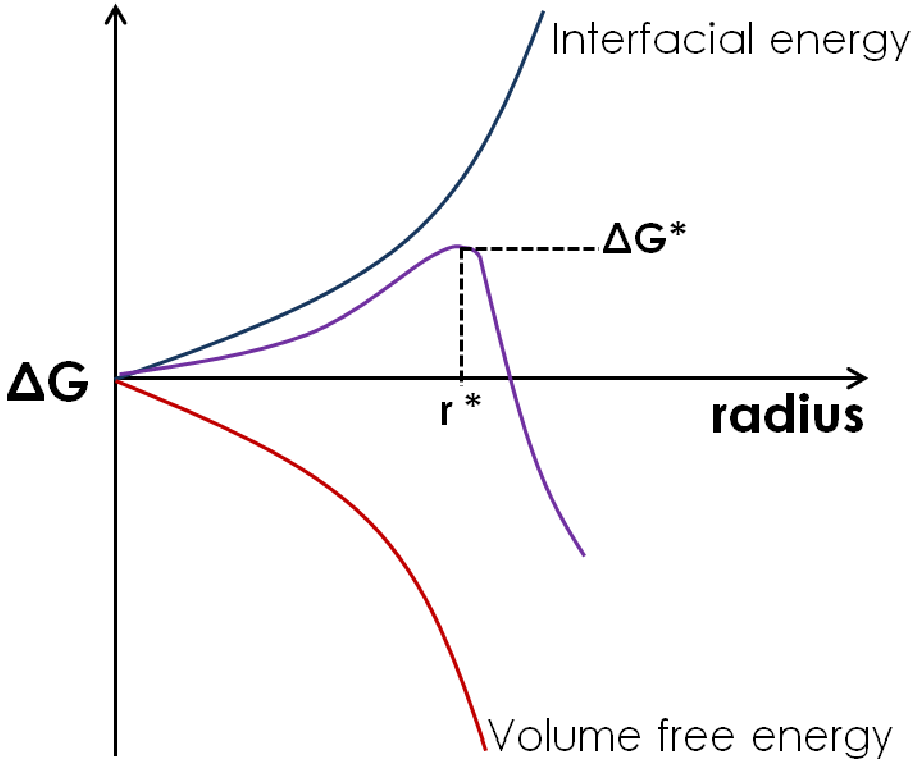


**Figure 2.11:** Free energy of nucleation as a function of cluster size.

In a homogeneous nucleation, as the concentration increases ions associate into small unstable clusters that dissociate if the critical radius, r*, is not reached. Energy is required to add molecules until the critical radius is reached. At a radius below r* the surface energy dominates, while above r* the volumetric energy dominates. This critical radius is approximately within the range of 10 to 1000 ions [9]. However, nucleation of crystals in biological systems is far from a homogeneous nucleation. In biological

systems the site of the mineral deposition is for the most part isolated from the environment. This isolated location is such that to control the size of the site to limit diffusion into and out of the system. The ion supply and removal then occurs by active pumping by organelles near the sites of mineralization. Biominerals are created through a heterogeneous nucleation where organic substrates and components affect nucleation by lowering the activation energy by lowering the interfacial energy (Figure 2.12). External molecules, ions and other surfaces are always present where the mineral can be deposited. Therefore the process can continue at lower saturation levels requiring less energy.

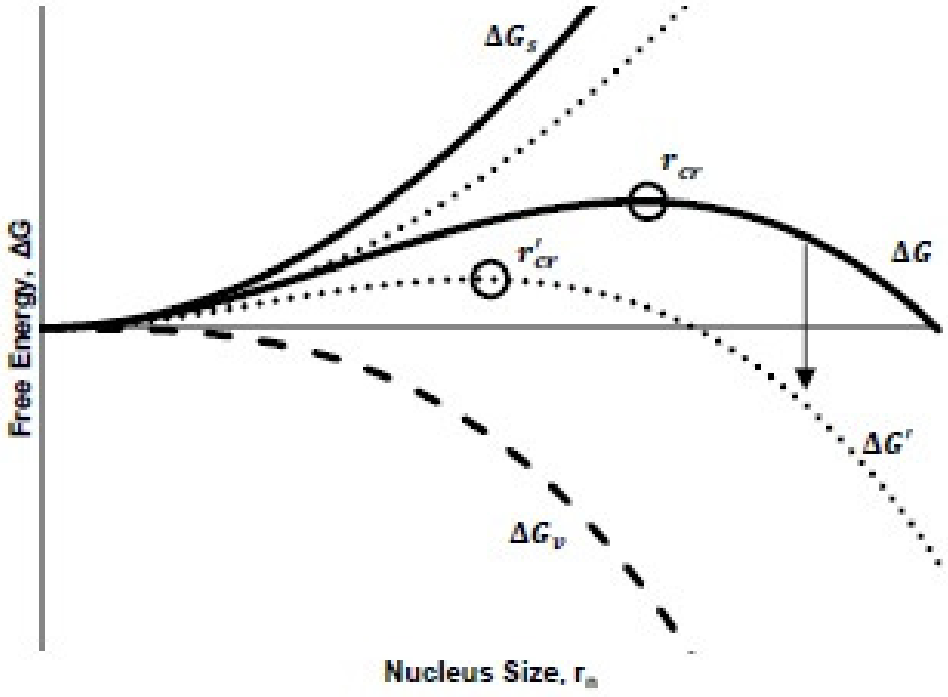


**Figure 2.12:** Heterogeneous nucleation compared to homogeneous nucleation. Primed values indicate parameters associated with a lowered free energy barrier due to heterogeneous nucleation. (source: Porter [87]).

Once nucleation occurs, the growth of the crystal may occur by two methods: ‘kinks’ or ‘screw dislocation’. Kink growth occurs by an inconsistent addition of ions on to the crystals where dislocations and steps may form (Figure 2.13). This occurs as tiny crystals form on a smooth face, an edge, or on a step forming a ‘kink’. Addition onto these ‘kinks’ is energetically favorable. Thus, kinks fill in preferentially and the crystal grows uniformly.

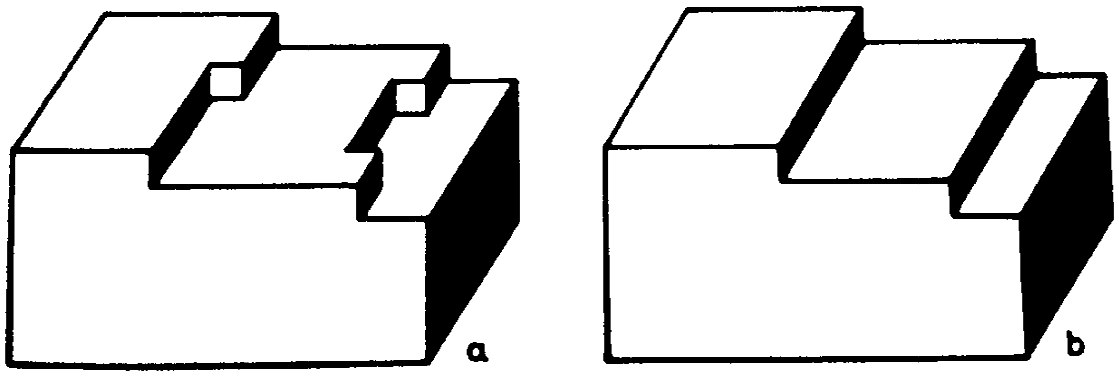


**Figure 2.13:** Surfaces of crystals showing (a) steps with kinks (growth sites) and (b) the result of flling these sites so that only steps remain. (source: Mann [7])

Growth by screw dislocation occurs by the inclusion of foreign ions or [88] mismatches in surface lattice which initiates a step. Then the growth occurs in a spiral manner, which turns into a growth pyramid with various steps (Figure 2.14).

The crystal growth is particular to an individual case. Some growth modifiers exist that can alter the process including:

1. The rate supply of ions
2. The rate of diffusion.
3. The adsorption and repulsion by the charges of ions in the crystal lattice.

4. The number of sites (or kinks) available for addition as this will affect the rate of adsorption
5. Other inhibitors as external ions can react and cover the lattice interfering with the adsorption process.

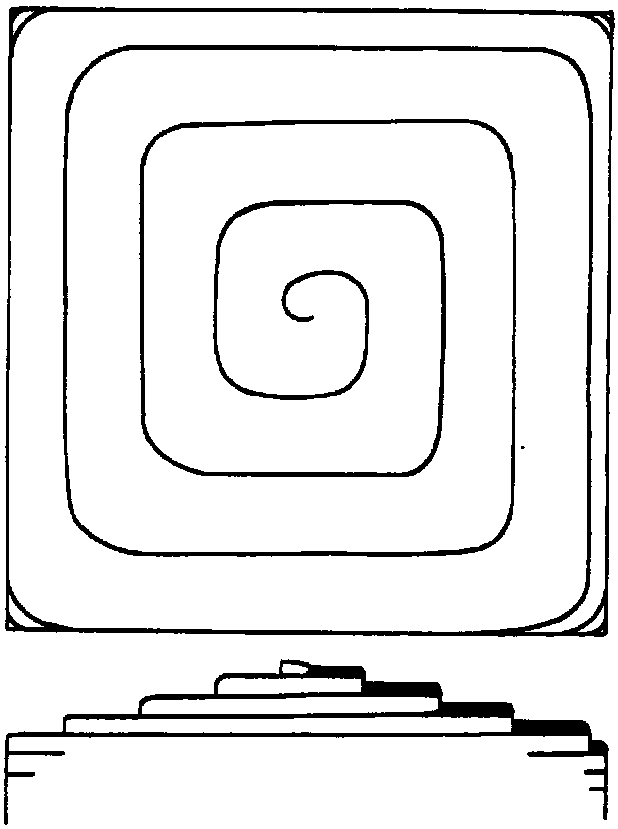

**Figure 2.14:** Growth pyramid due to a single screw dislocation (*source: Burton et al. [88])*

Finally, as previously mentioned, the organic substrate (or matrix) affects the mineralization process. The organic substrate controls mineralization by different methods as different organic constituents act out different functions such as [9]:

1. Anionic groups concentrate $Ca^{2+}$ ions on specific sites and induce supersaturation for nucleation.
2. Soluble matrix proteins inhibit mineral deposition and control mineralization.
3. Matrix proteins favor the growth of particular isomorphs.
4. Soluble matrix proteins are sometimes overgrown by the mineral and influence the strength of the crystal.
5. Insoluble matrix proteins are covered by reactive soluble proteins and function as a structural framework.

*2.2.2 Calcium Carbonate*

Calcium carbonate is the most abundant of the biominerals. Many polymorphs exist, including: calcite, aragonite, and vaterite (Table 2.1). Calcite is the most stable of the polymorphs at ambient conditions. Aragonite is a quite common polymorph at supersaturated aqueous solutions containing $Mg^{2+}$ at a molar ratio of Mg to Ca greater than 4, which is really common in seawater. Vaterite is less the less common of these as it is a metastable polymorph.

**Table 2.1:** Characteristics of the most important $CaCO_3$ mineral phases (adapted from Fricke and Volkmer [89]).

| Mineral (formula) | Crystal system (space group) | Spec. density [g/cm$^3$] | Solubility [-log $K_{sp}$] | Biologic occurrence |
|---|---|---|---|---|
| Calcite ($CaCO_3$) | Trigonal ($R\bar{3}c$) | 2.71 | 8.48 | Very Common |
| Aragonite ($CaCO_3$) | Orthorhombic ($Pmcn$) | 2.93 | 8.34 | Very Common |
| Vaterite ($CaCO_3$) | Hexagonal ($P6_3/mmc$) | 2.54 | 7.91 | Rare |

In the case of biological materials, these minerals are not isolated in living organisms, but connected with the organic materials, forming complex hierarchically structured composites. In the case of the abalone shell, the different polymorphs exist within the shell and are separated in different sections by a precise control of the outer epithelium.

Each structure regardless of complexity is formed directly by a single layer of epithelial cells. These cells are involved in movement of mineral ions to the site of deposition and in the secretion of organic matter that will become the matrix of the deposit [90]. In mollusks, ion movement is bidirectional and occurs through six compartments: the outer medium, body epithelium, blood and tissues, mantle epithelium, extrapallaial fluid, and the shell (Figure 2.14). The ions are provided from the environment and from the animal's metabolism.

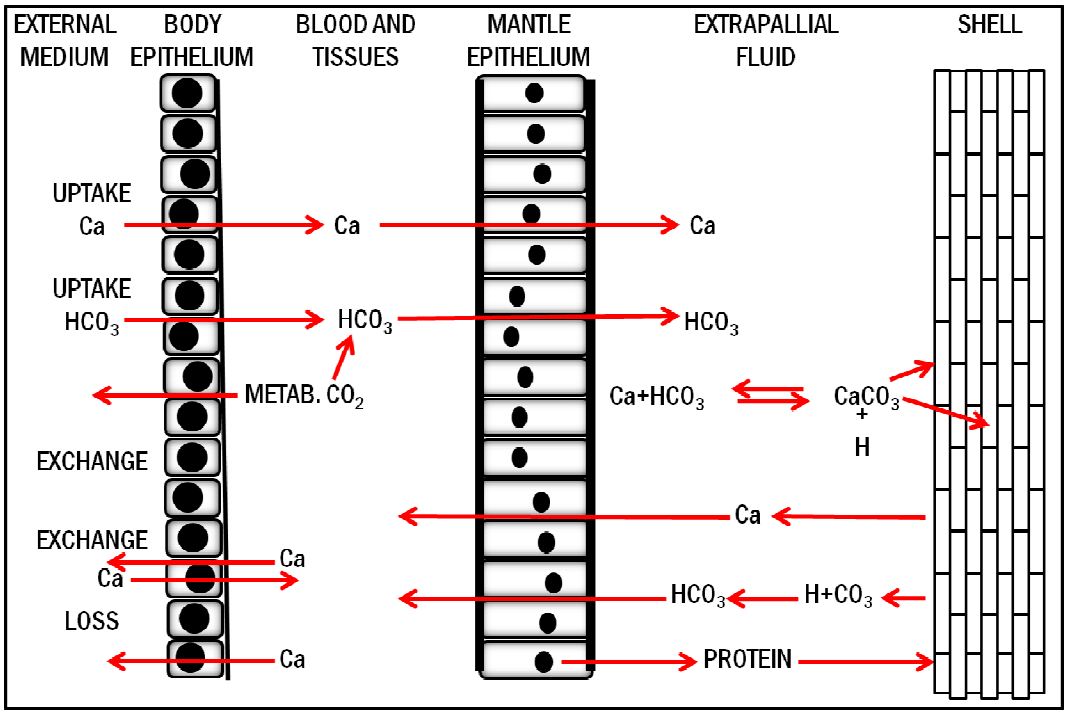


**Figure 2.14:** Ion movement through compartments allowing deposition and nucleation (adapted from Wilbur and Saleuddin [90]).

Calcium enters from the hemolymph down an electrochemical gradient but when the calcium ions leave the epithelial cells they require an increase of energy that is supplied by adenosine triphosphate (ATP) to surpass the extrapallial fluid. Then, crystal formation requires even more energy to raise ion activities above solubility constant.

*2.2.3 Growth of Abalone Nacre*

Although the mechanisms of Biomineralization of abalone nacre are not completely understood there has been much effort in providing reasonable explanations on the subject.

The UC Santa Barbara group was a pioneer in the field with their in vitro studies in which “flat pearls” were produced by red abalone [16, 19, 91]. This work revealed that a specialized nucleating sheet of protein governs the first nucleation of highly oriented crystals of calcite to form a “primer”, then differential secretion of two different families of soluble polyanionic proteins mediate the “genetic switch” controlling the transition from the synthesis of calcite to the production of aragonitic nacre, and the soluble polyanionic proteins cooperatively direct the crystallization process, controlling polymorph selection and atomic lattice orientation.

In addition, because the structure of nacre covers a large distance maintaining its order, further theories have risen to explain additional mechanisms. The first is the crystallization within preformed organic matrix compartments [34, 92-94].

A second is a quantized secreation and subsequentent crystallization (a layer by layer formation of the organic matrix and mineral crystals) [71, 95].

The third theory is heteroepitaxial capping [96], a termination of the crystal growth, followed by heteroepitaxial nucleation of the next crystal layer.

These theories propose that each crystal layer is nucleated on the organic matrix. Other models imply that nacre is not formed by a direct nucleation of each layer on the organic matrix, but through a continuous growth of the aragonite crystals from layer to layer through holes or pores existing in the intertile organic layers [14, 48, 95, 97, 98]. The main experimental support for this model is that tiles remain atomically coherent and unicrystalline from layer to layer and the intertile organic matrix has been significantly

studied [71] and the pores have been visualized [14, 44, 45, 48, 99-101]. By this model, the pores control the position of the nucleation sites for the tile growth and thus the aragonite grows as a single crystal maintaining its crystallographic alignment in the c-, a- and b-axis.

Other models explaining the coherence crystallographic orientation between neighboring tables exist. Studies by Checa et al. [43] hypothesize a different model of that proposed by Nakahara [99] model for gartropod nacre growth) of preformed organic matrix compartments in where the intertile organic membranes are formed after the organic rich core of the tiles. This model suggests that first the tile grows in height with its tip embedded within the surface membrane and an organic rich core is formed as the growing tablet absorbs its components. Then, as the growth of the c-axis ends, a new intertile organic membrane is secreted and finally the growth of the new tile begins (Figure 2.15).

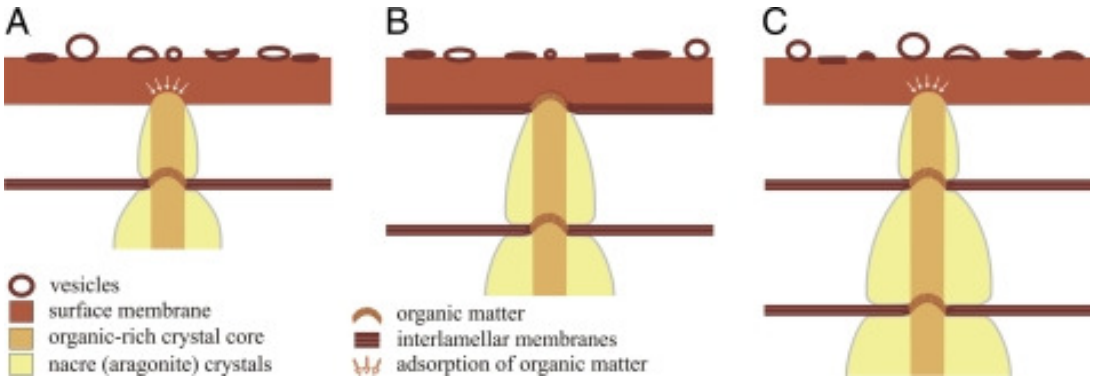


**Figure 2.15:** Scheme for the formation of incipient nacre tablets. (*A*) The tablet core grows rapidly in height with its tip immersed within the surface membrane. An organic-rich core is formed as the growing tablet absorbs components of the surface membrane. (*B*) At the same time that vertical crystal growth ceases, a new interlamellar membrane is secreted at the nacre side of the surface membrane. During this time interval, organic material may precipitate on top of the tablet core. (*C*) Growth of a new tablet commences. (source: Checa et al. [43]).

Much effort has been done to understand the growth and formation of the abalone shell; however, for the purpose of this study the study reported by Lin and Meyers [38] is the most relevant. This past study investigated the various transition periods which occur during the process of shell formation.

Inorganic $CaCO_3$ goes through morphological changes between the mesolayers (Figure 2.16a). These mesolayers, or growth bands are 20 μm thick and are distributed a couple of hundred of micro-meters apart. These differences in morphology are shown in Figure 2.16 b where the growth occurs from bottom to top. These five regions were identified by tiled (A); block-like aragonite (B); organic/inorganic mix (C); organic (D); and spherulitic (E). It is worth mentioning to note that prior to the arrest of growth, the characteristic tiles are replaced by a block-like structure followed by a immense deposition of the organic layer. Lin and Meyers [38] summarized the sequence of events that occur between the formations of a mesolayers Figure 2.17.

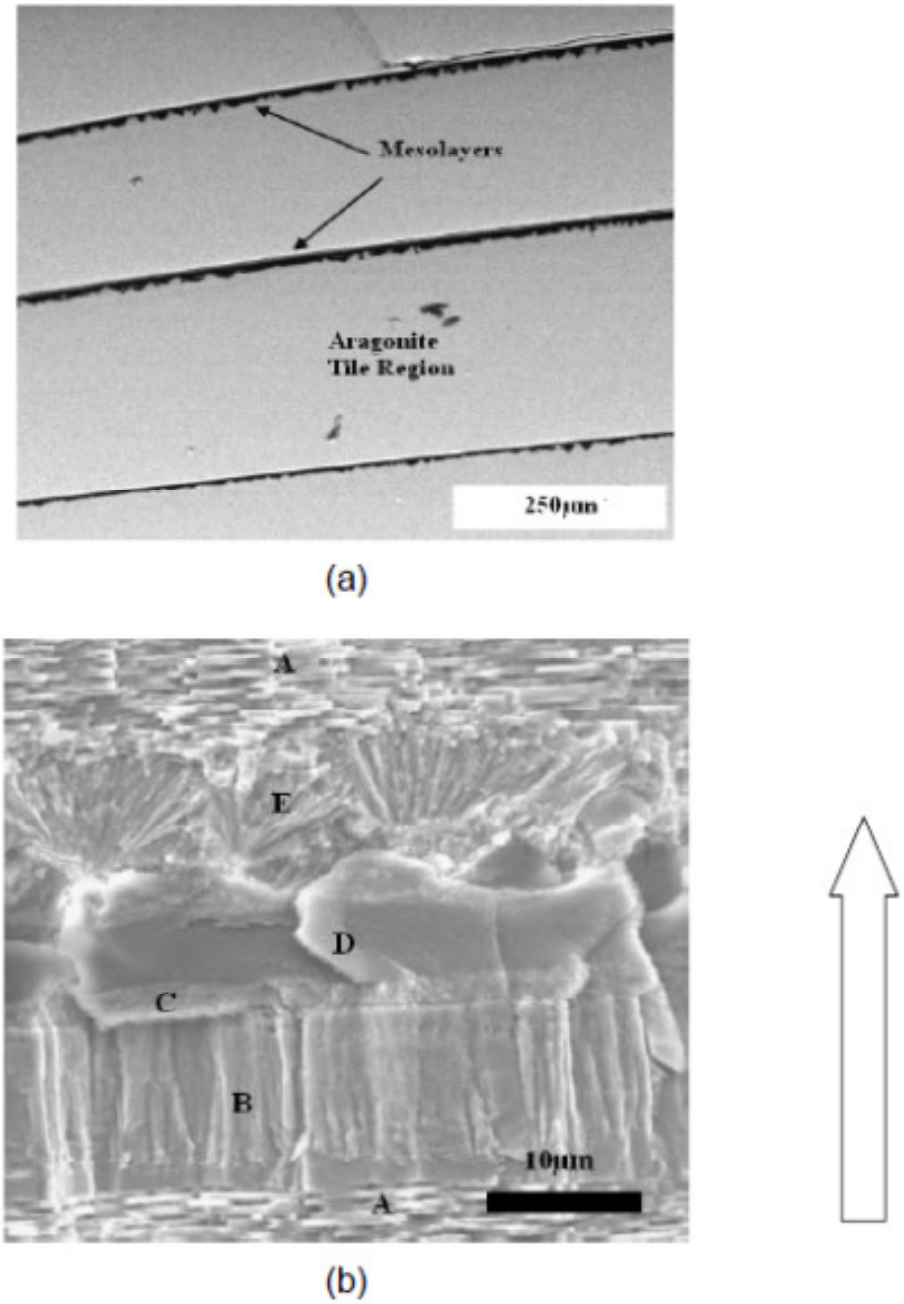


**Figure 2.16:** (a) Macrostructural view of a cross section of the *Haliotis rufescens* shell. Growth bands are observed separating larger regions of nacre, (b) SEM micrograph of fracture surface; direction of growth marked with arrow (source: Lin and Meyers [38]).

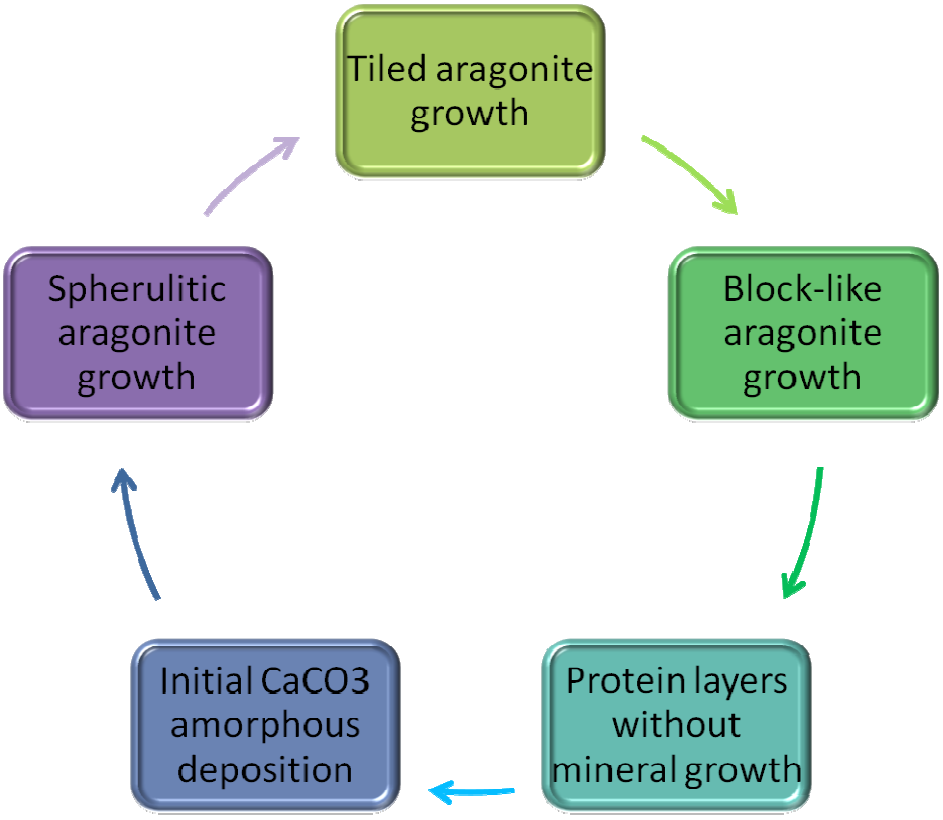


**Figure 2.17:** Order of events during mesolayer growth in nacre (source: Lin and Meyers [24]).

In the study, the flat pearl technique (as described in chapter 3) was utilized to observe the development of these different areas over a period of time. However, it is very important to note that this study was conducted with red abalone maintained in constant conditions. The abalone was maintained that is in water at ~15° C and with abalone fed regularly. The results are summarized in Figure 2.18. One week after implantation a precursor amorphous aragonite is begins to appear on the substrate. Two weeks after implantation, the precursor aragonite has spread across the entire substrate. On the lower half of Figure 2.18 it can be noticed that the morphology of deposited

mineral transitions to spherulitic aragonite between the second and third week. After three weeks of implantation the tops of each spherulitic bundle appear flattened. After four weeks of implantation, the spherulites are fully formed as a result of the divergent growth of aragonite columns along the fast growing c-axis direction. They spread apart into a lower density as growth continues after five weeks of implantation. Between five and six weeks of implantation the aragonite morphology transitions towards the regular tiled aragonite microstructure as shown at the top of Figure 2.18.

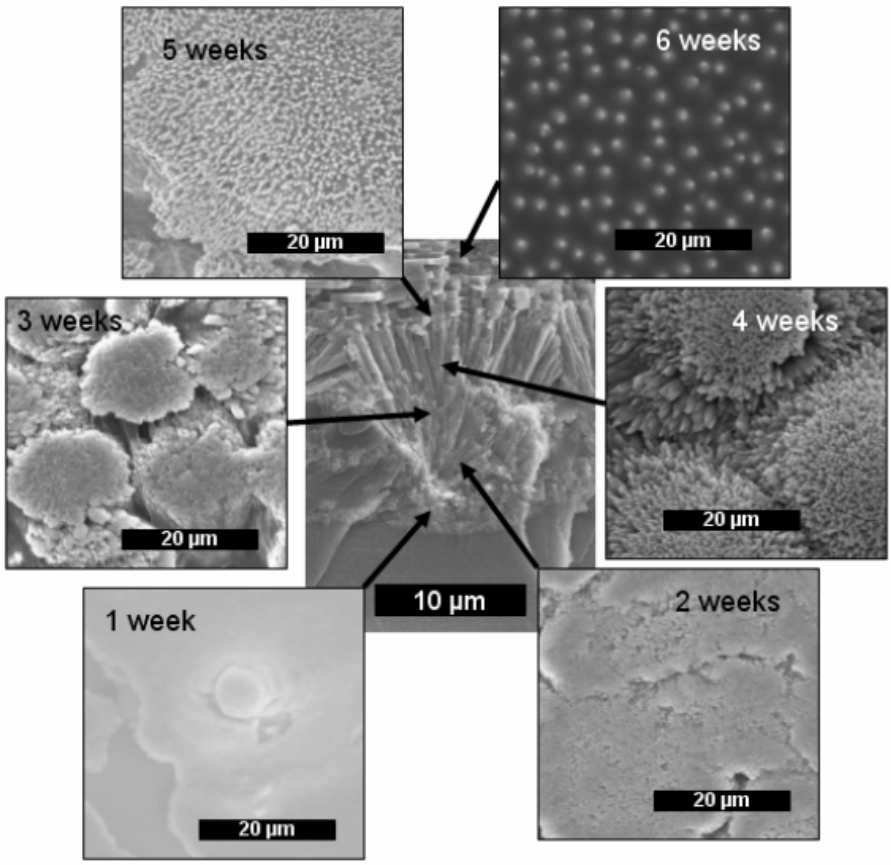


**Figure 2.18:** Summary of sequential growth from flat pearl and trepanning experiments (source: Lin and Meyers [24]).

Additionally, transmission electron microscopy was performed on the aragonite tiles. The TEM images of two samples are shown in Figure 2.19. The results show a high degree of crystallographic texture aligned normal to the plane of the tiles. The tiles show a consistency in orientation which supports the 'growth sequence through mineral bridges' theory proposed by Meyers et al. [48] that will be described in depth in chapter 4.

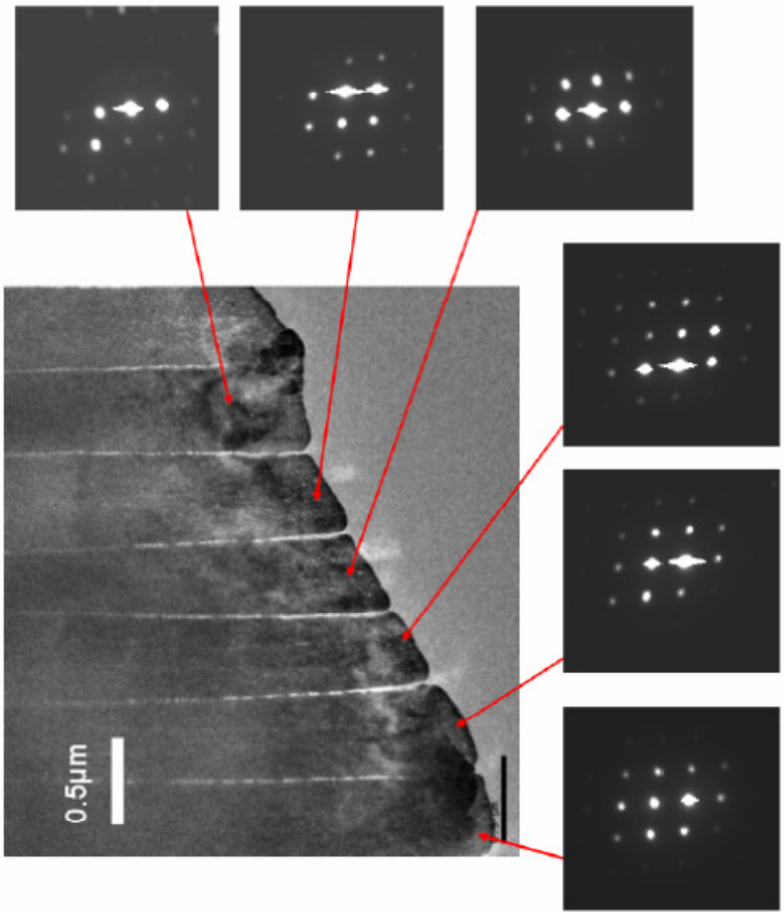


**Figure 2.19:** Transmission electron microscopy of tiled aragonite nacre with selected area diffraction (source: Lin [65]).

Lin and Meyers [38] hypothesized that this transition may occur as the ends of each spherulitic needle become nucleation sites for aragonite tiles. The intermittent deposition of the organic matrix which is believed to inhibit crystal growth [35] molds the spherulitic aragonite needles into an increasingly laminate structure, eventually reaching the steady-state aragonite tile formation. At six weeks the tops of the terraced cone tile columns can be seen to protrude through intermittent thin organic sheets. They are spaced approximately 3-5 μm apart, indicating a density much less than the density of spherulitic needles.

Lin [24] proposed that the animal forms the structure of the shell through a mechanical-chemical action, and by this also allows for the flattening observed in the shell. This mechanical interaction of the animal is believed to mold the design of the shell as it is built. The abalone has a strong muscle contraction between the foot and the shell, which approximates to equal and opposite force applied normal to the growth surface of the shell, shown schematically in Figure 2.20. As the animal moves along a surface it twists also twisting the epithelial layer in the mantle. This produces a sanding effect over the shell. This study is further supported by the results discussed in chapter 5.

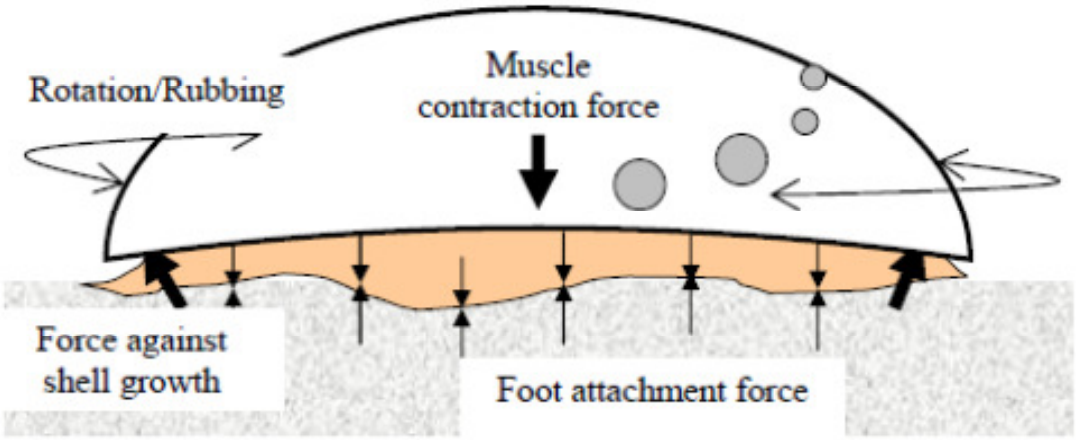


**Figure 2.20:** Schematic of the forces acting on the growth surface of the shell (source: Lin [65]).

The growth rate was approximated to 1 tile per day, or 0.5 µm/day ($5.78 \times 10^{-12}$ m/s). However, as it will be demonstrated, the growth rate in abalone can vary extremely. Lapota et al. [102] report growth rates for red abalone to average at around 100 µm/day (in length). Zaremba et al. [19] reports maximum growth rates of 5µm/day, while Fritz et al. [17] describe growth velocities averaging to 14 µm/day.

Additionally, it is noteworthy that it was reported by Lin [65] that after six months of the controlled culturing of the abalone, changes in the growth patterns were noticed. Environmental changes occurred in the circulating seawater in the holding tank which caused a change from the tiled aragonite to a block-like structure identified by Su et al. [20] as aragonite. This sample was reported to be brittle in comparison to previous samples. These changes were believed to be changes in the physical status of the animal due to the changes in environment. It is this issue that was of interest and was addressed and investigated in this current report.

## 2.3 Mechanical Properties and Structure Relationship

### *2.3.1 Untreated Nacre: Early Work*

Much work has been done on quantifying the mechanical properties of nacre. In 1977, one of the earliest experiments was reported by Currey [55]. He performed tensile, compressive, and bending tests on many bivalves, gastropods, and cephalopods. Results concluded that the bending fracture strength ranged between 56 to 116 MPa. The characteristic stress-strain curves show an elastic region followed by plastic behavior before failure. In 1988 Jackson [103] gave values of elastic moduli at approximately 70 GPa (dry) and 60 GPa (wet) and tensile strength of approximately 170 MPa (dry) and 130 MPa (wet) in nacre from the shell of a bivalve mollusc, *Pinctada imbricata*. In another study in 1990 Sarikaya et al. [41] reported a fracture toughness of 8±3 MPa $m^{1/2}$ of nacre in four-point tests and a fracture strength of 185±20 MPa in three-point bend tests. These results are above most conventional ceramics and comparable to ceramic matrix and metal matrix composites.

### *2.3.2 Untreated Nacre: Compression studies*

*Perpendicular to layered structure*

Quasi-static compression and tension tests were performed previously by Menig et al. [51] and Lin [65]. Lin et al. results are presented in Figure 2.21, they predict a 50% failure probability occurring at approximately 250 MPa for compression perpendicular to the layered structure. This is lower than previous results by Menig et al. [51] of approximately 540 MPa; however, both results are within one order of magnitude and probably due to slight differences in specimen preparation. It is important to note that

because of irregularities in the shell, the results were presented with use of a statistical analysis to quantitatively evaluate the mechanical properties. Therefore the Weibull distribution [104] is applied to quasi-static and dynamic compression data with purpose of giving a clear picture from a scattered range of data points.

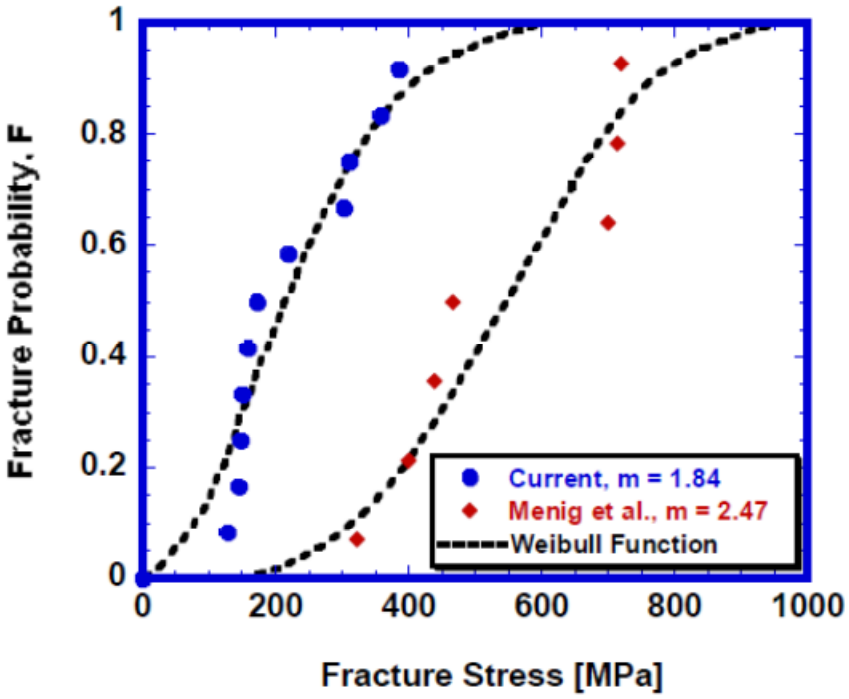


**Figure 2.21:** Compressive strength of freshly sectioned nacre perpendicular to layered structure (source: Lin [65]).

Results from both tests are presented in the Figure 2.21, the diamond makers represent the study by Menig et al. [51], and the circular markers represent the study by Lin et al. [65]. The dotted lines represent the statistical Weibull curve that would correlate to these data points, a Weibull function "m" is found for each data point, 1.84 and 2.47 for the Lin [65] and Menig et al. [51] studies respectively.

*2.3.3 Untreated Nacre: Tension Studies*

*Perpendicular to layered structure*

In previous work by Lin et al. [65] 3mm diameter pucks of nacre were removed from the shell using a diamond coring drill and mounted in cement glue then tested in tension. Thus the samples were cut so that the measurement could be done in the direction perpendicular to the planes of growth. Figure 2.22 from Lin [65] shows the Weibull analysis of nacre in tension perpendicular to the layered structure. Lin found the 50% failure probability at around 5 MPa, which a similar Weibull moduli in tension and compression (2-tension, 1.8-2.47-compression). It is also interesting to note that there is an extreme difference in strength in tension versus compression (ratio on the order of 100, this difference is much higher than that found in conventional brittle materials ratio on the order of 8 to 12).

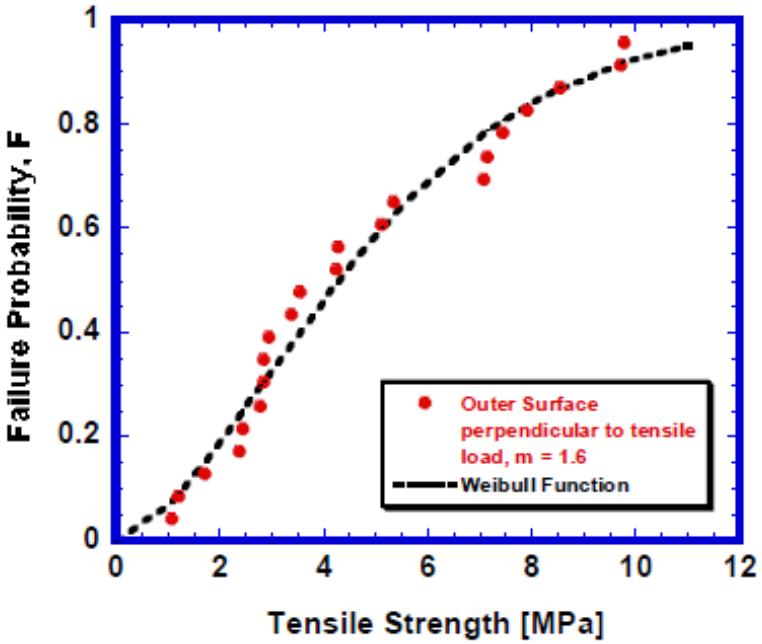


**Figure 2.22:** Weibull distribution of tensile strength perpendicular to layered structure (source: Lin [65]).

*Parallel to layered structure*

Tensile strength studies parallel to the growth planes were additionally performed [65]. "Dog-bone" shaped samples were sectioned from the shell and tensile tests were performed parallel to tile planes in quasi-static loading at a strain rate of 0.05 mm/min. Figure 2.23 shows the Weibull statistical analysis of the results obtained, where a 50% failure probability when a load of approximately 65 MPa was applied and the Weibull parameter was found to be 1.8. Other results from Jackson [103] and Barthelat [64] demonstrate a higher value, 170 MPa and 100 MPa respectively. It is interesting to note that in all cases the shell shows a lower tensile strength when loaded in the perpendicular direction to the tiles than in the parallel direction and shows the mechanical anisotropy of nacre. Figure 2.24 shows a summary of these results.

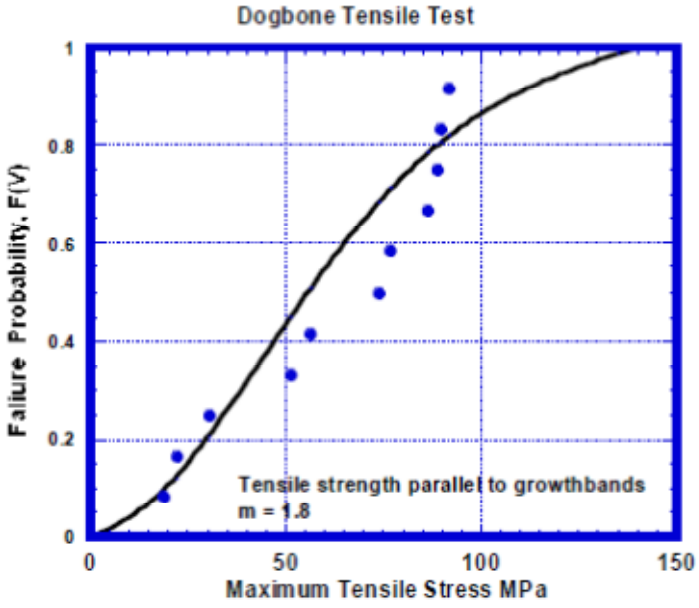


**Figure 2.23:** Weibull distribution of tensile loading parallel to layered structure (source: Lin 2008b).

The mechanical behavior of abalone nacre suggests three main points to be considered. Firstly, the work of fracture in monolithic calcium carbonate was approximately 3000 times less than the ones measured in nacre [55]. Secondly, previous tests show that the hydration is particularly important for the toughness of nacre, e.g. the work of fracture of dry nacre is approximately 350–450 J/m$^3$ and could go up to 1240 J/m$^3$ in wet conditions [103]. Finally, the mechanical performance exhibited strong orientation dependence and a significant strain-rate sensitivity.

The results can be combined to show the mechanical anisotropy of nacre, recapitulated in Figure 2.24. Perpendicular to the layers, nacre exhibits great anisotropy (3-5 MPa vs. 540 MPa). However, when the load is applied parallel to the tiles there is little difference in tensile and compressive strength (65-170 MPa vs. 235 MPa). Additionally, the shell exhibits greater compressive strength when loaded perpendicular to the tiles compared to loaded parallel to the tiles.

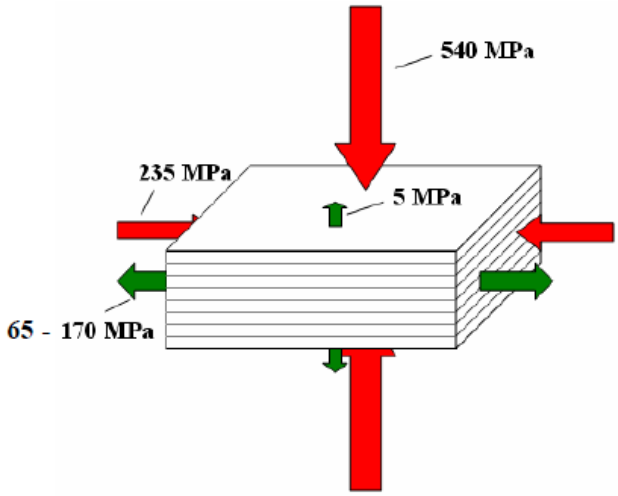


**Figure 2.24:** Strength of nacre with respect to loading direction, parallel lines represent growth bands (source: Lin [65]).

*2.3.4 Untreated Nacre: Scratch Testing and Nanoindentation*

Scratch and nanoindentation tests have been another technique applied to nacre in hopes of resolving the many toughening mechanisms. Mineral bridges embedded within the organic matrix and the asperities on the surface of the tiles are believed to contribute to the toughness of the shell and scratch tests may allow a simple experimental method to uncover some of their effect.

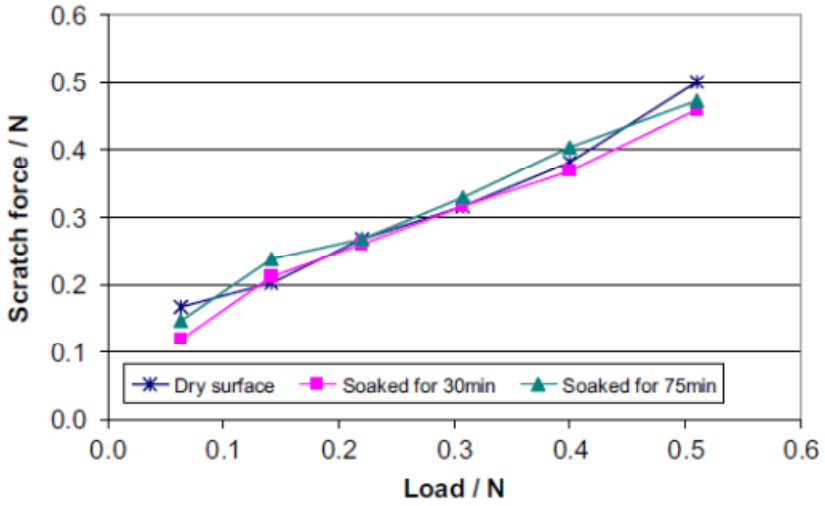


**Figure 2.25:** The average scratch force as a function of the applied load for inner shell surfaces with different hydration levels (source: Leung et al. [105].

Scratch tests (a simplified grinding procedure) can represent the mechanisms of chip formation. Micro-scratch tests have been performed on the surfaces of wet and dry nacre from green mussel shells [105] to compare the effect of hydration in the nacre (Figure 2.25). They report positive linear relationships and characteristics between the scratch force and load. Additionally, similarity on the curves suggests that hydration periods did not have much of an effect on the variation of scratch force on the surface. However, they report opposite results for indentation tests (Figure 2.26), where the

Vickers hardness increases when the nacre is hydrated and the hardness increases with the period of soaking.

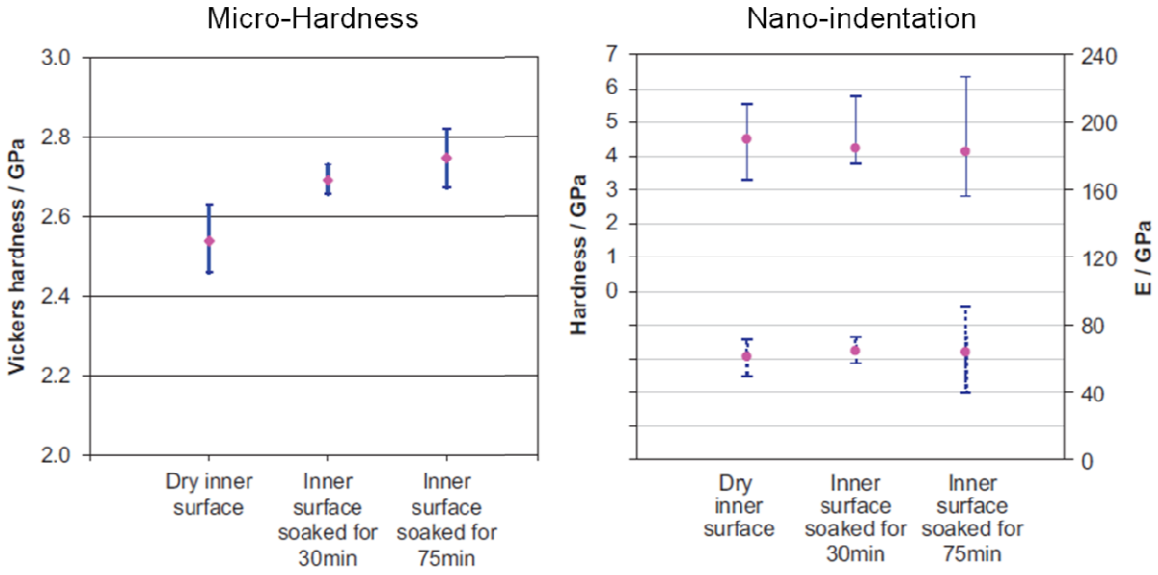


**Figure 2.26:** Variation of Vickers hardness and micro-hardness with different levels of hydration. The upper part of the nano-inentation chart in solid lines shows the nano-indentation hardness, whereas the lower part of the chart in dotted lines shows the modulus of elasticity (source: Leung et al. [105]).

Additional scratch tests on the nacre of Pinctada maxima [106] were performed to understand how the material behaves under different scratch tool geometries and processing parameters. Other tests on natural nacre have been performed in particularly to establish the influence of the cutting speed, the deepness of the cut and the changes in the normal force and tangential force. They report an increase in force with the increase in the depth of the cut (Figure 2.27), which is due to the bigger contact between the material and the tool. Additionally, they show that the tangential forces remain below the normal forces which indicate that the material is easier to remove in the tangential

direction (parallel to the surface of the layers). Variation in cutting speed increases the normal and tangential forces up to 60 N and 30 N correspondingly.

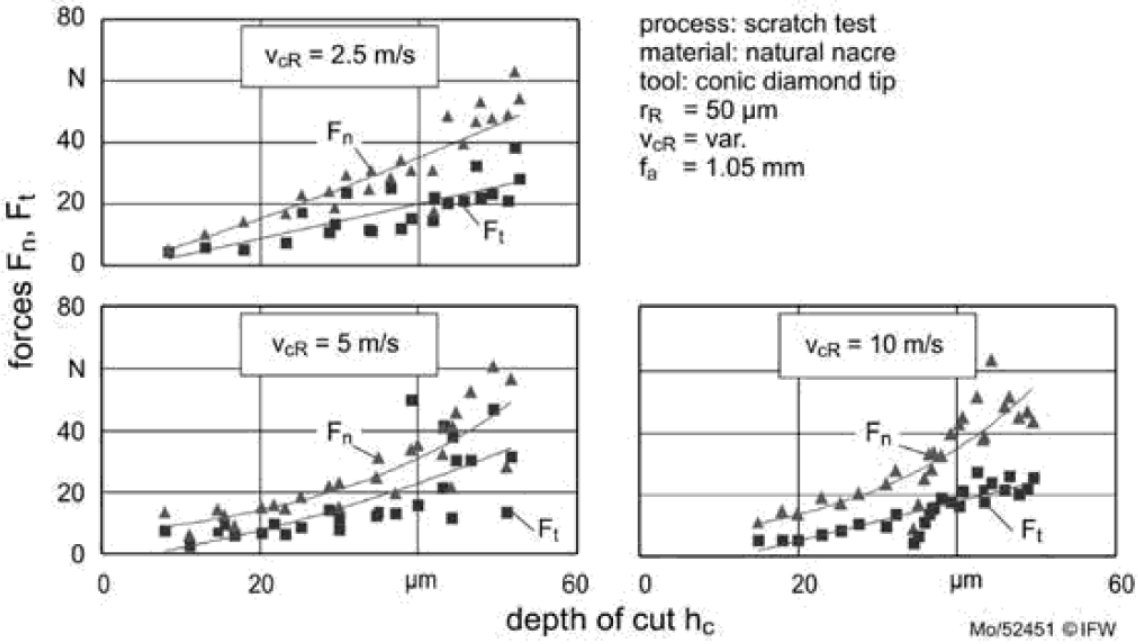


**Figure 2.27:** Influence of the cutting speed (vcR) and depth of cut (hc) variation on the normal force (Fc) and the tangential force (Ft) (source: Denkena et al. [106, 107]).

Furthermore another interesting indentation study is that from Bezares et al. [46] in where nano-indentation is performed on dry and hydrated abalone nacre and compared to monolithic aragonite and to heat treated abalone nacre. They report that the Young's modulus varied with the indentation depth (Figure 2.28) (as depth increased there was an initial exponential decrease in modulus following to a taper to a constant value)[46]. These results additionally suggest two important matters: firstly, that the out-of-plane modulus of nacre is not the same as monolithic aragonite (which is commonly assumed, e.g. Values of 70, 80, and 100 GPa have been used in previous models of nacre as the

Young's modulus of the biomineral by for example Wang et al. [108], Barthelat et al. [109], and Gao et al. [62] respectively) and that the organic layer might influence by maintaining the sample hydrated. These significant results will be described in further detail in section 2.3.5.

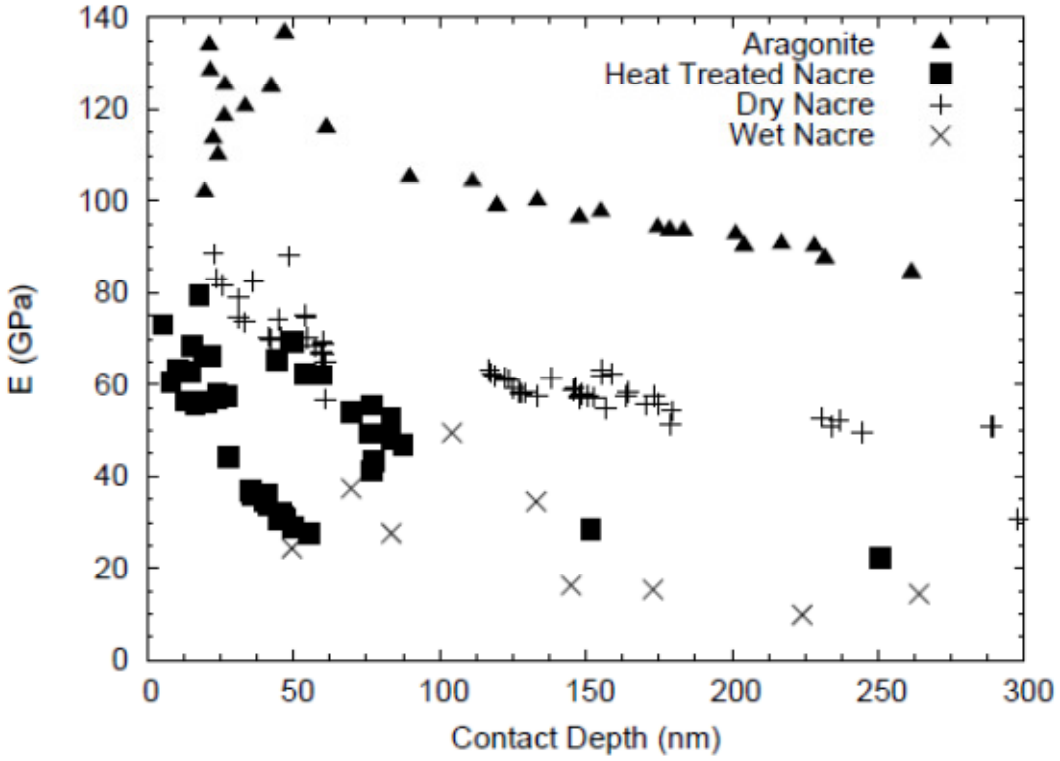


**Figure 2.28:** Young's modulus *vs.* indentation depth for monolithic aragonite, heat treated nacre, dry nacre, and wet nacre. (source: Bezares et al. [46])

*2.3.5 Treated Nacre: Deproteinized and heat treated nacre*

The mechanical response of the aragonite tiles has been a subject of interest. The aragonite ceramic is considered to have a plastic response and presumably viscoplastic. Additionally, because of the content of organic component within the tiles that forms the

'nano-grain' structure the aragonite tiles in nacre shows a higher toughness when compared to monolithic aragonite. This is believed to be an effect of the micro-crack deflection within the 'nano-grains' and crack blunting [67].

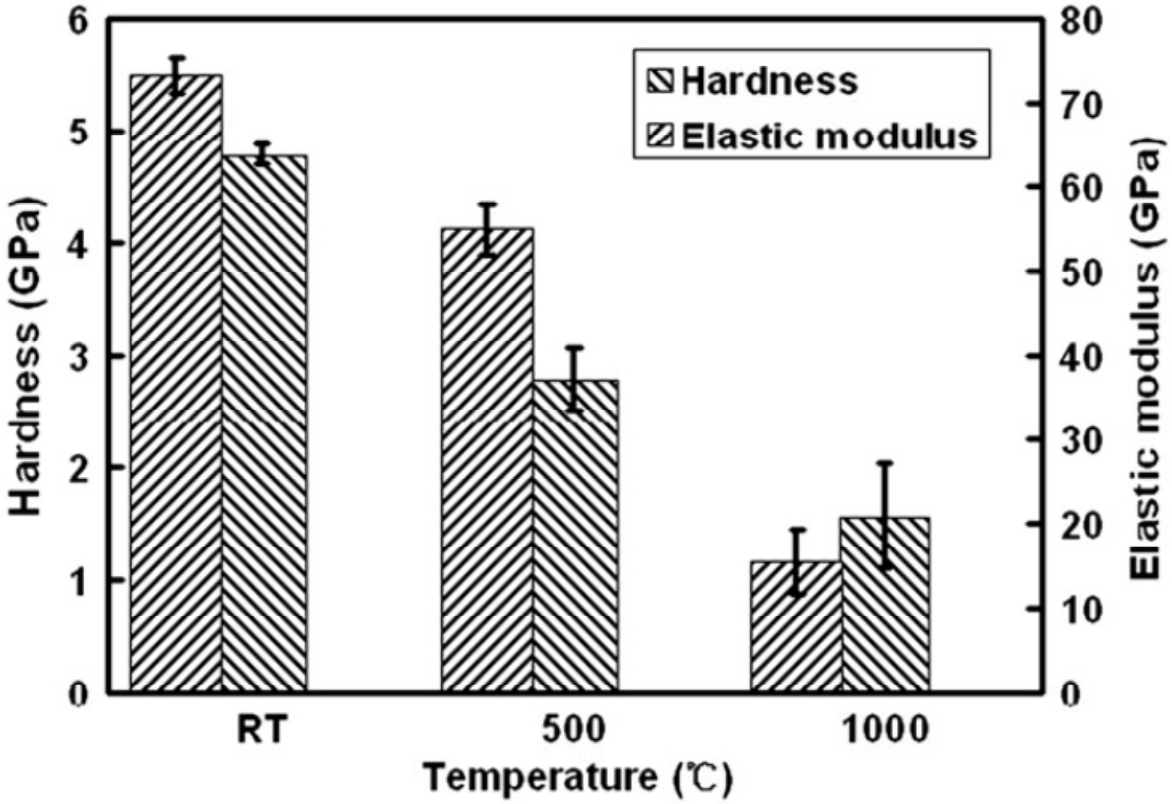


**Figure 2.29:** Hardnesses and elastic moduli of the fresh and heat treated nacre. (source: Huang and Li [110])

One method of testing the mineral component in nacre is to isolate it by either chemical deproteinization or heat treatment. Huang and Li [110] performed characterization and mechanical testing (nano-indentation)of heat treated nacre at temperatures of 500 and 1000 °C. They report that when heat treated nacre retains the brick and mortar structure, however, goes through a phase transformation from aragonite to calcite at 500 °C and then to calcium oxide at 1000 °C. When nano-indented, the

untreated nacre exhibits a shallower indentation and less of a indentation displacements than when heat treated at 500 °C. Additionally, more pop-in marks are reported at the 500 °C heat treated nacre than in the untreated nacre, suggesting that the heat treated nacre is more brittle. Huang and Li's [110] results are summarized in Fig. 2.29 where they report a higher hardness and elastic modulus for the untreated nacre. Their results suggest that this decrease in hardness and elastic modulus might be due either to the phase transformation or the loss of the organic constituent.

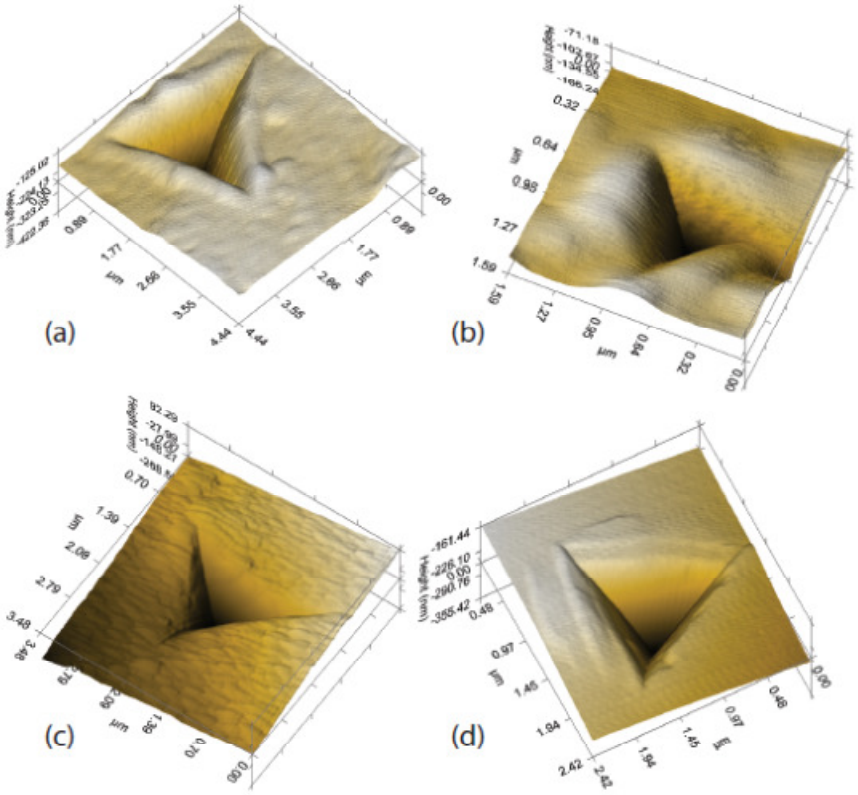


**Figure 2.30:** Indentation profiles on: (a) dry nacre. There are pileups around edges; (b) wet nacre. The blunted appearance of the indentation is related to the compliance of the wet nacre seen from its relatively low modulus; (c) heat treated nacre. The material appears compacted and similar to what happens to sand when it is heated and grains begin to fuse together; and (d) monolithic aragonite. The uneven pileup indicates anisotropy. (source: Bezares et al. [46])

Further tests on heat treated nacre were performed by Bezares et al. [46] in which the specimens were treated for 12 hours at 200 °C. They report differences in the indentation profiles (Figure 2.30) where the untreated wet nacre profiles show more pileups and are more blunted than the profiles for the heat treated nacre. The heat treated nacre profile showed no pile-ups and was described as a 'loosely compacted granular material.'

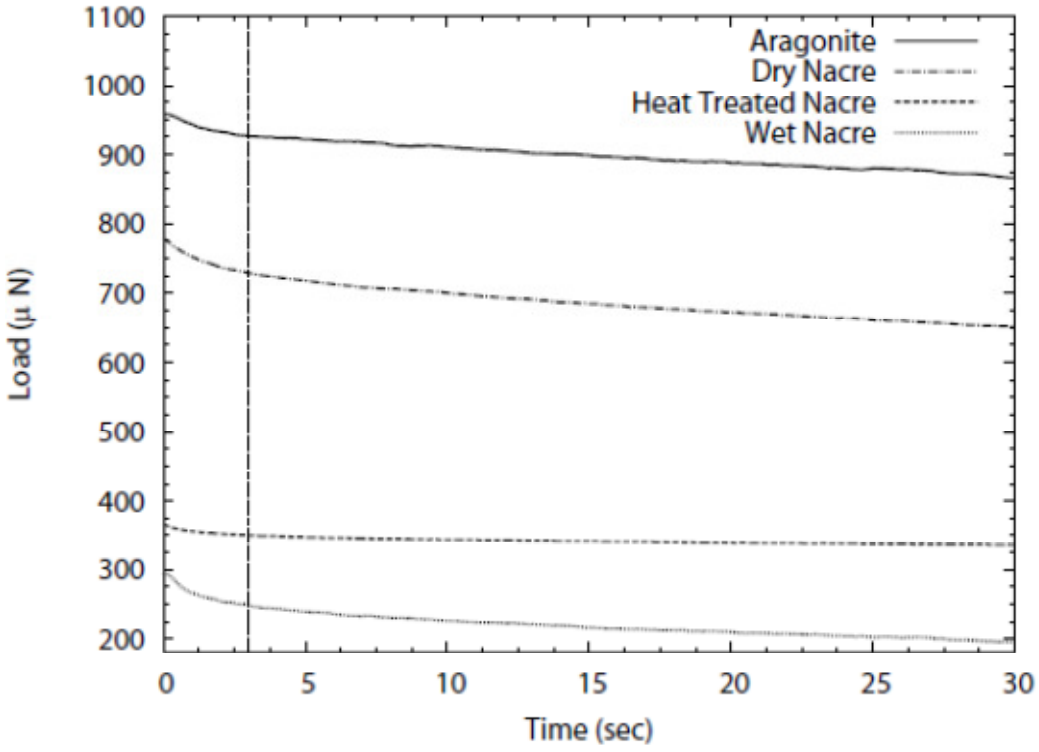


**Figure 2.31:** Relaxation curves for monolithic aragonite, heat treated nacre, dry nacre, and wet nacre. Note the greater amount of relaxation observed in wet nacre and the nearly absent relaxation observed in heat treated nacre. (source: Bezares et al [46])

Additionally viscoplasticity was tested on the nacre tiles and compared to that of the monolithic aragonite. Relaxation tests were performed which show the effect of the organic constituent on time-dependent behavior. Relaxation is pronounced in untreated

(both dry and wet) nacre (Figure 2.31) and less in heat treated nacre. This study concludes that nacre behaves as a viscoplastic solid that behaves as a loosely bound granular material when heat treated. Furthermore, comparing the heat-treated specimens and the untreated specimens it is notable that the organic component has an effect on the time-dependent behavior. The organic component embedded within the mineral tiles causes a toughening of the material and a lower hardness and stiffness compared to monolithic aragonite. Furthermore they might also contribute in retaining moisture which might lead to additional energy dissipation.

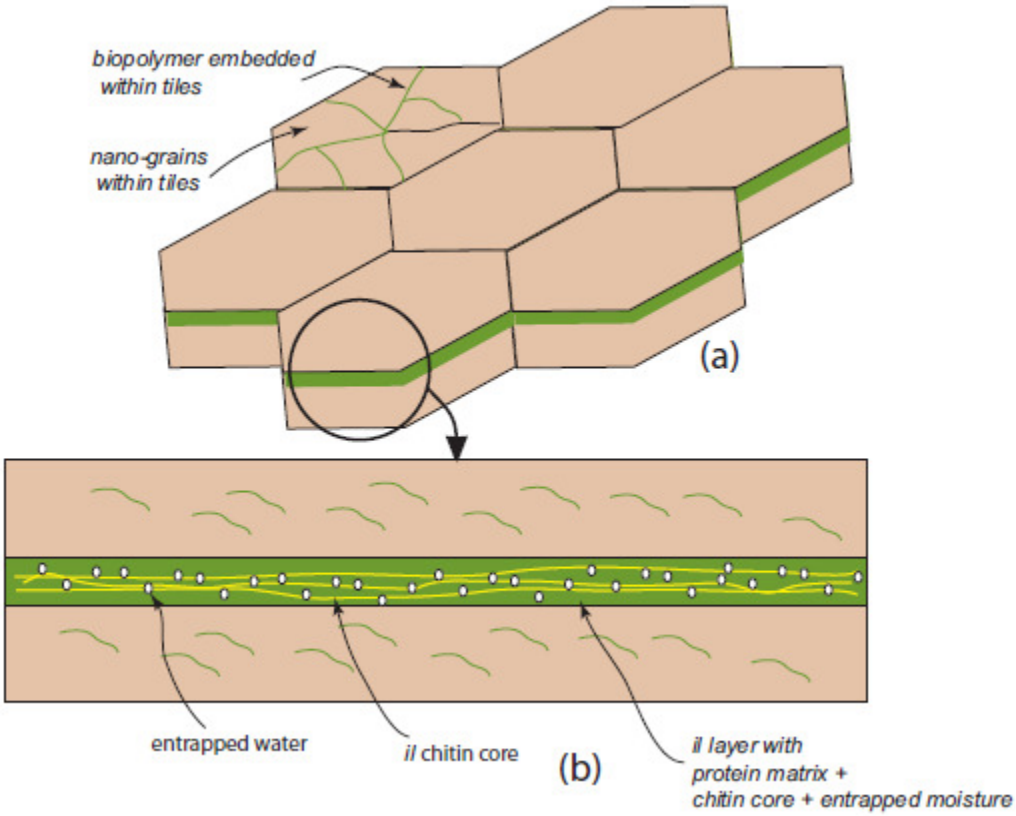


**Figure 2.32:** Paradigm for the structure and performance of nacre. (a) Bricklike layered tile composite composed of high aspect ratio toughened ceramic CaCO3 tiles within a biopolymer matrix; (b) the biopolymer matrix, which is itself viscoelastic, is composed of a chitin core within a hydrated protein matrix. Note that the tiles are themselves toughened by the incorporation of an intra-tile biopolymer network (source: Bezares et al. [46])

*2.3.6 Treated Nacre: Demineralized and Decalcified Nacre*

A limited number of studies have been performed on the mechanical properties of the organic intertile layers. Semiquantitive evaluation of the mechanical strength of the organic interlayer was conducted based on the sag exhibited by the dry organic layer held between terraced cones [25]. In this study the membrane is assumed to be circular and the deflection is calculated based on its own weight (Figure 2.33). The membrane is considered to be fixed and the radial forces are assumed zero at a zero deflection. The maximum deflection is expressed in terms of known parameters such as:

$$\omega_{max} = \frac{\rho h g a^2}{4N} \tag{2.5}$$

Where *ω is the* deflection, *h is the* thickness of the membrane, a, is the radius of the membrane, ρ is the density; *N* is the tensile force per unit length which is represented by stress multiplied by unit thickness:

$$N = \sigma h \tag{2.6}$$

The biaxial stress in the membrane under the weight is:

$$\sigma = \frac{\rho g a^2}{4\omega_{max}} \tag{2.7}$$

The nominal biaxial strain is defined as:

$$\varepsilon = \frac{L-2a}{2a} \tag{2.8}$$

They assumed the angle between the planes of growth (a and b) and the edges of the sagging membrane to be very small to that:

$$\sin\theta \cong \tan\theta = \frac{\partial\omega}{\partial r} = \frac{\omega_{max}}{a} \tag{2.9}$$

$$L = 2\pi R \frac{\theta}{180^{\circ}} = 2\pi \frac{a^2}{\omega_{max}} \frac{\theta}{180^{\circ}} \tag{2.10}$$

They assume the density of the organic layer to be 1.5 g/cm$^3$, the thickness to be 30 nm and the radii at 2.5 and 5 µm. By this they calculate the axial stress and plot it as is Figure 2.34 and the elastic modulus (the biaxial stress divided by the biaxial strain). They approximate that at a deflection of 0.5 µm (which is what is apparent from their micrograph) they attain a biaxial elastic modulus of 100 Pa. These results suggest low values of flow strength, concluding the organic interlayer exhibits viscoelastic behavior.

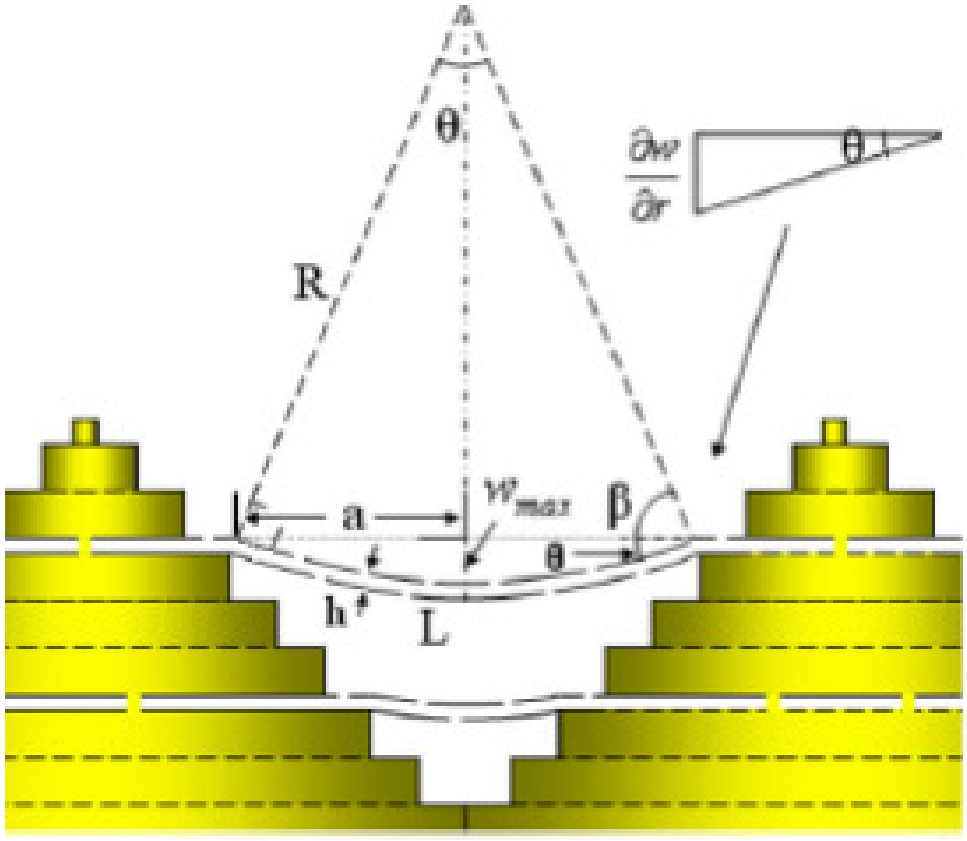


**Figure 2.33:** a) Side view of intermediate tile growth through organic layers on flat pearl five weeks after implantation. (b) Schematic showing terraced growth and organic membrane sagging under its own weight (source: Meyers et al. [25]).

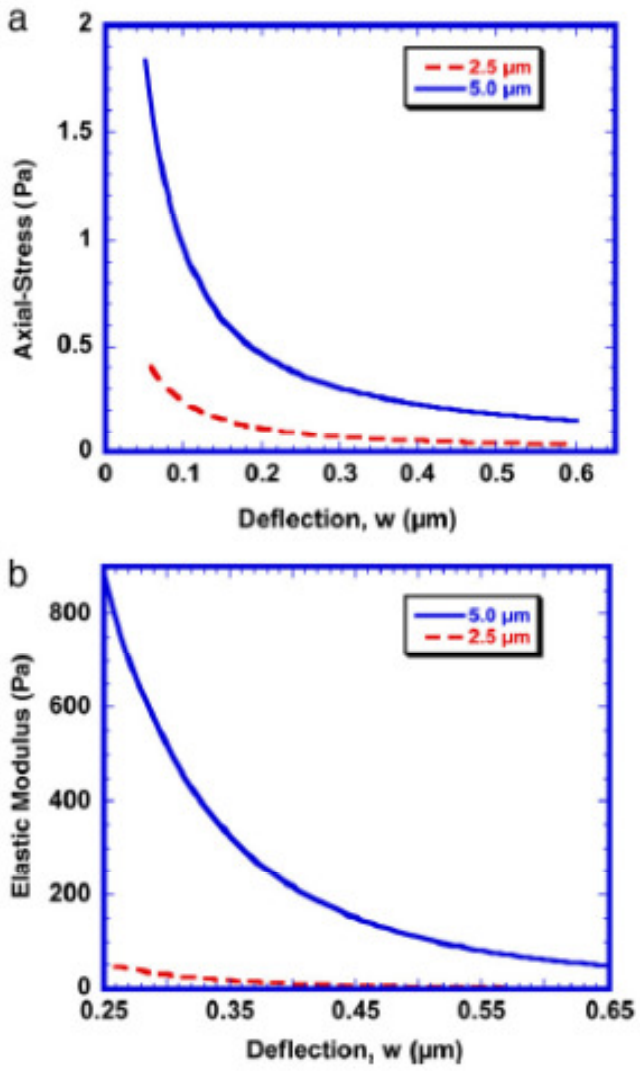


**Figure 2.34:** Calculated (a) stress, and (b) elastic modulus of organic layer as a function of deflection for two circle radii (source: Meyers et al. [25]).

On the other hand, later nanoindentation measurements performed on the dry organic layer by Meyers et al. [48]. They demonstrated that the organic interlayers exhibited considerable resistance. For these experiments a Berkovich tip was lowered and touched the organic matrix before encountering the mineral tile (Figure 2.35). The load penetration curves demonstrated a drastic change from when the tip penetrates the top of the tile versus when it encounters the organic matrix. The latter situation results

with a curve where a plateau at P~100 μN corresponding to the resistance of one dry organic layer. These measurements were used to estimate the resistance of the organic layer to deformation and/or failure. There was a drastic increase in strength from the values obtained by measuring the sag in the membrane attributed to the high sensitivity of the structure to the strain rate and the degree of hydration. These results suggest that the organic intertile layer is initially very soft and pliable and gradually hardens as it dries.

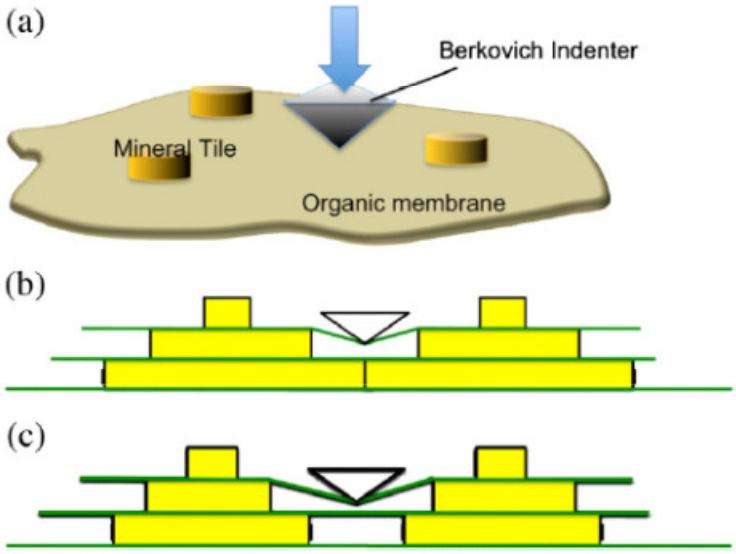


**Figure 2.35:** Representation of nanoindenter deforming organic layer; (a) tridimensional representation of indenter deforming organic layer; (b) configuration of single organic layer with a mineral underneath; (c) configuration of organic layer that is joined with lower level by deflection (source: Meyers et al. [48])

Similarly, AFM tests on the organic constituent have been performed [111]. Which report their behavior as a time dependent response that can be declared as viscoelastic, however, these results were focused more on the role of the proteins and how they contribute to the adhesion properties. Furthermore, monotonic tensile and time

dependent relaxation experiments were performed by Bezares et al. [45] on the mechanical properties of the organic constituent in nacre. These experiments revealed that the tissue comprising the intertile organic layers within nacre followed a constitutive response conforming to a visco-elastic standard linear solid. The elastic modulus was reported to be within a range of 0.143 GPa < E < 0.44 GPa (Figure 2.36). These results, however, failed to include the effects of the thick organic mesolayers which may in fact have an effect on the overall toughness of the nacre.

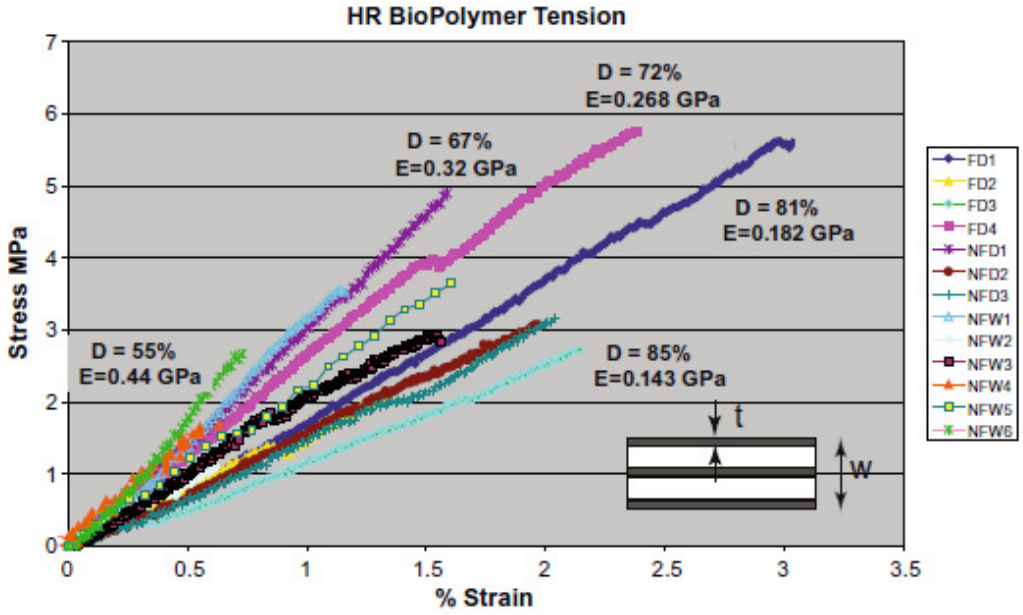


**Figure 2.36:** Quasi-static uni-axial stress vs. strain response of Fixed Dry (FD), Not-Fixed Dry (NFD), and Not-Fixed Wet (NFW) specimens. Tests were performed at a nominal strain rate of $10^{-4}$ $s^{-1}$, at 20 °C. D is the percent of interlamellar layers damaged during sample preparation. This was estimated based on visual inspection of samples just prior to testing. E is the tensile modulus of an individual biopolymer layer. Within the insert, w is the specimen thickness and the average thickness of interlamellar layers within intact nacre (source: Bezares et al. [45])

More recently, Dastjerdi et al. [101] performed tensile tests on the isolated organic layers of three different shell types: pearl oyster, top shell, and red abalone. These results suggest that growth lines (mesolayers) play an important role in the mechanical behavior as they are thick regions that do not dissolve in the demineralization process. They are able to withstand an evident amount of applied stress, giving the organic material in the abalone shell a higher stiffness compared to the other shells.

### *2.3.7 Structure and Property Relationship*

The high toughness exhibited by nacre has been mainly attributed to the difficult and indirect fracture path that occurs in the material. However, there are many contributions to the high toughening properties of nacre beyond that of the brick and mortar structure of nacre. The proposed toughening mechanisms are as follows:

1) Combination and organization of the tiles and the organic constituent (Figure 2.39). Sumitomo proposed [112] that nacre is designed in a matter such that if a stress is applied in the normal direction to the tile plane the organic constituent will act in a ductile manner and prevent uncontrolled crack growth, this however is assuming the shell is in a hydrated state. In a dry state, the organic material acts brittle [46, 58]. In addition, Smith et al. [113] suggested that the proteins making up the matrix of this organic membrane act as a strong adhesive joining the mineral tiles (Figure 2.37). Thus, when increasing the applied stress this biopolymer elongate in a step-like manner (Figure 2.38) contributing to the overall high toughness of nacre. This mechanism is still a debatable subject and further investigation is needed.

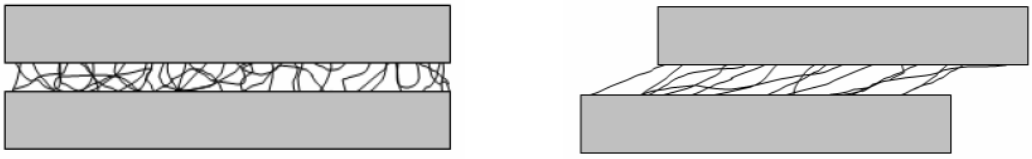

**Figure 2.37:** Organic layer acting as a viscoelastic glue (source: Lin [65]).

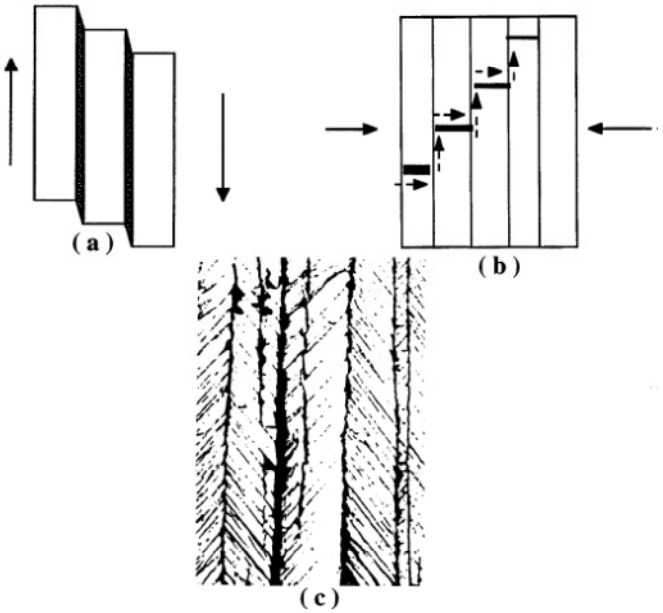


**Figure 2.38:** Principal mechanisms of damage accumulation in shells: (a) viscoplastic deformation of organic layers; (b) crack deflection by organic layers; (c) delocalization of damage (source: Menig et al. [51]).

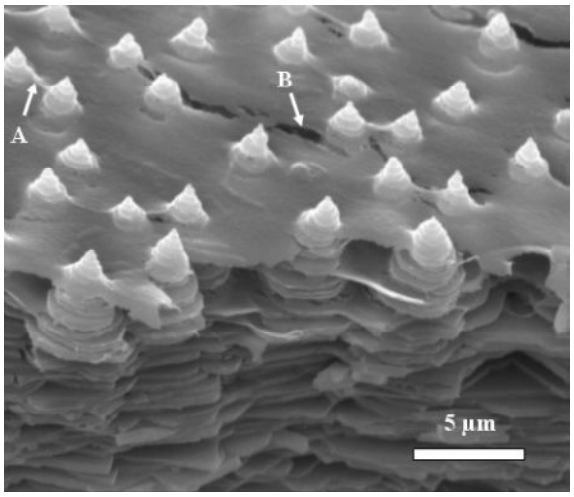


**Figure 2.39:** Side view of intermediate tile growth through organic layers on flat pearl five weeks after implantation (source: Lin [65]).

2) Asperities on the surface of the aragonite tiles (Figure 2.40) are also considered to attribute to the mechanical response of nacre. Wang et al. [108] and Evans et al. [61] hypothesis that a stress where inelastic deformation occurs, these asperities contribute to the shear resistance between tiles.

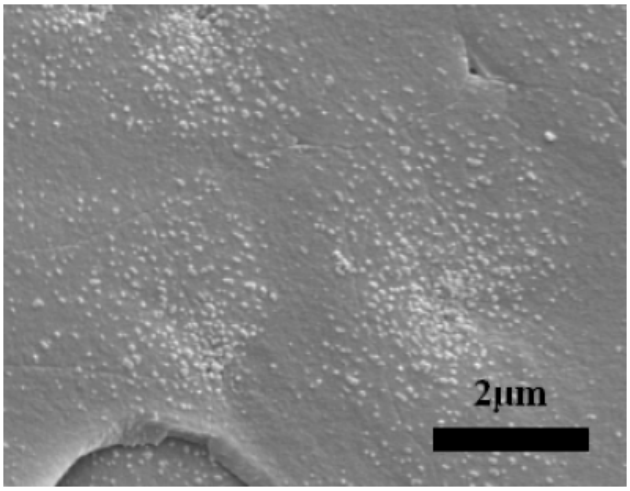


**Figure 2.40:** Asperities, many of which are remnants of mineral bridges, concentrated at the center of an aragonite tile after 9 hours of deproteination (source: Lin [65]).

3) Mineral bridges are also considered as great providers of toughness. Song et al. [80, 81], Velazquez-Castillo et al. [114], Meyers et al. [25] confirmed the existence of interlamellar mineral bridges that are approximately 50nm in diameter. These mineral bridges are shown in different views in Figures 2.41, 2.42, and 2.43. These mineral bridges reinforce weak interfaces and are considered to be the main source of the weak tensile strength observed in the direction perpendicular to the layered structure. Lin and Meyers [38] predict that because of the small diameter of the bridges, the tensile strength depends on the theoretical strength and not determined by the critical flaw size. Additionally, the distribution of the bridges of the bridges is optimized so that they act as a crack deflection mechanism.

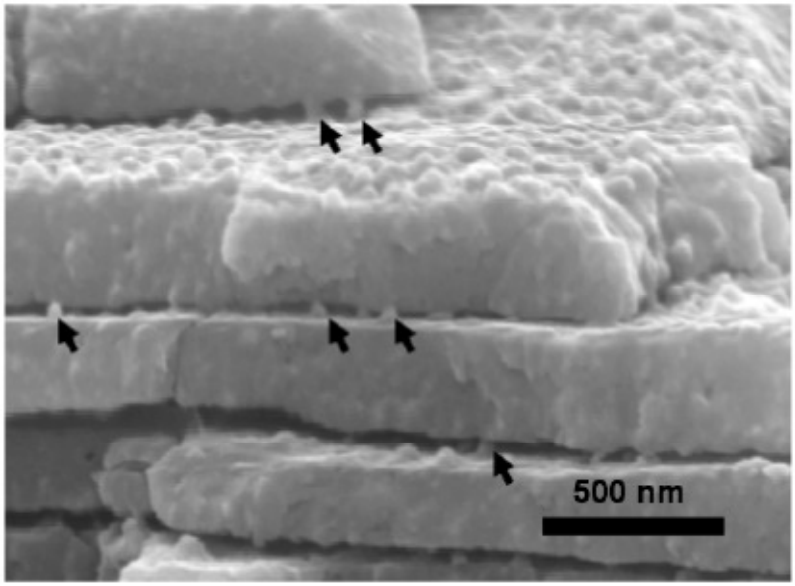


**Figure 2.41:** Mineral bridges (marked by arrows) between aragonite tiles after 9 hours of deproteination (source: Lin [65]).

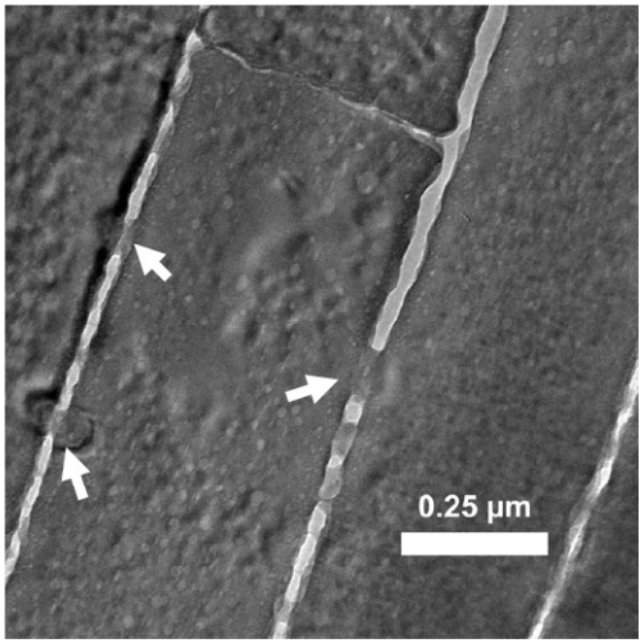


**Figure 2.42:** Transmission electron micrograph of nacre crossection showing mineral bridges between tile interfaces (source: Lin [65].

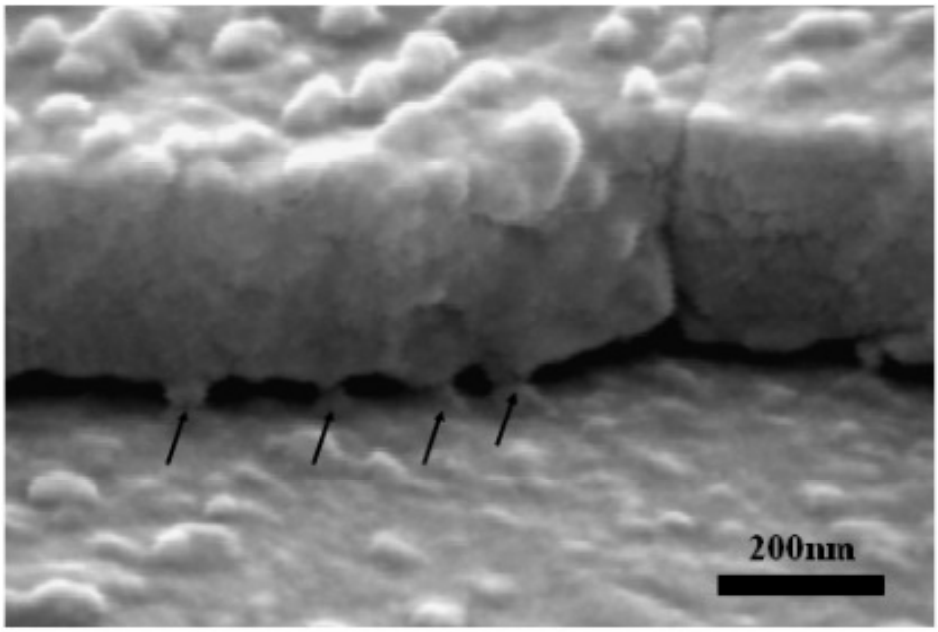


**Figure 2.43:** Mineral bridges (marked by arrows) between tile layers (source: Lin [65]).

It is suggested the actual mechanism of toughening of abalone nacre is the combination of all three components combined synergistically. As plastic deformation takes place, the breakage of mineral bridges may form the asperities that resist shear. The organic constituent then acts as an organic glue. Figure 2.44 depicts schematically the toughening methods.

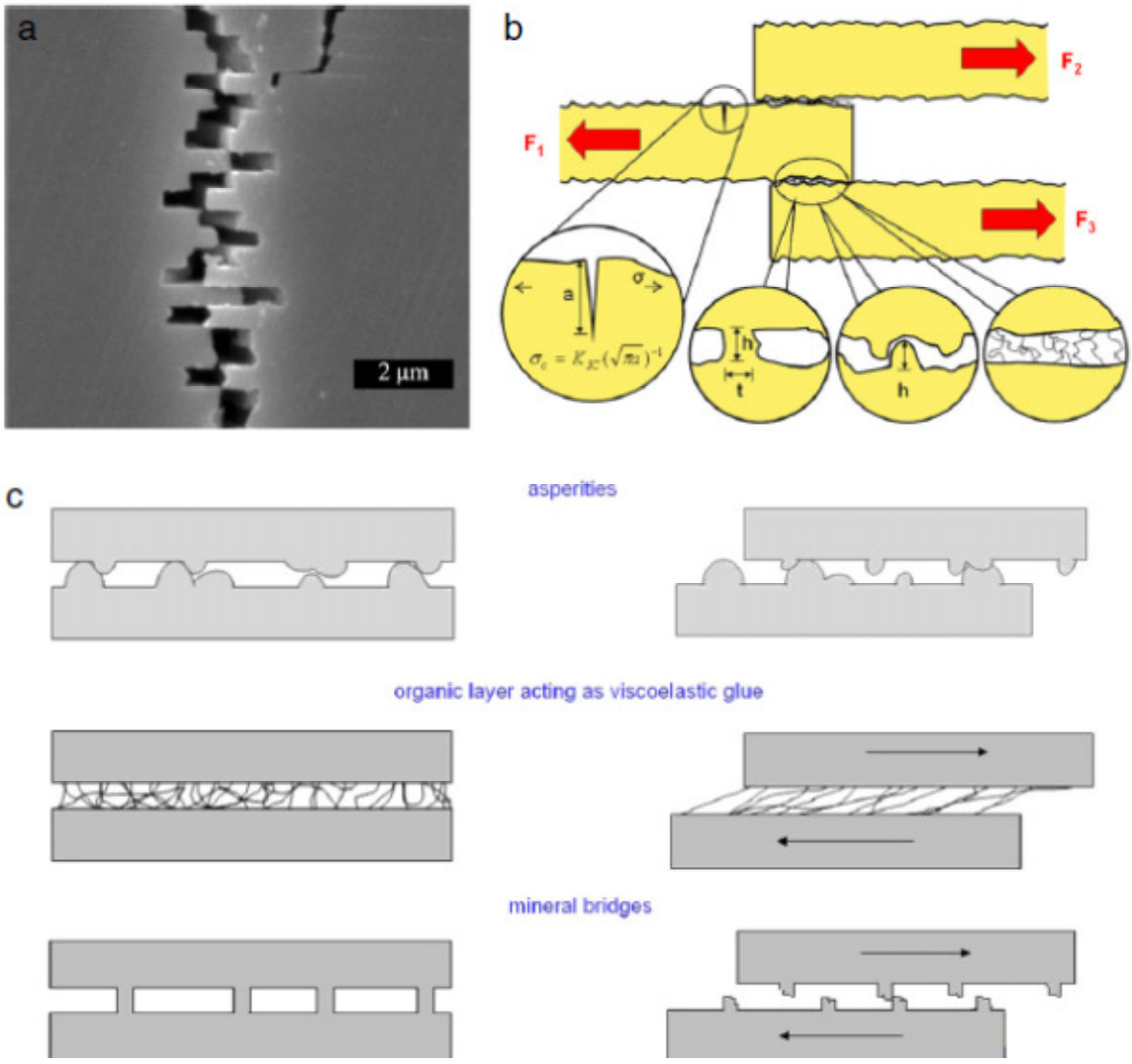


**Figure 2.44:** Origin of toughening in nacre: (a) SEM micrograph showing sliding of tiles in tensile loading; (b) balance between tile fracture and intertile shear; (c) details of three mechanisms of intertile shear: asperities, organic layer acting as viscoelastic glue, and fracture of mineral bridges. (source: Meyers et al. [6].

However, there are other theories that have been attributed to the energy dissipation beyond the brick-and-mortar structure of nacre. These other mechanisms are:

1) The hierarchical structure of nacre ranging to the nanoscale. Gao et al. [62, 115] showed that in nanocomposites show a structure where the mineral particles are at a nanometer size so that strength is optimized and it allows for a high tolerance of flaws. The strength (measured by hardness) decreases as the size becomes larger. This decrease in strength occurs because the existences of flaws are in greater dimensions as the sample size is increased. The decrease in hardness is connected to the larger ease of generation of defects as the indentation size is increased. Toughness, or the ability to resist crack propagation, contrarily increases (Figure 2.45). As stated before, minerals reach the theoretical strength value when the scale is reduced to a nanometer scale. Additionally, Fratzl et al. [116, 117] showed that by having a layered structure with two materials of two distinct elastic moduli can lead to a shielding/anti-shielding effect at the crack tip.

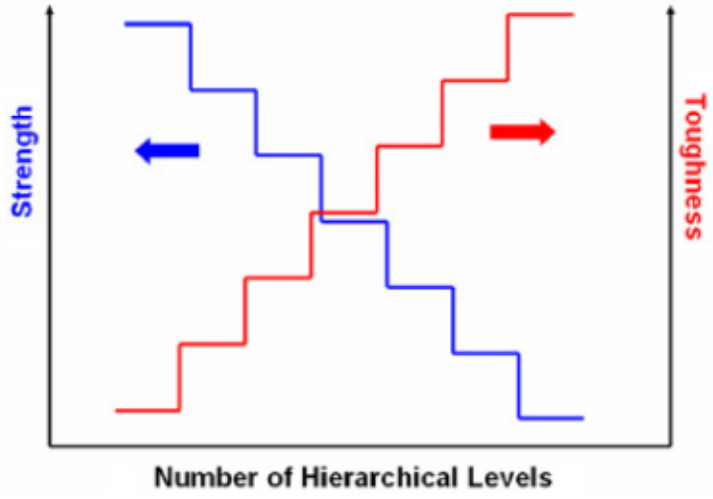


**Figure 2.45:** Strength and toughness as a function of number of hierarchical levels. (source: Meyers et al. [6])

2) The shape and position of the aragonite tiles are also believed to be toughening mechanisms:

   a. Katti et al. [63, 118] reported a mismatch of layering of the aragonite tiles, e.g. the layers of tiles are not placed one over another, but 'interlocked' (Figure 2.46). This interlocking demonstrated to have an important role of the behavior by restricting a catastrophic failure of the nacre.

   b. Barthelat [57] reports that additionally, the waved surfaces sometimes perceived in the aragonite tiles can also act as a lock and prevent tile sliding.

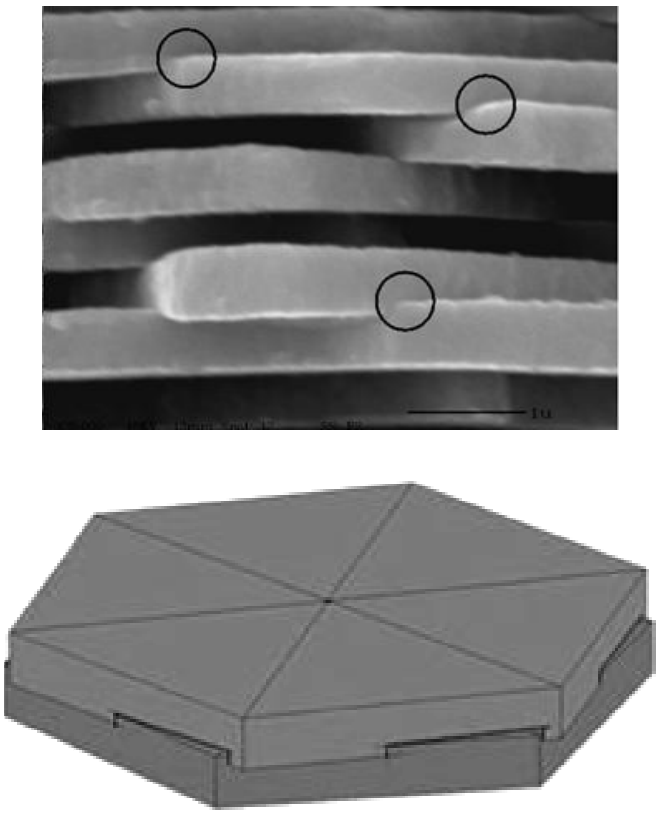

**Figure 2.46:** SEM micrograph showing interlocks in nacre. Schematic representing the mismatch in layering giving rise to interlocks (source: Katti & Katti [63])

3) Finally, the tiles may not be considered as fragile monolithic $CaCO_3$ but are considered to have embedded organic component and by some are considered as nanocrystalline [46, 67, 119]. Therefore the tiles act as a tough ceramic with a reduced stiffness and hardness when compared with monolithic aragonite.

Additionally, the overall structure of nacre has been modeled by the developing of constitutive models and finite element models (FEM). The nacre tiles have been described as viscoplastic, while the interlamellar layers are considered as viscoelastic. Parameters have been attained experimentally, via means of time relaxation tests [46] and indentation tests, for example [18, 46, 55, 64, 67, 110, 111, 119-124].

From relaxation tests, the demineralized nacre (fully hydrated) was fitted to a standard linear solid model (equation 2.11); where the parameters where found to be $E_0$ = 0.668 ± 0.088 GPa, $E_1$ = 0.311 ± 0.092 GPa, and the relaxation time τ = 140 ± 4 s [46].

$$\sigma = \int_0^t E(t-t')\left(\frac{de}{dt'}\right)dt' \tag{2.11}$$

Where *E(t)* is the instantaneus Young's modulus, given by:

$$E(t) = E_0 + E_1 e^{\frac{-t}{\tau}} \tag{2.12}$$

Where $E_0$ is the Young's modulus, τ is the characteristic time, η is the viscosity, σ is the Cauchy stress, and *e* is the engineering strain.

The instantaneous Young's modulus is given by:

And the characteristic time by:

$$\tau = \frac{\eta}{E_1} \tag{2.13}$$

The aragonite tiles were considered as viscoplastic materials, whose constitutive properties were modeled using the rate dependent plasticity overstress model by Perzyna [125],

$$\dot{\bar{\varepsilon}}_p = \frac{\sigma_Y}{\eta_p}\left\langle \frac{\sigma}{\sigma_Y} - 1 \right\rangle^n \tag{2.14}$$

where $\dot{\bar{\varepsilon}}_p$ is the equivalent plastic strain rate, $n$ is the rate-sensitivity exponent, $\sigma_Y$is the yield stress, $\eta_p$is the plastic viscosity, and $\sigma$ is the Cauchy stress.

Plastic straining happens when the yield condition $\sigma > \sigma_Y$ is satisfied, which is incorporated *via* the Macaulay bracket $\langle\rangle$ ($\langle f \rangle = f$ if $f > 0$, and $\langle f \rangle = 0$ if $f \leq 0$). The rate-sensitivity exponent $n$ was then set to unity so that equation (2.) becomes:

$$\dot{\bar{\varepsilon}}_p = \frac{\langle \sigma - \sigma_Y \rangle}{\eta_p} \tag{2.15}$$

The Young's modulus was estimated to that of monolithic aragonite $E_{aragonite} \approx$ 114 GPa, the yield stress $\sigma_Y \approx$ 10 GPa, and the plastic viscosity $\eta_p \approx$ 5000 GPa·s and performed simulations for short and long term simulations. Results showed that there is ahort term viscoelastic behavior with a characteristic time of 1 second and a long term viscoelastic effect at 50 seconds that might be attributed to the hydration effects of the interlamellar layers. Thus a simulation following viscoelastic parameters at 0.7 seconds (Figure 2.47) and 45 seconds (Figure 2.48).

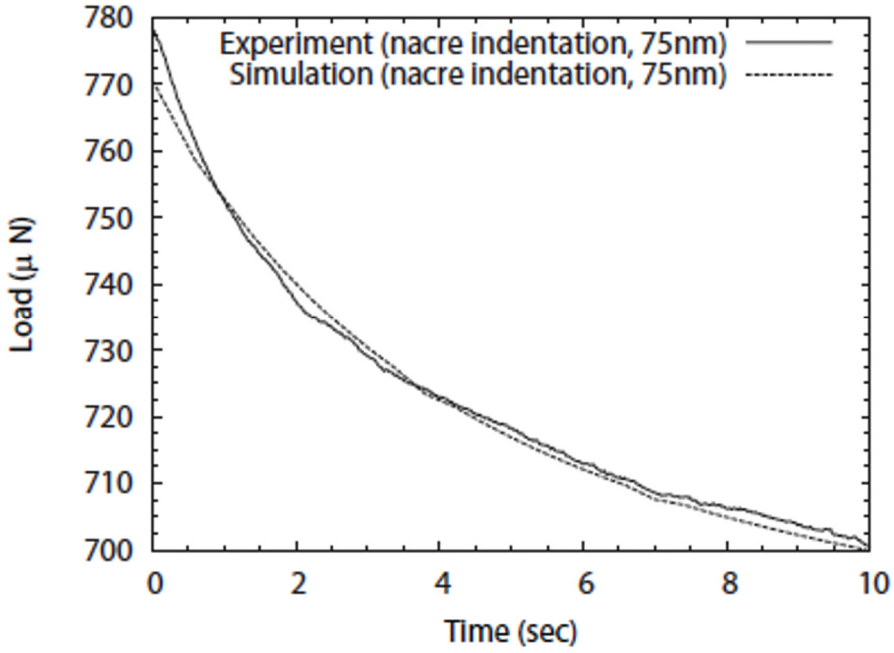


**Figure 2.47:** A short-term simulation of nacre indentation relaxation. The depth of indetation is 75 nm (source: Bezares [46]).

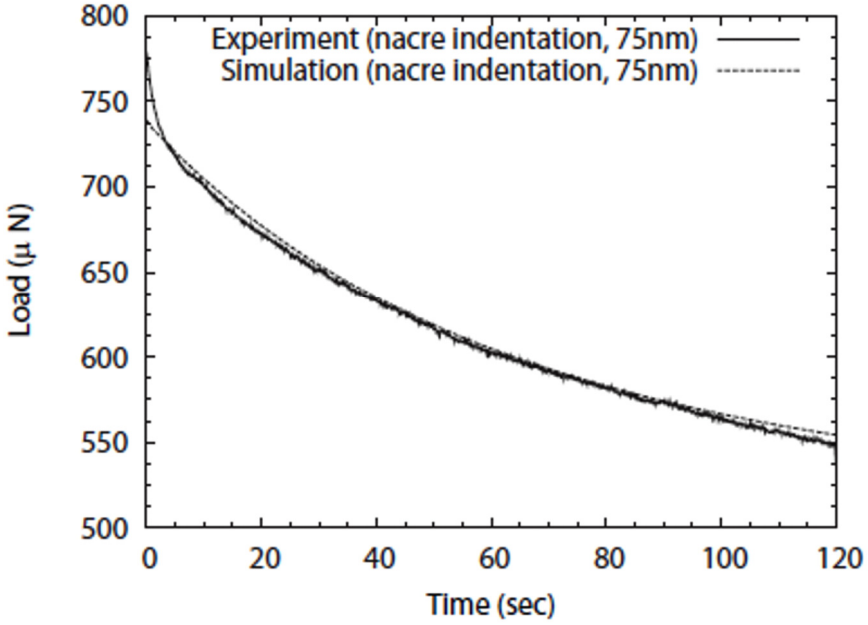


**Figure 2.48:** A long-term simulation of nacre indentation relaxation. The depth of indentation is 75 nm (source: Bezares [46]).

Because of this viscoelastic response, results show that monolithic aragonite cannot serve as an appropriate model for nacre tiles, as the interlamellar layers comprise a time dependent constitutive response of nacre and for still another mechanism of energy dissipation during deformation.

# CHAPTER 3

# EXPERIMENTAL METHODS

The different experimental methods, treatments, equipment, and facilities utilized through this study will be described.

## 3.1 Culturing Facilities

Red abalone is held in an open water system (Figure 3.1) at Scripps Institution of Oceanography, where sea water is continuously and directly cycled from the Pacific Ocean. The animals are fed giant kelp (*Macrocystis pyrifera*) on a regular schedule which is collected directly from the Pacific Ocean. Furthermore, abalone of adequate (~5-6 inches in length) size and age were selected and labeled and transferred to a separate 45 liter open water fish tank so that environment could be monitored and controlled in accordance to the particular experiment.

This tank had direct access to continuously circulating sea water, providing a natural environment with steady pH. Animals were continued to be fed giant kelp (*Macrocystis pyrifera*) at different schedules and the mean temperature was controlled. Three different conditions were considered with individual experiments carried out, varying average temperature and the feeding rate of the animal (Table 3.1).


**Figure 3.1:** Abalone culturing facilities (a) Large open water tank and (b) 45 liter open water fish tank at the Scripps Institution of Oceanography.

**Table 3.1:** Experimental conditions; temperature and dietary condition.

| Condition | Water Temperature | Feeding Schedu |
|---|---|---|
| 1 | 21 ± 2 °C | Regularly |
| 2 | 15 ± 2 °C | Regularly |
| 3 | 20 ± 2 °C | Not Fed |

## 3.2 Specimen Collection, Preparation, and Characterization

*3.2.1 Flat Pearl:*

The 'flat pearl' technique, first used by Wada et al. (Wada et al. 1958, 1959) then in the US by the U.C. Santa Barbara group [14, 17, 19] and later applied by Lin et al. [24], was utilized to extract specimens for growth observations. Glass slides 15 mm in diameter were implanted in live abalone (glued in only one spot using Superglue®) to the growth surface of the shells. The mantle was pressed back (retracted) with a flat stainless steel scalpel with rounded edges and the slides were glued to the growing edge of the animal (Figure 3.2). Various locations along the growing edge were selected. The largest quantity of slides allowed by the size and surface of the animal was implanted on each abalone. In Figure 3.2, six slides were implanted and are shown by arrows. No copper was used in the process because of the negative reaction abalones have with the metal. Once securely adhered, the mantle relocated itself over slides over the period of approximately 24 hours. The slides were implanted for periods of 1–3 weeks and then extracted weekly for examination. At least one slide from each of the abalone was removed weekly and prepared for scanning electron microscopy (SEM) and atomic force

microscopy (AFM) characterization. Before examination each slide was washed in purified water to remove salt build up. For SEM preparation, the slides where air dried and sputter coated with gold-platinum.

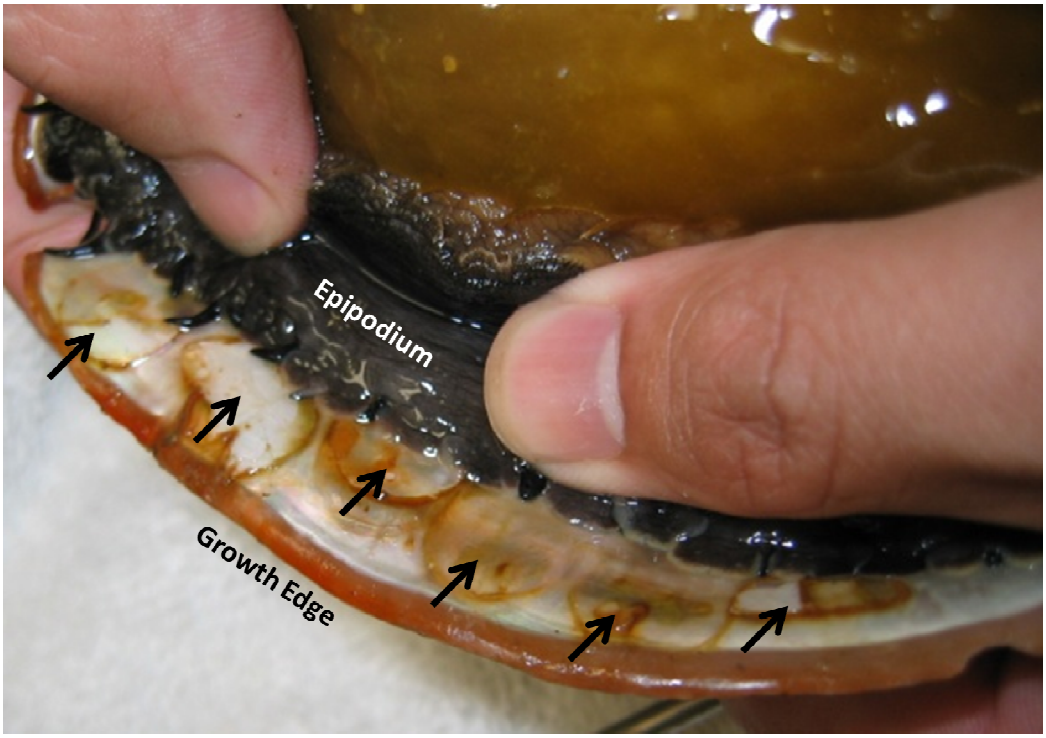


**Figure 3.2:** Glass slides (depicted by arrows) embedded in abalone shell**.**

*3.2.2 Demineralization and Deproteinization of Nacre:*

To characterize the structure of the organic interlayer purely without interference of the major amount of mineral in the shell, the mineral has to be removed fully carefully so that the organic material is not disrupted. A common process of demineralization was employed using 0.6 N HCl. Thin slices of nacre were sectioned from the growing edge of fresh abalone shells, washed in deionized water, and placed in the diluted HCl solution at 20°C for one week. Fully demineralized samples can be seen in Figure 3.3.

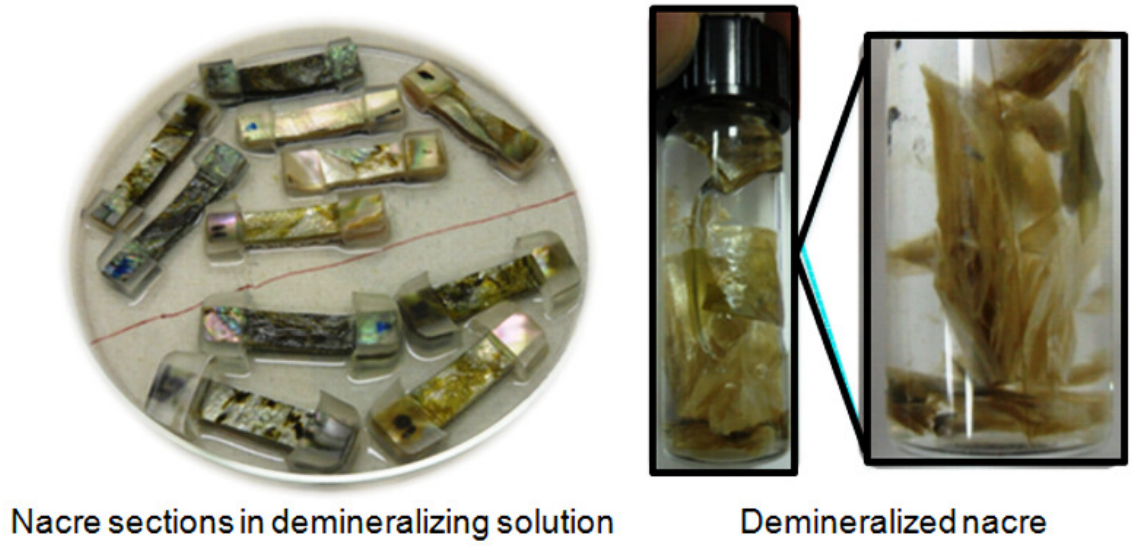


**Figure 3.3:** Nacre sections in demineralizing solution and completely demineralized abalone nacre. Separation of layer occurs as the mineral is removed and the material looses most of its structural integrity.

Embedded untreated nacre specimens where demineralized in the method described by Bezares et al. [44] in 0.6 M EDTA, pH 8.0. Once demineralized, specimens were placed in DI water for 24h prior to testing to ensure the specimen was hydrated. Demineralized specimens where examined visually to document if mesolayers were visible prior to testing. Because the mesolayers consist of thicker layers of protein they appear much darker than the organic interlayers when demineralized.

Removal of all organic material from the original nacre was performed by submerging the specimen in 0.5 N sodium hydroxide (NaOH) at 20°C for 10 days under constant, gentle shaking (Figure 3.4). It is noteworthy to mention that great effort was done in finding the ideal solution and time frame to perform this experiment. The time the specimens were exposed to the solution was varied, and different concentrations of

the solution were used. We selected the appropriate concentration and time frame by inspectingthe treated samples by scanning electron microscopy prior to the tensile testing. Higher concentrations damaged the sample (Figure 3.5 where the nacre was treated with higher and lower concentrations than 0.5 N NaOH) and lower concentrations and less time frame revealed that the organic component had not dissolved and was still visible under the microscope. The selected concentration gave the best combination, where the tile structure remained in-tact while the organic material was not observed anymore.

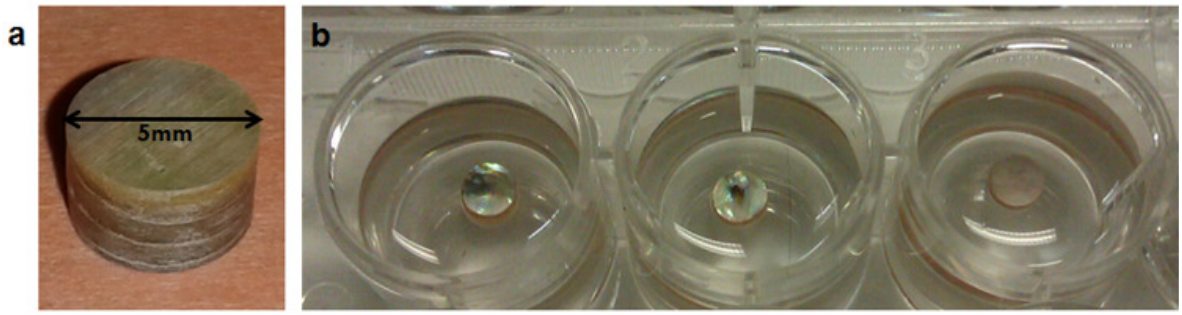


**Figure 3.4:** Sample preparation of deproteinized nacre

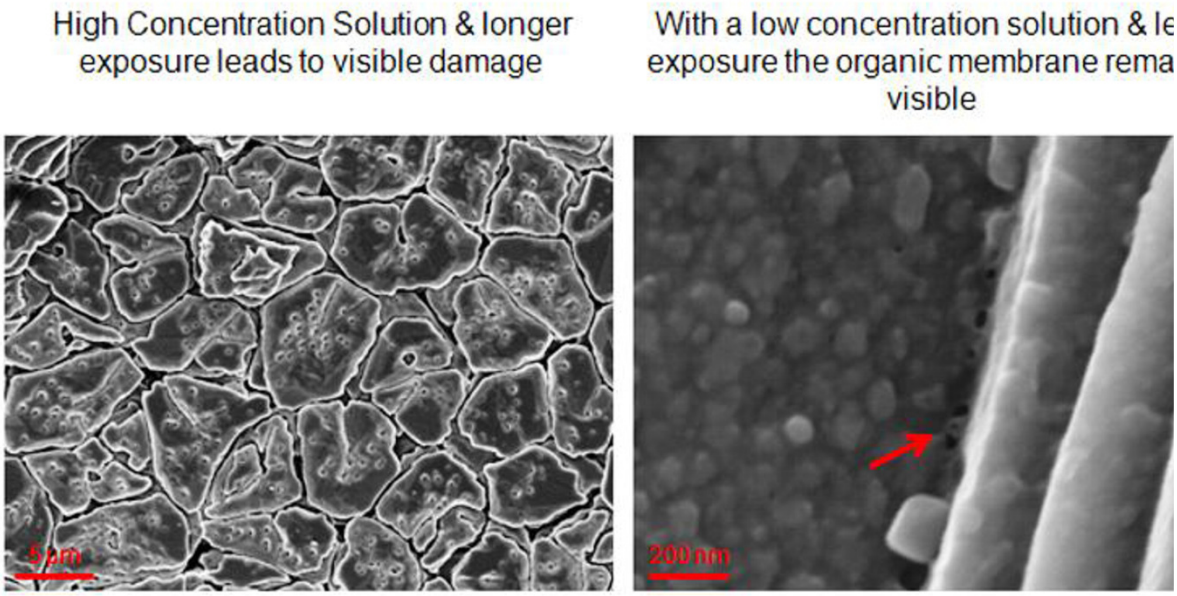


**Figure 3.5:** Deproteinized nacre where higher concentrations damaged the sample and lower concentrations and less time frame revealed that the organic component had not dissolved and was still visible under the microscope.

*3.2.3 Shell Sections for Tensile Testing of Demineralized Nacre*

Sectioning was performed from two fresh abalone shells that were previously held and raised in an open water tank at the facility at the Scripps Institution of Oceanography at La Jolla, CA. Specimens were cut and polished in long rectangular sections where the length and width of the specimen was fixed to 12.5mm by 6mm, respectively, and where the thickness of the specimen was varied (Figure 3.6 a,b). The calcitic layer was removed via wet grinding, where only the nacreous layer remained. The sectioning of was performed with extreme care to ensure that the lengths of the shells were cut perpendicularly to the growth of the shell (Figure 3.6b). In addition, grinding and polishing was carried out to achieve with close precision a parallel alignment between the specimens' surface and the shells' growth planes. This was done with the purpose of

assuring there was an engagement of the layers and less damaged caused in the process of demineralization. Furthermore the sections were ground in thickness to control and approximate the number of organic interlayers and to vary the number of mesolayers that could exist in each specimen. Variance in thickness would then give specimens that would contain mesolayers and some specimens that would avoid mesolayers.

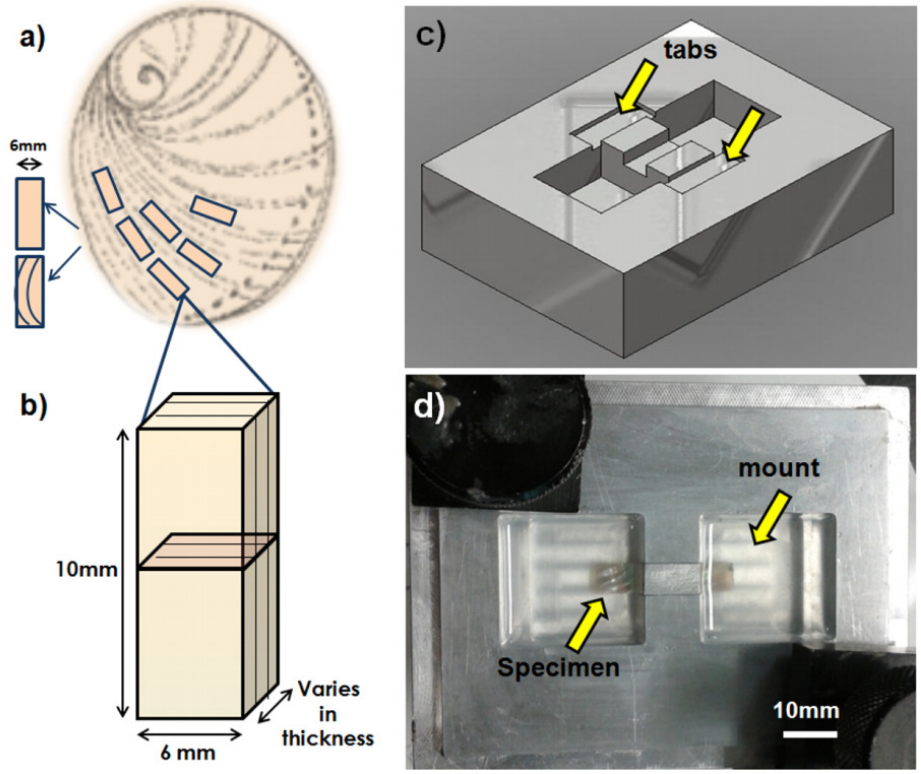


**Figure 3.6:** Specimen preparation for demineralized nacre. a) Orientation of sectioning, b) Specimen dimensions, c) Mounting mold design, d) Mold showing the nacre specimen embedded in the epoxy.

*3.2.4 Shell Sections for Tensile Testing of Deproteinized Nacre*

Cylindrical pucks of nacre, 5 mm in diameter, were drilled from fresh abalone shells using a diamond coring drill. Care was taken when drilling the pucks perpendicular to the concavity of the surface of the shell (Figure 3.7) ensuring the inner

nacre layers would be as parallel to the edge of the specimen as possible. Specimens where then grinded and polish to remove external calcite layer and to create a flat edge.

*3.2.5 Embedding and Mount Setup*

Preliminary demineralization nacre studies demonstrated that the nature of the behavior of the material would be too vulnerable for a traditional tensile test arrangement. Previous studies [45] showed an elegant set-up, where the edges of untreated nacre were first embedded exposing a specific section of the nacre which was then demineralized. However, this study also suggested that major damage was caused in the embedding and handling of the demineralized nacre. As the nacre is demineralized, the integrity of the material is decreased and the specimens become pliable. It is the calcium carbonate that provides the majority of the stiffness in nacre and when removed, any mishandling of the exposed organic constituent can damage the specimen. To avoid further problems in the handling and engaging of the specimens when testing a specialized mounting mold was designed (Figure 3.6 c,d). This mold permitted for the untreated nacre specimens (of various thickness) to be positioned in the center of the mold, where only the edges would become embedded in the acrylic, exposing 10mm in length x 6mm width x specific thickness of the specimen that would undergo demineralization when in contact with the solution. To ensure an easy handling of the demineralized nacre the edges of the mount would be connected by two thin tabs of acrylic. Then, once the mount edges were engaged and positioned in the machine grips for testing and the entire test setup was ready, then the two thin tabs would be cut allowing for the load to be applied only on the demineralized nacre.

For the testing of the mineral nacre pucks a setup was created to decrease damage that could occur to the specimens. Once the nacre loses all of the organic constituents it becomes brittle and fragile. To reduce any pre-loading prior to testing, the pucks were mounted in an acrylic setup that allowed gripping and handling of the sample (Figure 3.7 b). Given the setup and the nature of the brittle material tests were performed under an isostress loading where the ultimate tensile strength was recorded.

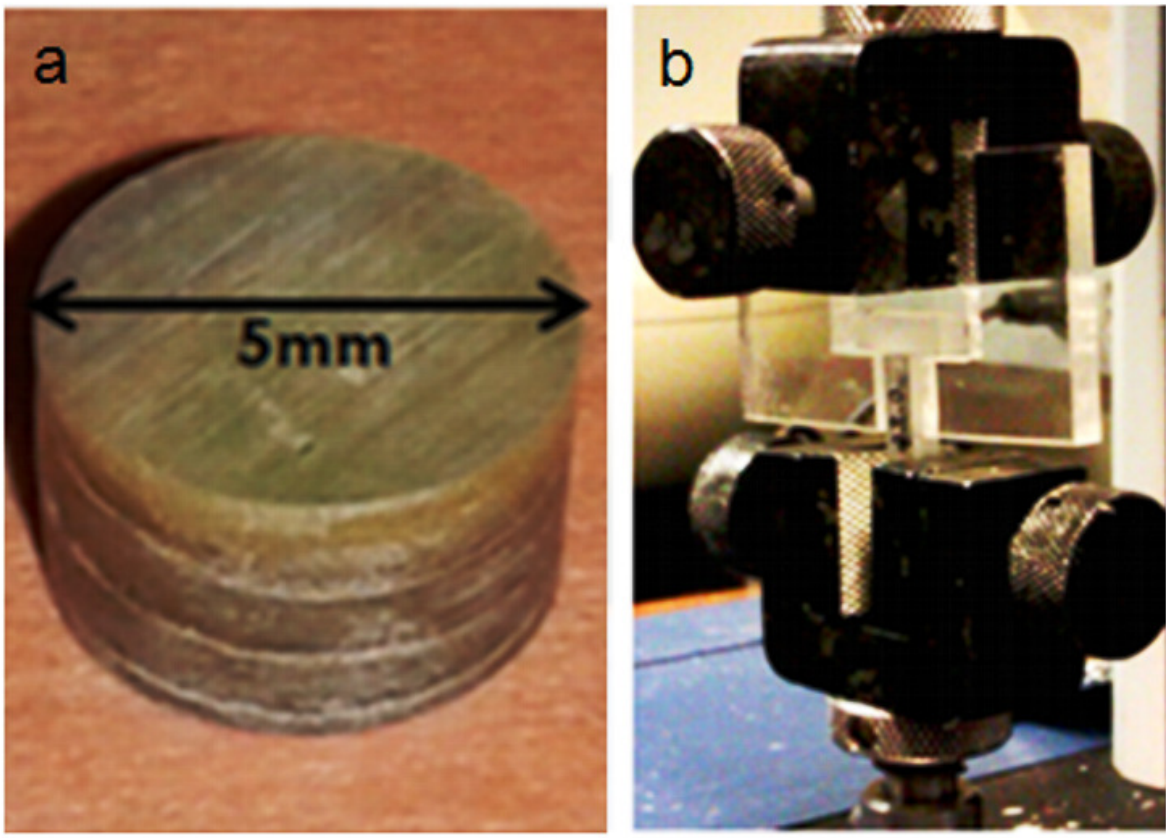


**Figure 3.7:** a) Drilled puck of untreated nacre and b) Tensile setup to pull apart the untreated and deproteinized pucks.

*3.2.6 Shell Sections for micro-scratch testing*

Nacre sections (3cm x 3cm) were directly cut from fresh red abalone shell. Specimens were polished to attain a flat surface. These specimens were prepared to be tested and observed in two directions: top surface and cross-section (Figure 3.8). Deproteinized specimens were then treated as described in section 3.2.2 and embedded in epoxy.

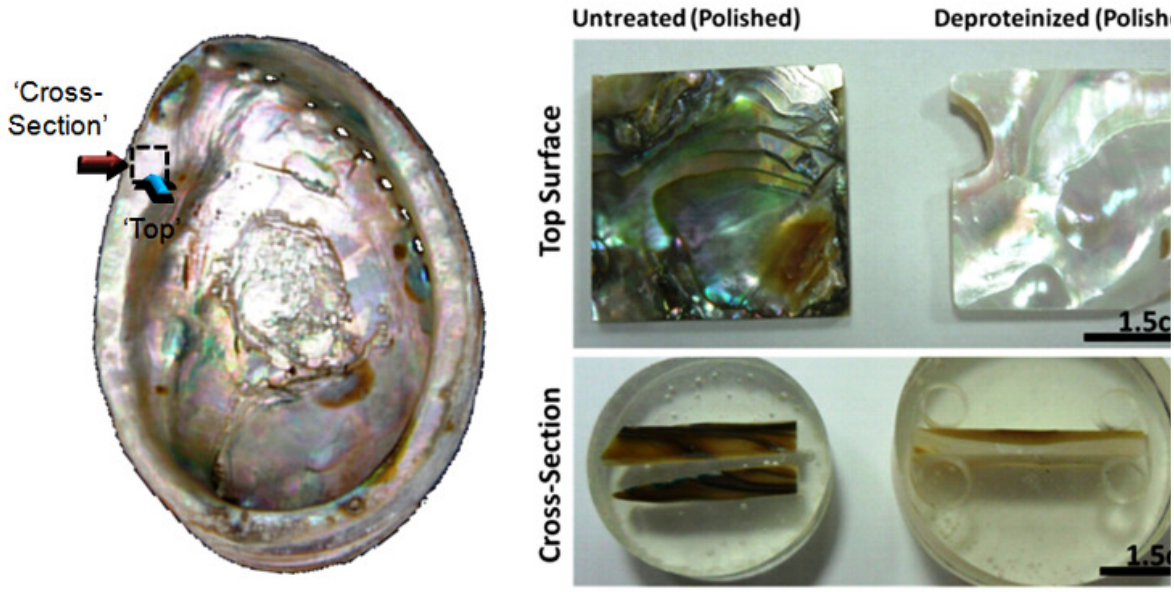


**Figure 3.8:** Sample preparation for nanoscratch and nanoindentation

## 3.3 Mechanical Testing

### *3.3.1 Tensile Tests*

Tensile Testing on the demineralized nacre was then performed in a desktop Instron 3342 system under a strain rate of $10^{-2}s^{-1}$ and $10^{-4}s^{-1}$. Tensile Testing on the isolated mineral was performed under a strain rate of $10^{-2}s^{-1}$.

### *3.3.2 NanoScratch Experiments*

Nanoscratching was performed utilizing a CSM Nano Scratch Tester (NST) (Figure 3.9) specially suited to characterize practical adhesion failure of thin films and coatings, with a typical thickness below 800 nm. Samples were tested by applying a progressive load up to 1000 mN for specimens tested in cross-section, and by applying a progressive load up to 600 mN for specimens tested on the top-surface. The scratch length varied from 2 to 3 mm depending on the available surface area. At least 6 high-quality scratches were performed on each specimen. Specimens were then observed by SEM to understand the failure behavior. Representative results will be discussed in the following section.

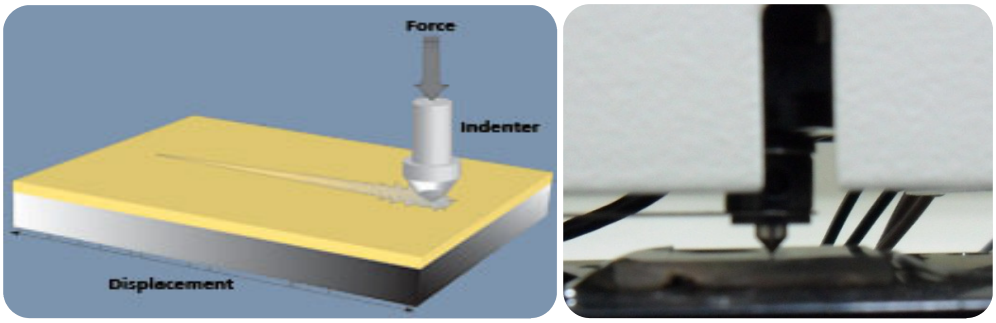


**Figure 3.9:** Nano-Scratch Setup

*3.3.3 Nanoindentation Experiments*

Nanoindentation experiments were performed at the *National Taipei University of Technology* with Hysistron nanoindentation system (Figure 3.10). Indentation was performed in various regions of the untreated and deproteinized nacre at various loads (300 mN to 500 mN). Indented specimen was observed sequentially by AFM.

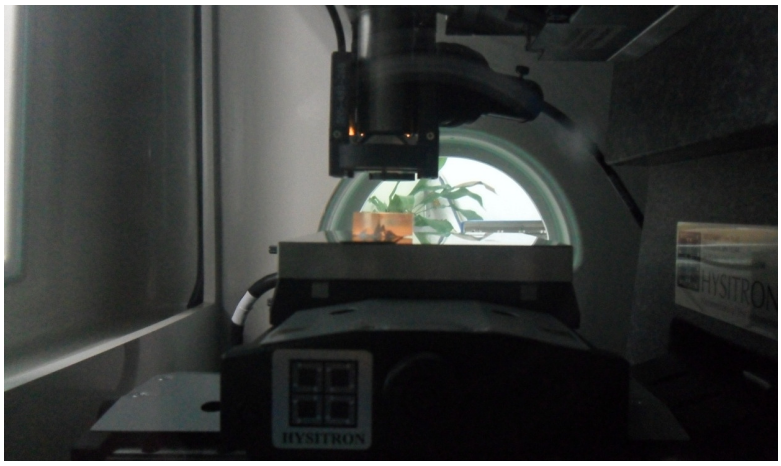


**Figure 3.10:** NanoIndentation setup for untreated and deproteinized nacre.

## 3.4 Structural Characterization

### *3.4.1 Structural Characterization of Epithelium*

Tissue from the interpallial layer of mantle from the red abalone foot was removed from live specimens. Small slices (~1 cm) were cut from various sections of the abalone (Figure 3.11). Then each section was re-sectioned into two parts. Samples were $CO_2$ critical point dried and gold-platinum coated for observation in the ESEM in high vacuum mode.

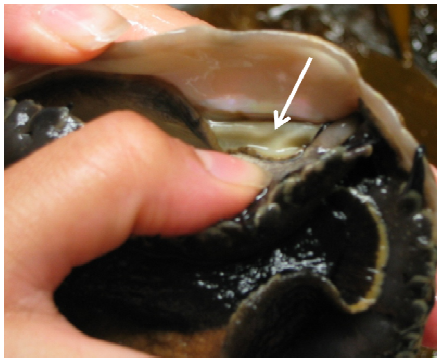

**Figure 3.11:** Abalone mantle pushed back revealing epithelium (depicted by arrow) prior to excision.

*3.4.2 Scanning Electron Microscopy Observations on the Structure of Nacre*

A major component of this research was structural observations enabled through a Phillips XL30 environmental scanning electron microscopy (ESEM). Thus it becomes relevant to discuss some of aspects of this technique, its limiting factors, and how it was used to characterize the various specimens studied here.

The scanning electron microscope (SEM) is a very popular and useful tool utilized by materials scientists. This device allows researchers to observe and characterize easily a variety of organic and inorganic materials, including natural materials, on micrometer to nanometer scales. The scanning electron microscope was first proposed by Knoll in 1935 [126] and first constructed two years later by van Ardenne. This technique has progressed with time leading to many advances that improved the capability of SEM. Commercially; the first SEM was built by A.D.G. Stewart at Cambridge Scientific Instrument Company. This first generation model has served as the foundation for modern and modified commercial SEMs.

A basic schematic of the SEM components is shown in Figure 3.12. The microscope consists of a series of parts including a column and an electron gun to provide an electron beam that scan the specimen. The electron beam is emitted by the electron gun and then passed through electron lenses consisting of magnetic materials that are controlled by the scan coils (shown in Figure 3.12 b). The electron beam scans the specimen and produces different types of electrons such as secondary electrons, backscattered electrons, and Auger electrons. Due to the distinct electronic properties of secondary electrons, they are utilized to analyze the topography of the specimen. The

backscattered electrons are also sometimes utilized because they aid in portraying differences in roughness and elemental composition. A computer system as shown in Figure 3.11 a is used to obtain electron data and transform it onto an image; especially for modern SEMs this digitalized imaging system is an essential part of the model.

(a)

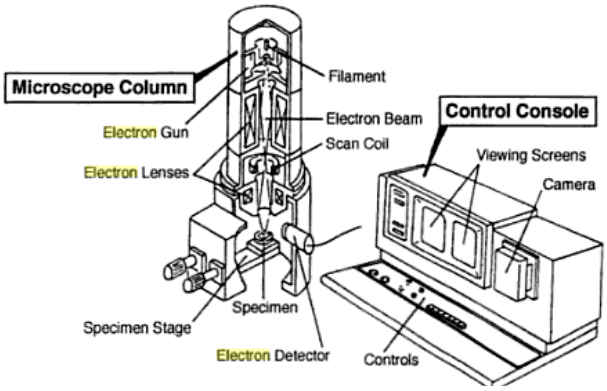


(b)

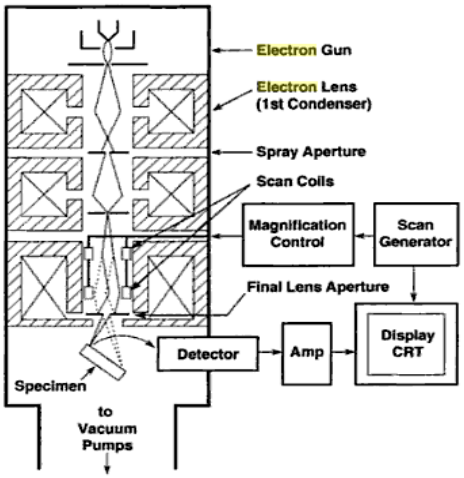


**Figure 3.12:** (a) Basic components and the control console of SEM, (b) the detail in the chamber of SEM (*source*: Goldstein et al. [127]).

Because SEM images are generated through the detection of electrons that are emitted from the sample that is bombarded by the highly focused electron beam, it is

important that the specimen is conductive. Because natural materials, in particular the abalone shell, are not naturally conductive it must be covered by a thin layer of gold plating. This coating layer is invisible to the SEM detector, while allowing the material to behave as conductive. In addition, localized heating may occur at the observation site, which can cause structural damage or difficult analysis process. This was mostly avoided by increasing the amount of metallization. Both an environmental SEM (FEI) at Scripps Institute of Oceanography (SIO) with accelerating voltages of 15-20 kV and a field emission SEM (FEI) with EDS at the Nano3 Laboratory in Calit$^2$ were used for characterization (Figure 3.13).

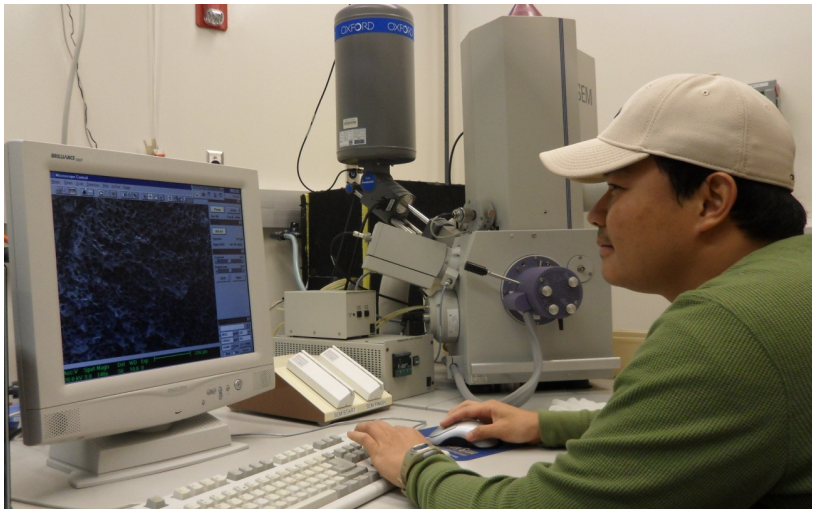

**Figure 3.13:** Scanning Electron Facility at Calit2 at UCSD

*3.4.3 Atomic Force Microscopy*

Atomic force microscopy (AFM) was also utilized to confirm the shell formation results obtained by scanning electron microscopy. The AFM cantilever scanned the top

surface of the growth specimens prepared utilizing the flat pearl method and positioned onto a piezoelectric mount (Figure 3.14). As the tip is brought onto proximity to the sample's surface, forces between the tip and the sample create a deflection of the cantilever in accordance to Hooke's law. The deflection is then measured by using a laser spot reflected from the top surface of the cantilever into an array of photodiodes. The AFM can be operated in various modes, most commonly static and dynamic modes. For this study, the AFM was utilized using contact mode in a static state. In other words, the cantilever remained in contact as it was dragged through the surface of the specimen.

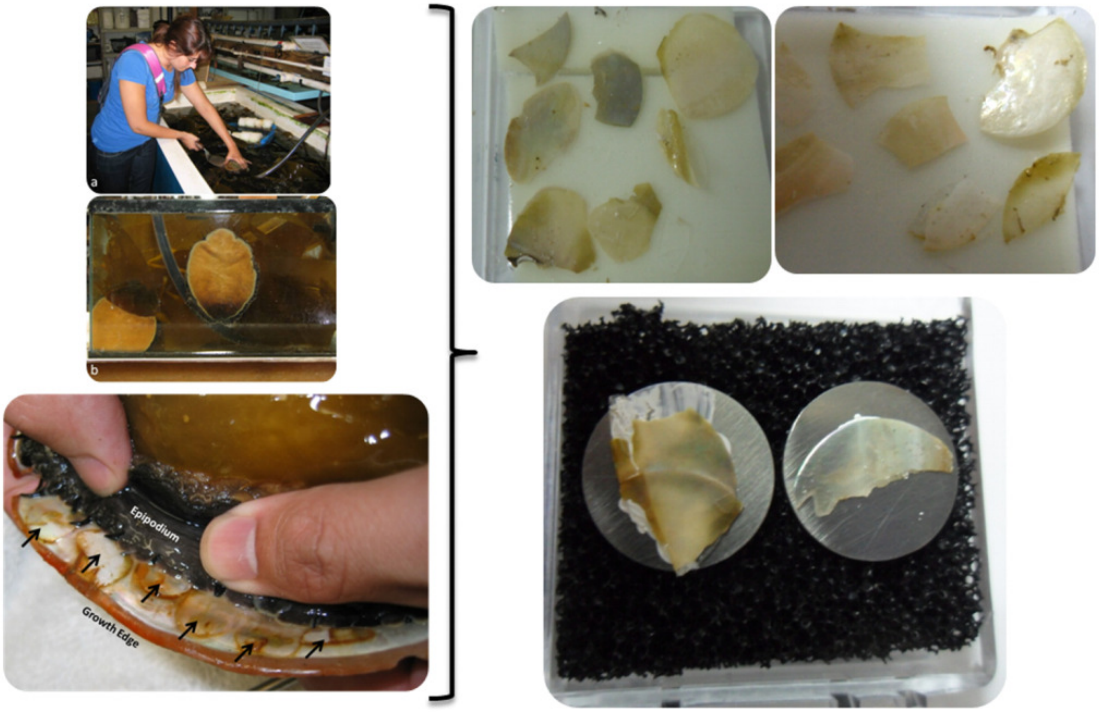


**Figure 3.14:** AFM specimens utilizing flat pearl method preparation.

Samples were prepared implanted growth surfaces for observations through Atomic Force Microscopy (Figure 3.15). Two instruments were used; A Veeco Scanning Probe Microscope located at the Nano3 Laboratory in Calit[2], and an Atomic Force Microscope in National Tsing Hua University in Professor's Duh's Laboratory at the with the help of Pao-Sheng Chen and Yu-Chen Chan.

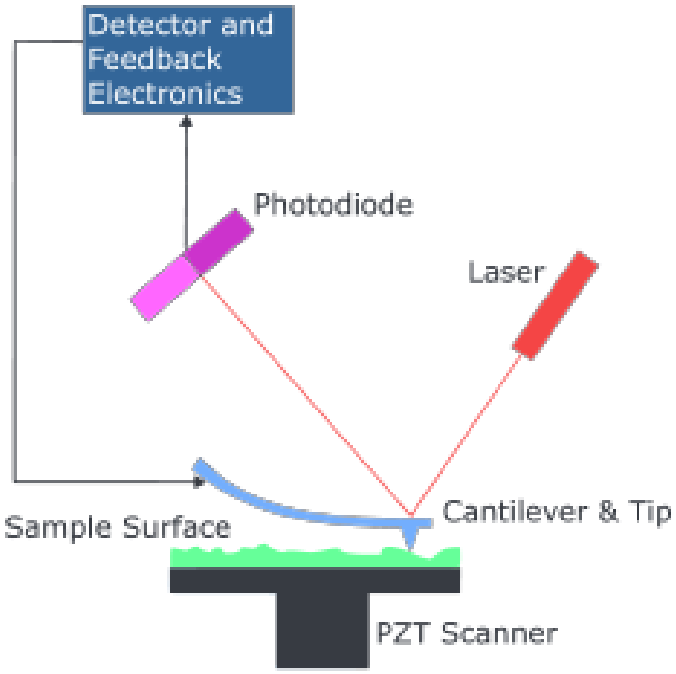


**Figure 3.15:** Schematic diagram of Atomic Force Microscope

### *3.4.4 Critical Point Drying:*

Demineralized specimens of nacre sectioned from the growing edge of the abalone shell were then dehydrated completely in a progressive manner in ethanol and $CO_2$ critical point dried so that the structure was maintained. They were then flushed with 25%, 50%, 75%, and 100% ethanol for periods exceeding 40 minutes at each stage. They were then placed in a critical point drying machine and drenched in liquid $CO_2$ under

high pressure. The temperature of the critical point chamber was then raised to the point in which liquid $CO_2$ directly becomes vapor, which freezes the material leaving the organic interlayer intact without deformation.

### *3.4.5 Transmission electron microscopy preparation and imaging:*

### *Fixation, Staining, and Embedment of Tissue*

Preparation for transmission electron microscope (TEM) specimens of the epithelium was performed using a procedure typical for animal tissue preparation. Because biological materials contain large quantities of water and the TEM works in vacuum, the water must be removed. However, the structure is altered by drying the tissue directly, thus, to avoid these changes the structure, the specimens must be fixed. By fixation the molecules become cross-linked with each other and preserve the structure. For the current work, the outer surface of the epithelium (which is in contact with the growth edge of the shell) was cut using a precise scalpel into 1mm thick sections. Specimens were oriented and fixed immediately after. A primary fixation was performed by immersing the tissue sections in 2.5% Paraformaldehyde, 2.5% glutaraldehyde in 0.1 M Cacodylate buffer, pH 7.4 for 2 hours in ice. A primary wash was then done by washing the specimens 5 times with a (3 minute duration in between) in 0.15 M cacodylate buffer. Then a secondary fixation was done by placing the specimens in 1% osmium tetroxide in 0.15 M cacodylate buffer, pH 7.4 for 2 hours in ice. A secondary wash consisting of 3 washes with 5 minute duration in between in double distilled water. Then the specimens where stained in 1% uranyl acetate in 25% ethanol and incubated at 8° C overnight.

The specimens where then washed again with double distilled water 5 times, in the final wash the specimens were allowed to sit in the double distilled water 5 minutes. Dehydration was then performed by immersing the specimens in 1 x 10 min. in 20% ethanol, 1 x 10 min. in 30% ethanol, 1 x 10 min. in 50% ethanol, 1 x 10 min. in 70% ethanol, 1 x 10 min. in 90% ethanol, 3 x 10 min. in 100% ethanol (EM grade) 3 x 10 min. The vials were replaced to ensure no humidity remained. The specimens where then infiltrated and gradually embedded in Spurr's resin (10.0 ml Noenyl Succinic Anhydride, 5.0 ml Epoxy-cyclo-hexane-carboxylate, 2.0 Dow Epoxy Resin 736, 0.2 ml Diamethyaminoethanol) by being placed in a 33/67, 50/50, 67/33, 75/25 Spurr's resin/etanol, and 3 X 100% Spurr's resin solution (placed for 24 hours each exchange). Polymerization was then performed by orienting and placing the oriented specimens in an aluminum tray in a 60°C oven for 24 hours (Figure 3.16).

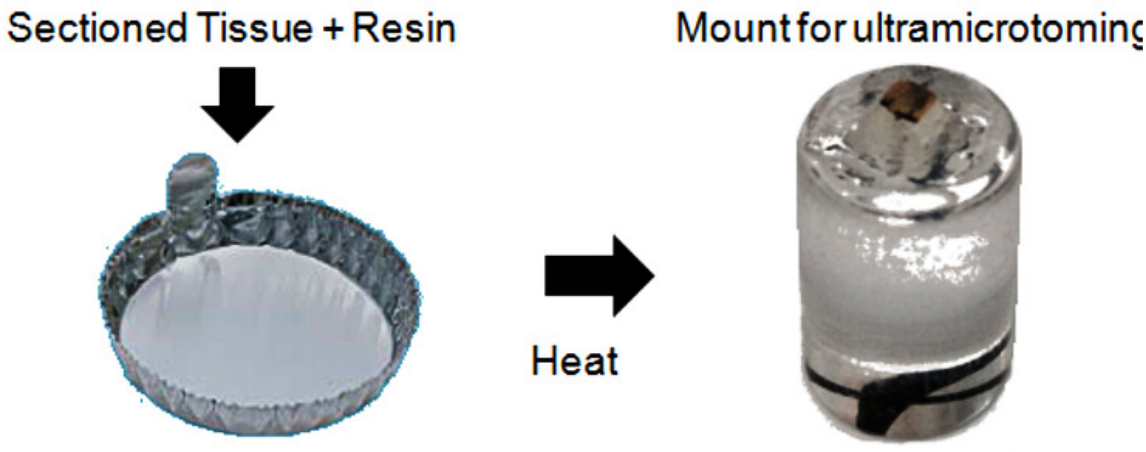


**Figure 3.16:** Mounting of the stained and fixed tissue specimens.

*Sectioning for TEM observation*

To image the specimens in the TEM it has to be of such low density that the electrons are allowed to travel through the tissue. Thus, the embedded tissue was cut into thin sections (~70-90 nm thick) by a glass knife in a ultramicrotome (Figure 3.17). The ultramicrotomed sections were then placed on a copper grid for TEM observation.

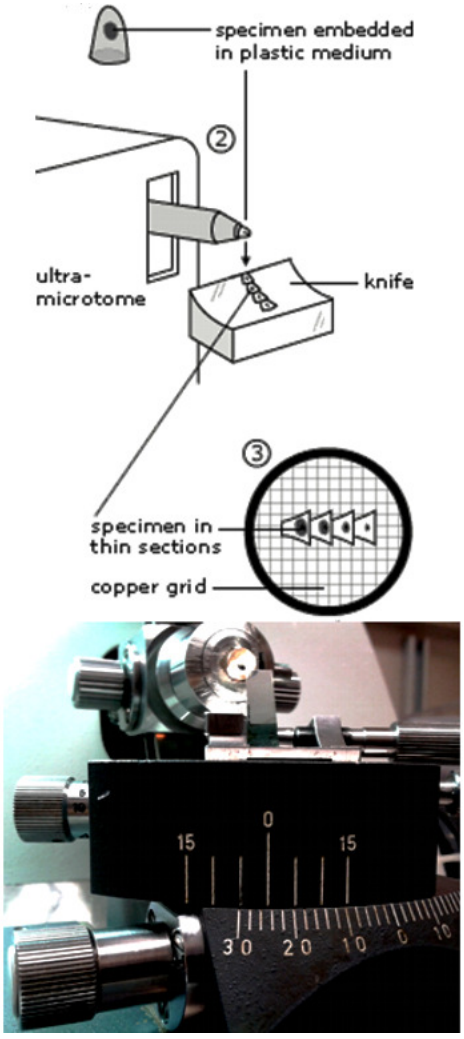


**Figure 3.17:** Schematic and actual setup of ultramicrotoming procedure.

# CHAPTER 4

# RESULTS AND DISCUSSION

The following chapter has been divided into three main components:

- Growth Experiments
    - Flat pearl growth experiments: SEM and AFM observations
    - Epithelium characterization: SEM and TEM observations
    - Organic constituent and its influence on growth
- Mechanical testing and observations of demineralized nacre
    - Imaging of fracture surfaces, nano interlamellar layers, and mesolayers
    - Quasi-static tensile tests
- Mechanical testing and characterization of deproteinized and untreated nacre.
    - Quasi-static tensile tests
    - Micro-scratch experiments
    - SEM observations of fracture surfaces
- Modeling of the organic membrane.
    - Constitutive model of demineralized nacre under quasi-static uniaxial tension
    - Analysis of the expansion of hole in the organic interlamellar membrane subjected to tension

An analysis and discussion of the results is presented within each subsection.

## 4.1 Growth Experiments

### *4.1.1 Characterization of Growth Surfaces*

This section will describe the results of the mineral deposition on the glass slides obtained by utilization of the flat pearl method. It will become clear that the morphology of the deposited mineral varies extensively with alterations in ambient conditions. This section will attempt to explain why these structural differences occur.

Flat pearl deposition experiments were utilized to expand the knowledge of results obtained by Lin et al. [24]. Growth experiments were performed for a period of three weeks, following the similar methodologies utilized by Lin et al. [24] (for detailed explanation see chapter 2). Because the tests were performed under some critical conditions, e.g. lack of nutrition, it was not possible to extend the growth period for an extreme length of period of time without the fatality of the animal which would in turn alter the results. Therefore, for comparison purposes only results taken for a period of up to three weeks will be discussed here.

Tests were conducted in the three different environmental conditions demonstrated dissimilar results. The investigation in warm water (21 °C) revealed that the aragonite tiles formed after only one week (Figure 4.1). Furthermore, the folding organic layers which are approximately 20 nm thick (marked by arrows) can be observed. Conversely, in cold water (15° C) (Figure 4.1 b) or with food limitation (20°C) (Figure 4.1 c), observations after one week showed only the slight start of the precursor aragonite spread across the substrate and some of the deposited mineral transitioning to spherulitic aragonite. Slides from the additional abalone were also observed and confirmed the same results. In addition, it is interesting to note, that not only was there an immense

difference in the morphology of the sample, but also the amount of deposition. Figure 4.2 shows the most noticeable difference in quantity of deposition, where the coverage exhibited under a well fed and warm environment (Figure 4.2 a) can be compared with conditions deficient in nutrients.

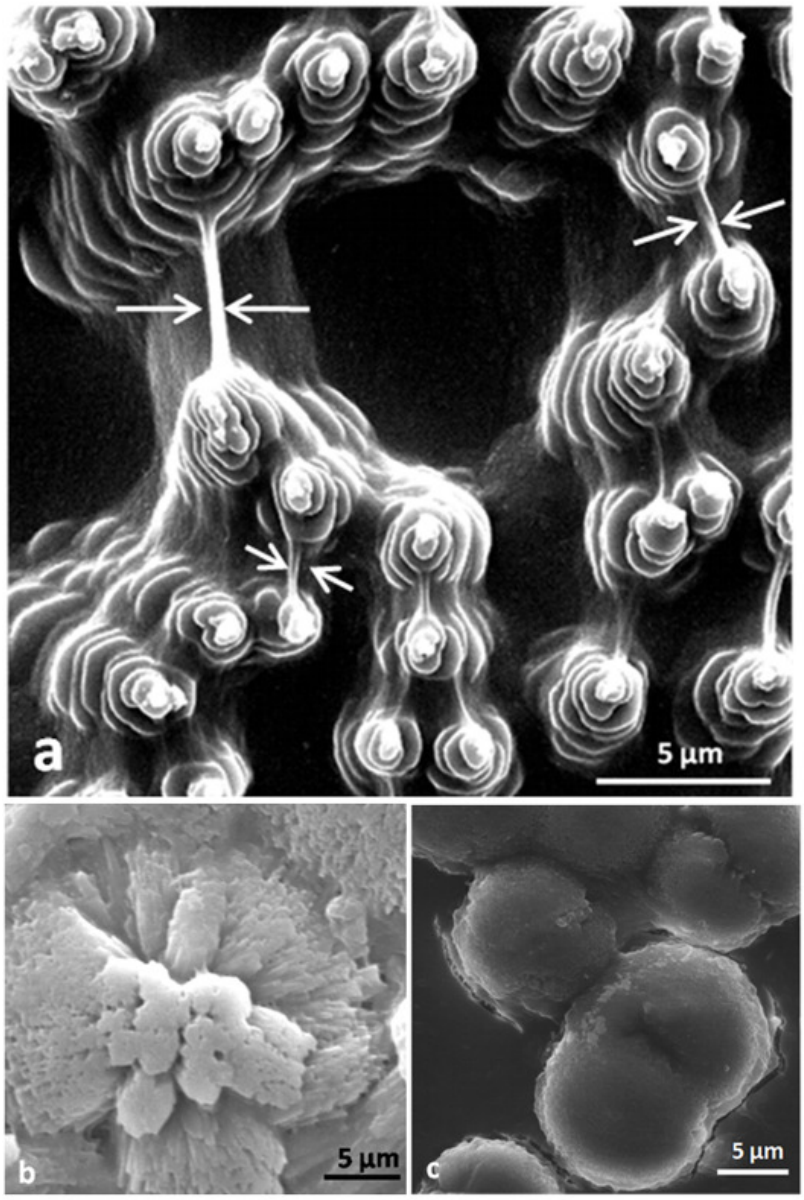


**Figure 4.1:** Sequential growth results 1 week after implantation. a) Growth at 21°C with abalone regularly fed; b) Growth at 15°C with abalone regularly fed; c) Growth at 20°C without food available.

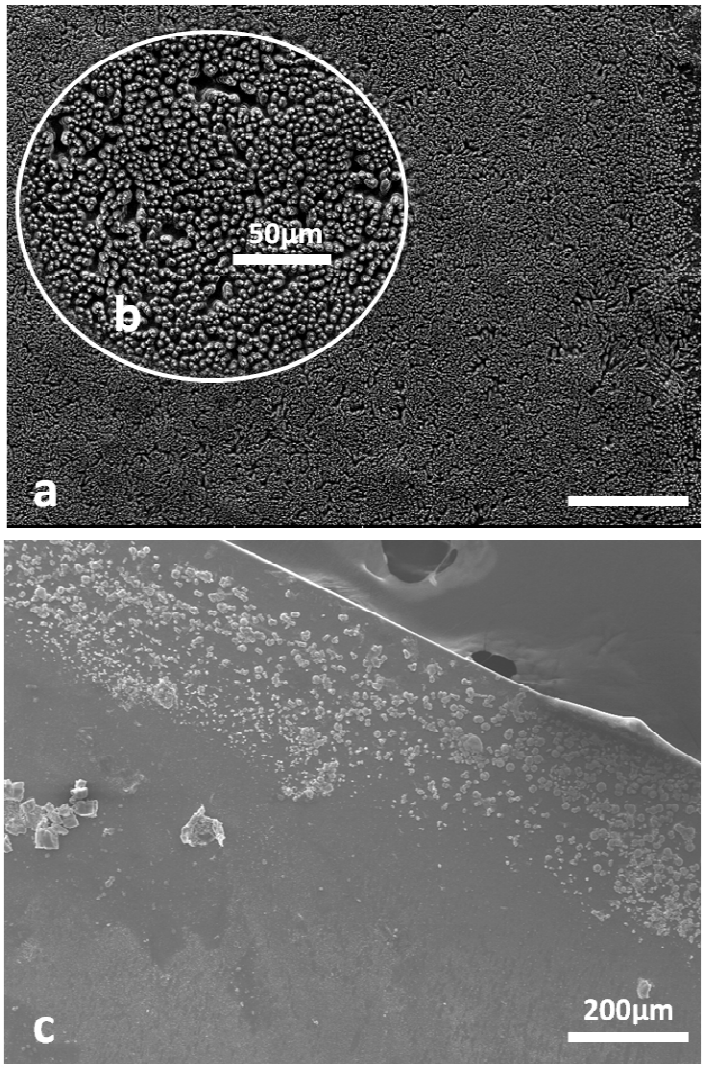


**Figure 4.2:** Sequential growth results 1 week after implantation. a) Growth at 21°C with abalone regularly fed showing the coverage exhibited by the tiles (top view); b) higher resolution of top view of growth at 21°C with abalone regularly fed (top view); c) Growth at 20°C without food available.

Moreover, after week 2 demonstrated similar aragonite tiles (Figure 4.3 a) when the growth was conducted in warm water (21 °C). In contrast, uniform spherulitic aragonite was observed in cold water (15 °C) (Figure 4.3 b) or under no feeding conditions (20 °C) (Figure 4.3 c). Interestingly, the spherulitic aragonite observed when the animal was not fed tends to be less radiated compared to the structure in colder water.

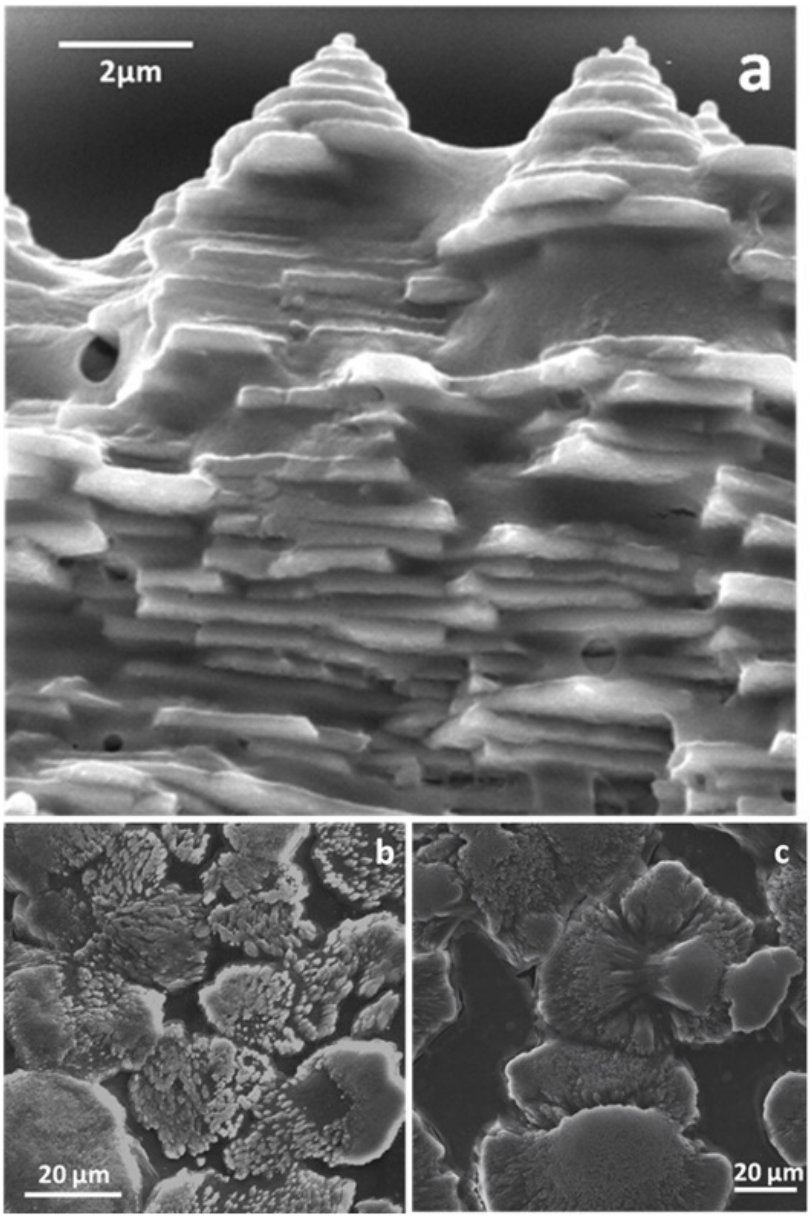


**Figure 4.3:** Sequential growth results 2 weeks after implantation. a) Cross-sectional view of growth at 21 °C with abalone regularly fed; b) Growth at 15 °C with abalone regularly fed; c) Growth at 20 °C without feeding.

After three weeks of growth in warm water (21 °C), a uniform and high number of staked aragonite tiles (terraced cones) were observed (Figures 4.4 a and 4.4 b). It can

be noted from Figure 4.4 a that because the height of the terraced cones is the same, an even deposition is formed. In addition, from this cross-sectional view, a continuous membrane formed by the organic layer can be observed. From Figure 4.4b it can be noted that the top of the terraced cones appears to be of a consistent diameter (~400 nm). On the contrary, after three weeks of implantation, the tops of each spherulitic bundle form a plateau for test at 15 °C (Figure 4.4 c) and test without feeding (20 °C) (Figure 4.4 d). In addition, the thin organic membrane can be observed (Figure 4.4 c).

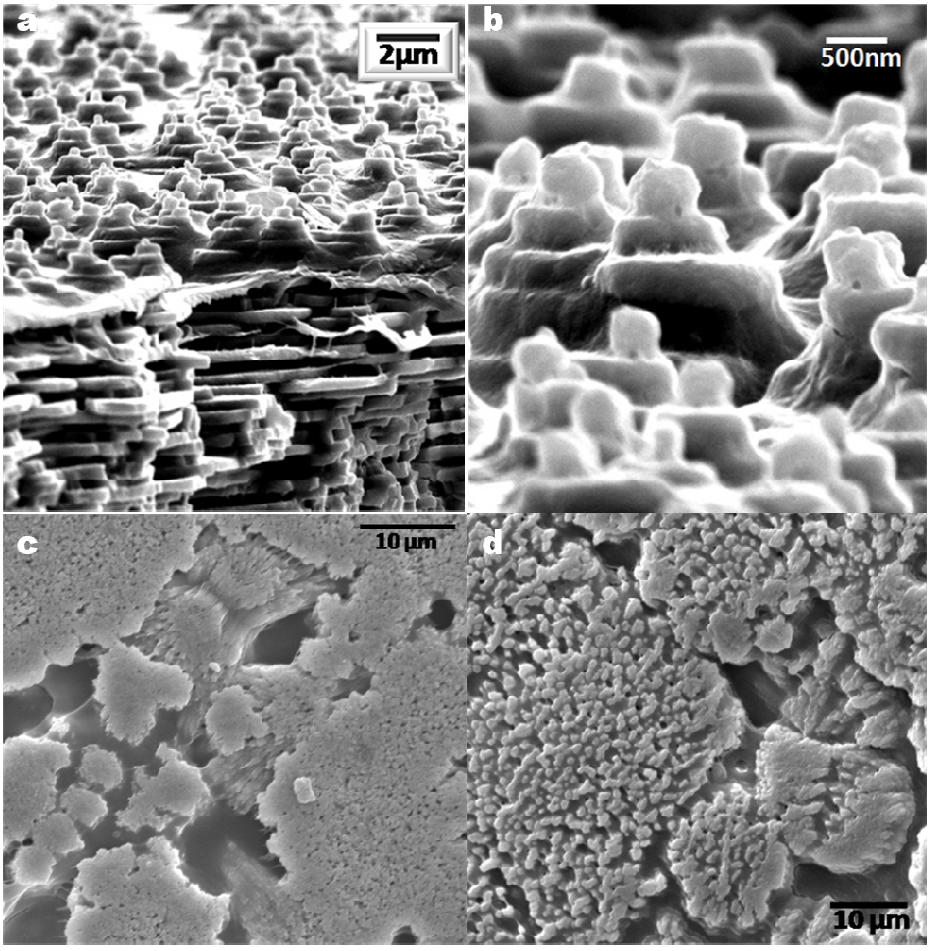


**Figure 4.4:** Sequential growth results after 3 weeks of implantation. a) Growth at 21 °C with abalone regularly fed (cross-section); b) Detailed view of aragonite tile morphology; c) Growth in 15 °C with abalone regularly fed; d) Growth in 20 °C without food available.

AFM confirmed all the features observed by SEM. Figure 4.5 shows the growth surface in 21 °C. These mineral projections (terraced cones) are approximately 2 μm high, containing about four layers from the top of the cones. This corresponds to the thickness of the tiles, (~0.5 μm). One can also see in Figure 4.5, on the sides of the protrusion, which represent terraced cones, the organic interlayer in a tent-like formation. This is similar to the configurations seen in Figures 4.2, 4.3 and 4.4 a,b, in which a thin organic layer covers terraced cones and demonstrates that the organic layer, in its fully hydrated condition, stretches under its own weight. On the other hand, it acquires substantial strength when it is dry [48]. In contrast to this, Figure 4.6 demonstrates that only the spherulite morphology is attained with growth in water at 15 °C. Some distortion exists as the AFM tip does not capture very well the lateral details. It should be clarified that the rate of the transition from initial randomly arranged $CaCO_3$, a spherulitic transient phase, to final aragonite tile growth reported here is not the growth rate of the nacre, which is also affected by temperature and food availability [128]. Sequential growth results discussed by Lin et al. [24] demonstrated the shell growth required various transitory phases to reach the steady-state growth of aragonite tiles. Aragonite tile formation was achieved after approximately 6 weeks of precursor transitory phases (this previous study was performed at 15 °C and the animal was fed regularly). The growth surfaces (Figure 4.1 b and 4.3 b) show dominating spherulitic pattern and columnar growth which is comparable to the results for three to four weeks described by Lin et al. [24]. In contrast, when the temperature was warmer (21 °C), the transitions occurred faster. At this temperature, the transitory phases cannot be observed as the steady-state growth of aragonite tiles is reached by week one. Additionally, when the animal was not

fed, the transitions occurred later. The columns observed in the limited food condition at 20 °C tend to be less radiated and the surface less smooth when compared with the growth surfaces attained at 15 °C. It is believed that the predominant columnar growth of the aragonite mineral is interrupted by the deposition of thin organic intertile layer [48]. The lack of nutrients and lower temperature may reduce the production of the organic layer (chitin and proteins), which leads to an unimpeded rapid columnar growth instead of the steady-state growth of the aragonite tiles.

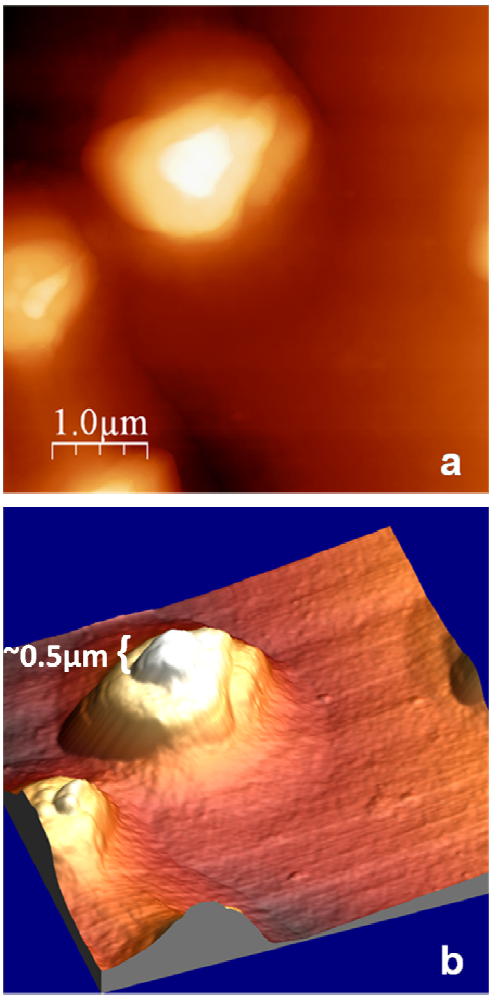


**Figure 4.5:** Atomic force microscopy of growth surface in 21 °C showing the aragonite tile growth. a) Top view; b) Tridimensional view.

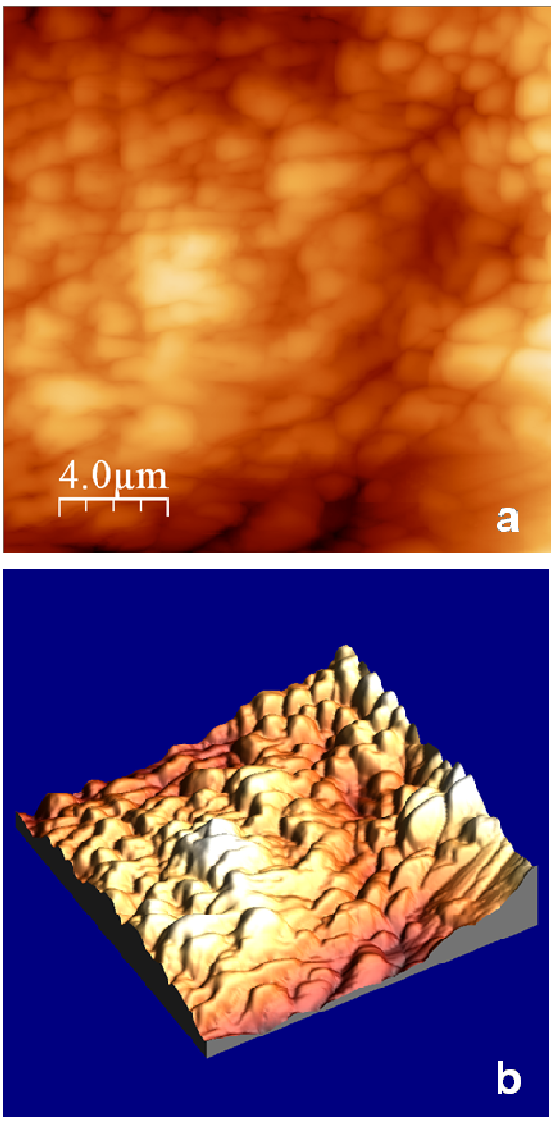


**Figure 4.6:** Atomic force microscopy of growth surface at 15 °C showing the columnar structure. a) Top view; b) Tridimensional view.

Figure 4.7 shows characteristic AFM images of the growth surfaces. In where the characteristic aragonite tile and brick morphology characterized by the terraced cones, not clearly visible due to the organic interlayer in a tent-like formation. The organic interlayer covers the tops of the tiles and blurs the steps of the terraced cones. Figure 4.8 shows the transition zone, or spherulite aragonite which appears rough.

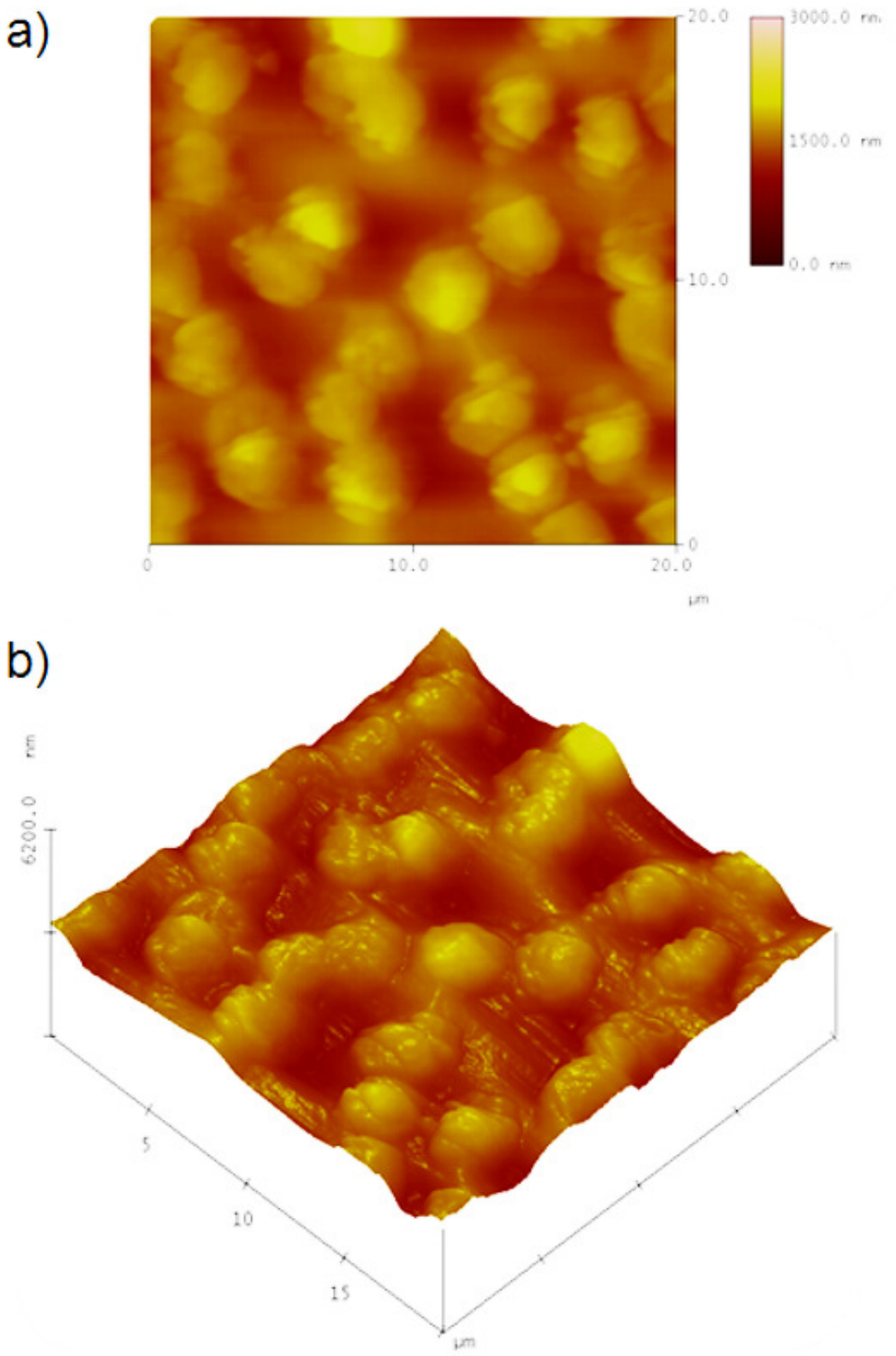


**Figure 4.7:** AFM image of the characteristic morphology of nacre brick and mortar structure. a) Top view; b) Tridimensional view.

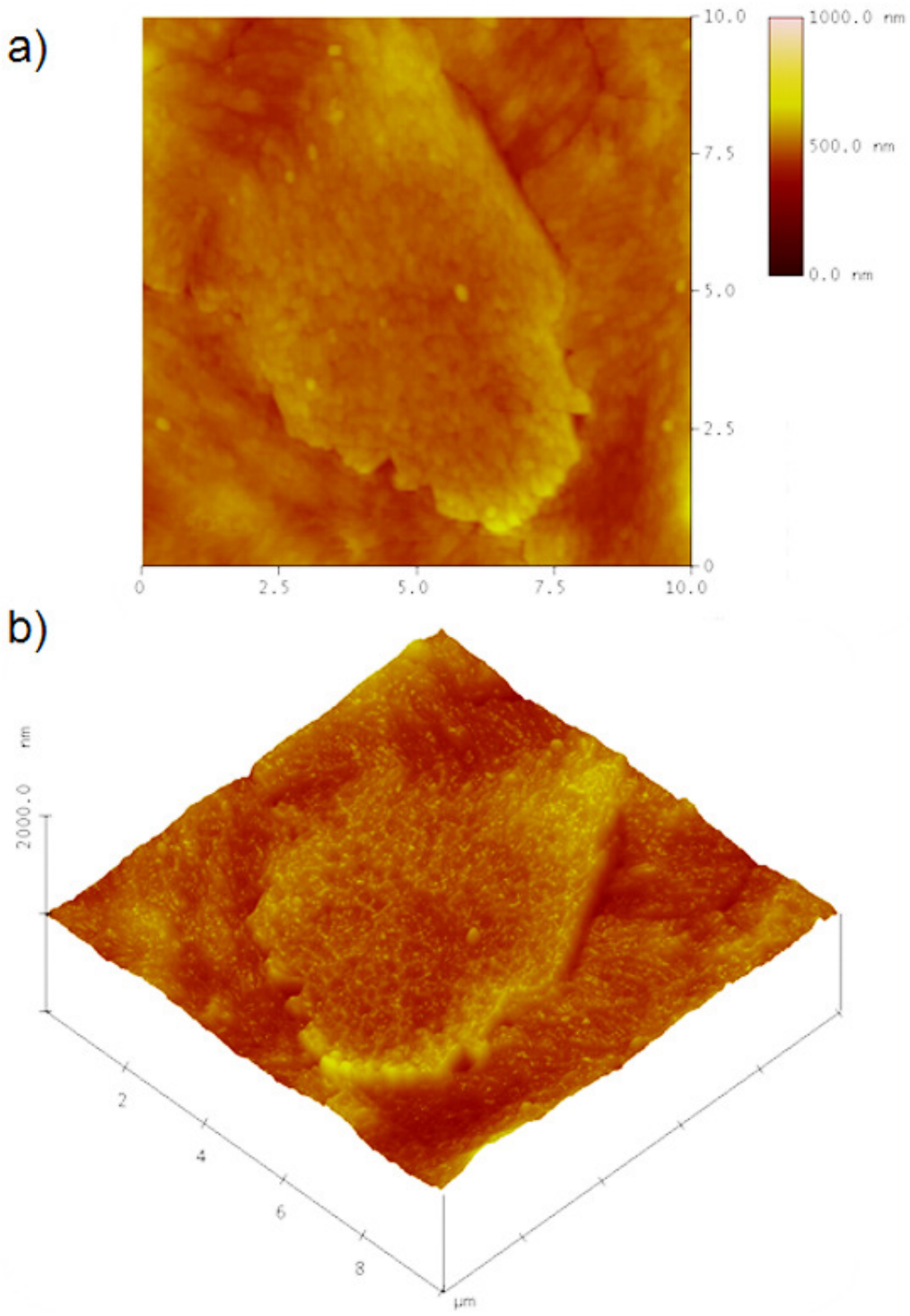


**Figure 4.8:** AFM image of spherulitic aragonite that forms in the transition zone of the nacre. a) Top view; (b) Tridimensional view

*4.1.2 Epithelium Observations*

Shell diversity in gastropods, bivalves and other mollusks are achieved through the ordered secretion of proteins and other molecules along the length of mantle [8, 129-140]. In haliotis, it is believed that the mantle edge is involved in prismatic layer ingrowth, and the whole mantle surface is involved in the thickening of the nacreous layer [141-145]. Shell layer production of at least organic matrix has been assigned to the external mantle epithelium. Despite these recent advances in determining the biochemical basis of the biomineralization process and a growing number of studies on matrix protein characterization, there is still some controversy about the cells involved in matrix protein secretion [146]. Some work [147] suggests that the direct supply of material for shell growth is not from adjacent mantle cells but that the shell material deposition is from a distant epithelial site involving a maturation step within the extrapalleal fluid. Regardless, little is known about the tissue distribution of the external epithelium with regard to shell matrix protein production. And due to the double crystallography of the shell's external layer (containing 2 polymorphs) it is hypothesized that the front edge of the mantle is able to synthesize matrix proteins for both aragonite and calcite [146].

Indeed, the different organic components produced by the mantle are responsible for the properties of the layers in the shell. One component produced and found within the organic constituent is Lustrin-A [4, 18] which is considered to affect fracture resistance and the elastomeric properties of the nacreous layer. Other components, such as the macromolecules isolated from calcitic or nacreous environments can direct the type of polymorph of $CaCO_3$ that will be deposited [19, 73, 148]. Although of great interest,

these components have not been fully studied due to the difficulty of purification. The shell matrix proteins are mostly insoluble, highly acidic or complexed with minerals [149].

The incorporation of these organic components in the shell surface and shell matrix is not only important in the structure and mechanical properties, but also by serving as feedback on the gene expression activity of the mantle throughout the life of the animal [150]. The frontal edge of the mantle is quite complicated and divided into separated areas that can be controlled to form the separate layers in the shell [146].

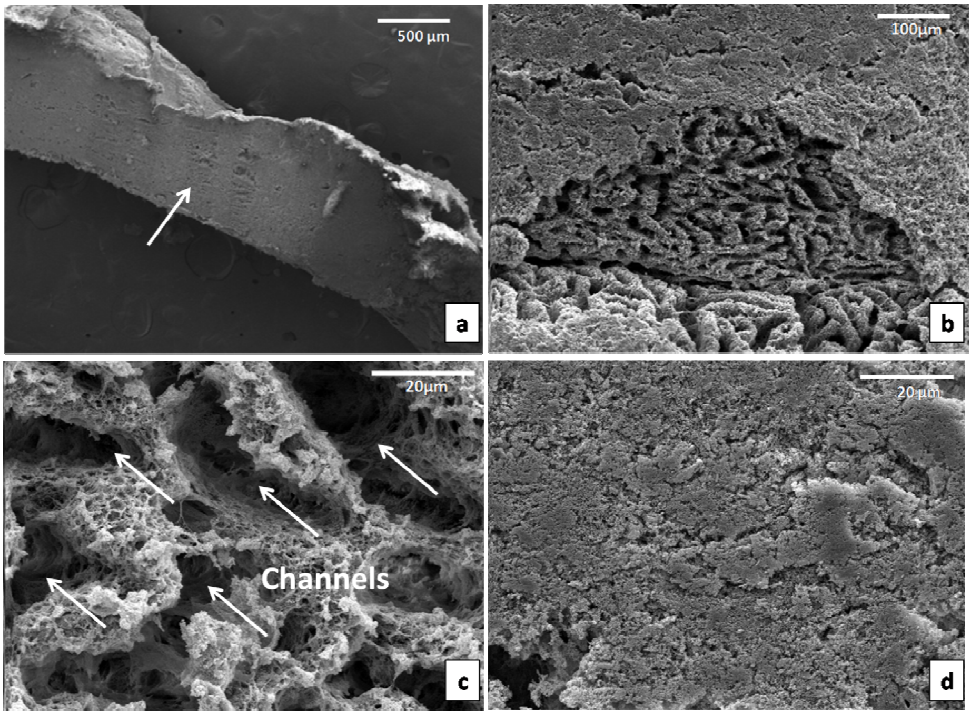


**Figure 4.9:** a) Sectioned epithelium; surface in contact with growing edge of shell depicting flat outer surface (arrow) and areas where surface was scraped off; b) Detailed view where surface was scraped off; c) Array of channels within epithelium (channels depicted by arrows); d) Detailed view of flat outer surface of epithelium.

To understand the relationship among the nacre, mantle, and the extrapallaial fluid, the mantle epithelium was characterized via scanning and transmission electron microscopy. Inspection of the mantle reveals the secretory epithelium which is in direct contact with the inner surface of the shell (Figure 4.9 a, denoted by arrow).

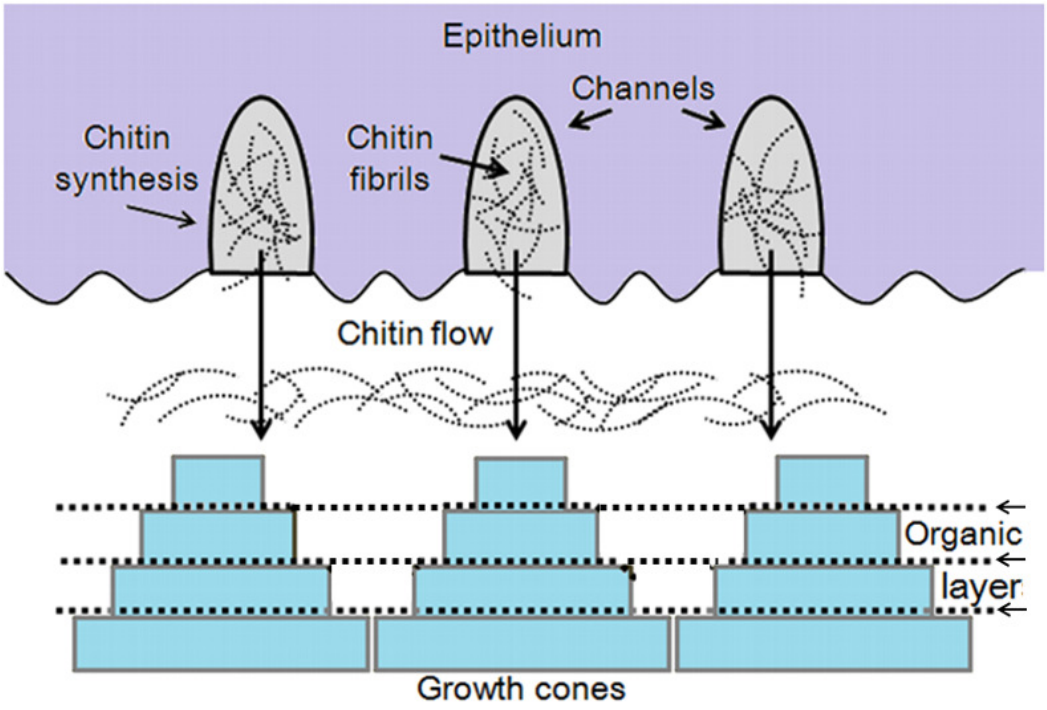


**Figure 4.10:** Schematic depicting hypothetical mechanism by which epithelium generates chitin fibrils and 'squeezes' them onto growth surface.

This part of the animal is the critical component in the mineralization of the shell, since it is only separated from the growing surfaces by the small extrapallial space. SEM inspection (Figure 4.9 a) shows a top section of the outer surface of the epithelium and an area where the top surface is scraped off (Figure 4.9 b). The relatively smooth outer surface of the epithelium (Figure 4.9 d) suggests that the epithelium mechanically flattens

the growing surface by sliding over the shell, producing a molding effect [24] analogous to a potter molding clay. From the scraped surface one can observe that an array of channels exists inside the epithelium (detailed view of the channels shown in Figure 4.9 c). Lin et al. [24] and Meyers et al. [48] proposed that ions are allowed to diffuse through these channels. In addition, these channels may provide support for the synthesis of chitin and its intermittent extrusion onto the growth front (Figure 4.10).

Further inspection of the mantle epithelial layer via SEM shows cilia (from ciliated epithelium cells). Ciliated epithelium cells are long in shape and have hair-like protrusions (cilia) (Figure 4.11). Cilia project of the plasma membrane with cores made up of microtubules that are arranged uniformly in longitudinal orientation, known as, (9+2) orientation. The core of each cilium contains nine microtubules doublets located peripherally and two single microtubules in the center. They range in length from 5 to 10 μm and the diameter is about 0.2 μm. Cilia are sometimes motile and beat towards a specific direction and facilitate the transfer and movement of particles at the surface (to move the cell bodies and other sweeping processes). The cilia in epithelial cells provide chemosensation, thermosensation and mechano-sensation. More importantly, cilia secrete mucous, and form a layer apical to the epithelial layer. They are also responsible for other secretion, releasing soluble proteins and downstream them of fluid-flow. In the case of the abalone and the formation of its shell, they may act by secreting mucous, and form a layer apical to the epithelial layer.

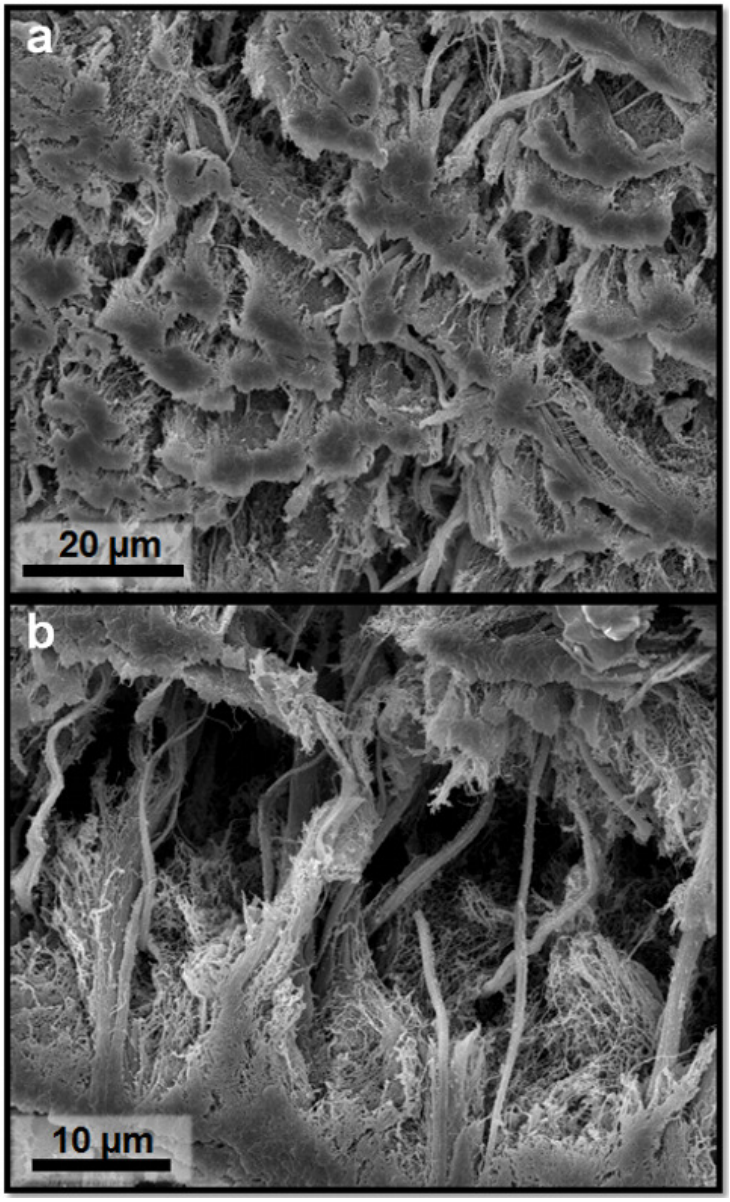


**Figure 4.11:** SEM micrograph of the surface of the mantle epithelium showing the cilia (hair-like protrusions).

The epithelium is typically lined by columnar epithelial cells (that range between 4 to 5 µm in length) seated on the basal lamina interspersed with ciliated cells and different types of secretory cells embedded in the subepithelial space and glandular cells. Figure 4.12 is a schematic that represents the edge of the mantle which shows the cilia

interspaced by microvilli. Although debate exists on the specific functions of the structure, the observance of microvilli proposes that there is a secretion of substances responsible for shell or periostracum construction. The microvilli which were firstly identified by Nakahara [37]. The microvilli have dimensions of 100 nm in diameter and 400 nm in height (Figure 4.13), which correlate well with the pattern of holes in the organic layer and the thickness of the tiles. Thus, it is proposed that a mechanism of templating is taking place as shown in Figure 4.14.

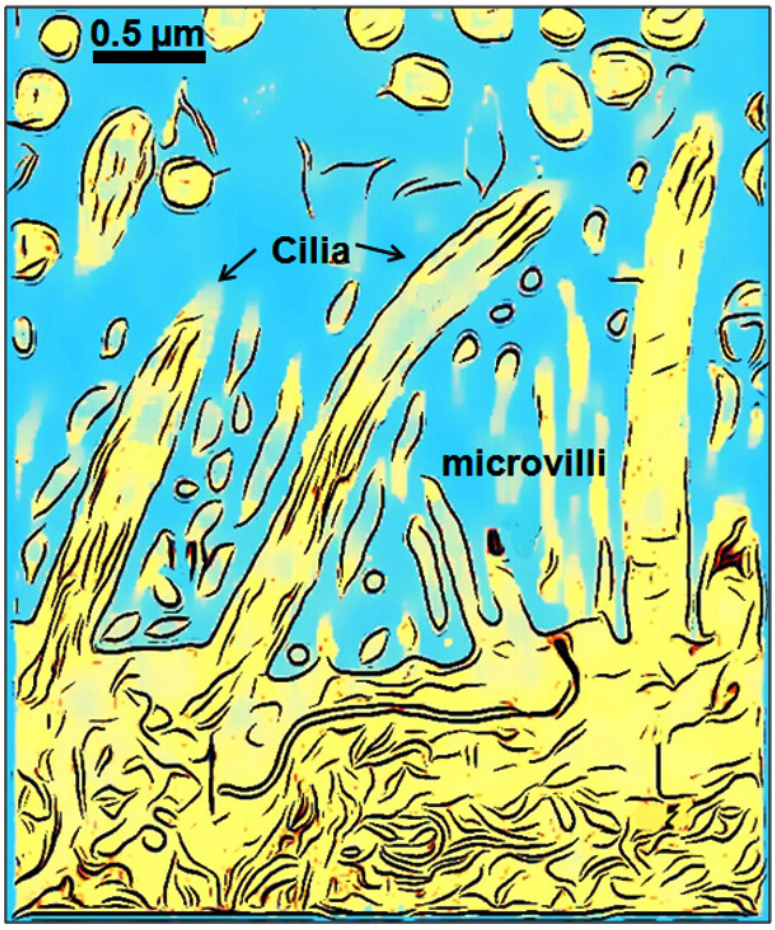


**Figure 4.12:** schematic that represents the edge of the mantle which shows the cilia interspaced by microvilli

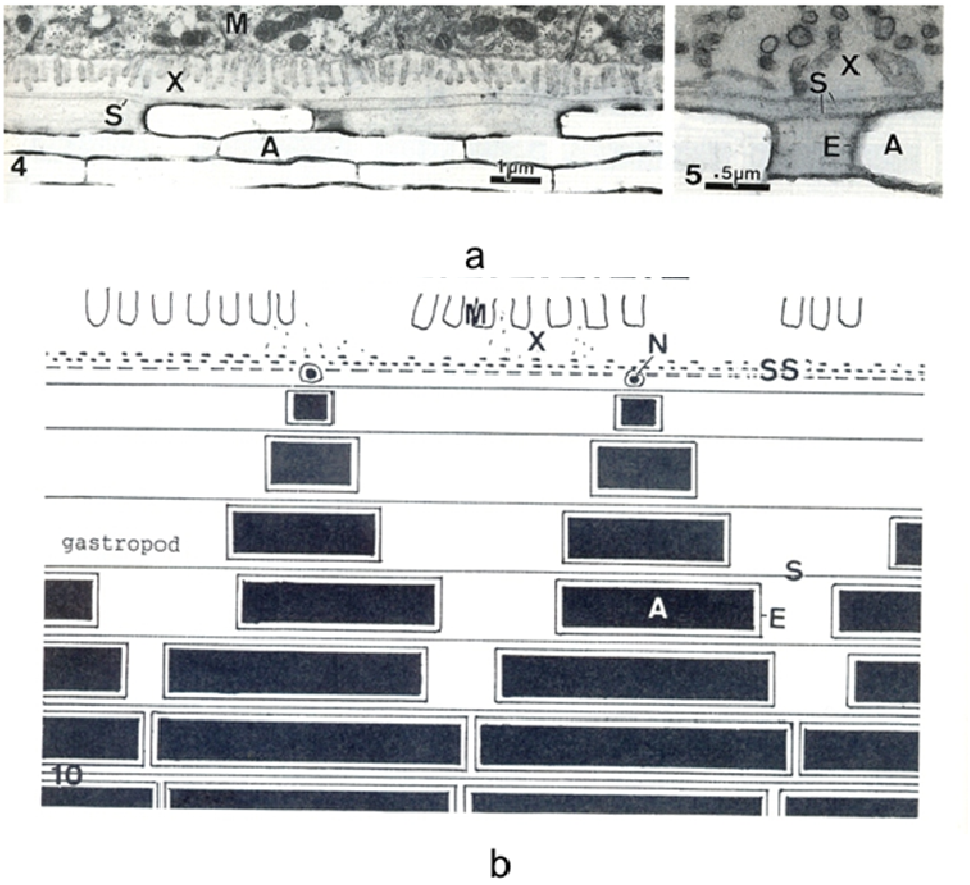


**Figure 4.13:** Microvilli depictions in nacre. (a) TEM of section of nacre from *Pinctada radiate*. Note the visible microvilli at the edge of the mantle epithelium (M) and extrapallial space (X). (b) Schematic illustration of nacre formation in gastropods. Aragonite tablets (A); Organic sheets (S); surface sheet (SS); Organic envelope surrounding crystals (E); Newly formed crystals (N); and part of epithelium (M) and extrapallial space (X). (*source*: Nakahara [37])

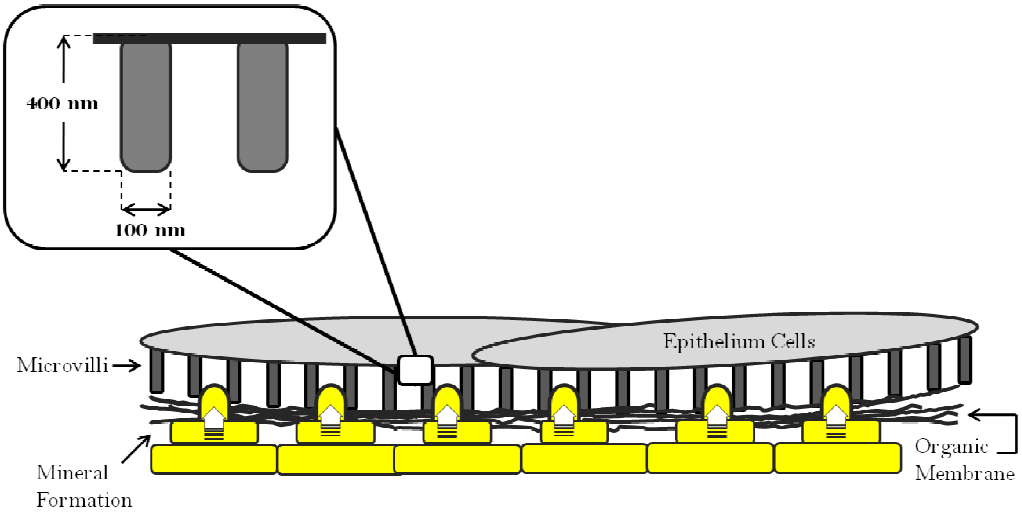


**Figure 4.14:** Schematic depiction of the epithelium cells containing the microvilli which are approximately 100 nm diameter and 400 nm height which involves in the deposition and position of the organic membrane.

Transmission electron microscopy results show mostly ciliated and secretory cells (Figures 4.15, 4.16, 4.17) and subepithelial glands (Figure 4.18). The structure of these vary (by different cell types) according to the particular function [151, 152]. It has been shown that aragonite and calcite is deposited in the prismatic layer, either simultaneously or by rapid changes in mineralization under the control of the mantle epithelium cells [153, 154]. Additionally, in other types of haliotis it has been demonstrated that across the prismatic layer, calcite and aragonite were deposited simultaneously and those terraces at the surface can change from calcite to aragonite or vice versa within shorts periods of time [155].

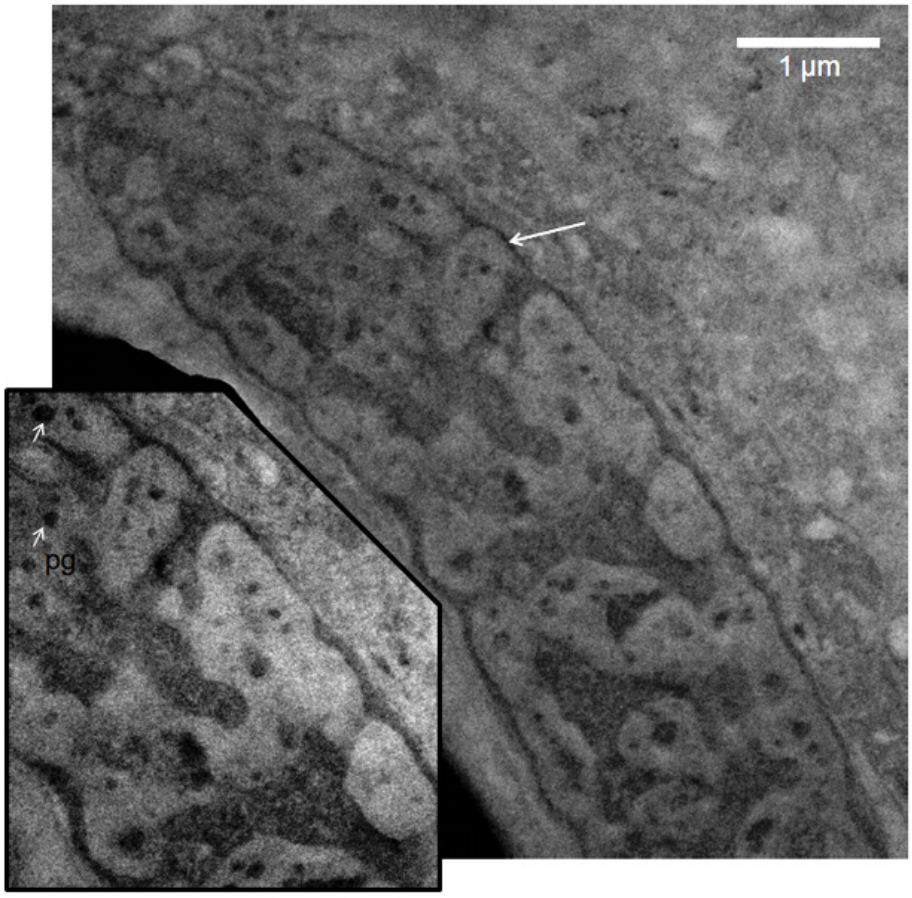


**Figure 4.15:** Transmission electron micrograph showing a secretory cell; boundary marked by arrow and detail showing the pigmented granules 'pg' (arrows).

Mucous cells are found between the columnar epithelial cells with electron lucent secretory product. The secretory cells and subepithelial glands commonly contain various types of glycoconjugates that can be specifically detected performing a histochemistry study, which is beyond the spectrum of this work. However, mucoid substances such as glycoproteins and mucopolysaccharids do not have a high affinity to electron microscopic staining agents; thus, those vesicles will appear less electron-dense in the transmission electron micrographs.

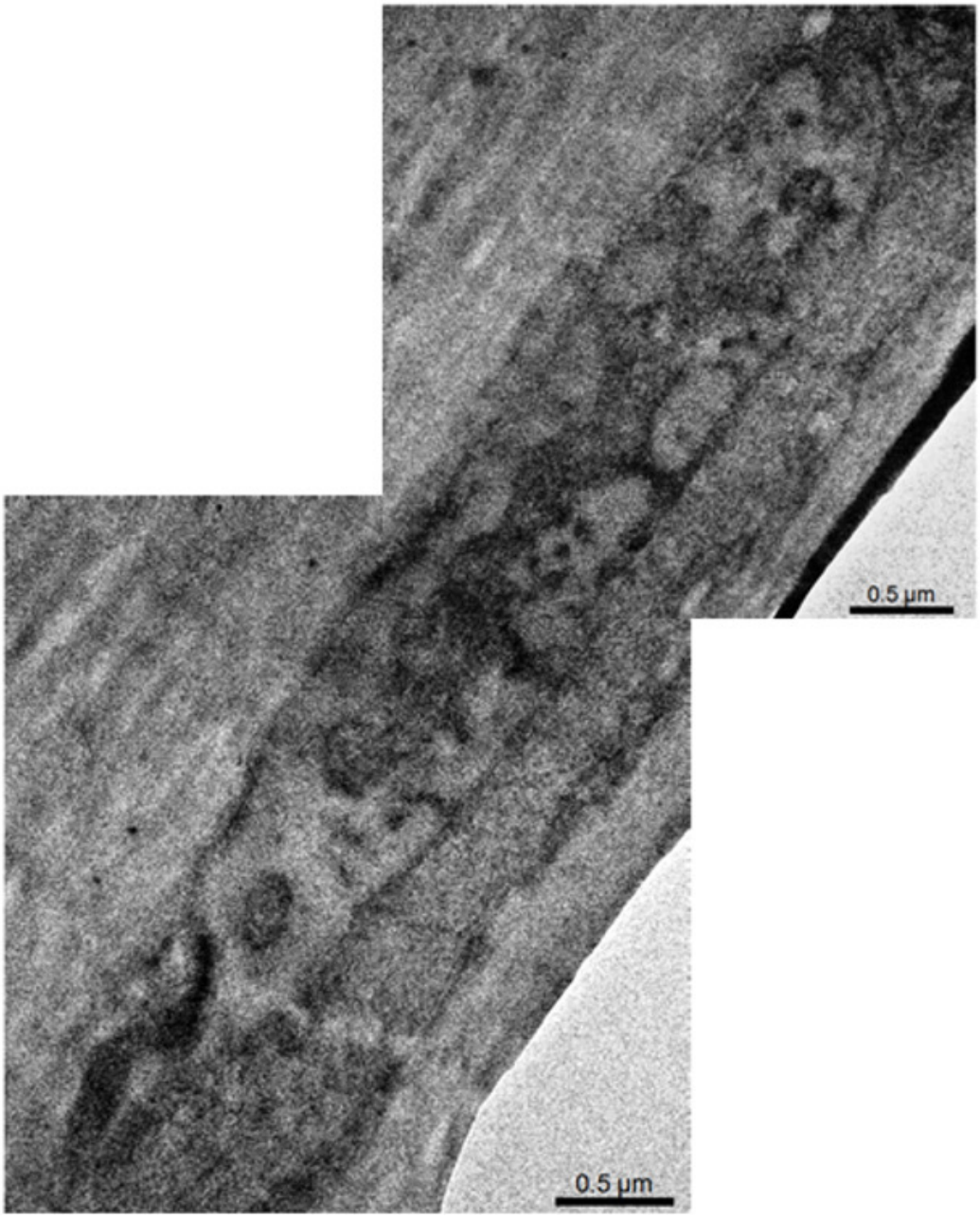


**Figure 4.16:** Transmission electron micrograph showing a secretory cell; distinguishable by the secretory granules.

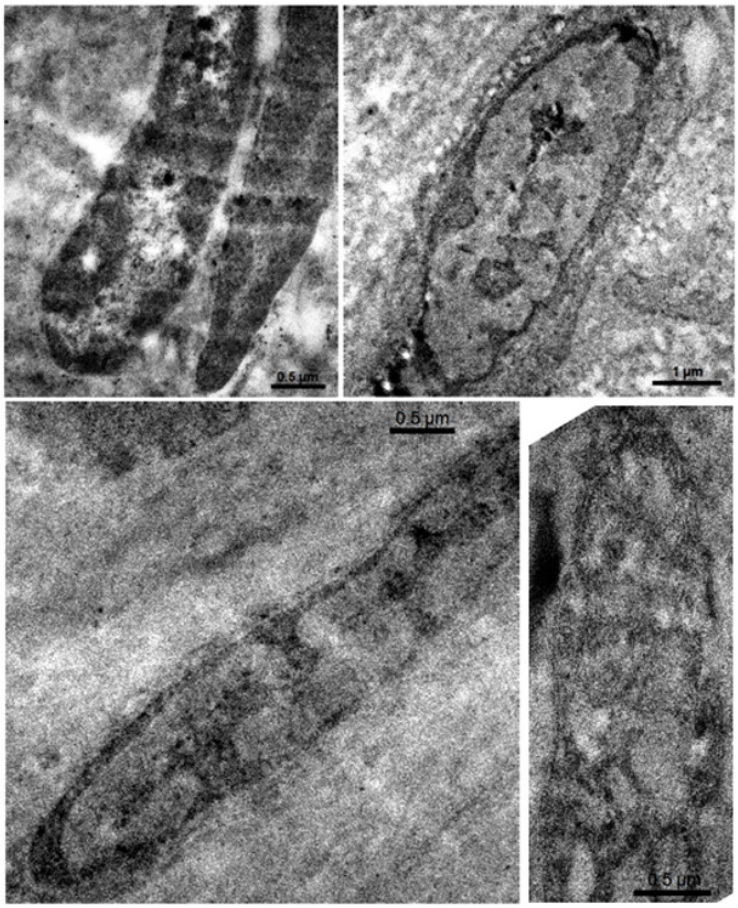


**Figure 4.17:** Transmission electron micrographs of various cells. Cells appear elongated, approximately 5 µm in length and 1 to 2 µm in width.

Secretory vesicles are vesicles that border a unit membrane that deliver secretory product to the extracellular space. Many types of secretory vesicles exist, in gastropods or in mollusks in general mucous vesicles are commonly observed.

Mucous vesicles contain mucoid substances such as glycoproteins. In Figure 4.18 the substance light as the components are relatively electron lucent. Mucous secretory vesicles are common in epithelial cells. They may deliver secretions in different matters such as:

Exocytosis; where the vesicles fuse with the cell volume. No cell volume is lost in the process (as no cytoplasm is released). This is the most common type of secretion.

Apocytosis: The vesicles gather in the apical part of the cell and proteins from the cell membrane bind to proteins at the border of the lipid droplets which then protrude into the lumen. With the fusion a bit of cytoplasm and the covering of the cell membrane is released. Some cell membrane and cytoplasm are lost with every secretion and reduce the cell volume. This type of secretion is rare.

Holocytosis: The entire gland cell fills with secretory vesicles that fuse. The epithelial cells eliminate the contact with the basement membrane and pushes forward to the lumen by increase of the basal cell layer. At a certain distance from the basement membrane the cell degenerates as it can no longer receive nutrition through diffraction. As the nucleus dissolves the secretion product fills the cell. Finally, the cell membrane is destroyed and the products are released.

Avesicular secretion: The product can easily pass the cell membrane without the need of a transporter.

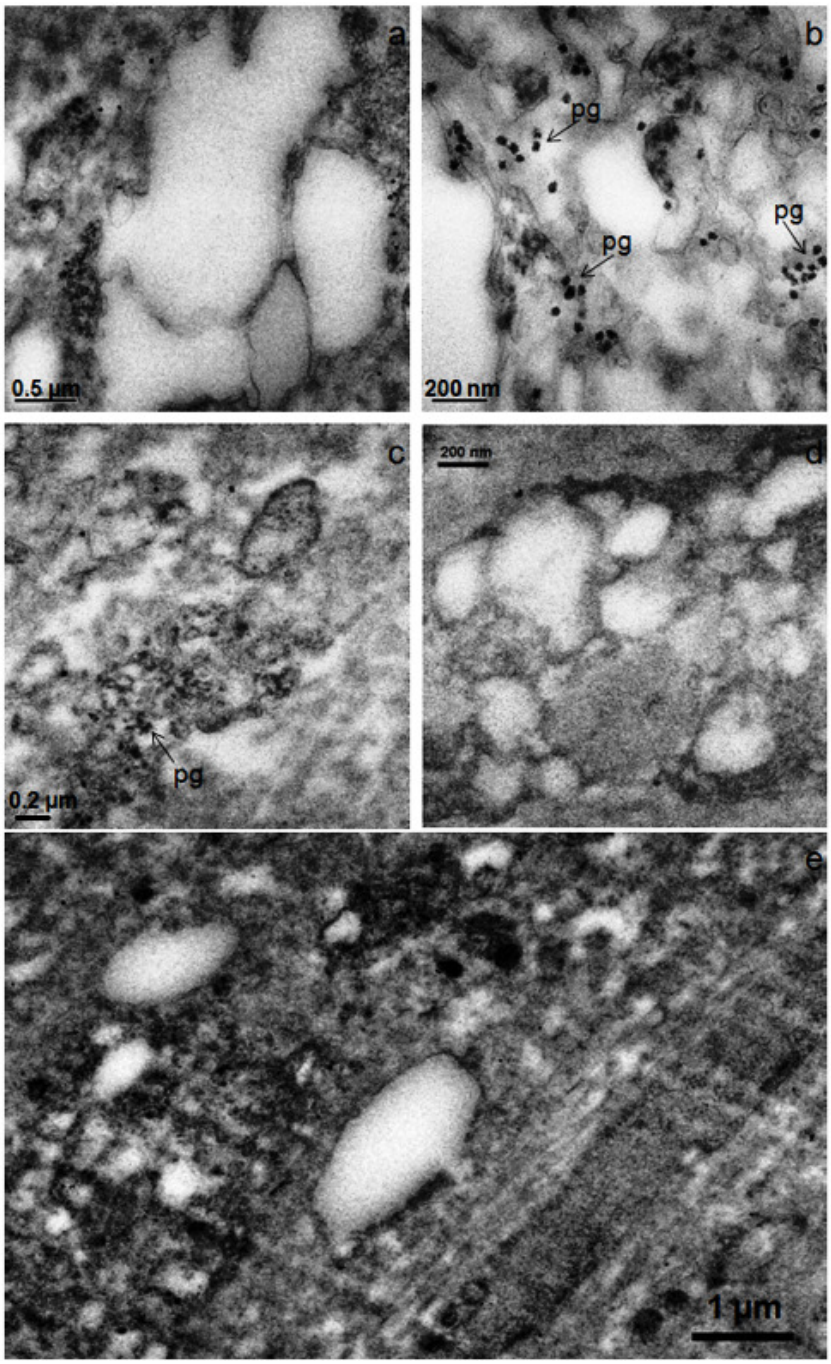


**Figure 4.18:** Transmission electron microscopy of subepithelial glands commonly contain various types of glycoconjugates. Vesicles will appear less electron-dense in the transmission electron micrographs because they do not have high affinity to electron microscopic staining agents. Pigmented granules are visible in b) and c) (denoted by arrows and 'pg').

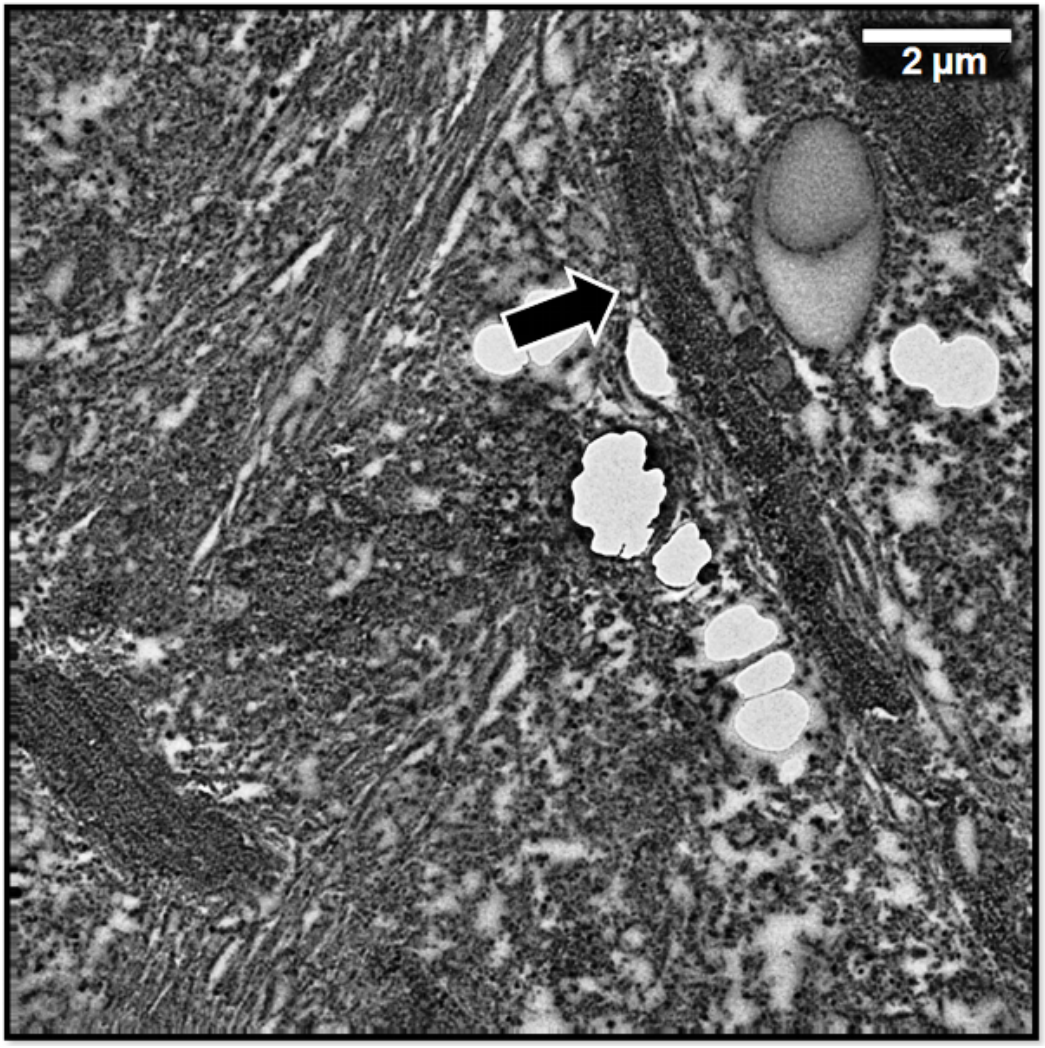


**Figure 4.19:** TEM micrograph of epithelial mantle showing cilia and a mucous vesicle with electron lucent secretory product.

There is a mucus layer found within the extrapaillal space and also on the foot of the abalone. This mucus serves different purposes, including the protection, lubrication, motion, adhesion, and in the case of the mucus found in the extrapallaial space even the transport of substances to for the formation of the shell. This mucus layer is produced by the secretory cells and subepithelial glands. The ions are provided from the environment

and from the animal's metabolism. Various pigments can be found within the epithelial cells, for example: melanin, carotenoid, bilichromes [156]; however differences in the secretory cells exist in different species. For example nine different types of secretory cells have been recognized in the marine gastropod, *Patella vulgate*, while a different distribution of secretory cells has been reported in another limpet *Acmaea tessulata* [157]. Similarly, ten different secretory cells have been reported in the marine gastropod *Littorina littorea* [158].

Additionally, the interior of the mantle shows collagen, distinguishable by the 67 nm banding pattern. From the image of Fig. 4.20, the length the D-period in the fibres was measured to be in the range of 57 - 58 nm. The measured period falls into the range of collagen fibril D-period although it is not the exact 67 - 69 nm band that is often reported in soft connective tissues.The stereological effect might explain this variation of D-period estimation (e.g., a slight tilt can change the period estimation).

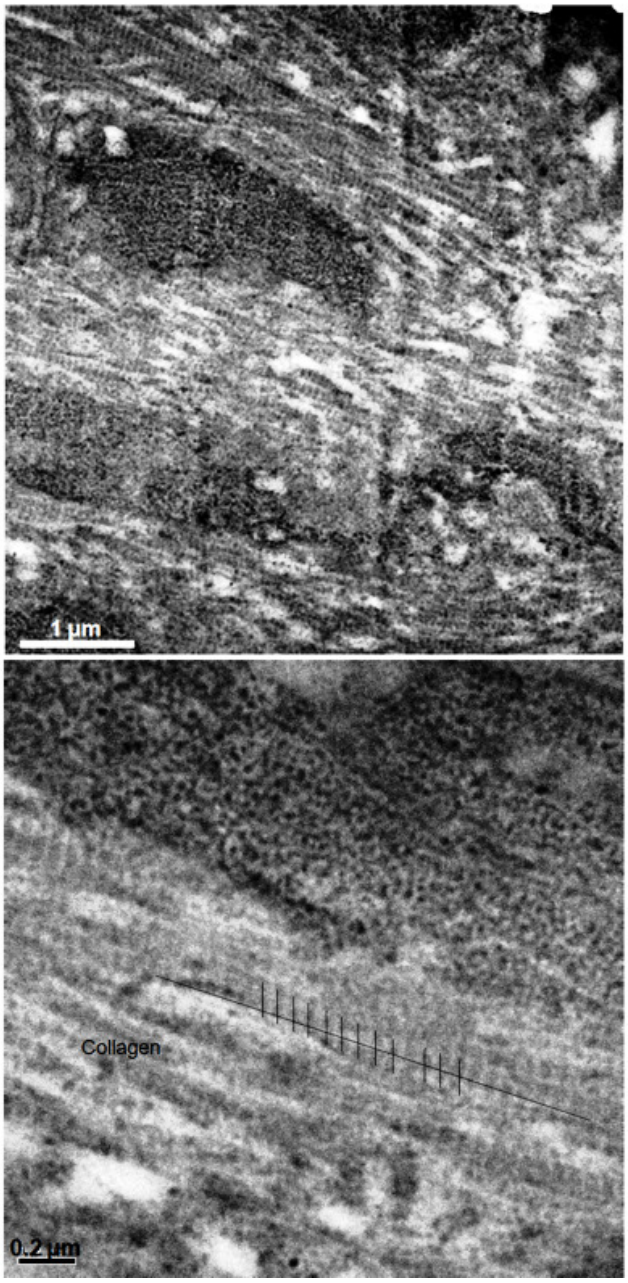


**Figure 4.20:** TEM image and schematic of epithelium showing collagen within the inner section of the mantle.

Results here show the different contributors of the mantle to the formation of the shell. Furthermore, Fritz et al. [17] mentioned that epithelial cells may respond to a down regulation of nacreous matrix production until the calcite protein matrix is

established. The shell structure is a result from the interaction through the extrapallial fluid (mucous) between the cell and the mineral interface. In which the mineral surface is monitored and recognized by the cells which undergo a genetic switch controlling the matrices, production and subsequently, the structure of the mineral.

In abalone, epithelial secreting cells show flexibility according to the cyclic activity [146]. This controls the delivery of the organic matrix material in a precise time frame. Growth experiments here add to these results as the rhythm of active zones of the epithelium can be the result of a combined response to physiologic inducing factors (factors that may be affected by environmental changes) from the mollusk soft body and to local inducers provided by the shell itself.

*4.1.3 Organic constituent and its influence on growth*

The sectioned and demineralized shell samples from the growing edge revealed areas of thin organic intertile layer (Figure 4.22) in arrays of stretched holes. This organic intertile layer is believed to be periodically deposited (every ~0.5 μm) by the epithelium in the animal. It is composed of a thin biopolymer protein framework secreted by epithelial cells [8]. This organic layer is an important characteristic and has been studied successively [25, 38, 44, 45, 48].

Lin and Meyers [38] investigated the thicker regions (20 μm) of organic layer that exist between the shell's mesolayers. These thick layers are believed to be formed by seasonal fluctuations where calcification is interrupted. Subsequently, Meyers et al. [48] further noted the role of the organic matrix (20-50 nm thick) interlayer in the formation of the $CaCO_3$ aragonite matrix into 0.5 μm thick tiles. Moreover, Meyers et al. [48]

showed further evidence of the chitin network that forms the structural component of the intertile layer and characterized it by SEM, AFM, and nanoindentation. Furthermore, Bezares et al. [44, 45] described the structure of demineralized tissue and examined its mechanical response. In addition to being a key element in the excellent mechanical properties, it is also an important component in regulating the growth of the aragonite. This layer slows down the growth of the aragonite in the rapid growth (c-axis) direction.

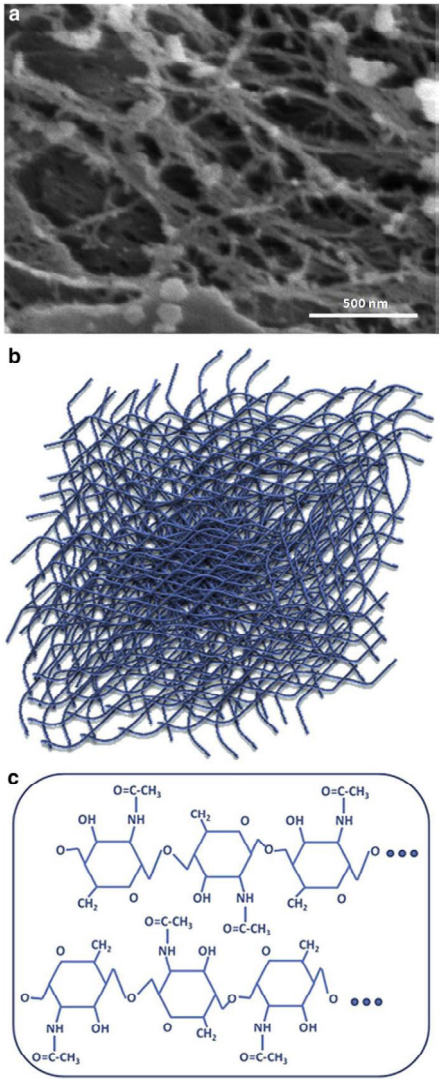


**Figure 4.21:** a) Demineralized shell revealing randomly oriented chitin fibrils from intertile layers; b) schematic representation of organic intertile layer composed of chitin fibrils. c) Schematic structure of chitin.

These results are in agreement with growth mechanism proposed by Meyers and coworkers [24, 25]. The growth of the mineral is allowed to proceed through the orifices in the organic layer as the transport of calcium and carbonate ions is permitted through the holes in the organic layer (Figure 4.22a). Figure 4.21 shows randomly oriented chitin macromolecule fibrils [10, 43, 48, 129, 159, 160] considered to be the structural component of the organic layer. There are two hypotheses explaining the formation and growth of the tiles: (a) Organic scaffold, into which $Ca^{2+}$ and $CO^{3-}$ ions penetrate, combine, and precipitate [44, 45]. (b) Periodic deposition of organic layer with holes, retarding the growth of aragonite crystals in the *c* direction (perpendicular to the growth surface) [48, 65]. The organic scaffold hypothesis requires intricate genetic engineering. On the other hand, the periodic chitin deposition hypothesis is directly regulated by the mantle. The results obtained by Lin et al. [65], Meyers et al. [48], and here strongly support the periodic deposition hypothesis, a mechanism well described by Schäffer et al. [14] and Belcher et al. [14, 16]. Especially significant is the fact that the layers between laterally adjacent tiles are much thinner than the horizontal ones (parallel to the growth surface), as shown in Figure 4.22 b. Of importance also is the identification of chitin synthesis sites in the cavernous channels within the epithelium; it is proposed that they are extruded onto the growth surface by mechanical action from the abalone foot.

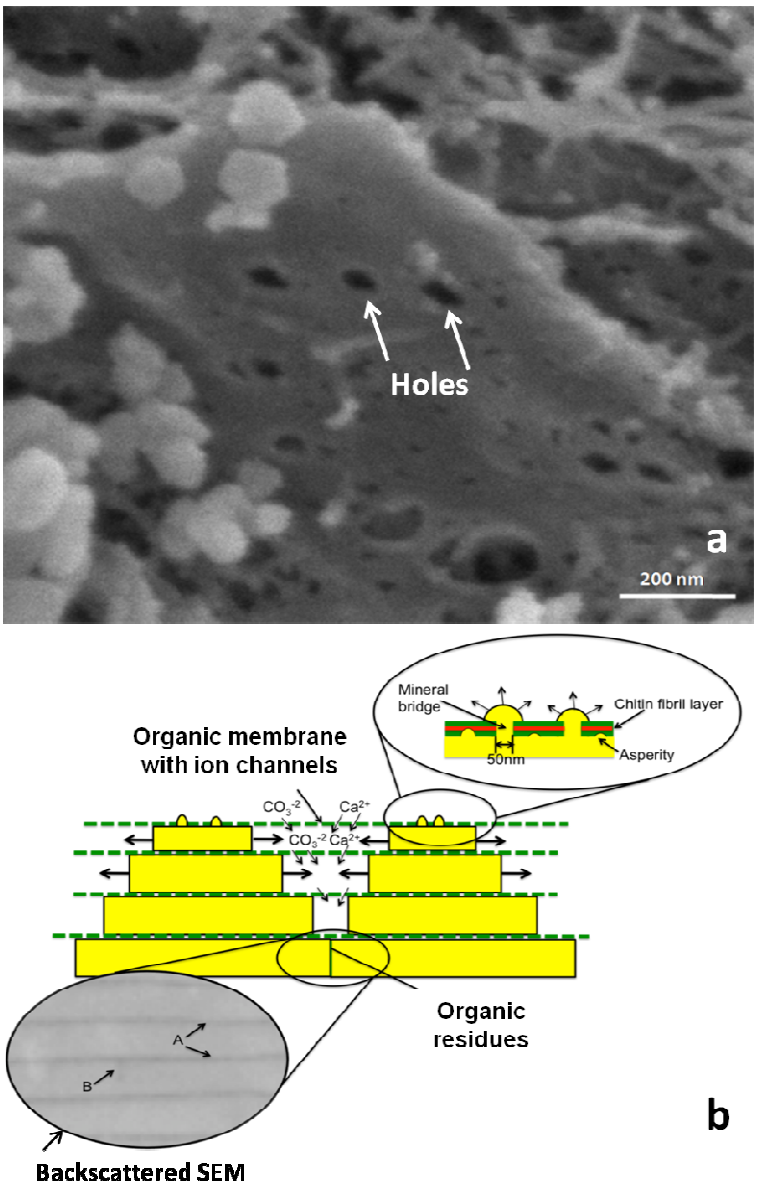


**Figure 4.22:** a) Thin intertile organic layer showing holes; b) Proposed Mechanism of growth of nacreous tiles by formation of mineral bridges as depicted by Meyers et al. [48]; organic layer is permeable to calcium and carbonate ions which nourish lateral growth as periodic secretion and deposition of the organic intertile membranes restricts their flux to the lateral growth surfaces. Arrows A designate organic interlayer imaged by SEM; arrow B designates lateral boundary of tile. (*source*: Lin [65]).

Figure 4.23 (a) represents the possible sequence in which growth could occur through mineral bridges. The growth sequence is as follows; (i) organic scaffolding forms

as interlamellar membranes between the layers of tiles arresting *c*-direction growth, (ii) a new tile begins growth through the porous membrane, (iii) the new tile grows in every direction, but faster along the *c*-axis, (iv) a new porous organic membrane is deposited, arresting *c*-axis growth of the new tile while allowing continued *a* and *b*-axis; growth, mineral bridges begin to protrude through the second organic membrane while sub-membrane tiles continue to grow along the *a* and *b*-axis, sub-membrane tiles abut against each other; a third tile begins to grow above the membrane.

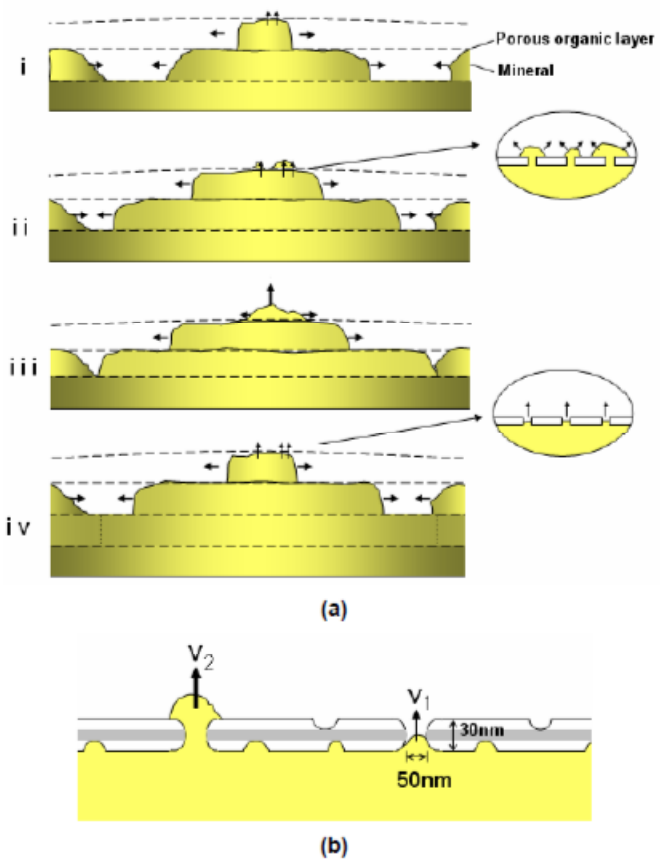


**Figure 4.23:** (a) Growth sequence through mineral bridges (b) Detailed view of mineral bridges forming through holes in organic membranes (*source*: Lin [65]).

As shown, the bridges are believed to be the continuation of mineral growth in the *c*-axis from a previous layer of tiles. They protrude through the growth arresting layers of proteins, creating a site on the covering orgaic layer where mineralization can continue. These mineral bridges are the seed upon which the next tile forms. A schematic view of mineral bridges enabling growth through a permeable organic membrane is shown in Figure 4.23b. Holes in the organic nanolayer, which have been identified by Schäffer et al. [14], are thought to be the channels through which growth continues. Mineral growth above the membrane is faster than growth in the membrane holes because of the increase in contact area with surrounding calcium and carbonate ions. Since these holes are small (30–50 nm diameter) the flow of ions is more difficult, resulting in a reduction of growth velocity to V1<<V2 (Figure 4.23b). V2 is the unimpeded growth velocity in the *c* direction.

The supply of $Ca^{2+}$ and $CO_3^{2-}$ ions to the growth front is enabled by their flow through the holes in the membranes. This explains why the tiles have a width-to-thickness ratio of approximately 20 whereas the growth velocity in the orthorhombic *c* direction is much higher than in the *a* and *b* direction.

## 4.2 Mechanical Testing and observations of demineralized nacre

### *4.2.1 Imaging of fracture surfaces, nano interlayers, and mesolayers*

Figure 5.16 shows an optical micrograph (post-demineralization) of a cross-sectional cut exposing the interface between the demineralized (Figure 5.24a) and the untreated nacre (Figure 4.24 b). It can be noted that the section of the nacre specimen remained in-tact, retaining its original geometry. This confirms that the embedding

procedure was successful in exposing only the desired section of the nacre to the demineralizing solution while exerting a good grip on the untreated edge. As the removal of the mineral proceeds the organic interlayers are exposed and a loss of integrity occurs.

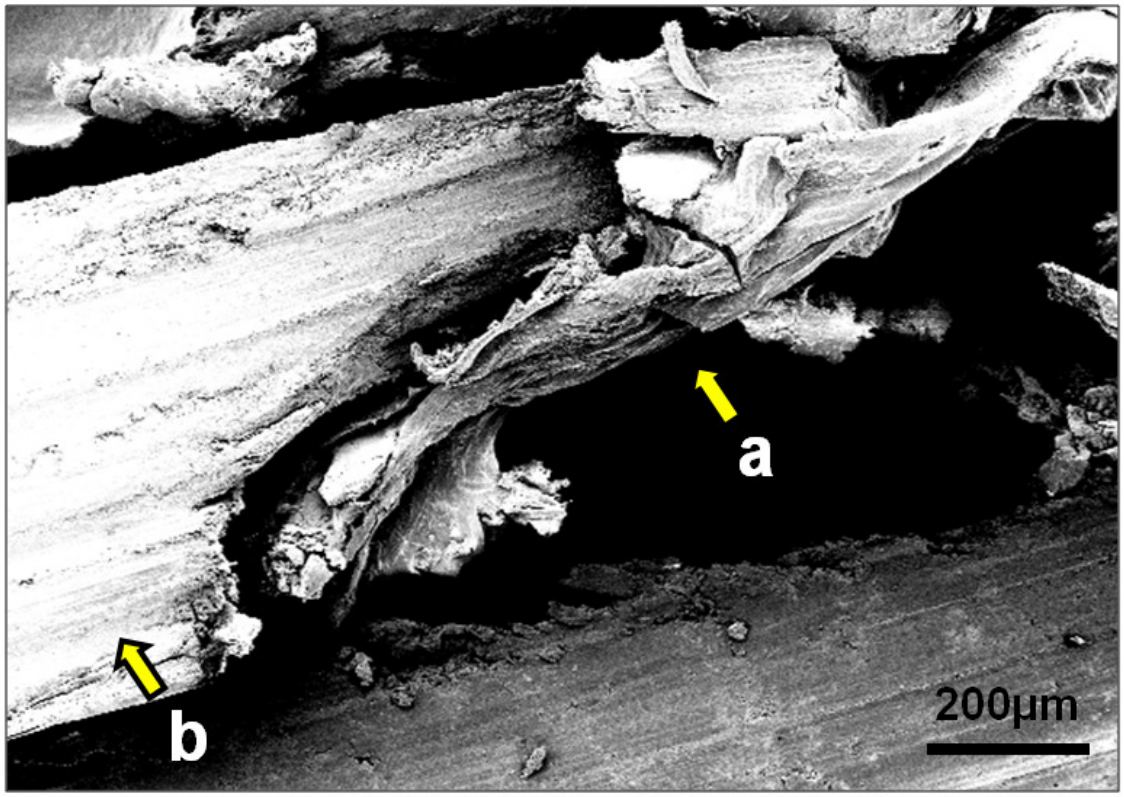


**Figure 4.24:** Optical micrograph (post-demineralization) of a cross-sectional cut exposing the interface between the demineralized (a) and the untreated (b).

However, the thicker mesolayers do not exhibit such loss of integrity. Figure 4.25 shows 3 mesolayers (depicted by arrows) that retain some stiffness unlike the organic interlayers that crumble and aggregate due to their much lower thickness (~20 nm vs. ~20

μm). These observations enable the determination of number of mesolayers present in each specimen, necessary for the calculation of cross-sectional area.

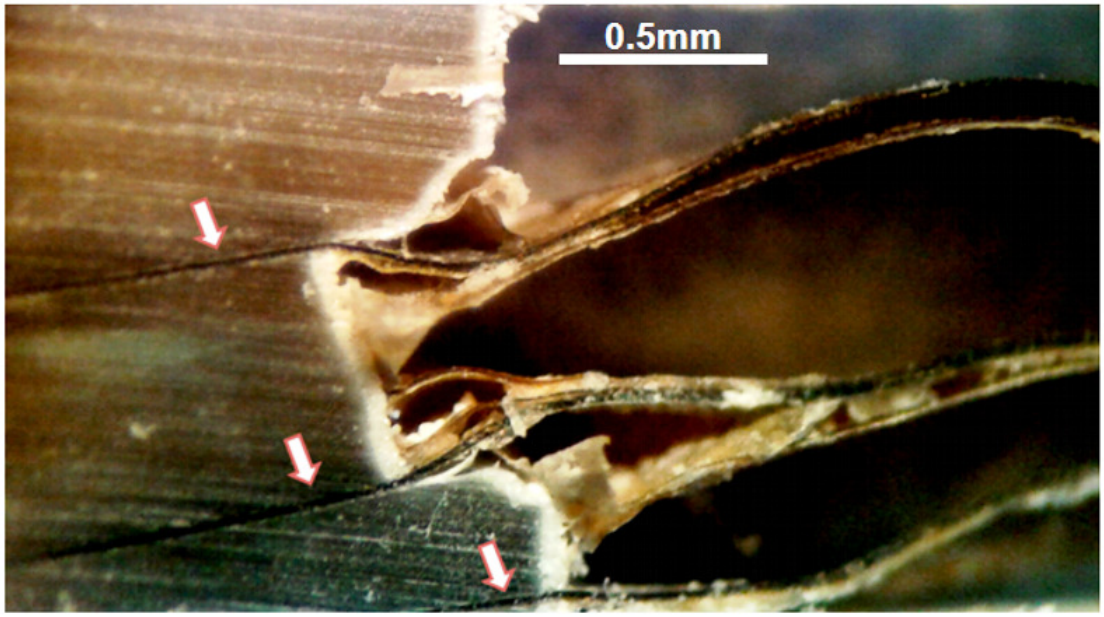


**Figure 4.25:** Interface between demineralized and untreated nacre; showing three mesolayers (depicted by arrows) that retain stiffness unlike organic interlayers that crumble and aggregate in-between.

Following the mechanical testing, the gauge section of the specimens where sectioned carefully and prepared for scanning electron microscopy observation. Each specimen prepared contained a considerable amount of interlayers that upon preparation retained their individual structure but tiled on top of each other. Figure 4.26 illustrates a panoramic (edge) view of this sequence of layers, that when upon closer inspection (Figure 4.26 b and 4.26 c) one can see the individual tile imprints. Further inspection (Figure 4.26 d, e, f) depicts the porous structure that is the result of a network of fibers. The pores have an average radius of ~20 nm with a standard deviation of 8 nm.

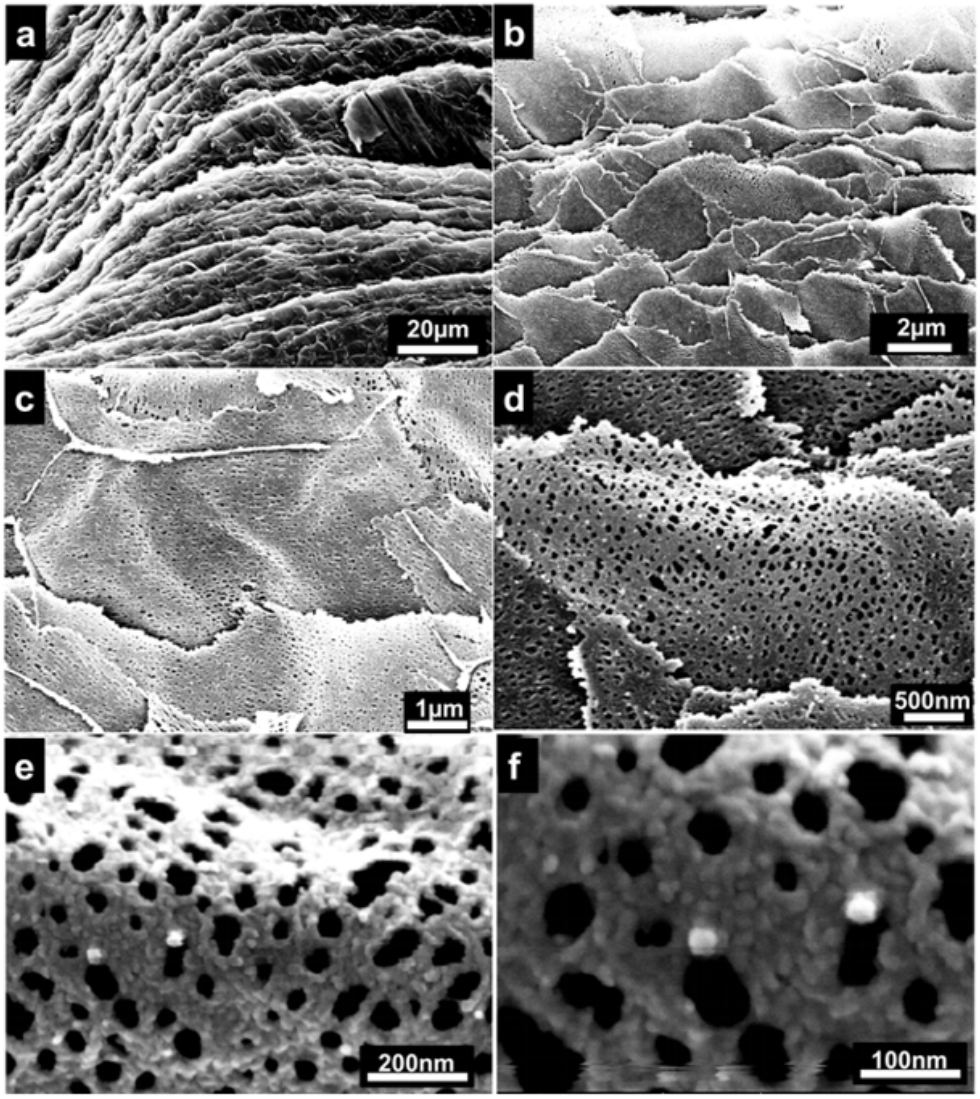


**Figure 4.26:** Sequence of layers (a and b) of demineralized nacre, that when upon closer inspection (b and c) one can see the individual tile imprints and nano pores (e and f).

Furthermore, Figure 4.27 a top view of the interlayers stacked upon one another. This section of the demineralized nacre was taken near the gauge cross-section where most of the damage due to the mechanical testing was done. It can be noted that the pores stretch and tear due to the applied force on the specimen. Analysis of the pore extensions will be discussed in further detail in section 4.3.2.

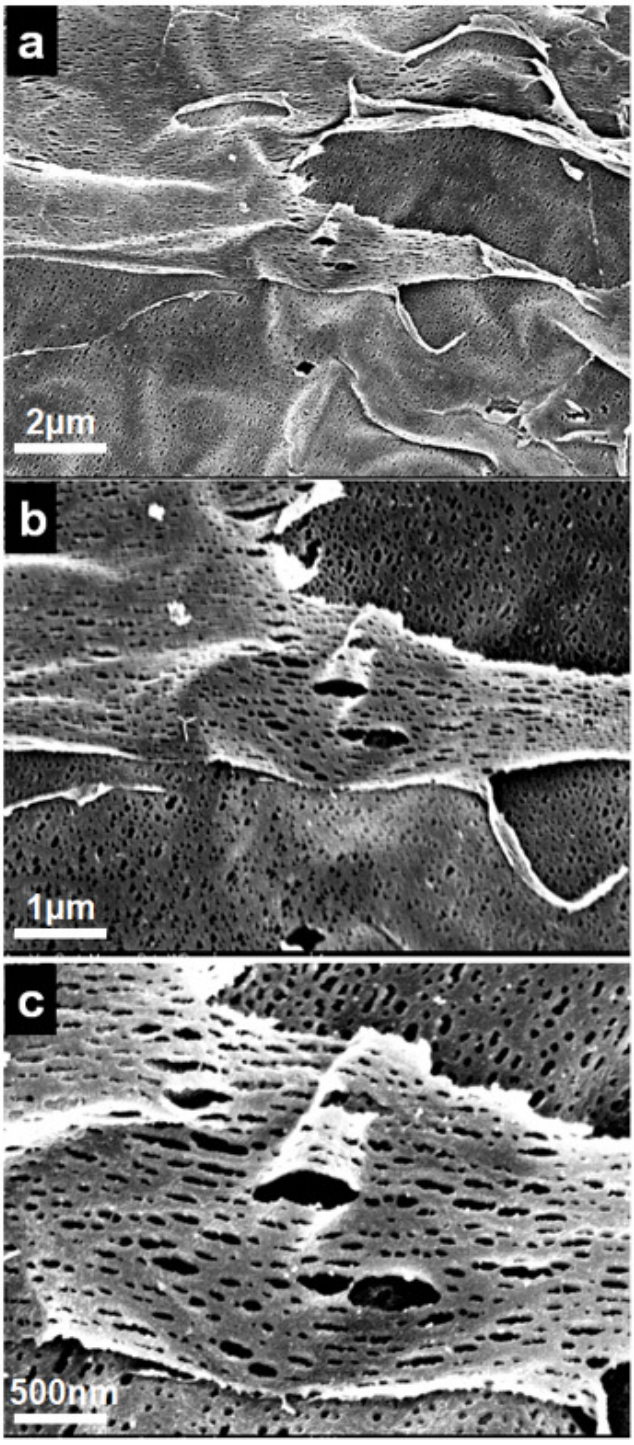


**Figure 4.27:** a) Top view of the interlayers stacked upon one another. This section of the demineralized nacre was taken near the gauge cross-section where most of the damage due to the mechanical testing was done. b) Close-up view showing the tear of the layer and c) Elongated and torn holes in the nanolayer.

*4.2.2 Quasi-Static Tensile Tests*

The axial stress was calculated by approximating the number of organic layers (both nano and meso) that would be contained in each specimen. Given that the specimen thickness was varied from 0.18 mm to 3 mm thick, the amount of organic constituent can vary considerably among specimens. Additionally, the aragonite tile size and shape has been a topic of debate. The tile thickness has been approximated to be within a range of 0.4 to 0.5 μm reaching a range up to half its thickness [42, 161, 162]. For the purpose of this study (calculation of organic interlayers per sample), simple quantification of the tile thickness was performed. Figure 4.28a shows a BSEM micrograph of a polished surface of nacre depicting horizontal organic layers (dark lines) where thickness measurements where done. Figure 4.28 b-f show a series of measurements of the thickness over several layers. The tile thickness averaged 0.56 μm with a standard deviation of 26 nm. The shape of the tiles has been previously described as 'wedged' [57, 58, 163, 164] rather than flat. This was proposed to play a role in the shear strength of the nacre by inhibiting inter-tile sliding and tile pull out. However, current results suggest differently. The thickness is plotted against a displacement on five adjacent tile layers. For each separate layer, the plot has a unique pattern, showing that some tile areas might be a bit thicker than others. However, if tiles had a 'wedge' shape, this would be visible in the plot and would provide it a periodicity in every layer (as depicted in the hypothetical case in Figure 4.28 g). The number of nanolayers present in each specimen was estimated by considering the original (untreated) thickness of each specimen and assuming that an interlayer of 20 nm thick exists for every tile layer.

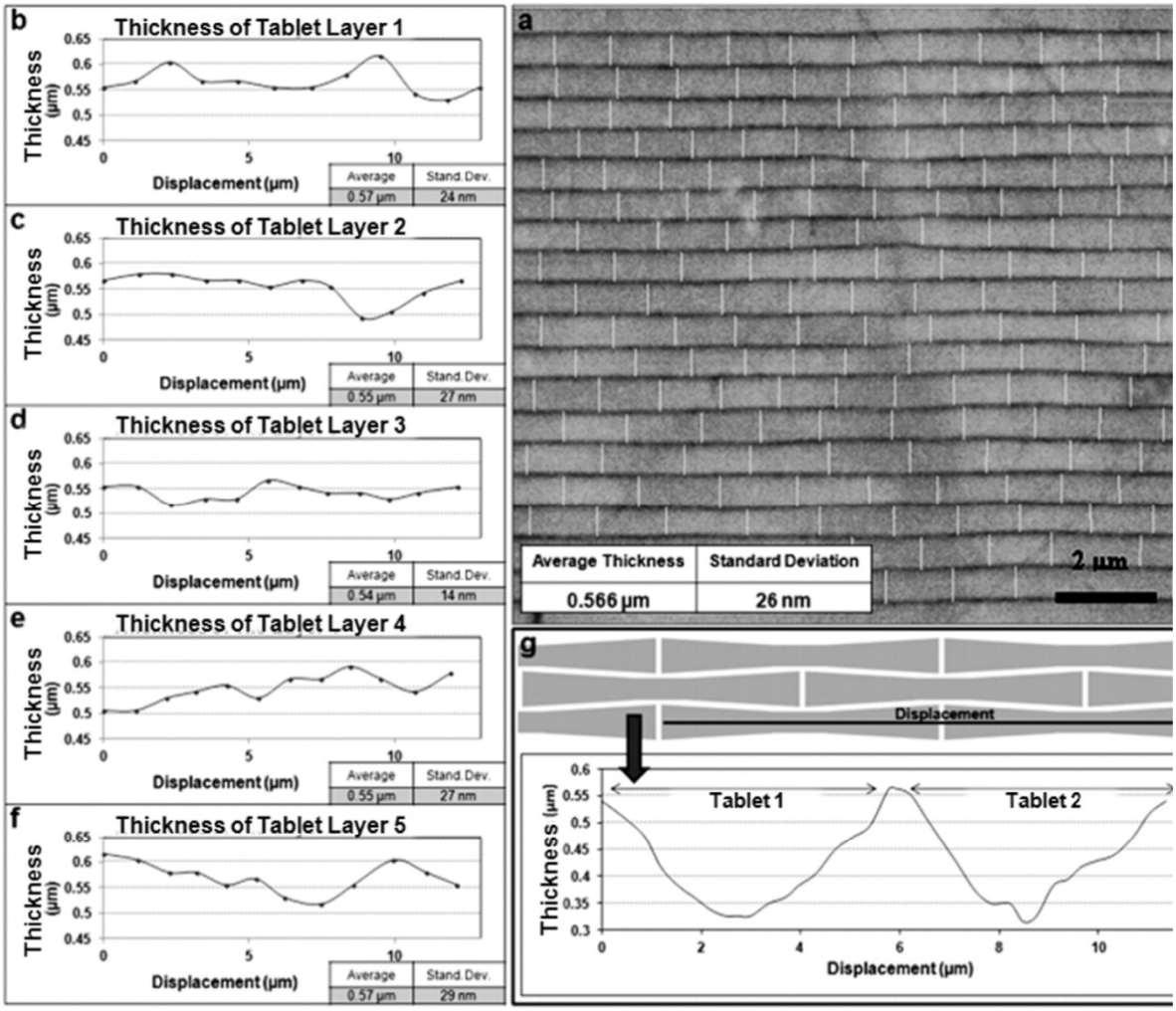


**Figure 4.28:** (a) BSEM of polished surface showing horizontal organic layers (dark lines). Note the vertical lines separating tablets laterally are not (or only faintly) visible. (b–f) Thickness variation of five adjacent tablet layers. (g) Schematic and thickness variation if tablets were wedge-shaped.

Quasi-static tensile tests were performed on the demineralized specimens described above; results are shown in Figure 4.29. Specimens were tested at a strain rate of $10^{-2}$ $s^{-1}$, at 20 °C while water was continuously misted over the specimens ensuring the demineralized nacre would remain hydrated over the duration of the test. The number of thick layers of protein was estimated by optical microscopy. The samples varied from having no mesolayers present up to specimens with 5 mesolayers; the quantity of

mesolayers in each specimen is labeled beside each plot. The elastic modulus was estimated where the values are within a range of 12.5 MPa ≤ E ≤ 115 MPa.

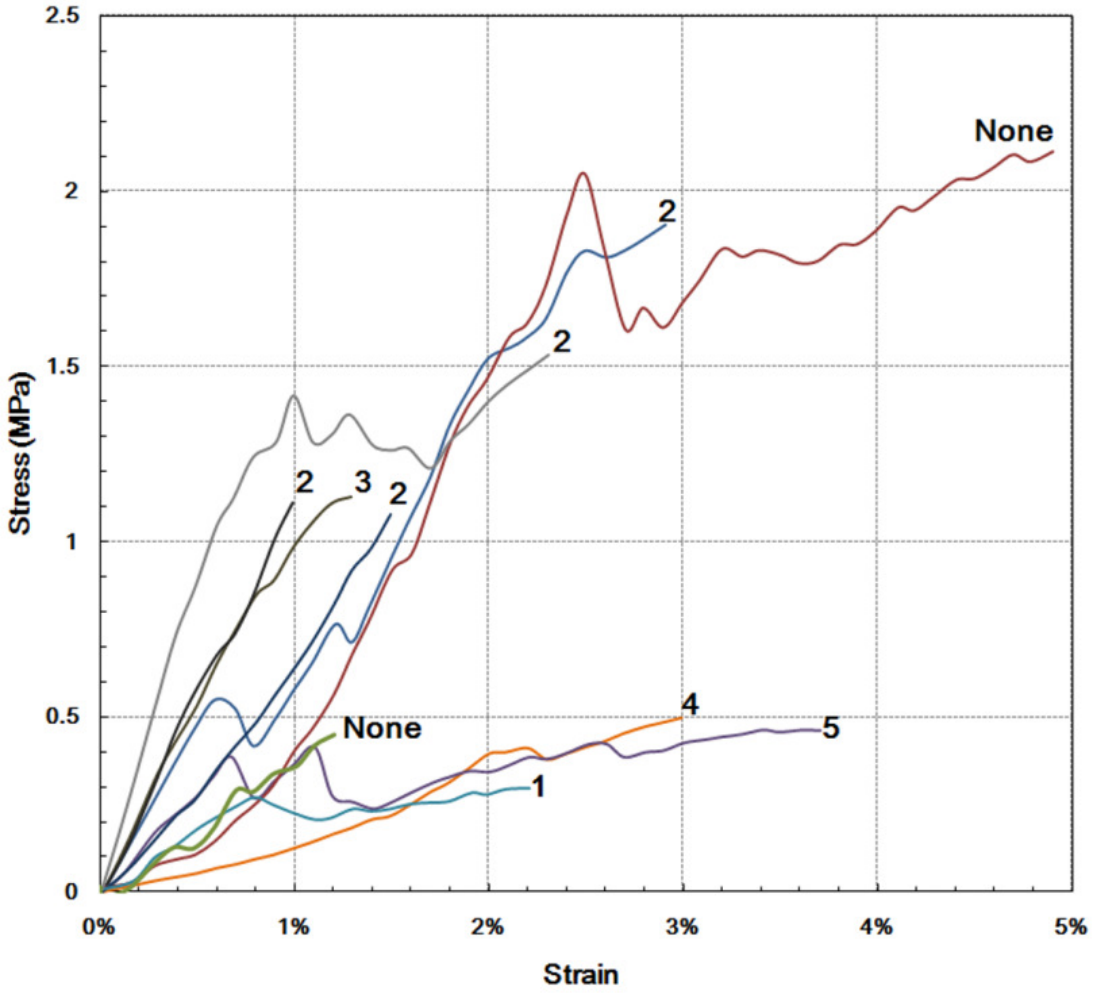


**Figure 4.29:** Quasi-static tensile tests of demineralized nacre. Value adjacent to each plot represents the number of mesolayers present in each specimen.

Additionally, testing of the demineralized nacre was performed at a lower strain rate ($10^{-4}s^{-1}$) and the results were surprising. Figure 4.29 shows several curves for tests performed at strain rates of $10^{-2}$ $s^{-1}$ and slightly slower at $10^{-4}$ $s^{-1}$. These results show that demineralized nacre exhibits a rate-dependence behavior. The elastic modulus was estimated and the values are in the range 12.5 MPa ≤ E ≤ 115 MPa (for strain rate $10^{-2}$ $s^{-}$

$^{1}$) and 1 MPa ≤ E ≤ 7.2 MPa (for strain rate $10^{-4}$ $s^{-1}$). These results (Figure 5) show that demineralized nacre exhibits a rate-dependent behavior. It is possible to estimate this viscoelastic behavior from the equation:

$$E = C\dot{\epsilon}^{d} \tag{4.1}$$

which is commonly applied to biological materials, especially bone, and is known as the Ramberg-Osgood equation. Assuming the values of 50 MPa and 3.5 MPa for *E* at strain rates $10^{-2}$ $s^{-1}$ and $10^{-4}$ $s^{-1}$, respectively, the value of the exponent d is 0.57.

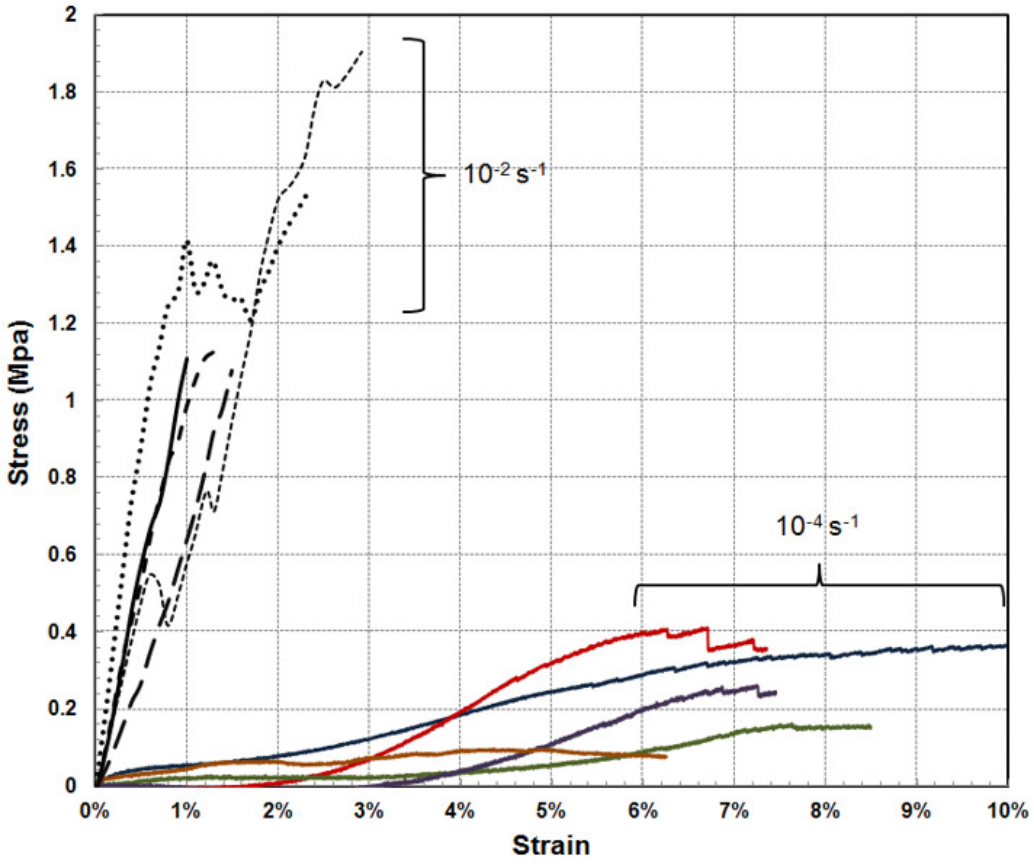


**Figure 4.30:** Rate-dependent behavior of demineralized nacre. Dashed plots represent specimens tested at a strain rate of $10^{-2}$ $s^{-1}$ and solid plots represent specimens tested at a strain rate of $10^{-4}$ $s^{-1}$.

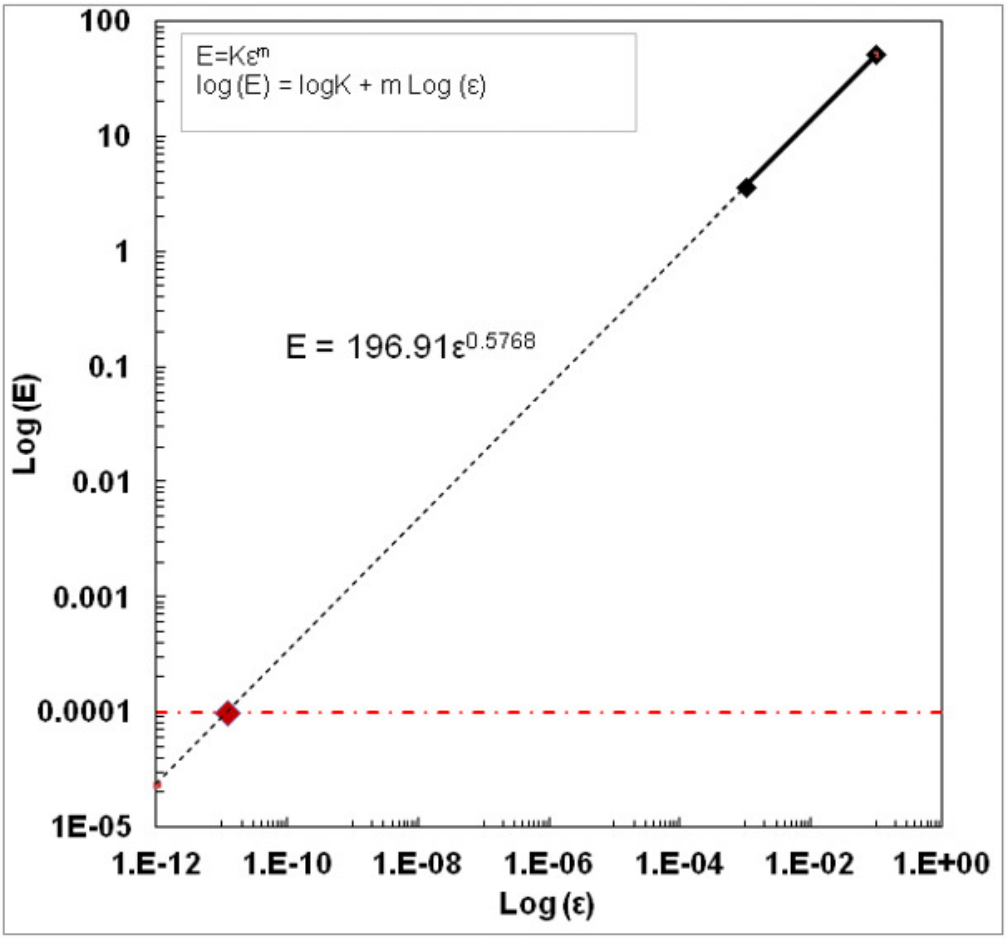


**Figure 4.31:** Strain rate sensitivity of demineralized nacre estimated by applying the Ramberg-Osgood equation

Weibull statistics are employed to characterize and compare of results to those previously obtained by Bezares et al. [45]. Presented in Figure 4.32 are the statistical summaries of their mechanical tests on demineralized nacre in quasi-static tension, with failure probabilities of 50% being reached at ~3.1 MPa. In comparison, the failure probabilities of 50% obtained here (Figure 8: Current, nano and mesolayers) are ~1.1 MPa. Differences in values may be accounted to the detail that in the experimental procedure described by Bezares et al. [45] mesolayers are not considered when

computing the axial stress. As a comparison, the axial stress was re-computed assuming mesolayers were non-existant in the specimens (Figure 4.32: Current, nanolayers). By this method UTS values increase to 2.5 MPa and approximate to those values attained by Bezares et al. [45] (Figure 4.32: Bezares et al., 2010).

As mentioned earlier, the formation of mesolayers can be induced by temperature and feeding fluctuations [165]. When temperature drops, mineralization is arrested and it allows for the formation of a mesolayer. Thus, it is believed that in many cases farmed abalone do not experience these temperature fluctuations and thus not form mesolayers. Shaw et al. [10] report observations on farmed abalone in which no mesolayer are present. In the current study, the abalone were obtained from the Scripps Institute of Oceanography open water facilities where they were exposed to natural water temperature fluctuations similar to those that wild abalone experience.

Dastjerdi et al. [101] tested three different shell types: red abalone, pearl oyster, and top shell. Of these, only red abalone contains mesolayers. Their results show that lower strength values and higher failure strain values are attained for pearl oyster and top shell than red abalone. They claim this noticeable difference in modulus is a result of the mesolayers that are found in red abalone. Our results are in good agreement with those presented by Dastjerdi et al. [101] for abalone nacre (fail at a similar strength value), with a mean strength value of 1.75 MPa ± 0.5 MPa and failure strain is 2% ± 1 (Figure 19: Dastjerdi et al.). The failure process was similar to their results exhibiting first the delamination of mesolayers, when they are present in the specimen, followed by a failure normal to the growth line. It is interesting to note that the stress-strain response (Figure

4.30) is similar for both specimens that contain and do not contain any mesolayers. This suggests that the organic nano and mesolayers have the same mechanical response.

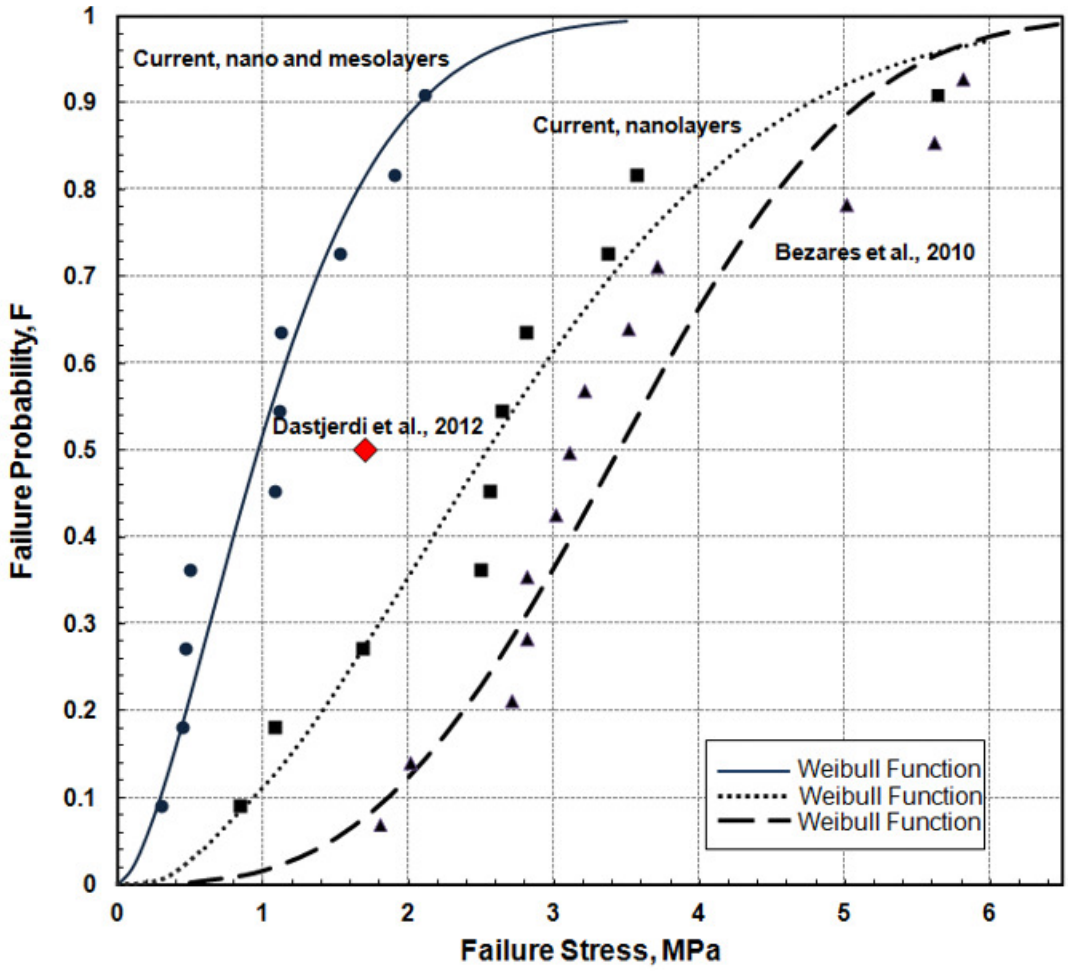


**Figure 4.32:** Weibull distribution of tensile strength of demineralized nacre showing: current results (including nano and mesolayers), results presented by Bezares et al. [45] (Bezares et al. (2010)) and what would values here would look like is the assumption that no mesolayers were present (Current, nanolayers). Additionally a diamond point was added to reflect findings by Dastjerdi et al. 2012 [101] where the average strength of the material was found to be ~1.75MPa.

## 4.3 Mechanical Testing and observations of Deproteinized Nacre

### *4.3.1 Structural Observations*

Figure 4.33 shows the cross-sectional view of the nacre after deproteinization. The mineral tiles remain completely intact, retaining their ~500 nm thickness and shape (Figure 4.33 a, b). In Figure 4.33 c shows two edges of neighboring tiles where one can note the nanoaspereties (shown by arrows) from the upper and lower tile in close proximity (if not connecting) the upper and lower tiles.

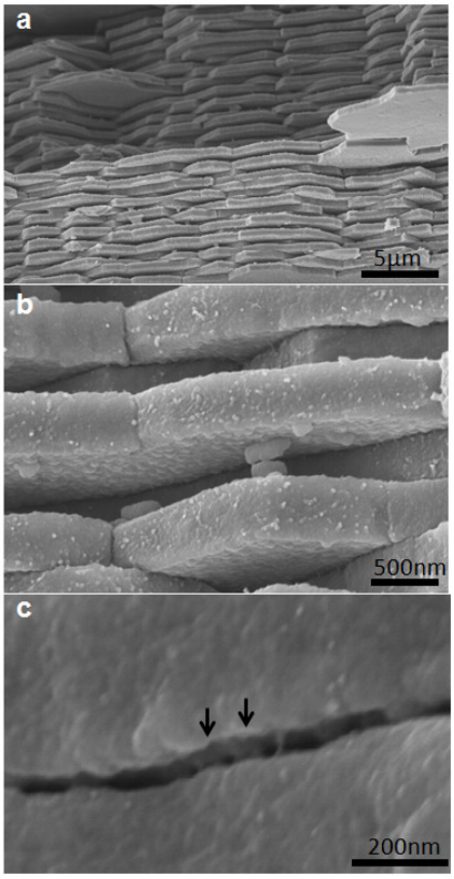


**Figure 4.33:** a) Cross-sectional view of the nacre post-deproteinization retaining the structure of the mineral tiles (~400-500nm in thickness). b) and c) Neighboring tiles exposing nanoasperities on upper and lower tablet.

Subsequent to testing, the fracture surface of the puck was observed via SEM. Figure 4.34 shows one of these surfaces (taken as a birds-eye-view). Figure 4.34 a shows the different tile layers (depicted by arrows) that were peeled off as the load was applied. Closer inspection of this surface (Figure 4.34 b, c, d) reveals nanoasperities that cover the entire tile surface. The aspereties appear to have an average radius of ~33 nm and to cover the surface with a uniform distribution. The average diameter of the asperities approximates well to the nanopore diameter in the organic interlayer.

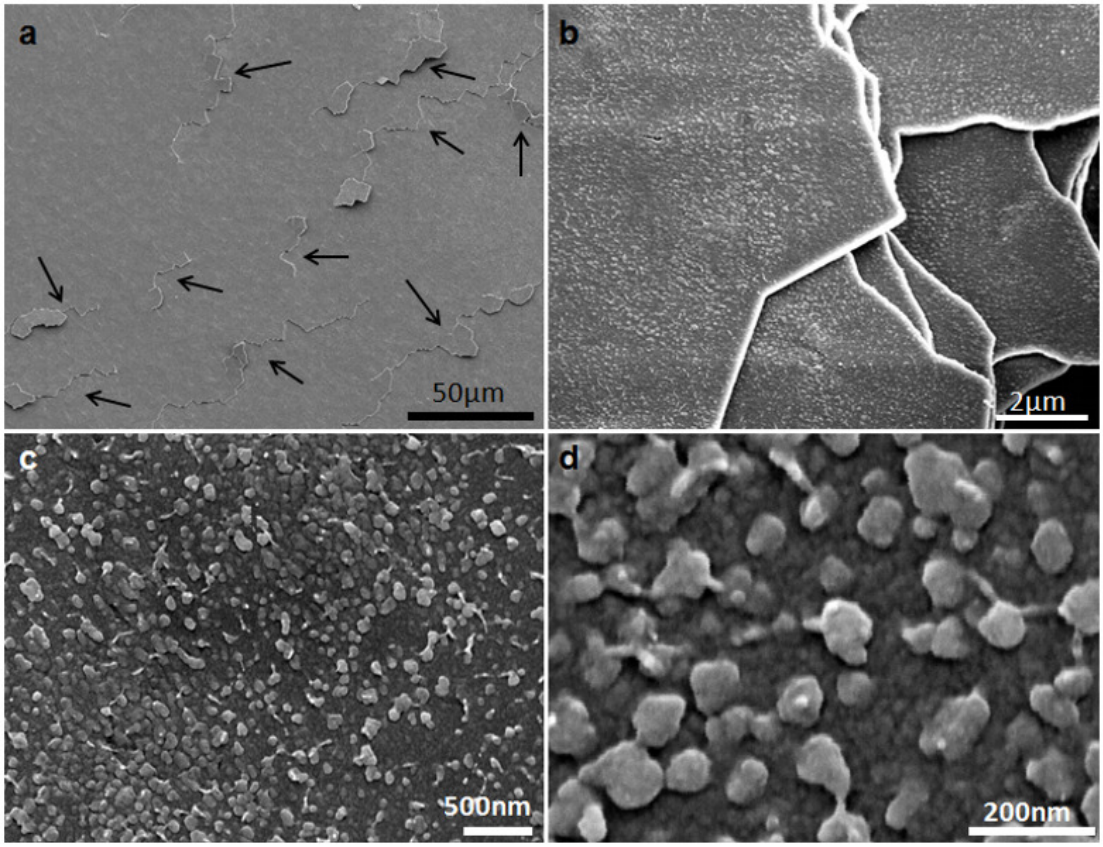


**Figure 4.34:** 'Birds-eye-view' of fracture surface showing different tile layers peeled off as load is applied. Nanoasperities that cover the surface with an uniform distribution

*4.3.2 Deproteinized Nacre: Tensile Tests*

Figure 4.35 shows the Weibull analysis of nacre in quasi-static tension with load perpendicular to layers. While the Weibull distribution [104] is usually used for flexural strength and is representative of extreme-value statistics, here it is applied to a variety of quasi-tensile data with intention of creating a clear picture from a scattered range of data points.

The Weibull analysis was applied by means of the equation:

$$F(V) = 1 - \exp\left[-\left(\frac{\sigma}{\sigma_0}\right)^m\right] \tag{4.2}$$

Which can be transformed into:

$$lnln\left[\frac{1}{1-F(V)}\right] = m(ln\sigma - ln\sigma_0) \tag{4.3}$$

Where F(V) is the failure probability, *m* is the Weibull modulus and $\sigma_o$ is a characteristic strength. The parameters $\sigma_o$ and *m* are experimentally obtained by plotting the two sides of the equation and finding the value of lnσ when lnln(1/1-F) equals zero, and taking the slope the best fit line, respectively. The Weibull curve yields an S-shaped distribution from which the failure probability at a certain stress can be computed. In general we can describe the 50% failure probability as the characteristic strength of the material.

The current results, presented in Figure 4.35, predict a 50 percent failure probability occurring at approximately 0.325 MPa for tension perpendicular to the

layered structure. This is an extremely, especially when we consider that the tensile strength perpendicular to the layer plane for untreated nacre is on the order of 3-4 MPa (plotted in Figure as well as values from reference [25]) These results are consistent with the ones by Lin et al. [25] or which at 50 percent failure probability occurs at 4.1 MPa.

A comparison between the structural observations of isolated organic material and the isolated mineral allows for interesting implications. The pores found within the organic interlamellar layer enable (a) the flow of ions to continue the mineralization process and (b) the formation of mineral bridges between adjacent tile layers. Given that this is the fracture surface of the tested specimens, some of the nanoasperities are indeed fractured mineral bridges. The nanoasperities on the surface of the mineral tiles and the holes within the organic matrix sheet were quantified. The average radius of the the pores is ~20 nm (standard deviation of 8nm) compared to that of the asperities which is ~33 nm (standard deviation of 16 nm). This difference in diameter size might be because as the nacre is demineralized the nanopores in the organic interlamellar layer are no longer stressed and thus are able to shrink. Thus, the pores are somewhat stretched by the nano asperities when the entire nacre structure is intact. Previous studies show that mineral bridges appear as circular columns with diameter of 38~54 nm [166] and 25-55 nm [167], while the pores exhibit a diameter ranging from 5-50 nm. The average diameter of the nanoasperities measured here is larger than these previous reported values, but the average value for the pore diameter is in good agreement with results by Song and Bai [79].

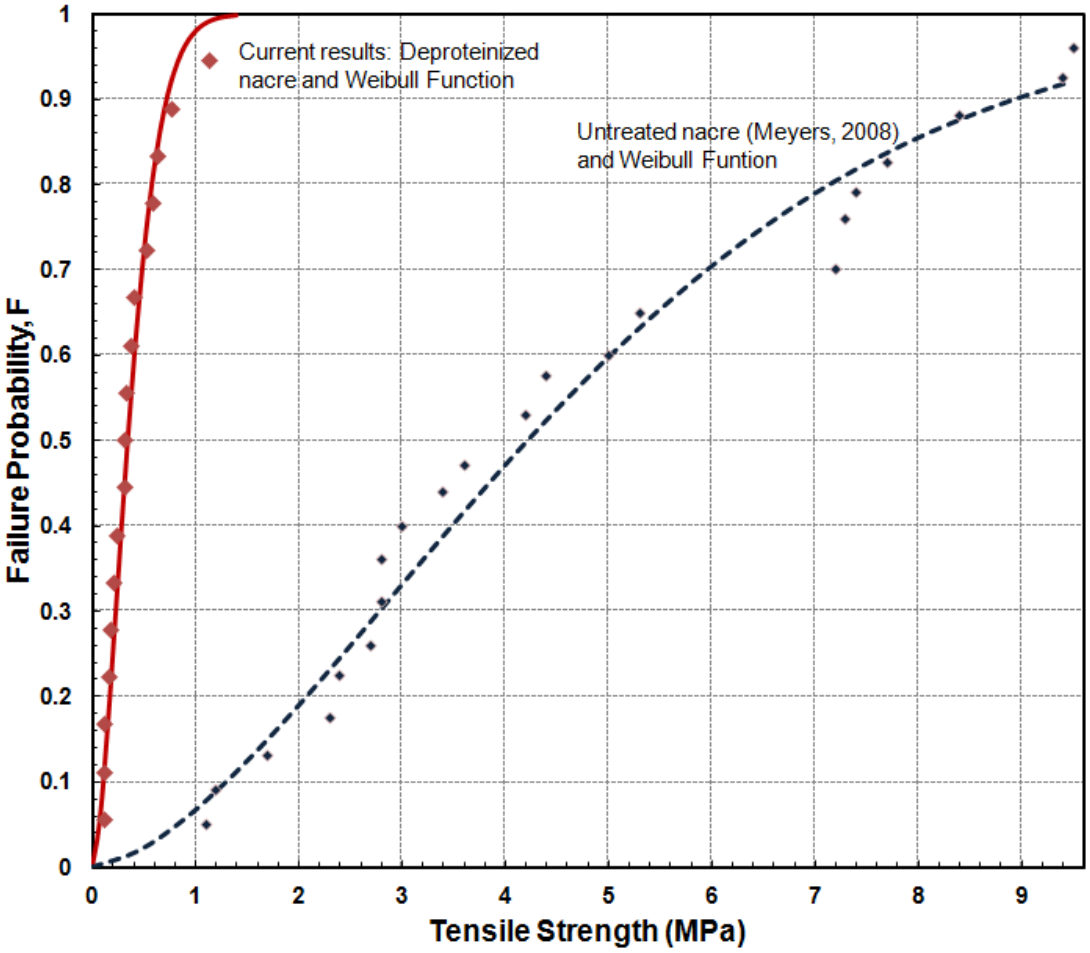


**Figure 4.35:** Weibull distribution of tensile strength perpendicular to layered structure of deproteinized nacre and previous results obtained by Meyers et al. [25].

There is still a debate on the fraction of asperities that actually connect to form mineral bridges. Gries et al. [167] and Checa et al. [168] suggest than in some cases these asperities do not connect but only protrude from neighboring tiles. Current results show that the nanoasperities cover ~33% of the surface of the mineral tiles, compared to the area provided by the pores, which is estimated to be ~18%. The discrepancy between total area occupied by the nanoasperities to that of the pores suggest that only a fraction of the nanoasperities are mineral bridges. This might also justify the difference in

diameter size between pores and nanoasperities. Furthermore, the areal fraction covered by the pores in the organic interlamellar layer (~18% of tile surface area) is similar to values estimated by Song and Bai [79] (~15% of the surface area of the tiles). This in turn provides a better estimated value of the area that is covered by 'true' mineral bridges. Calculations by Song and Bai [79] provide a value of ~1,600 mineral bridges per tile (tile diagonal ~1.8-6.2 μm); here we estimate 3,000 nanoasperities per tile (tile diagonal of ~8 μm). Additionally, Song and Bai [79] propose that the average density distribution of mineral varies, decreasing from the center to the periphery of the tiles. In contrast, the current observations show a uniform distribution of nanoasperities throughout the entire surface area of the tiles.

Mineral bridges are believed to regulate the tensile strength (perpendicular to shell surface), thus increasing the fracture toughness by controlling the crack extension pattern in nacre [8, 36]. The current results, presented in Figure 4.35, predict a 50 percent failure probability occurring at approximately 0.325 MPa for tension perpendicular to the layered structure. This is an extremely low value compared to the hypothesized theoretical value. The mineral bridges (~40 nm in diameter and ~20 nm in height) approach the critical scale for monocrystal aragonite which is ~30 nm. Thus, the strength should be reaching the theoretical value which for monocrystal aragonite is ~ 3.3 GPa. However, in the current experiments, the material reaches far below that value implying that the material is then not defect-free. This can be due to three speculations: (a) the existence of an organic phase embedded in the mineral and the organic material surrounding the mineral bridges [46, 82] deteriorates the integrity of the bridges during

the deproteinization process leading to the creation of cracks or defects in the mineral bridges (Figure 10 a); (b) some of the mineral bridges/ connections are damaged or broken prior to testing, lowering their strength (Figure 4.36 b); (c) that the usually observed protrusions are not in fact mineral bridges.

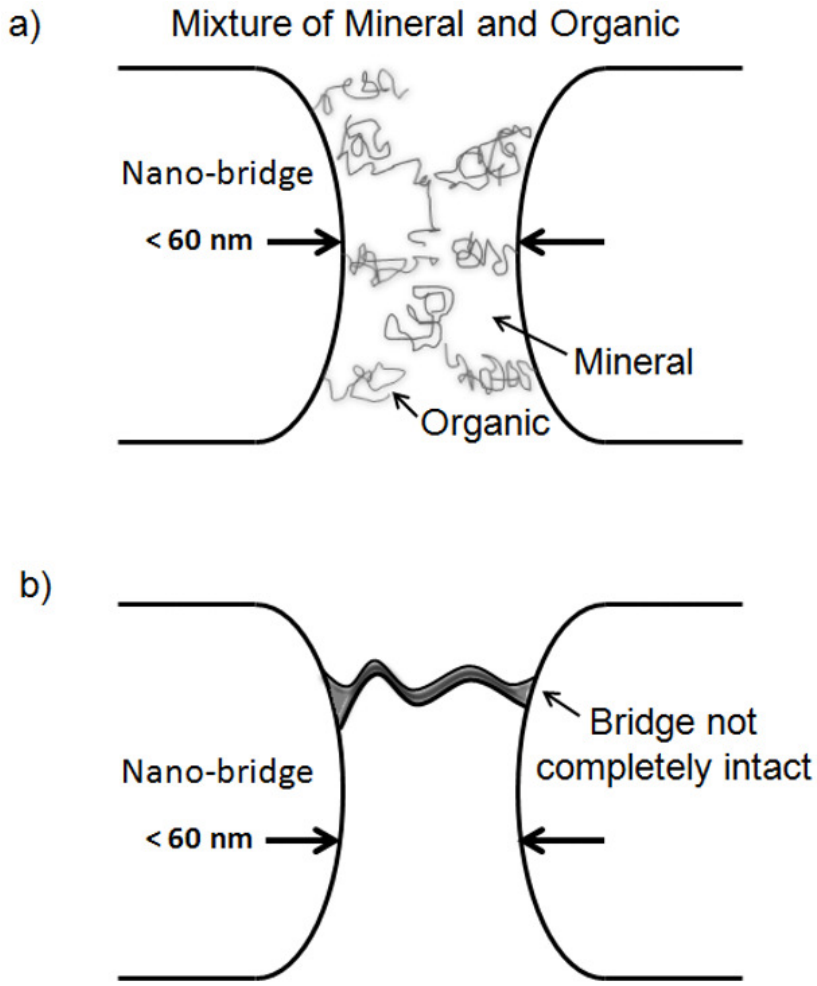


**Figure 4.36:** Schematic of mineral bridges. a) Representation of a mineral bridge containing organic component which can be deteriorated during the deproteinization process. b) Representation of a mineral bridge that may not be intact and thus not contributing to the strength of the nacre when tested in tension perpendicularly to tile layers.

*4.3.3 Micro-scratch Test*

Figure 4.37 shows selected plots on the various sets of tests: a) untreated nacre tested along the top surface, b) deproteinized nacre tested along the top surface, c) untreated nacre tested along the cross-section d) deproteinized nacre tested along the cross-section. Noticeable features were observed. When tested from a 'top surface,' as expected the treated (deproteinized) nacre fractures at lower loads than the untreated nacre; where major fractures began at initial loading (3 mN) and where the specimen fractured completely at loads lower than <100 mN. The scratch is linear not showing an explicit point of fracture and almost no resistance to penetration. In comparison the untreated nacre does exhibit a more evident breaking limit, on average at ~27 mN. In cross-section the deproteinized nacre exhibited more of a resistance to scratching and demonstrated an explicit breaking point at ~120 mN. Specimens tested on the cross-section, show that untreated nacre does not exhibit a precise frictional force limit; there is a gradual cracking which is more evident by SEM observations. Furthermore, on untreated samples, mesolayers have an effect on the behavior and the frictional force. When tested in cross-section, mesolayers were encountered in various occasions, when the indented tip meets a mesolayer, the scratch is deflected from its original path and follows through the mesolayer (Figure 4.38). It is also noticeable from the plot that the measured force increases as the mesolayer is encountered giving an increased the resistance to motion suggesting mesolayers add plowing friction.

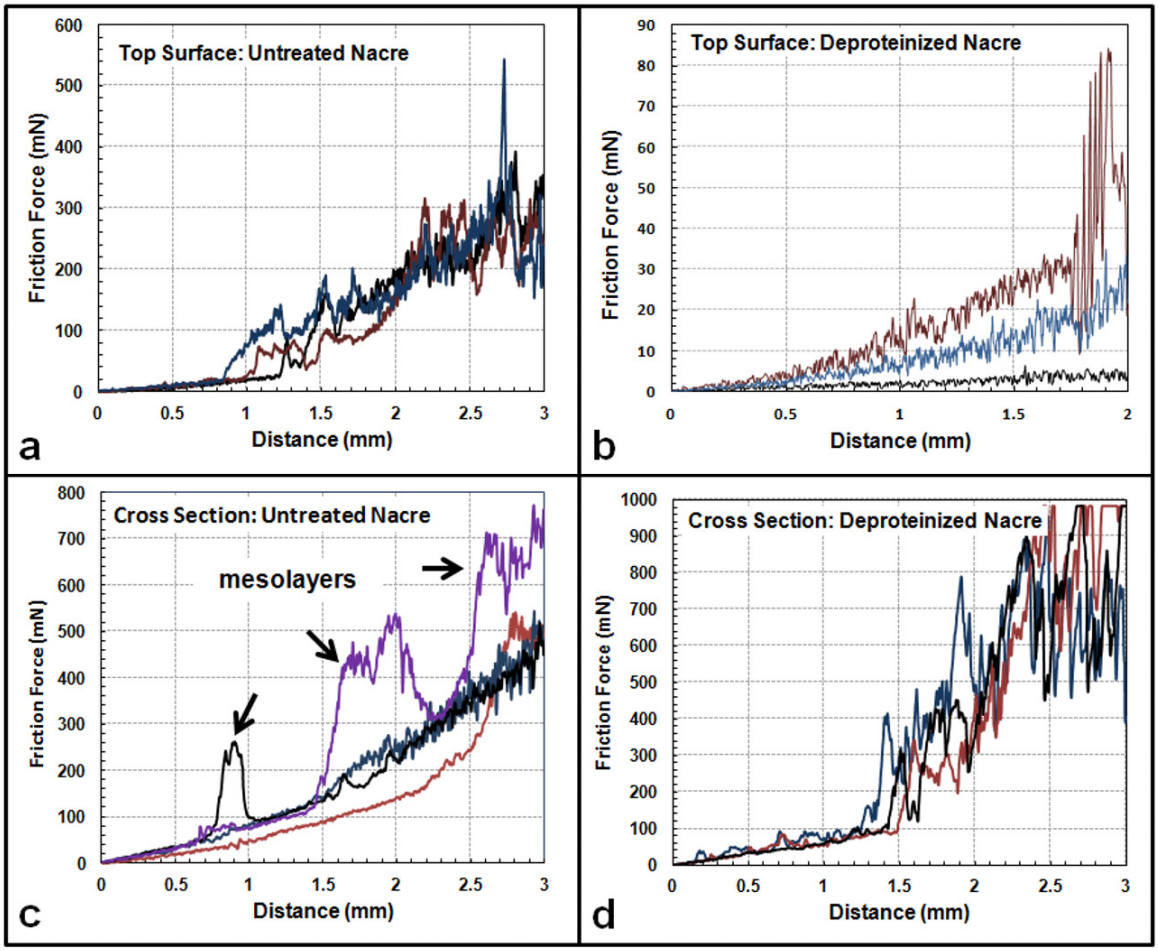


**Figure 4.37:** Microscratch force plots of: a) untreated nacre tested along the top surface, b) deproteinized nacre tested along the top surface, c) untreated nacre tested along the cross-section d) deproteinized.nacre tested along the cross-section.

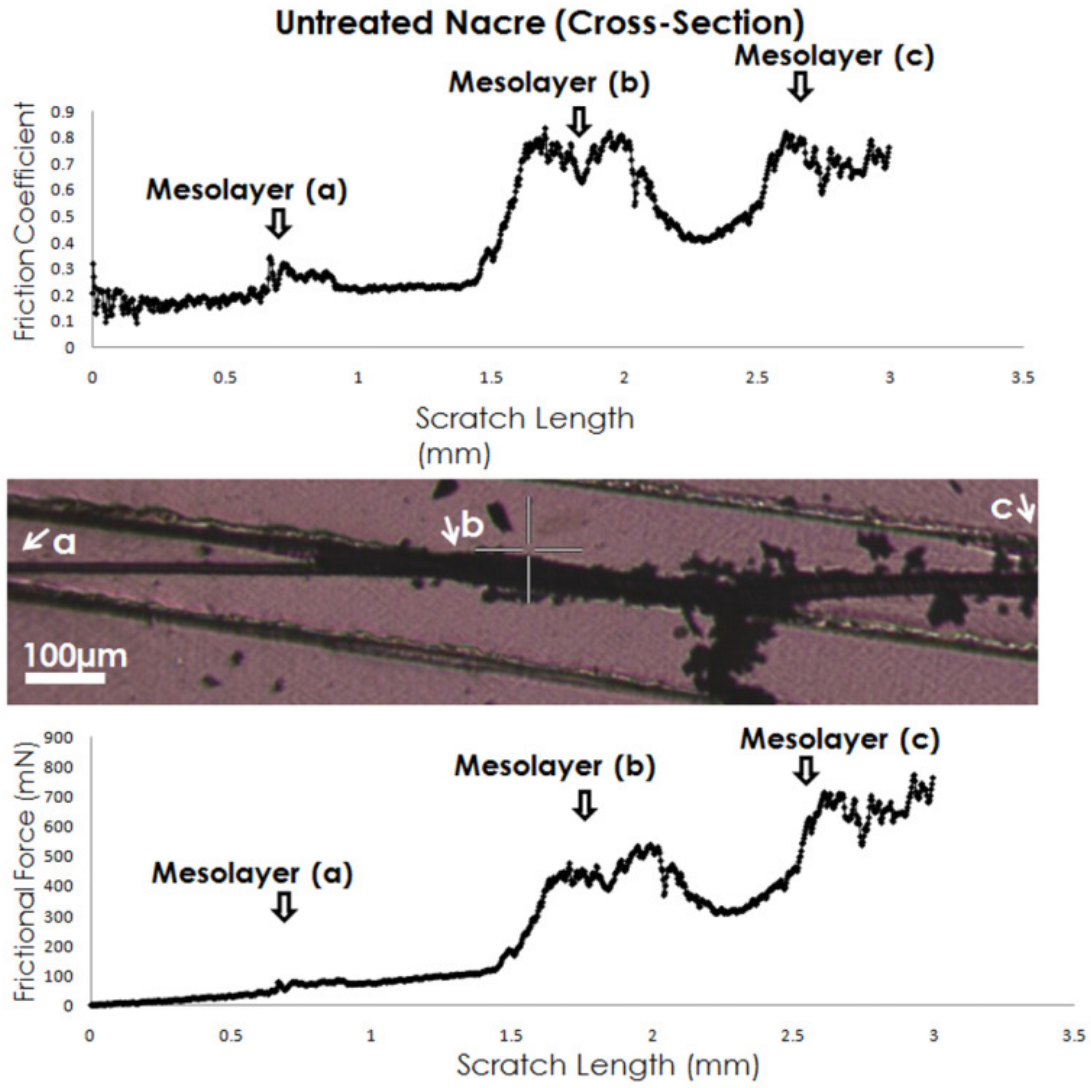


**Figure 4.38:** Micro-scratch test showing the effect of intersecting mesolayers on the frictional force curve. Furthermore, mesolayers cause a deflection on the scratch direction

In addition, various differences in the material behavior were exhibited. Firstly, it was observed that nacre exhibits a higher resistance to failure when tested in cross-section than from the top surface, in both, untreated and deproteinized specimens. Therefore, when tested in cross-section a higher load (up to 1000 mN) had to be applied compared to the lower load (up to 600 mN) that was applied when testing the top surface.

It is believed that this may be an effect of the structure. In untreated specimens when tested in cross-section the crack must undergo a complex path to propagate. As the crack advances it encounters an organic interlayer every 0.5 μm, adding resistance to the propagation.

Figures 4.39 and 4.40 show representative SEM images of the failure of the untreated and deproteinized nacre. Figure 4.39 shows the deformation of the untreated nacre and Figure 4.40 shows the deformation of deproteinized nacre when tested at the top surface. The untreated nacre shows interesting details. For instance, as the material breaks it still maintains its structure. From the top left image the edges of the tiles can be observed and the cracking occurs only through the interface between the tiles. Additionally, when the complete fragmentation occurs, the tiles are split in chunks (still maintaining their shape). Another interesting feature is the organic interlayer which remains and retains its location even after the impact.

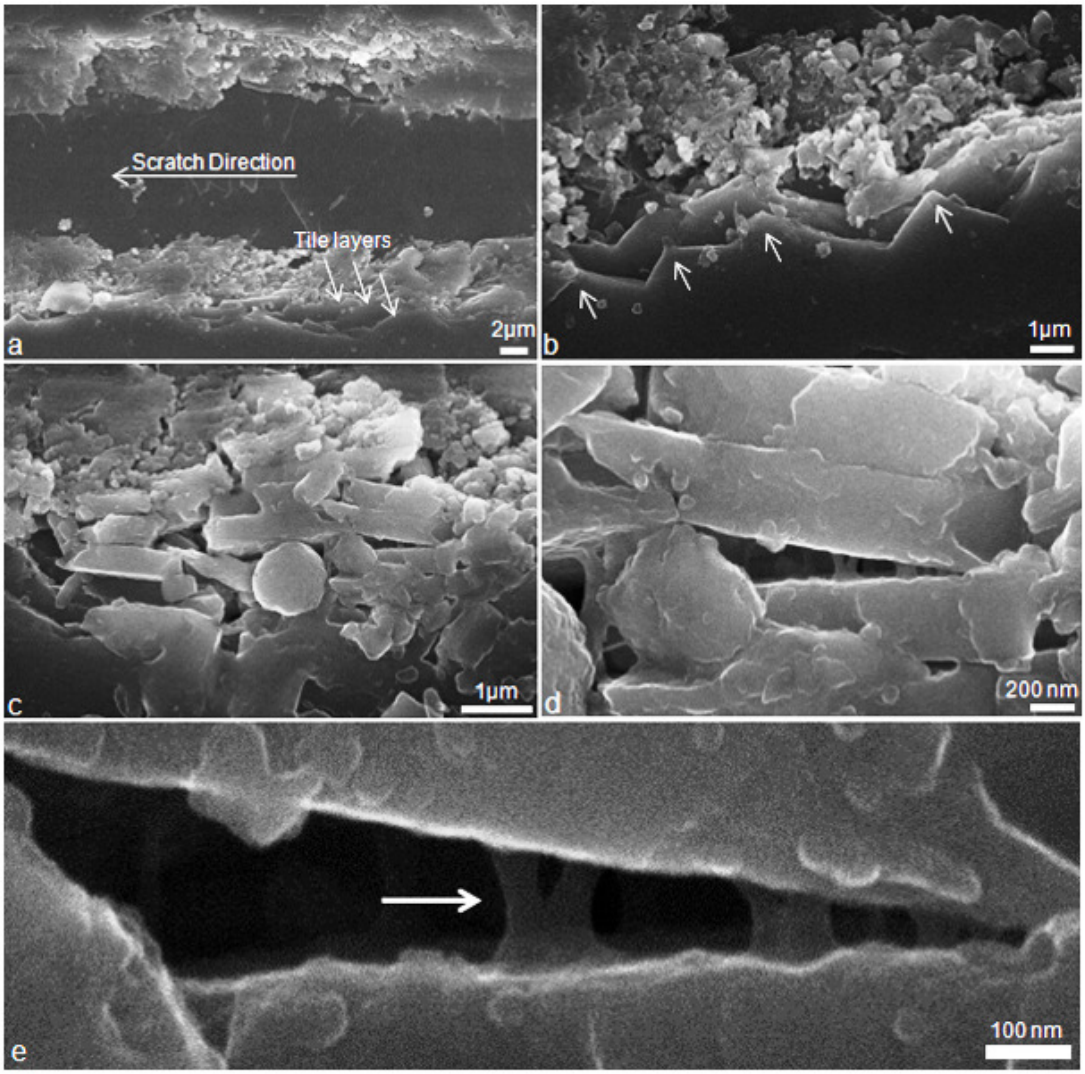


**Figure 4.39:** SEM micrographs of untreated nacre tested at the top surface. Edges of tiles, tile separation and organic interlayer remains can be observed.

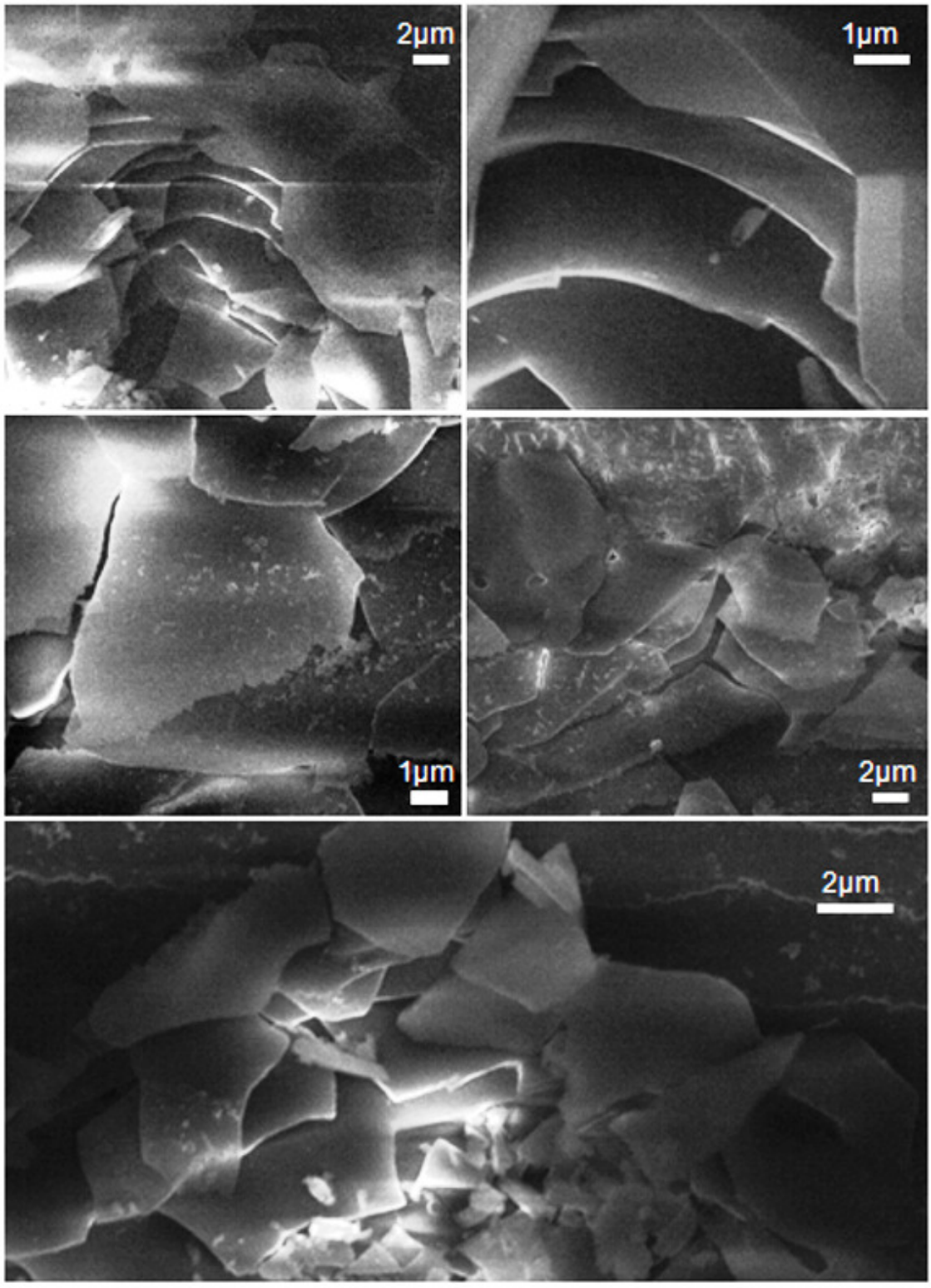


**Figure 4.40:** SEM micrographs of deproteinized nacre tested at the top surface. Debris and brittle fracture can be observed on deproteinized nacre.

Figure 44 shows the characteristic deformation features of untreated nacre tested on the cross-section. The deformation occurs by first the splitting at the tile interface, then as the load is increased there is a resistance to crack propagation by the layering structure. This resistance causes a crack deflection. As the applied load increases fracture occurs by both, trans- and inter-tile ways. Finally, as the limit is reached there is a complete delamination of the tiles.

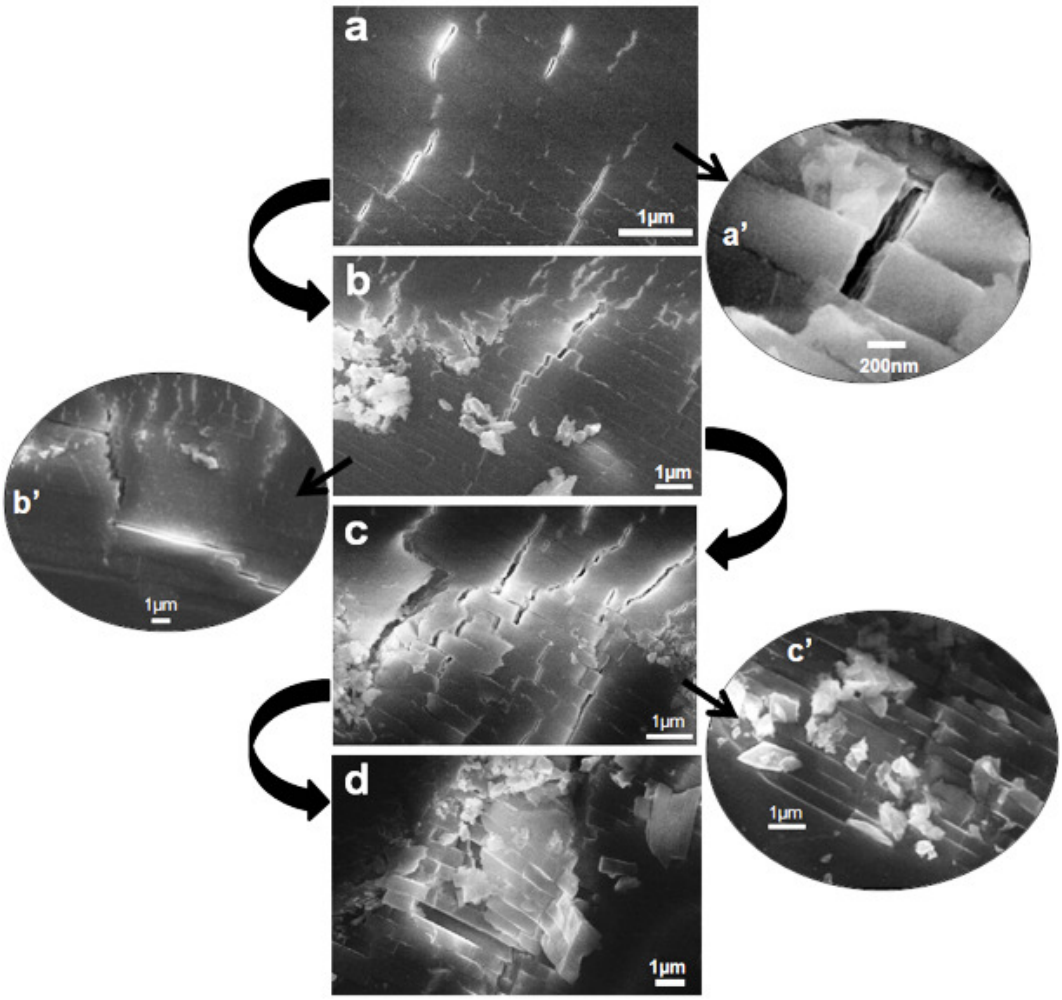


**Figure 4.41:** SEM micrograph of tested untreated nacre on the cross-section. Opening at interface, crack deflection, trans and inter tile fracture, and complete failure occurs sequentially. Features such as organic layers can be observed.

Figure 4.42 shows the characteristic deformation features of deproteinized nacre tested on the cross-section. The typical deformation occurs by trans and inter-tile fracture at low loads, crack propagation as the load increases and a unobstructed fracture propagation. Finally, as the load reaches its maximum there is complete shattering of the material and debris is all that remains. Interesting features that are observable are the mineral bridges that remain between the tiles and the noticeable roughness and asperities exhibited on the surface of the tiles.

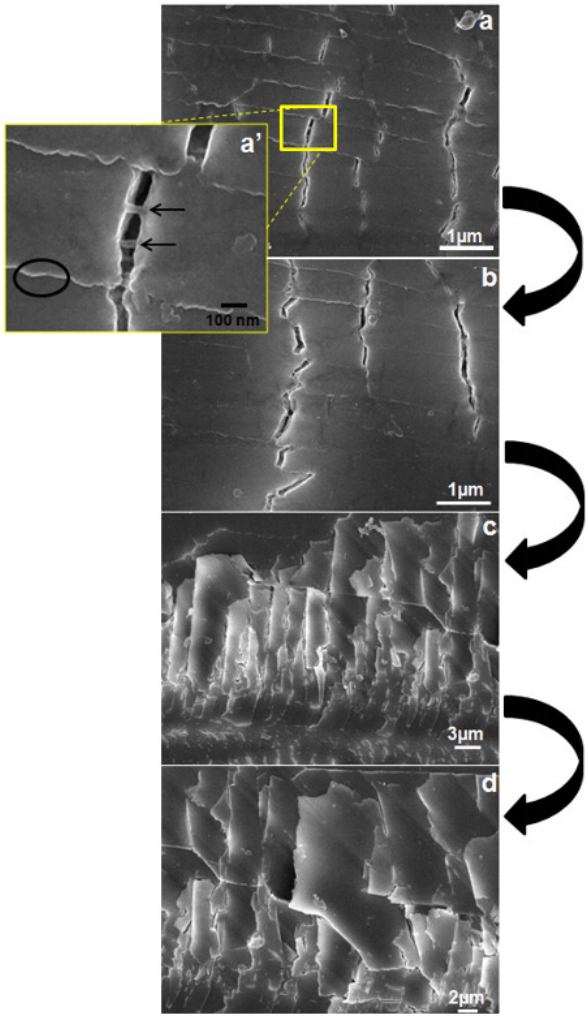


**Figure 4.42:** Micrograph of tested deproteinized nacre on the cross-section. Trans and inter tile fracture, crack propagation, unobstructed fracture, and complete shattering occurs subquentially. Features such as asperities and mineral bridges can be observed.

*4.3.4 Nanoindentation Experiments*

Nanoindentation results gave further insight on the crack propagation through the tiles. Indentation marks were made in the center region of a polished tile and the load was applied to initiate a crack. Figure 4.43 shows AFM observations of an indentation on the center of the tile of untreated nacre. Figure 4.44 show an indent which caused a crack to propagate, as the crack reaches the edge it causes aperture at the tile interface. The crack primarily propragates by pushing the mineral tiles apart and traveling though the interface.

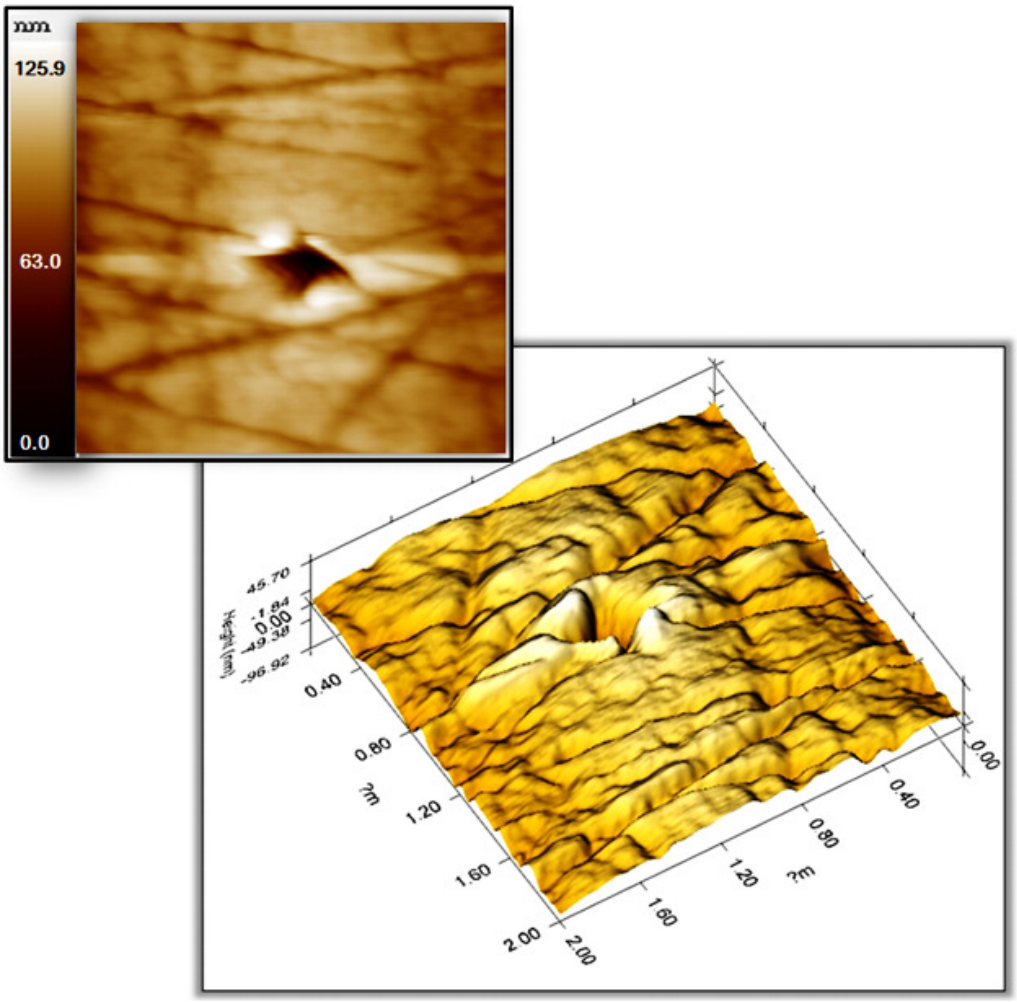


**Figure 4.43:** AFM image of indentation on untreated nacre on the center of tile

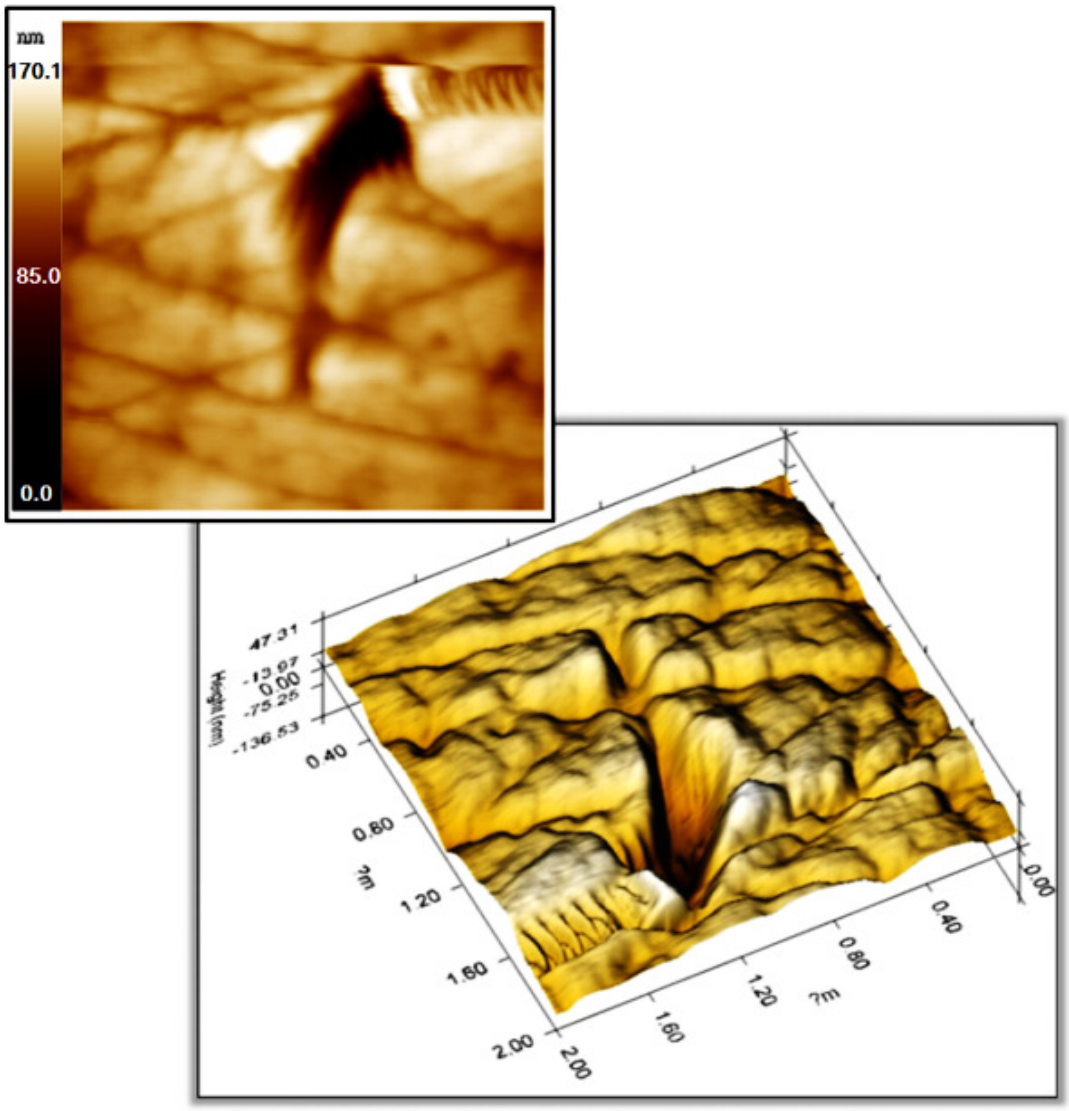


**Figure 4.44:** AFM image of indentation on untreated nacre which causes aperture at the tile interface

Penetration in deproteinized nacre proved to be complicated due to the rough nature of the specimen. As it can be seen from Figure 4.45, the indentation is barely noticeable and is easily concealed within the surface roughness. Further testing and better sample preparation is required for accurate results. These results agree with previous nanoindentation results by Bezares et al. [46], where heat treated nacre was described as granular. In this study, when the organic component is removed it also alters the structure of the mineral tiles, suggesting that in fact there is an embedment of organic constituent that impacts the mechanical properties.

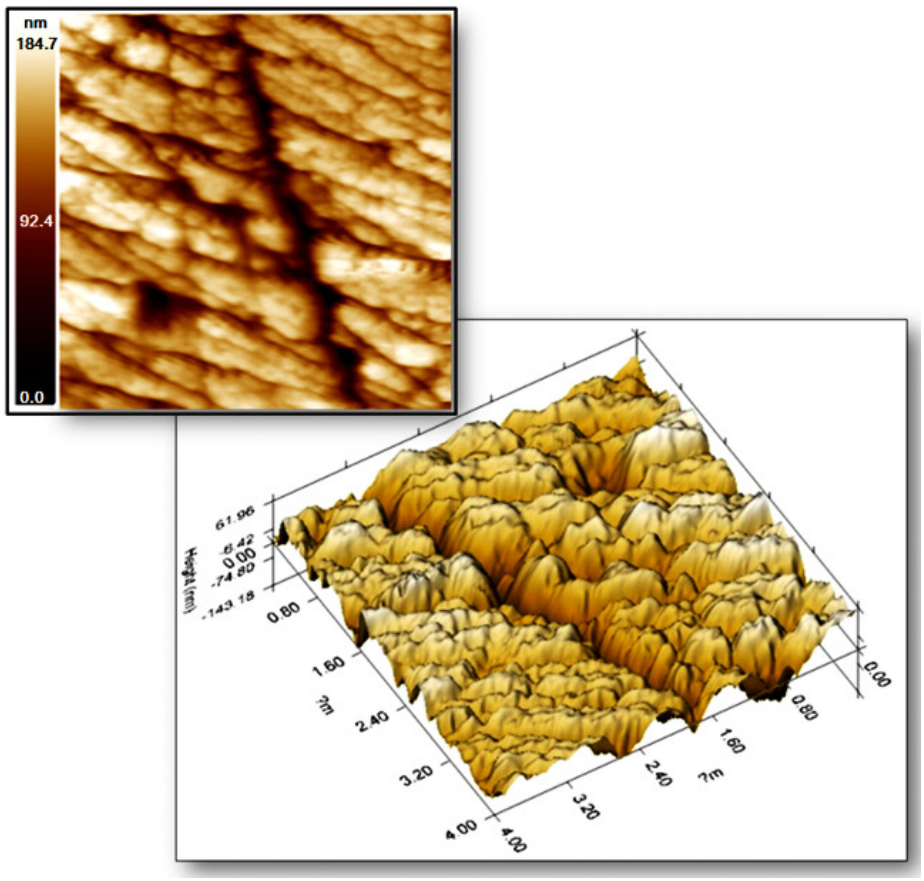


**Figure 4.45:** AFM image of nanoindent on deproteinized nacre. Extreme roughness conceals indent

**4.4 Modeling of the organic membrane**

The standard linear solid model (Zener) is a modified version of the basic Maxwell deformation model for polymers. It consists of a Maxwell element (linear spring and dashpot in series) in parallel with a linear spring (Figure 4.46). It is mainly used to describe the viscoelastic behavior of polymers and describe the creep and stress relaxation behavior. The springs represent the deformations that occur due to the bending and stretching of interatomic bonds, while the dashpot extensions are not recoverable and representative of intermolecular slippage.

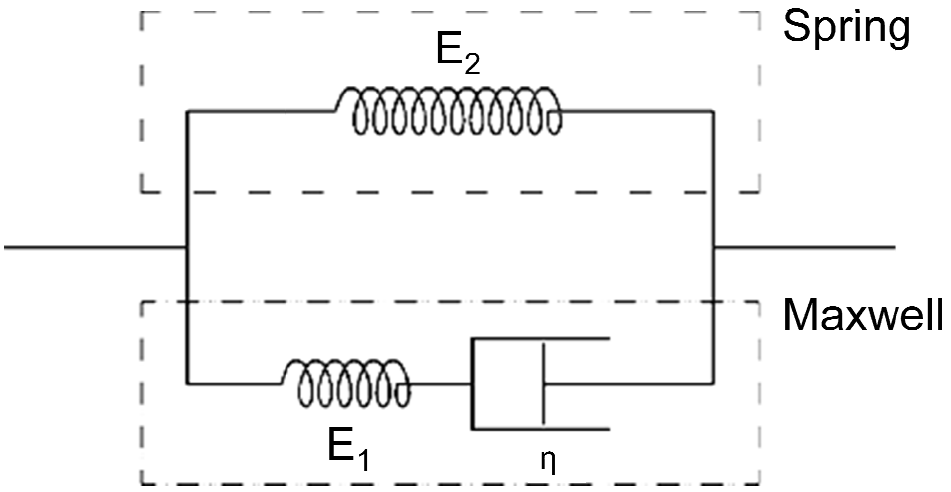


**Figure 4.46:** Schematic diagram of the Standard Linear Solid model consisting of a Maxwell element (linear spring and dashpot in series) and a linear spring in parallel.

Due to the dashpot element, when the mechanical model is subjected to a tensile stress, the behavior will depend on the rate of loading. Given the observed strain rate effects in the experimental results, the standard linear solid model was applied and parameters were approximated as described below.

In the standard linear solid model, the stress is separated into $\sigma^e$, the independent equilibrium stress in the spring $E_2$, and $\sigma^v$, the rate dependent stress component in the spring $E_1$ and dashpot η.

$$\sigma = \sigma^e + \sigma^v \tag{4.4}$$

The strain is equivalent in both the $E_2$ and the Maxwell component. The initial modulus is the sum of the two spring modulus:

$$E = E_1 + E_2 \tag{4.5}$$

Where $E_2$ approximates the stress-strain curve without any viscosity effect [169-172].

The spring follows Hooke's law:

$$\sigma^e = E_2\varepsilon \tag{4.6}$$

While the Maxwell element is given by:

$$\sigma^v + \frac{\eta}{E_1}\dot{\sigma}^v = \eta\dot{\varepsilon} \tag{4.7}$$

Thus the total stress in the Standard Linear Solid model can be obtained as:

$$\sigma + \frac{\eta}{E_1}\dot{\sigma} = \dot{E_2\varepsilon} + \frac{\eta}{E_1}(E_1 + E_2)\dot{\varepsilon} \tag{4.8}$$

Thus, the solution to equation defines a stress-strain relationship at a constant strain rate, given by:

$$\sigma = E_2\varepsilon + \eta\dot{\varepsilon}[1 - exp^{\frac{-E_1\varepsilon}{\eta\dot{\varepsilon}}}] \tag{4.9}$$

In order to approximate $E_2$ in the Standard Linear Solid model, which is associated with the rate independent equilibrium stress. The equilibrium state was approximated to the stress–strain curve at the lowest strain rate ($\dot{\varepsilon}$= $10^{-4}$ $s^{-1}$) assuming the viscosity effect is minimal at this rate. The equilibrium stress-strain curve was fitted to a parabolic function (Figure 4.47), given by:

$$\sigma^e = -25.69\varepsilon^2 + 8.96\varepsilon \tag{4.10}$$

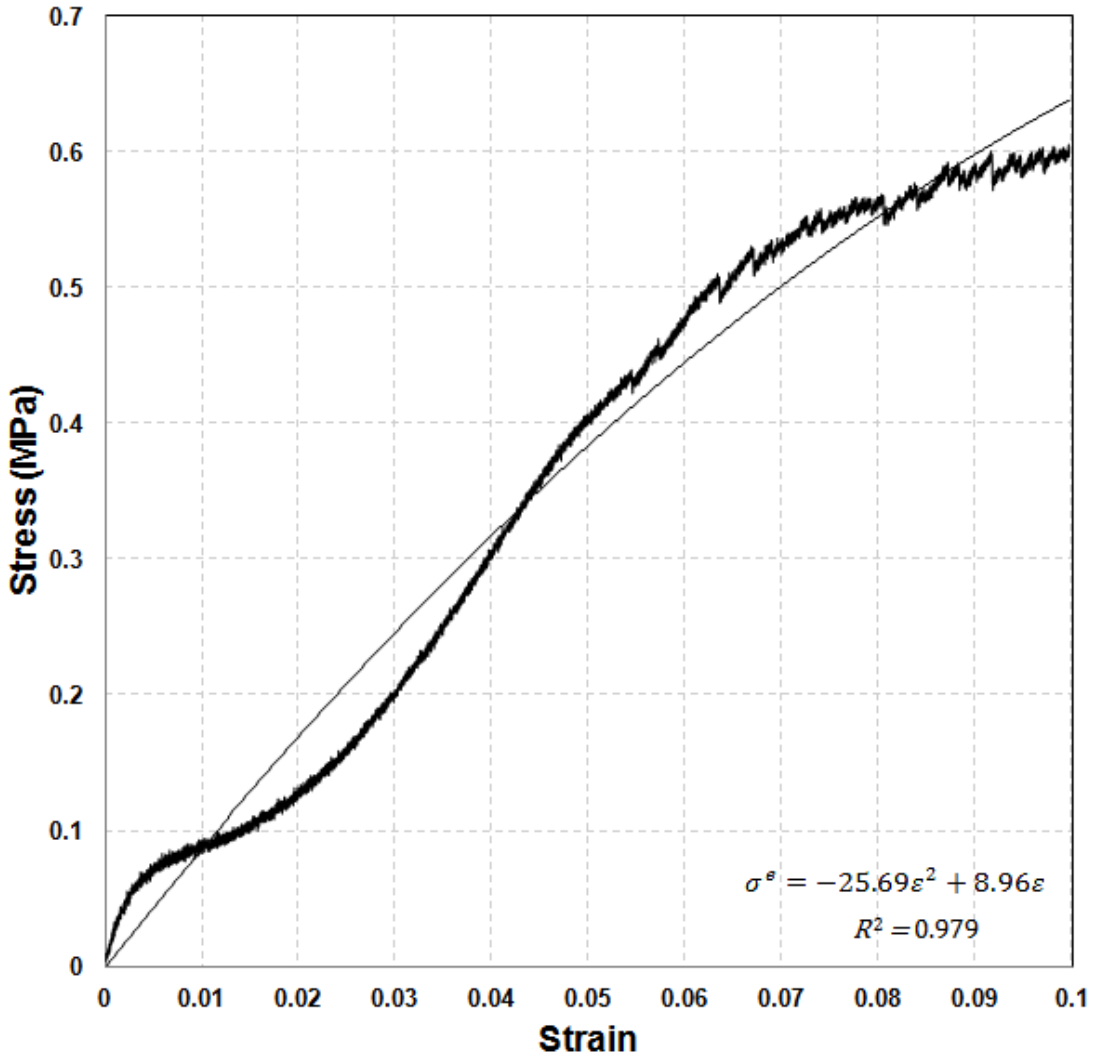


**Figure 4.47:** Equilibrium stress–strain curve approximated to the stress–strain curve at

the lowest strain rate ($\dot{\varepsilon}$= $10^{-4}$ $s^{-1}$).

Because,

$$\sigma^e = E_2\varepsilon \tag{4.11}$$

$E_2$ can be calculated:

$$E_2 = a\varepsilon + b = -25.96\varepsilon + 8.96 \tag{4.12}$$

The modulus of elasticity, E, is related to the strain rate. This relationship was obtained by averaging the Elastic Modulus from the experimental work, where at $\dot{\varepsilon} = 10^{-2}s^{-1}$ the modulus, E = 52.17 MPa and at $\dot{\varepsilon} = 10^{-4}s^{-1}$ the modulus, E = 3.66 MPa. Our experimental results show that the Elastic Modulus is dependent to the strain rate, however, given that the experimental work was performed at only two different strain rates, the relationship between the modulus and the strain rate is not known and can only be approximated. Thus, first, a linear relationship between the Elastic Modulus and the strain rate (Figure 4.48) was assumed.

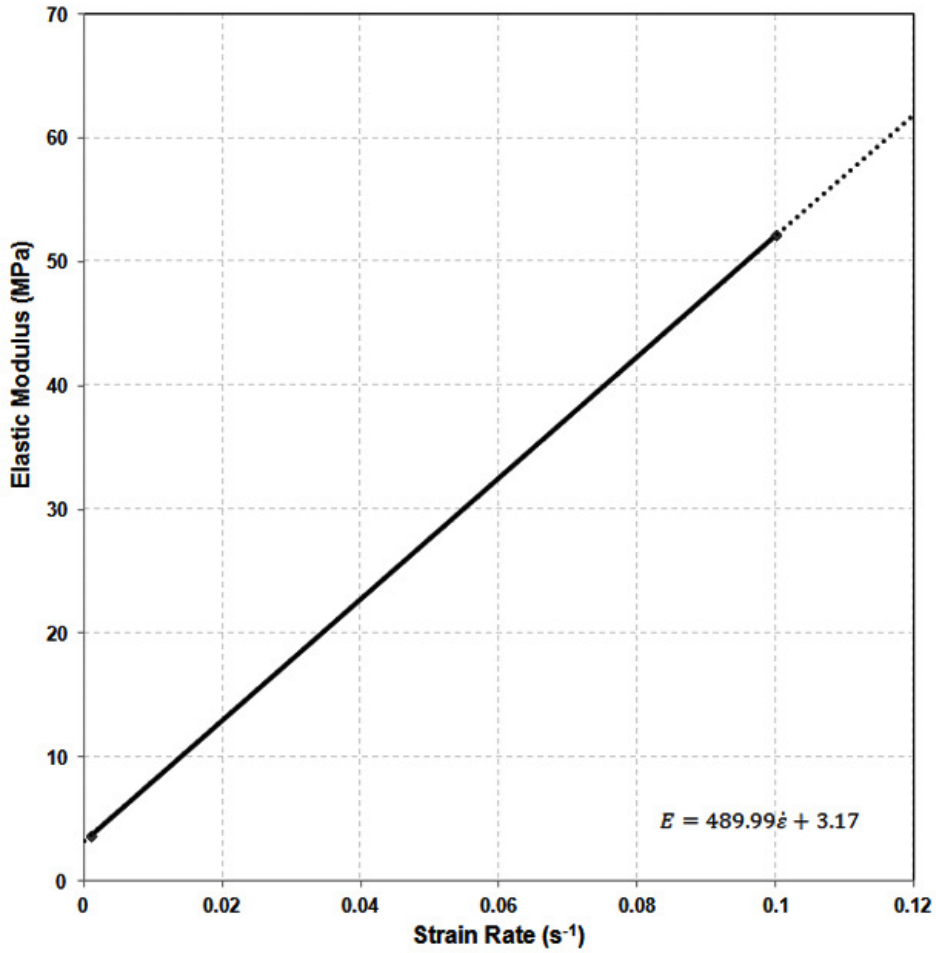


**Figure 4.48:** Linear relationship between E and strain rate obtained from equilibrium stress–strain curve in Standard Linear Solid model.

Assuming a linear relationship between the elastic modulus and the strain rate, we obtain that the modulus is related to the rate as:

$$E = 489.99\dot{\varepsilon} + 3.17 \tag{4.13}$$

$E_1$ can then be determined by subtracting the secant modulus, defined by $E_2$ at 1% strain [paper], from E. This variation of $E_1$ with strain rate is defined by:

$$E_1 = 489.99\dot{\varepsilon} + 5.53 \tag{4.14}$$

The solution of equation 4.9 defines the stress-strain relationship based on the Standard Linear Solid model:

$$\sigma = E_2\varepsilon + \eta\dot{\varepsilon}[1 - exp^{\left(\frac{-E_1\varepsilon}{\eta\dot{\varepsilon}}\right)}] \tag{4.15}$$

$$\sigma = (-25.96\varepsilon + 8.96)\varepsilon + \eta\dot{\varepsilon}[1 - exp^{\left(\frac{-(489.99\dot{\varepsilon}-5.53)\varepsilon}{\eta\dot{\varepsilon}}\right)}] \tag{4.16}$$

Using equation 4.16 stress-strain curves of the demineralized nacre at the two different strain rates, $\dot{\varepsilon} = 10^{-2}$ and $\dot{\varepsilon} = 10^{-4}$, can be obtained and compared with the experimental data. The viscosity value was taken from literature [[46]]. As can be observed from Figure 4.49, predictions based on the model show reasonable agreements with experimental data at $\dot{\varepsilon} = 10^{-2}$. At $\dot{\varepsilon} = 10^{-4}$ the stress-strain the model prediction is not as comparable to the experimental data.

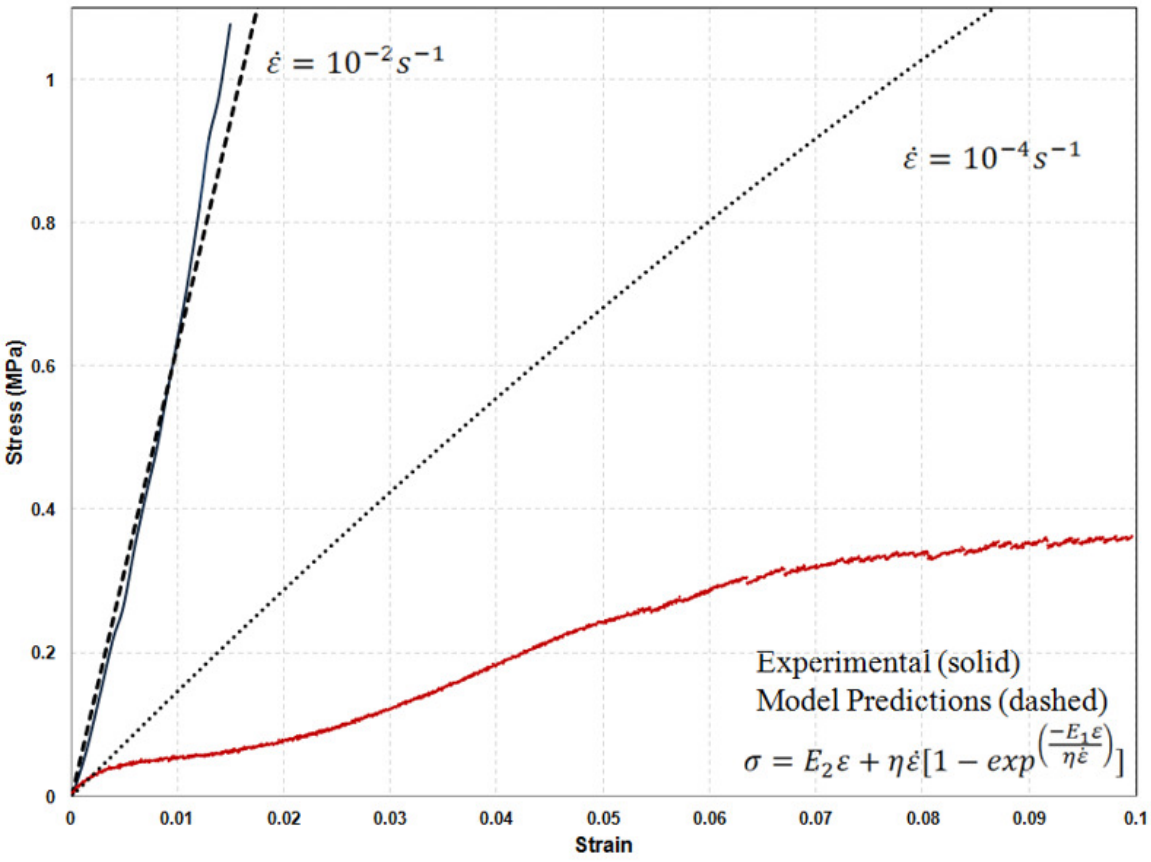


**Figure 4.49:** Tensile stress–strain curves for demineralized nacre obtained from experiment and Standard Linear Solid model at strain rate of $10^{-2}$ and $10^{-4}$ $s^{-1}$ assuming a linear relationship between the elastic modulus and strain rate.

The lack of agreement might be due to the assumption of a linear relationship between the modulus and the strain rate. Thus, instead, a logarithmic relationship (Figure 4.50) between the elastic modulus, E, and the strain rate, $\dot{\varepsilon}$ is assumed. We assume the following relationship between the modulus and strain rate:

$$E = 10.54 \ln \dot{\varepsilon} + 76.425 \tag{4.17}$$

Then $E_1$ can be obtained and the solution of equation 4.17 defining the stress-strain relationship would change such as:

$$\sigma = (-25.96\varepsilon + 8.96)\varepsilon + \eta\dot{\varepsilon}[1 - exp^{\left(\frac{-(10.54ln\dot{\varepsilon} - 76.425)\varepsilon}{\eta\dot{\varepsilon}}\right)}] \quad (4.18)$$

This is would alter the predicted model as shown in Figure 4.51.

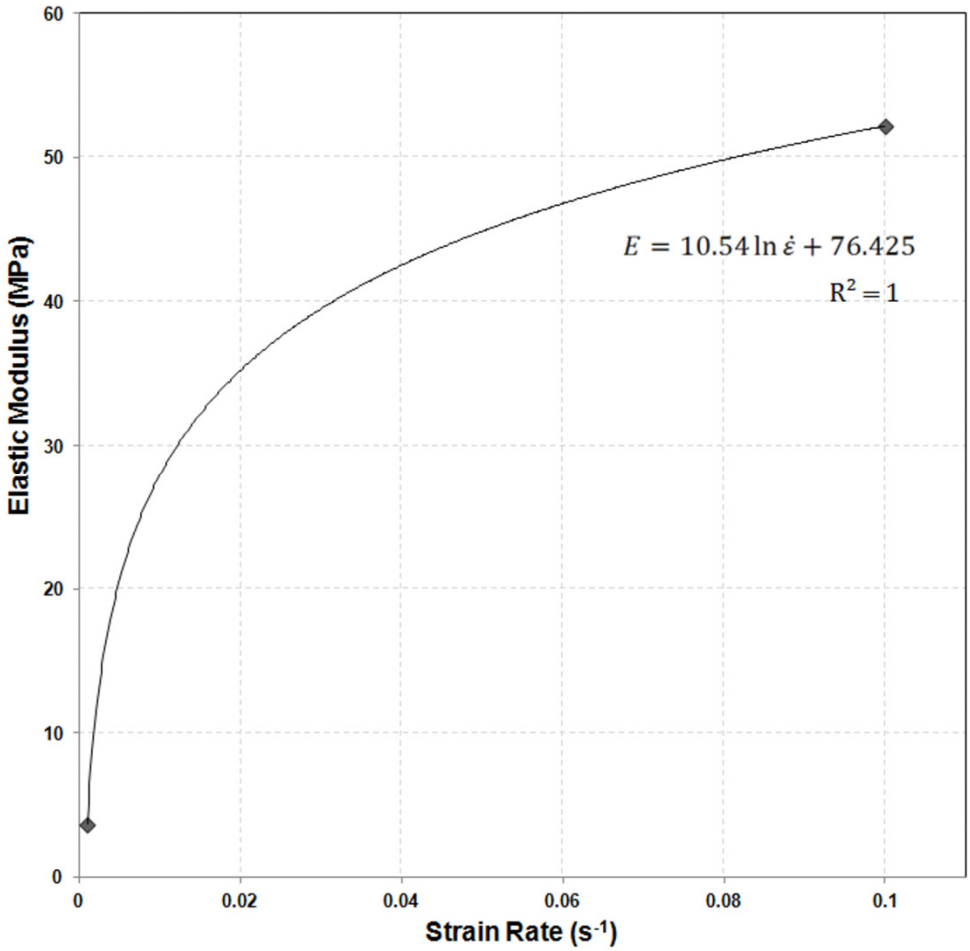


**Figure 4.50**: Logarithmic relationship between E strain rate obtained from equilibrium stress–strain curve in Standard Linear Solid model

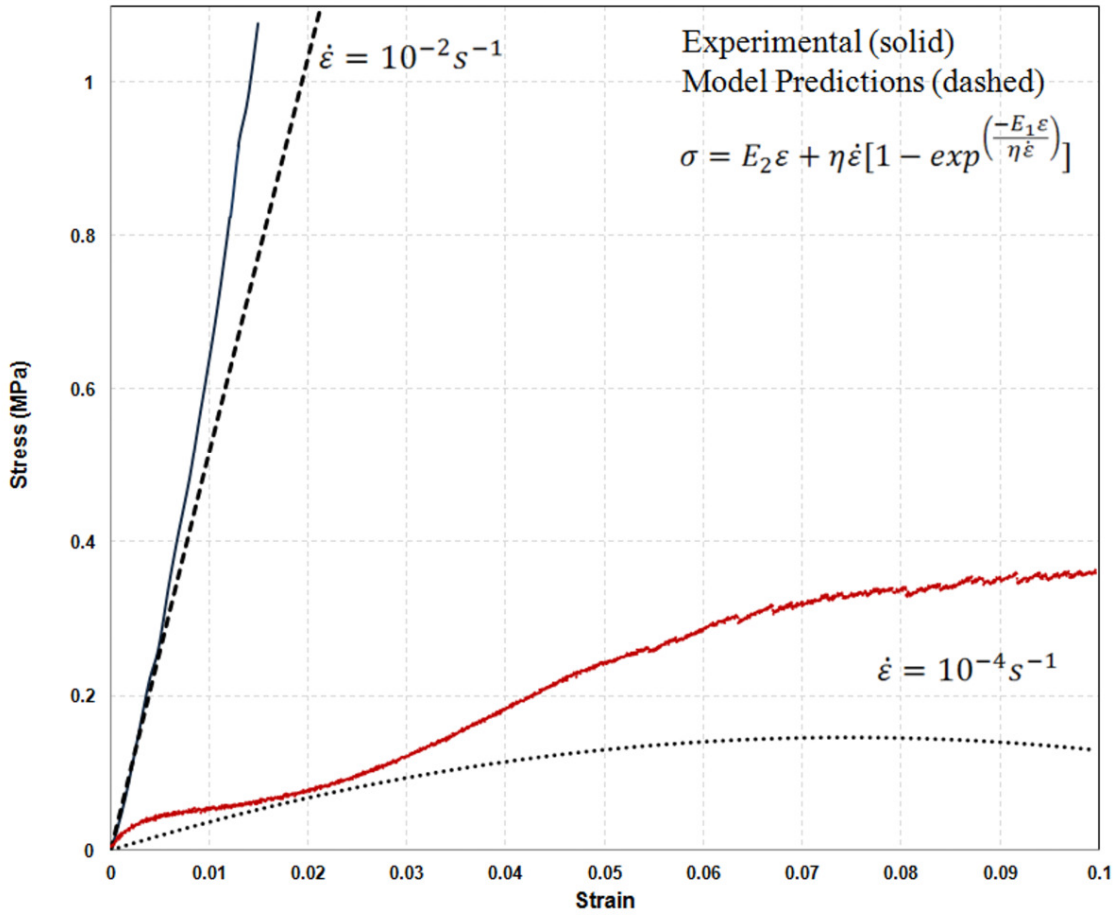


**Figure 4.51:** Tensile stress–strain curves for demineralized nacre obtained from experiment and Standard Linear Solid model at strain rate of $10^{-2}$ and $10^{-4}$ $s^{-1}$ assuming a logarithmic relationship between the elastic modulus and strain rate.

Given that experimental data falls somewhere within the range of the two predicted versions of the standard linear solid model, hints that the relationship between the elastic modulus and strain rate is somewhere within a linear and logarithmic relationship. Performing tensile testing at other strain rates would allow for a more accurate relationship between the modulus and the strain rate, providing better parameters for the constitutive equation. Additionally, stress-relaxation experiments could give the

correct spring constants allowing for a better fit. Additionally, the misfit could indeed be due to the simplicity of the standard linear solid model.

Most polymers do not relax with a single relaxation time as predicted with the standard linear solid model. Some additional (more complex) models may allow for a better fit. For example, Wiechert model illustrated in Figure 4.52 can have as many spring-dashpot Maxwell elements as are needed to approximate the distribution satisfactorily.

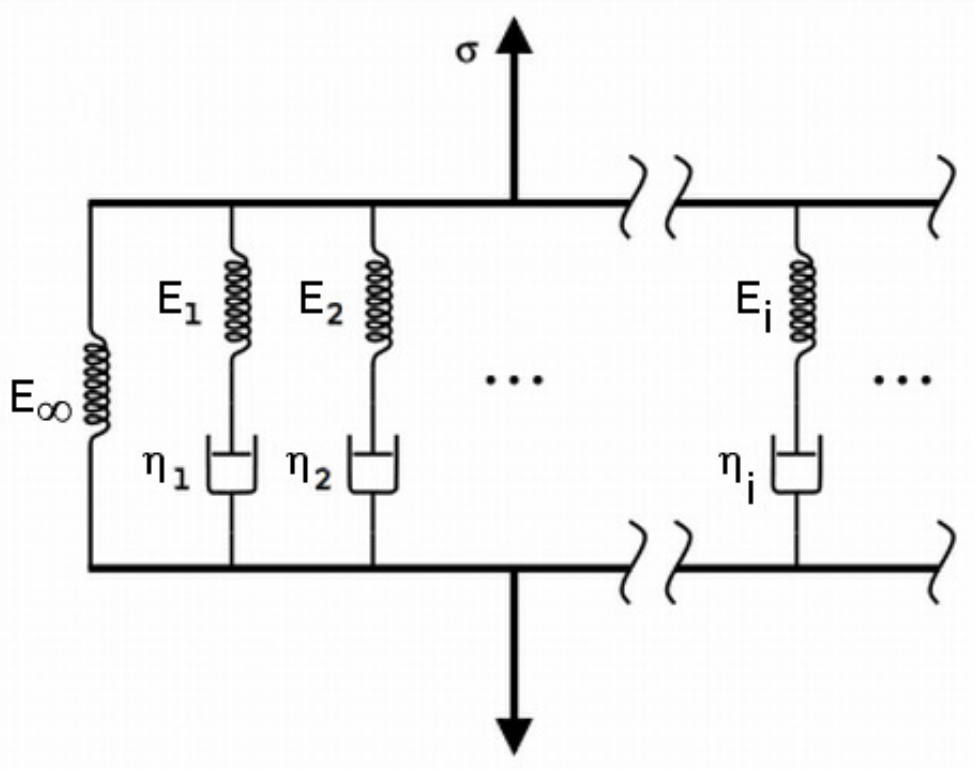


**Figure 4.52:** The Wiechert model.

*Analysis of the expansion of hole in the organic interlamellar membrane subjected to tension*

The organic interlayer in nacre has been the subject of a considerable number of structural and mechanical investigations [25, 44-46, 48, 75-77]. Meyers et al. [48] used nanoindentation and the sagging of the membrane to estimate its mechanical response, concluding the the flow stress is very low in the wet condition while the membrane becomes stiff and brittle in the dry state. Bezares et al [44-46] and Lopez et al. [173] established the mechanical response of the organic layer in tension and found it to be highly strain-rate dependent. The slope of the stress-strain curve increased from 12.5 MPa to 115 MPa when the strain rate was raised from $10^{-4}$ $s^{-1}$ to $10^{-2}$ $s^{-1}$.

An interesting observation that is highly relevant to both the growth mechanism of the nacre and the mechanical response is the porous structure of the organic interlamellar layers is that it interspersed with holes have diameters ranging between 20 and 50 nm and that the holes grow at a rate much larger than the applied strain. Belcher and Gooch [174] observed that the size of the holes increased significantly with stretching of the membrane. Additional observations by Meyers et al. [25] confirmed this and a qualitative argument was made based on the fact that the hoop stresses at the surface of the hole were twice the remote traction. The analytical treatment of membranes containing holes is well developed, the first efforts dating from the 1950's (Rivlin and Thomas [175]). More recently, Lubarda [176] presented a comprehensive treatment of the subject, applied to red blood cells.

The objective of this section is to obtain quantitative analytical solutions for the growth of the hole as a function externally applied stretching and to compare these results with observations of the organic layer subjected to uniaxial tension. These calculations increase our understanding of the contribution of this interlamellar layer to the toughness of nacre.

*Mechanical analysis of pore evaluation*

A hexagonal arrangement of holes is considered (Figure 4.52); from this arrangement we extract a single, separate representative areal element (Figure 4.53) we can assume an isoareal deformation, $A_0=A$ , where:

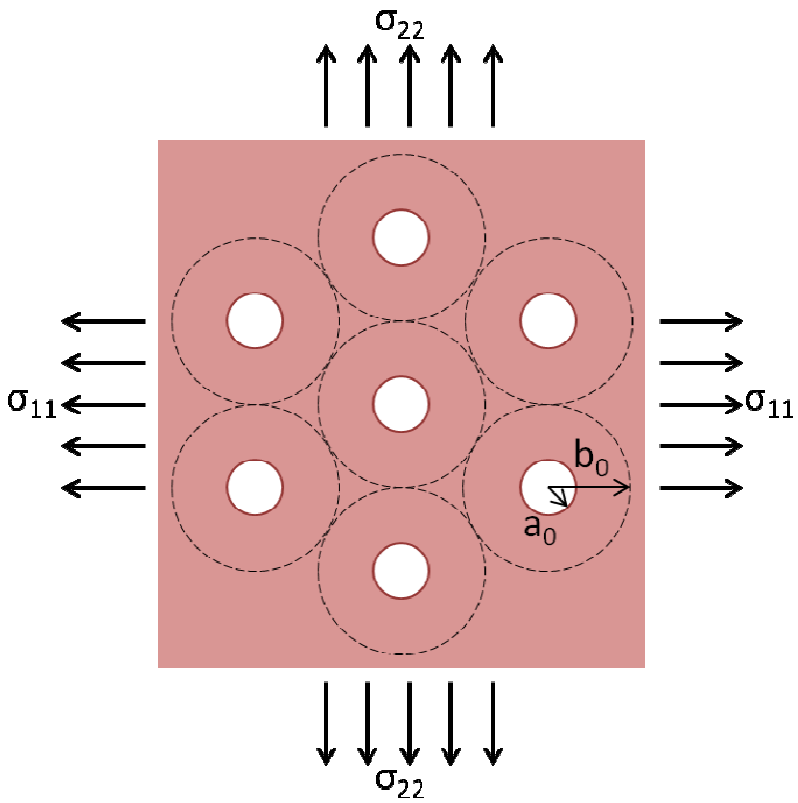


**Figure 4.53:** Hexagon arrangement of holes.

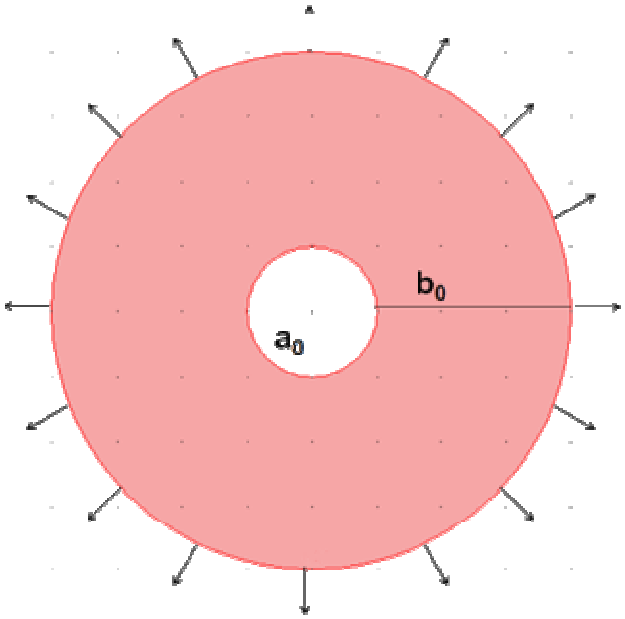


**Figure 4.54:** Separate representative areal element.

$$A_0 = \pi b_0^2 - \pi a_0^2 = \pi b_1 b_2 - \pi a_1 a_2 = A \tag{4.19}$$

$$b^2 - b_0^2 = a^2 - a_0^2 \tag{4.20}$$

Where $a_o$ and $b_o$ are the initial inner and outer radius, respectively. The corresponding values after stretching are $a_1$ and $a_2$, $b_1$ and $b_2$. In the case where $b_1$=$b_2$=$b$ and $a_1$=$a_2$=a, we have: $b^2 - b_0^2 = a^2 - a_0^2$ . This is justified by the fact that the thickness of the layer, 20-50 nm is equal to twice the diameter of the collagen fibrils (~10 nm). The thickness of the individual fibrils is not affected by the expansion, since they only slide by each other. Thus, the thickness of the layer is constant with extension and Poisson's ratio in plane is 0.

Thus, the engineering strain is defined as:

$$\varepsilon = \frac{b - b_0}{b_0} \tag{4.21}$$

Since $\varepsilon_{11} = \varepsilon_{22}$ (biaxial stress $\sigma_{11}=\sigma_{22}$)

Substituting equation 4.20 into equation 4.21:

$$\frac{b-b_0}{b_0} \times \frac{b+b_0}{b_0} = \frac{a^2-a_0^2}{b_0} \tag{4.22}$$

$$\varepsilon \times \frac{b-b_0+b_0+b_0}{b_0} = \frac{a^2-a_0^2}{b_0^2} \tag{4.23}$$

$$\varepsilon\left(\frac{b-b_0}{b_0} + \frac{2b_0}{b_0}\right) = \frac{a^2-a_0^2}{b_0^2} \tag{4.24}$$

$$\varepsilon(\varepsilon+2) = \frac{a^2-a_0^2}{b_0^2} \tag{4.25}$$

$$a^2 = b_0^2\varepsilon(\varepsilon+2) + a_0^2 \tag{4.26}$$

$$\frac{a^2}{a_0^2} = \frac{b_0^2}{a_0^2}\varepsilon(\varepsilon+2) + 1 \tag{4.27}$$

$$\frac{a}{a_0} = \left(\frac{b_0^2}{a_0^2}\varepsilon(\varepsilon+2) + 1\right) \tag{4.28}$$

For plotting ε vs. $\frac{a}{a_0}$ :

$$\frac{a}{a_0} = \left[\frac{b_0^2}{a_0^2}\varepsilon(\varepsilon+2) + 1\right] \tag{4.29}$$

$$\frac{b_0^2}{a_0^2}\varepsilon(\varepsilon+2) = \frac{a}{a_0} - 1 \tag{4.30}$$

$$\varepsilon(\varepsilon+2) = \frac{a}{a_0} - 1\left(\frac{a_0^2}{b_0^2}\right) \tag{4.31}$$

$$\varepsilon^2 + 2\varepsilon = \frac{a}{a_0} - 1\left(\frac{a_0^2}{b_0^2}\right) \tag{4.32}$$

The form shown in equation 4.33 is more convenient for plotting:

$$y = \frac{a}{a_0} - 1\left(\frac{a_0^2}{b_0^2}\right) \tag{4.33}$$

Thus,

$$\varepsilon^2 + 2\varepsilon = y \tag{4.34}$$

$$\varepsilon^2 + 2\varepsilon + 1 = y + 1 \tag{4.35}$$

$$(\varepsilon + 1)(\varepsilon + 1) = y + 1 \tag{4.36}$$

$$(\varepsilon + 1) = \sqrt{y + 1} \tag{4.37}$$

Where the negative component is disregarded (as ε is positive):

$$\varepsilon = \sqrt{y + 1} - 1 \tag{4.38}$$

Based on experimental observations, we approximate values for $a_0 = 20nm$, where $2 \leq \frac{a}{a_0} \leq 10$, and we plot them (Figure 4.54) for 3 (membrane to pore radius size ratios) cases:

$b_0 = 40\ nm$, So that $\frac{b_0}{a_0} = 2$

$b_0 = 60\ nm$, So that $\frac{b_0}{a_0} = 3$

$b_0 = 200\ nm$, So that $\frac{b_0}{a_0} = 10$

The initial porosity is defined as $(\frac{a_0}{b_0})^2$ and is shown in the same plot. It can be observed that for larger membrane to pore area, the pore expansion is highly sensitive to strain. Experimental observations show that the initial membrane to pore size ratio ranges between $2 \leq \frac{b_0}{a_0} \leq 3$. Assuming the organic interlayers are isotropic, strain values to ~10% are reached when (load is applied at a strain rate of $10^{-2}$ $s^{-1}$), suggests that a pore stretches of over 10x the initial pore size. Observations of the pore structure in the demineralized nacre (after the tensile load is applied) show pore size increases. In some cases pores stretch beyond 10x the initial pore size.

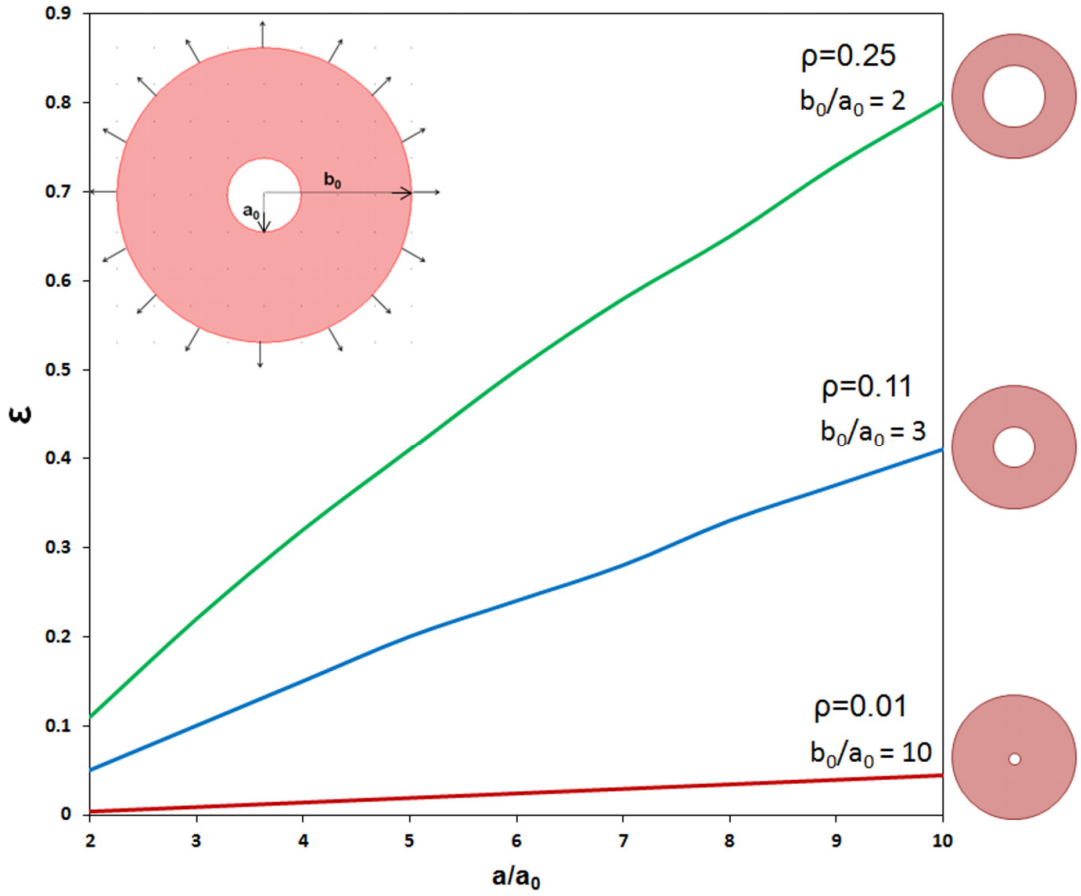


**Figure 4.55:** Strain values achieved compared on the relative pore to membrane size. Increase in normalized pore radius ($a/a_0$) with global strain for different values of porosity (defined as $\left(\frac{a_0}{b_0}\right)^2$). For $\frac{b_0}{a_0} = 10$, $a$ is equal to $10a_0$ for a strain of ε=0.03.

*Radial and hoop stresses*

We consider the membrane to be under an external traction $T$ ($\sigma_{11} = \sigma_{22}=T$). Where the the membrane has the initial (underformed) inner radius of $a_0$ and the initial (underformed) outer radius of $b_0$ (Figure 8), and where the initial radius at an arbitrary point of the membrane is $r_0$ (Figure 4.55). The radial and hoop stresses at $r$ can be calculated. The forces can be considered such as depicted in Figure 4.55. In order to determine the stresses inside the membrane as a function of its stretching we need the

equilibrium equation, a constitutive relationship, at the boundary conditions. The equilibrium equation in the radial direction is found from:

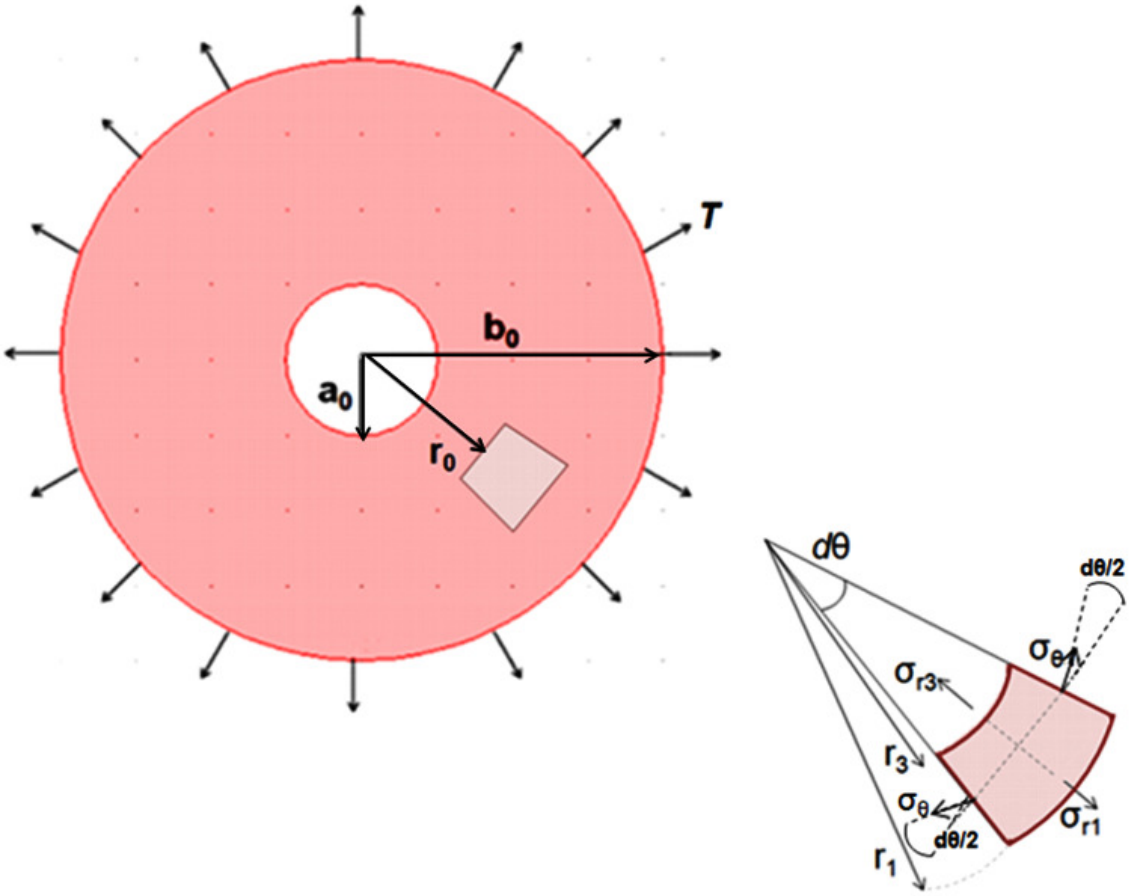


**Figure 4.56:** Stress analysis for circular pore in membrane subjected to external traction *T*.

The radial forces are given by:

$$1: (\sigma_r) r_1 d\theta = (\sigma_r r)_1 d\theta \tag{4.39}$$

$$3: -(\sigma_r r)_3 d\theta \tag{4.40}$$

The tangential forces by:

$$2: -(\sigma_\theta)_2(r_1 - r_2)\sin\left(\frac{d\theta}{2}\right) = -(\sigma_\theta)_2 dr\left(\frac{d\theta}{2}\right) \tag{4.41}$$

$$4: -(\sigma_\theta)_4 dr\left(\frac{d\theta}{2}\right) \tag{4.42}$$

The equilibrium equation predicts:

$$(\sigma_r r)_1 d\theta - (\sigma_r r)_3 d\theta - (\sigma_\theta)_2 dr\left(\frac{d\theta}{2}\right) - (\sigma_\theta)_4 dr\left(\frac{d\theta}{2}\right) = 0 \tag{4.43}$$

dividing by $\frac{dr}{d\theta}$ :

$$\frac{(\sigma_r r)_1 - (\sigma_r r)_3}{dr} - \frac{1}{2}[(\sigma_\theta)_2 + (\sigma_\theta)_4] = 0 \tag{4.44}$$

But:

$$\frac{d(\sigma_r r)}{dr} = r\frac{d(\sigma_r)}{dr} + \sigma_r\frac{d(r)}{dr} = r\frac{d\sigma_r}{dr} + \sigma_r \tag{4.45}$$

And the second term becomes:

$$\frac{1}{2}[(\sigma_\theta)_2 + (\sigma_\theta)_4] = \sigma_\theta \tag{4.46}$$

Thus,

$$r\frac{d\sigma_r}{dr} + \sigma_r - \sigma_\theta = 0 \tag{4.47}$$

We use a form of the Mooney-Rivlin for constitutive equation adopted by Lubarda [44] for a non-linear material. In radial coordinates it is in the form:

$$\sigma_r - \sigma_\theta = \mu\left(\lambda_\theta^{-2} - \lambda_\theta^2\right) \tag{4.48}$$

Where $\lambda_\theta$ is the stretch ratio in the shear modulus.

$$dr = r_0 d\lambda_\theta + \lambda_\theta dr_0 \tag{4.49}$$

$$dr_0 = \lambda_\theta dr \tag{4.50}$$

Where the initial radius $r_0$ to an arbitary point of the membrane becomes: $r = r(r_0)$

The principal stretches are defined as:

$$\lambda_\theta = \frac{r}{r_0} \text{ and } \lambda_r = \frac{dr}{dr_0}$$

And $\mu$ is the shear modulus of the membrane.

The differential equation then becomes:

$$\frac{d\sigma_r}{d\lambda_\theta} + \mu\left(\frac{1}{\lambda_\theta} + \frac{1}{\lambda_\theta^3}\right) = 0 \tag{4.51}$$

$$\frac{d\sigma_r}{d\lambda_\theta} = -\mu\left(\frac{1}{\lambda_\theta} + \frac{1}{\lambda_\theta^3}\right) \tag{4.52}$$

$$\int d\sigma_r = \int -\mu\left(\frac{1}{\lambda_\theta} + \frac{1}{\lambda_\theta^3}\right) d\lambda_\theta \tag{4.53}$$

$$\sigma_r = -\mu\left(ln\lambda_\theta - \frac{1}{2\lambda_\theta^2}\right) + D \tag{4.54}$$

$$\sigma_r = \frac{1}{2}\mu\left(\frac{1}{\lambda_\theta{}^2} - 2ln\lambda_\theta\right) + D \tag{4.55}$$

$$\sigma_r = \frac{1}{2}\mu\left(\frac{1}{\lambda_\theta{}^2} - ln\lambda_\theta^2\right) + D \tag{4.56}$$

Where: $\lambda_\theta = \frac{r}{r_0}$

$$\sigma_r = \frac{1}{2}\mu\left(\frac{r_0^2}{r^2} - ln\frac{r^2}{r_0^2}\right) + D \tag{4.57}$$

Following Lubarda [176], we eliminate *r* by making the substitution: $r^2 = r_0^2 + C$, and *D* is an integration constant, thus equation 4.48 can be written as:

$$\sigma_r = \frac{1}{2}\mu\left[\frac{1}{1+\frac{C}{r_0^2}} - ln\left(1 + \frac{C}{r_0^2}\right)\right] + D \tag{4.58}$$

Similarly, the hoop stress follows from equation 4.48:

$$\sigma_\theta = \frac{1}{2}\mu\left[2\left(1 + \frac{C}{r_0^2}\right) - \frac{1}{1+\frac{C}{r_0^2}} - \ln\left(1 + \frac{C}{r_0^2}\right)\right] + D \tag{4.59}$$

The boundary conditions are σ=0 when $r_0 = a_0$ and $\sigma = T$ when $r_0 = b_0$. Thus,

$$0 = \frac{1}{2}\mu\left(\frac{a_0^2}{a_0^2+C} - ln\frac{a_0^2+C}{a_0^2}\right) + D \tag{4.60}$$

$$T = \frac{1}{2}\mu\left(\frac{b_0^2}{b_0^2+C} - ln\frac{b_0^2+C}{b_0^2}\right) + D \tag{4.61}$$

Substituting *D* from Equation 4.60 into Equation 4.61 and dividing all terms by $a_0$ we solve numerically for *C* and *D* for $\frac{b_0}{a_0} = 2, 3, \text{and } 4$ (given the experimental observations on the membrane to pore ratio) and after setting *T*= 0.5μ. The normalized radial and hoop stress are plotted versus $r_0/a_0$ in Figure 9. The radial stresses vary from zero, at the inner radius to *T*, the applied traction, at the external surface. The hoop stresses at the internal surfaces of the voids are considerably larger than the ones in the outside. The

ratio of these stresses to the applied traction is ~1.62, ~1.76 and ~1.59 for porosities of 0.11, 0.25, and 0.0625 respectively. These results are in agreement with an earlier prediction by Meyers et al. [25].

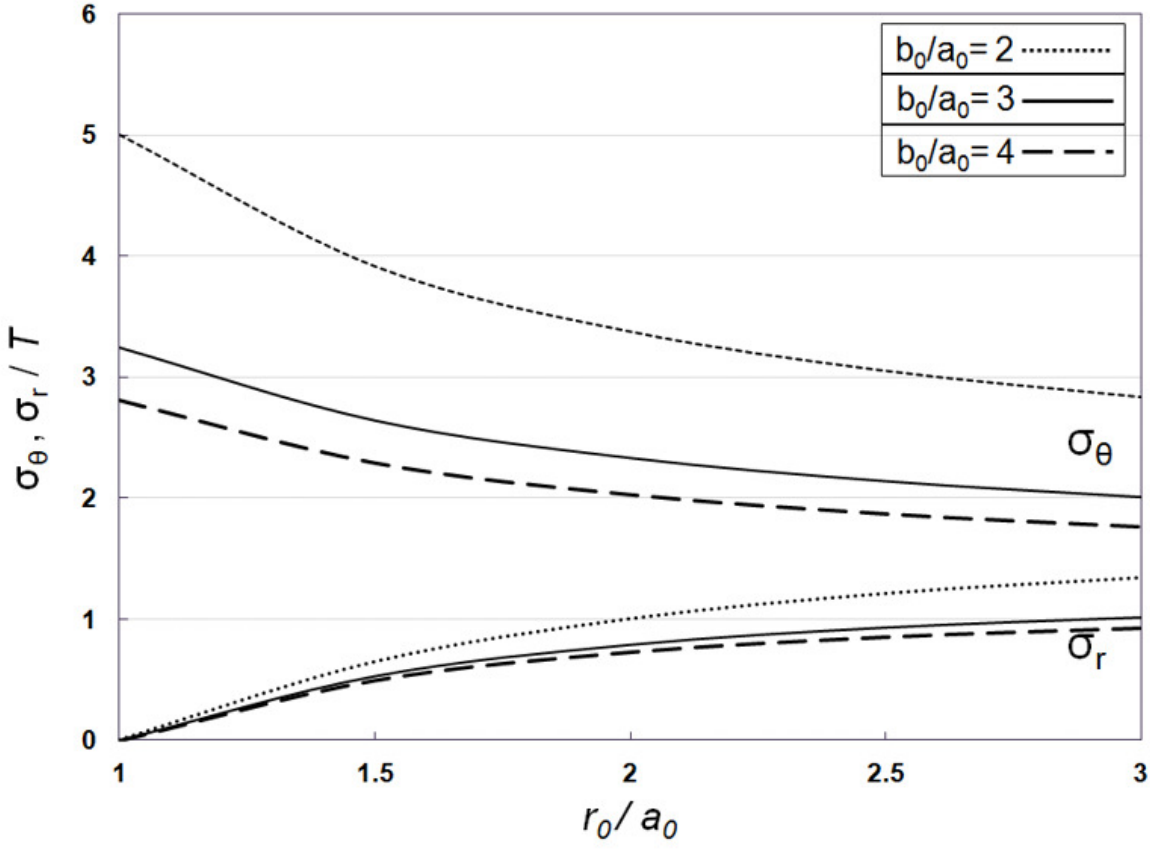


**Figure 4.57:** Variation of radial and hoop stress (normalized by *T*) with radius (for the case of $\frac{b_0}{a_0}$ =2, 3, and 4 and $T/\mu$ =*0. 5*.)

When the pore fraction is small, the fractional increase in pore size is many times higher than the externally applied strain. Thus, we explain the presence of pores that have increased from 20 to 200 nm in radius which are routinely seen in the organic layer. This requires that the Poisson's ratio in the plane be zero consistent with the chitin fibrils retaining their thickness. The thickness of membrane does not change as it stretches.

The radial and hoop stresses in the interlamellar layer are calculated as a function of radius *r*, for different porosities (0.11, 0.25, and 0.0625). The hoop stresses vary between 3*T* and 5*T* (*T* is the external traction) in the membrane, whereas the radial stresses increase from zero in the inside to close to *T* in the outside.

Chapter 4, in part, is a reprint of the material as it appears in Lopez MI, Chen PY, McKittrick J, Meyers MA. *Materials Science and Engineering C* 2010; 31: 238-245 and Lopez MI, Meza-Martinez PE, Meyers MA. *ActaBiomaterialia* 2014; 10 (5): 2056-2064 and in Lopez, Maria Isabel; Chen, Po-Yu; McKittrick, Joanna; Meyers, Marc Andre, *Bioceramics and Biotechnologies II*, Ed. J. McKittrick and R. Narayan, Ceram. Trans., 247, 37-46, Wiley & Sons, Hoboken, NJ, 2014. The dissertation author was the primary investigator and author of these publications. In addition, chapter 4, in part, has been submitted for publication of the material as it may appear in *ActaBiomaterialia* 2014. Lopez, Maria Isabel and Meyers, Marc Andre, 2014. The dissertation author was the primary investigator and author of this paper.

# CHAPTER 5

# CONCLUSIONS

The nacre from the shell of the abalone represents a biological composite of organic and inorganic phases which have structural hierarchies that range from the nano to the macroscale. The goal of this study is to contribute to the expanding knowledge base of biological systems serving as biomineralization and biomimetic models in hopes of inspiring novel techniques and designs. A growth study considering seasonal changes on the mollusk *Haliotis rufescens*, commonly known as the red abalone is presented. The structure-property relationship of red abalone nacre is investigated, focusing in the individual constituents (isolated mineral and isolated organic component) and comparing that to the integrated structure. A model to represent the mechanical response of demineralized nacre is attempted. From these examinations, the following preliminary conclusions can be made:

The combined utilization of the flat pearl technique and SEM observations allowed to determine that the rate of the transition from an initial random nucleation to the steady-state growth of aragonite tiles is achieved faster when the animal is kept at relatively warmer temperatures and regularly fed (21 °C) than when maintained in water at colder temperatures (15 °C) or with a limitation of food (21 °C).

High resolution SEM images showed evidence of a smooth surface, inner channels, and cilia in the epithelium. The epithelium provides a path for ion and chitin transport and the smooth outer surface mechanically flattens the growing surface of the

shell. These results are comparable to previous observation by Meyers and Lin [24, 48]. TEM observations show different types of subepithelial glands and secretory cells, and cilia. These components are important to the formation of the components that comprise nacre. Such as the mucus layer and other extrapallaial fluids that serves for protection, lubrication, motion, adhesion, and the transport of substances to for the formation of the shell.

Observations of complete demineralization of abalone nacre confirmed the sheets were composed of disordered layers of cross-linked protein chains. These are sections consisting of the intertile layer composed of the chitin network. Observed and studied previously by Meyers and Lin [25, 38, 48] and by Bezares [44, 45]. This organic component is believed to influence growth mechanism of aragonite tiles by retarding, periodically, the growth in the c-axis direction. These results are strong evidence supporting the growth mechanisms proposed by Meyers et al. [48].

From the mechanical testing of the demineralized nacre we have established the tensile strength of the organic interlayer (both nano and meso) and estimate it to be ~2 MPa at $10^{-2}$ $s^{-1}$. Whereas the tensile strength of abalone nacre parallel and perpendicular to the tile layer is ~100-150 MPa and ~3-5 MPa, the tensile strength of the organic layer is on the order of 2 MPa. Thus, the inherent resistance of the organic inter- and meso-layer contribute little to the overall strength. This organic interlayer has shown to be high strain rate sensitive, which is characteristic of organic hydrated composites. Additionally, the thickness variation of the nacre tablets was measured and found to be a small fraction of the mean tablet thickness (0.568 nm); the standard deviation is 26 nm,

indicating that the wedge mechanism of toughening does not operate in the nacre investigated.

From the mechanical testing of the deproteinized nacre we conclude that the behavior of the material, in particularly is strength, is far below that of its theoretical strength. Where the tensile strength in abalone nacre (perpendicular to layered structure) is ~4.2 MPa, compared to that of deproteinized nacre having a strength of ~0.33 MPa. Even though the organic matrix accounts for only 5 vol% of nacre, when it is removed the strength of nacre is reduced by ~92%. This may be in fact due to not only the removal of actual organic layers that have an effect of the weakening of the material - but also the removal of the organic material embedded within the actual mineral. By dissolving all organic component it might also damage other structural characteristics that add to the strength of nacre - for example the mineral bridges might be damaged by the removal of the organic component.

Additionally, scratch and nanoindentation results further illustrate the effect of the loss of the organic constituent. When tested on the top surface (on the c-axis of the shell) deproteinized nacre fractures at a lower load (major fracture observed at a frictional force <100 mN) and it does not show an explicit frictional force limit. Penetration in untreated nacre showed aperture at the tile interface while penetration in deproteinized abalone proved to be complicated due to the rough nature of the specimen due to the loss of the organic material. The deproteinized nacre is granular and fragile. Additionally, scratch results also show the anisotropic behavior of nacre. In the scratch experiments nacre exhibits a higher resistance to failure when tested in cross-section (when the surface is along the tile layers) than from the top surface, in both, untreated and deproteinized

specimens. Furthermore, when scratched, mesolayers have an effect on the behavior of the sample.

Imaging and characterization of deproteinized and demineralized nacre reveal that some of the nanoaspereties in fact correspond to grains, and not precisely a mineral bridge. Distribution and density of the nanopores within the organic interlayer correspond to a better estimate of the number of mineral bridges.

Modeling of the demineralized nacre show that demineralized nacre follows a viscoelastic behavior. The approximation of the spring parameters, following a logarithmic relationship between the elastic modulus and the strain rate, and their integration into a standard linear solid model approximates adequately to the experimental results.

Modeling performed in the pore size of the organic interlayer show the strain dependence on the pore size. At larger membrane to pore size ratios as pore expands and stretches the strain increase is minimal. Experimental observations show that the membrane to pore size ratios is approximately within a range of 2 and 3; and the highest strain value reached in the specimens at a lower strain rate is ~10%. Thus, it can be predicted that when the load is applied in the organic interlayers the pore expansion is beyond 10x the original pore size.

These results add to the global knowledge of nacre, and most importantly to specific characteristics in the formation, structure, and behavior of nacre that need to be addressed to form better bioinspired materials and components. It is noteworthy to mention that mollusk shells are already inspiring new and better synthetic materials. In

the biomedical field, it was shown that nacre can serve as a synthetic bioactive material. Nacre coatings can be transformed into apatite under mild-condition chemical methods [177, 178]. Thus, when nacre is integrated with bone tissue can stimulate the bone re-growth [179]. This makes it an excellent candidate for orthopaedic and dental fields.

Additionally, other attempts have been made by mimicking the nacre architecture by synthetically reproducing it by an adequate combination of inorganic crystals and organic polymers. Such as in the case of Oaki et al. [84, 180], which utilized the organic macromolecules as templates for the nucleation of the minerals and control of the final material's shape. Some of these have been by using a Biomimetic materials synthesis approach. This refers to utilizing methods similar to nature, either using living organisms or using the respective materials isolated from organisms to prepare inorganic products. An example of this is work reported by Katti et al. [181], which employed the learnings of the bottom-up approach to synthesize composites of chitosan and polygalacturonic acid with hydroxyapatite by allowing precipitation of hydroxyapatite in the presence of biopolymers.

Bioinspired materials synthesis is used when concepts found in natural biomineralization are applied to the preparation of inorganic products using artificial materials. For example, a very successful approach was shown by the UC Berkeley and Lawrence Berkeley National Lab, a group led by Ritchie and Tomsia [29-31, 182] in which layered materials were prepared through a freeze-casting method; the porous scaffolds were then filled with a second phase, e.g. an organic component, in order to produce a dense composite. They combined aluminum oxide and polymethyl methacrylate (PMMA). This technique permits the formation of layered composites in

various intricate shapes with outstanding mechanical properties very comparable to the structures exhibited by nacre. The alumina tiles resemble the role of the aragonite tiles and the organic interlayer is substituted by PMMA.

Additionally, nacre has inspired multilayer coatings of materials with low/high elastic moduli including Al/$Al_2O_3$, Zr/ZrN, PMMA/$Al_2O_3$. Which are synthesized by a combination of reactive RF sputtering and pulsed laser deposition. Results show that microstructural features with layer thickness ratios similar to that of abalone nacre (0.3-0.5 μm inorganics / 10-50 nm organics) (Figure 5.1) can be attained [183, 184].

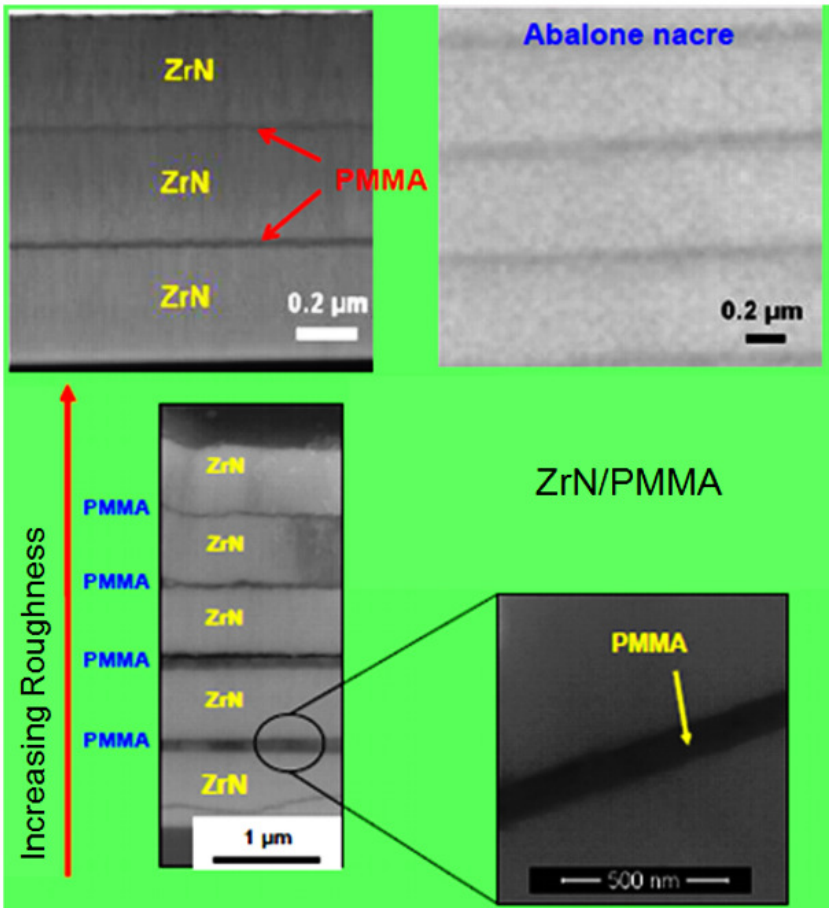


**Figure 5.1:** ZrN-PMMA Nacre inspired multilayer coating. Adapted from: Hirata et al., 2010 [184].

In conclusion, understanding the limited supply of materials available in biological systems and the narrow range of temperatures in which synthesis and processing takes place should aid in improving design principles of nature to amplify their effectiveness. Our current scientific and industrial capabilities can extend the biological manufacturing principles to a broader range of temperatures, pressures, and compositions, while retaining the essential features. Nature has designed and improved components and structures for 3.8 billion years, one should take this as a resource for innovation. Nature can act as a model, mentor, and measure so that these concepts can go beyond the way we design our planet, but also how we appreciate it.

## REFERENCES


[1] On Growth and Form - Thompson,Dw. Psychol Rep 1962;11:303-.

[2] Vincent JFV. Structural biomaterials. New York: Halsted Press; 1982.

[3] Currey JD. Bones : structure and mechanics. Princeton, NJ: Princeton University Press; 2002.

[4] Zhang SG, Marini DM, Hwang W, Santoso S. Design of nanostructured biological materials through self-assembly of peptides and proteins. Curr Opin Chem Biol 2002;6:865-71.

[5] Artz E. Biological and artificial attachment devices: lessons for materials scientists from flies and geckos. Materials Science & Engineering C 2006;26:1245-50.

[6] Meyers MA, Chen PY, Lopez MI, Seki Y, Lin AY. Biological materials: a materials science approach. J Mech Behav Biomed Mater 2011;4:626-57.

[7] Mann S. Biomineralization : principles and concepts in bioinorganic materials chemistry. New York: Oxford University Press; 2001.

[8] Lowenstam HA, Weiner S. On biomineralization. New York: Oxford University Press; 1989.

[9] Simkiss K, Wilbur KM. Biomineralization : cell biology and mineral deposition. San Diego: Academic Press; 1989.

[10] Sarikaya M. Microscopy of Self-Assembled Materials and Biomimetics - Preface. Microsc Res Techniq 1994;27:359-.

[11] Srinivasan AV, Haritos, G. K., and Hedberg, F. L. Biomimetics: Advancing Man-Made Materials Through Guidance From Nature. Applied Mechanics Review 1991;44:463-82.

[12] Mayer G, Sarikaya M. Rigid biological composite materials: Structural examples for biomimetic design. Exp Mech 2002;42:395-403.

[13] Mayer G. Rigid biological systems as models for synthetic composites. Science 2005;310:1144-7.

[14] Schäffer TE, IonescuZanetti C, Proksch R, Fritz M, Walters DA, Almqvist N. Does abalone nacre form by heteroepitaxial nucleation or by growth through mineral bridges? Chem Mater 1997;9:1731-40.

[15] Mann J. Natural products : their chemistry and biological significance. 1st ed. Harlow, Essex, England New York: Longman Scientific & Technical ;Wiley; 1994.

[16] Belcher AM, Wu XH, Christensen RJ, Hansma PK, Stucky GD, Morse DE. Control of crystal phase switching and orientation by soluble mollusc-shell proteins. Nature 1996;381:56-8.

[17] Fritz M, Belcher AM, Radmacher M, Walters DA, Hansma PK, Stucky GD. Flat Pearls from Biofabrication of Organized Composites on Inorganic Substrates. Nature 1994;371:49-51.

[18] Shen XY, Belcher AM, Hansma PK, Stucky GD, Morse DE. Molecular cloning and characterization of lustrin A, a matrix protein from shell and pearl nacre of Haliotis rufescens. Journal of Biological Chemistry 1997;272:32472-81.

[19] Zaremba CM, Belcher AM, Fritz M, Li YL, Mann S, Hansma PK. Critical transitions in the biofabrication of abalone shells and flat pearls. Chem Mater 1996;8:679-90.

[20] Su XW, Belcher AM, Zaremba CM, Morse DE, Stucky GD, Heuer AH. Structural and microstructural characterization of the growth lines and prismatic microarchitecture in red abalone shell and the microstructures of abalone "flat pearls". Chem Mater 2002;14:3106-17.

[21] Lin AYM, Meyers MA, Vecchio KS. Mechanical properties and structure of Strombus gigas, Tridacna gigas, and Haliotis rufescens sea shells: A comparative study. Mat Sci Eng C-Bio S 2006;26:1380-9.

[22] Meyers MA, Lin AYM, Seki Y, Chen PY, Kad BK, Bodde S. Structural biological composites: An overview. Jom-Us 2006;58:35-41.

[23] Meyers MA, Chen PY, Lin AYM, Seki Y. Biological materials: Structure and mechanical properties. Prog Mater Sci 2008;53:1-206.

[24] Lin AYM, Chen PY, Meyers MA. The growth of nacre in the abalone shell. Acta Biomater 2008;4:131-8.

[25] Meyers MA, Lin AYM, Chen PY, Muyco J. Mechanical strength of abalone nacre: Role of the soft organic layer. J Mech Behav Biomed 2008;1:76-85.

[26] Sanchez C, Arribart H, Guille MMG. Biomimetism and bioinspiration as tools for the design of innovative materials and systems. Nat Mater 2005;4:277-88.

[27] Luz GM, Mano JF. Biomimetic design of materials and biomaterials inspired by the structure of nacre. Philos T R Soc A 2009;367:1587-605.

[28] Kobayashi I, Samata T. Bivalve shell structure and organic matrix. Mat Sci Eng C-Bio S 2006;26:692-8.

[29] Launey ME, Munch E, Alsem DH, Barth HB, Saiz E, Tomsia AP. Designing highly toughened hybrid composites through nature-inspired hierarchical complexity. Acta Mater 2009;57:2919-32.

[30] Munch E, Launey ME, Alsem DH, Saiz E, Tomsia AP, Ritchie RO. Tough, Bio-Inspired Hybrid Materials. Science 2008;322:1516-20.

[31] Deville S, Saiz E, Nalla RK, Tomsia AP. Freezing as a path to build complex composites. Science 2006;311:515-8.

[32] Deville S, Saiz E, Tomsia AP. Freeze casting of hydroxyapatite scaffolds for bone tissue engineering. Biomaterials 2006;27:5480-9.

[33] Lin AYM, Meyers MA. Interfacial shear strength in abalone nacre. J Mech Behav Biomed 2009;2:607-12.

[34] Bevelander G, Nakahara H. An Electron Microscope Study of Formation of Nacreous Layer in Shell of Certain Bivalve Molluscs. Calc Tiss Res 1969;3:84-&.

[35] Nakahara H, Kakei M, Bevelander G. Studies on the Formation of the Crossed Lamellar Structure in the Shell of Strombus-Gigas. Veliger 1981;23:207-&.

[36] Wada K, Furuhash.T. Mineralization of Calcified Tissue in Molluscs .18. Acid Polysaccharide of Mantle Mucus of Some Marine Bivalves. B Jpn Soc Sci Fish 1971;37:13-&.

[37] Suga S, Nakahara H, Nihon Gakujutsu Kaigi., Kanagawa Academy of Science and Technology. Mechanisms and phylogeny of mineralization in biological systems. Tokyo New York: Springer-Verlag; 1991.

[38] Lin A, Meyers MA. Growth and structure in abalone shell. Mat Sci Eng a-Struct 2005;390:27-41.

[39] Fritz M, Morse DE. The formation of highly organized biogenic polymer/ceramic composite materials: the high-performance microaluminate of molluscan nacre. Curr Opin Colloid In 1998;3:55-62.

[40] Baeuerlein E. Biomineralization : progress in biology, molecular biology and application. 2nd completely rev. and extended ed. Weinheim: Wiley-VCH; 2004.

[41] Sarikaya M, Gunnison, K. E., Yasrebi, M. and Aksay, J. A. Mechanical property – microstructural relationships in abalone shell. In Materials Synthesis Utilizing Biological Processes. Materials Research Society 1990;174:109-66.

[42] Espinosa HD, Rim JE, Barthelat F, Buehler MJ. Merger of structure and material in nacre and bone - Perspectives on de novo biomimetic materials. Prog Mater Sci 2009;54:1059-100.

[43] Checa AG, Cartwright JH, Willinger MG. The key role of the surface membrane in why gastropod nacre grows in towers. Proc Natl Acad Sci U S A 2009;106:38-43.

[44] Bezares J, Asaro RJ, Hawley M. Macromolecular structure of the organic framework of nacre in Haliotis rufescens: implications for growth and mechanical behavior. J Struct Biol 2008;163:61-75.

[45] Bezares J, Asaro RJ, Hawley M. Macromolecular structure of the organic framework of nacre in Haliotis rufescens: implications for mechanical response. J Struct Biol 2010;170:484-500.

[46] Bezares J, Peng Z, Asaro RJ, Zhu Q. Macromolecular structure and viscoelastic response of the organic framework of nacre in *Haliotis rufescens*: a perspective and overview. Journal of Theoretical Applied Mechanics 2011;38:75-106.

[47] Case ST. Structure, cellular synthesis, and assembly of biopolymers. Berlin ; New York: Springer-Verlag; 1992.

[48] Meyers MA, Lim CT, Li A, Nizam BRH, Tan EPS, Seki Y. The role of organic intertile layer in abalone nacre. Mat Sci Eng C-Mater 2009;29:2398-410.

[49] Nakahara H, Kakei, M., and Bevelander, G. Electron microscopic and amino acid studies on the outer and inner shell layers of Haliotis rufescens. Venus Jpn J Malac 1982;41:33-46.

[50] Sarikaya M, Aksay IA. Nacre of abalone shell: a natural multifunctional nanolaminated ceramic-polymer composite material. Results Probl Cell Differ 1992;19:1-26.

[51] Menig R, Meyers MH, Meyers MA, Vecchio KS. Quasi-static and dynamic mechanical response of Haliotis rufescens (abalone) shells. Acta Mater 2000;48:2383-98.

[52] Nukala PKVV, Simunovic S. A continuous damage random thresholds model for simulating the fracture behavior of nacre. Biomaterials 2005;26:6087-98.

[53] Li XD, Xu ZH, Wang RZ. In situ observation of nanograin rotation and deformation in nacre. Nano Lett 2006;6:2301-4.

[54] Currey JD, Kohn AJ. Fracture in Crossed-Lamellar Structure of Conus Shells. J Mater Sci 1976;11:1615-23.

[55] Currey JD. Mechanical-Properties of Mother of Pearl in Tension. P Roy Soc B-Biol Sci 1977;196:443-+.

[56] Laraia VJ, Heuer AH. Novel Composite Microstructure and Mechanical-Behavior of Mollusk Shell. J Am Ceram Soc 1989;72:2177-9.

[57] Barthelat F, Espinosa HD. An experimental investigation of deformation and fracture of nacre-mother of pearl. Exp Mech 2007;47:311-24.

[58] Barthelat F, Tang H, Zavattieri PD, Li CM, Espinosa HD. On the mechanics of mother-of-pearl: A key feature in the material hierarchical structure. J Mech Phys Solids 2007;55:306-37.

[59] Tang H, Barthelat F, Espinosa HD. An elasto-viscoplastic interface model for investigating the constitutive behavior of nacre. J Mech Phys Solids 2007;55:1410-38.

[60] Katti DR, Katti KS. Modeling microarchitecture and mechanical behavior of nacre using 3D finite element techniques - Part I - Elastic properties. J Mater Sci 2001;36:1411-7.

[61] Evans AG, Suo Z, Wang RZ, Aksay IA, He MY, Hutchinson JW. Model for the robust mechanical behavior of nacre. J Mater Res 2001;16:2475-84.

[62] Gao HJ, Ji BH, Jager IL, Arzt E, Fratzl P. Materials become insensitive to flaws at nanoscale: Lessons from nature. P Natl Acad Sci USA 2003;100:5597-600.

[63] Katti KS, Katti DR. Why is nacre so tough and strong? Mat Sci Eng C-Bio S 2006;26:1317-24.

[64] Barthelat F, Li CM, Comi C, Espinosa HD. Mechanical properties of nacre constituents and their impact on mechanical performance. J Mater Res 2006;21:1977-86.

[65] Lin A. Structural and functional biological materials: abalone nacre, sharp materials, and abalone foot adhesion. La Jolla: University of California San Diego; 2008.

[66] Schneider AS, Heiland B, Peter NJ, Guth C, Arzt E, Weiss IM. Hierarchical super-structure identified by polarized light microscopy, electron microscopy and nanoindentation: Implications for the limits of biological control over the growth mode of abalone sea shells. Bmc Biophys 2012;5.

[67] Li XD, Chang WC, Chao YJ, Wang RZ, Chang M. Nanoscale structural and mechanical characterization of a natural nanocomposite material: The shell of red abalone. Nano Lett 2004;4:613-7.

[68] Fleischli FD, Dietiker M, Borgia C, Spolenak R. The influence of internal length scales on mechanical properties in natural nanocomposites: A comparative study on inner layers of seashells. Acta Biomater 2008;4:1694-706.

[69] Watabe N, Wilbur KM. Influence of the Organic Matrix on Crystal Type in Molluscs. Nature 1960;188:334-.

[70] Wada K. Studies on the mineralization of calcified tissues in molluscs. Bulletin of the Japanese Society for the Science of Fish 1964;9:1087-98.

[71] Towe KM, Hamilton GH. Ultrastructure and Inferred Calcification of Mature and Developing Nacre in Bivalve Mollusks. Calc Tiss Res 1968;1:306-&.

[72] Manne S, Zaremba CM, Giles R, Huggins L, Walters DA, Belcher A. Atomic-Force Microscopy of the Nacreous Layer in Mollusk Shells. P Roy Soc B-Biol Sci 1994;256:17-23.

[73] Falini G, Albeck S, Weiner S, Addadi L. Control of aragonite or calcite polymorphism by mollusk shell macromolecules. Science 1996;271:67-9.

[74] Addadi L, Joester D, Nudelman F, Weiner S. Mollusk shell formation: A source of new concepts for understanding biomineralization processes. Chem-Eur J 2006;12:981-7.

[75] Checa AG, Rodriguez-Navarro AB. Self-organisation of nacre in the shells of Pterioida (Bivalvia: Mollusca). Biomaterials 2005;26:1071-9.

[76] Cartwright JHE, Checa AG. The dynamics of nacre self-assembly. J R Soc Interface 2007;4:491-504.

[77] Yao N, Epstein AK, Liu WW, Sauer F, Yang N. Organic-inorganic interfaces and spiral growth in nacre. J R Soc Interface 2009;6:367-76.

[78] Levi-Kalisman Y, Falini G, Addadi L, Weiner S. Structure of the nacreous organic matrix of a bivalve mollusk shell examined in the hydrated state using Cryo-TEM. J Struct Biol 2001;135:8-17.

[79] Song F, Bai YL. Mineral bridges of nacre and its effects. Acta Mech Sinica 2001;17:251-7.

[80] Song F, Zhang XH, Bai YL. Microstructure and characteristics in the organic matrix layers of nacre. J Mater Res 2002;17:1567-70.

[81] Song F, Bai YL. Effects of nanostructures on the fracture strength of the interfaces in nacre. J Mater Res 2003;18:1741-4.

[82] Rousseau M, Lopez E, Stempfle P, Brendle M, Franke L, Guette A. Multiscale structure of sheet nacre. Biomaterials 2005;26:6254-62.

[83] Saruwatari K, Matsui T, Mukai H, Nagasawa H, Kogure T. Nucleation and growth of aragonite crystals at the growth front of nacres in pearl oyster, Pinctada fucata. Biomaterials 2009;30:3028-34.

[84] Oaki K, Imai H. The hierarchical architecture of nacre and its mimetic material. Angew Chem Int Edit 2005;44:6571-5.

[85] Watabe N. Decalcification of Thin Sections for Electron Microscope Studies of Crystal-Matrix Relationships in Mollusc Shells. J Cell Biol 1963;18:701-&.

[86] Garside J, Gibilaro LG, Tavare NS. Evaluation of Crystal-Growth Kinetics from a Desupersaturation Curve Using Initial Derivatives. Chem Eng Sci 1982;37:1625-8.

[87] Porter M. IN SITU CRYSTALLIZATION OF NATIVE POLY(3-HYDROXYBUTYRATE) GRANULES IN VARYING ENVIRONMENTAL CONDITIONS: UNIVERSITY OF HAWAI‘I AT MĀNOA; 2010.

[88] Burton WK, Cabrera N, Frank FC. The Growth of Crystals and the Equilibrium Structure of Their Surfaces. Philos Tr R Soc S-A 1951;243:299-358.

[89] Fricke M, Volkmer D. Crystallization of calcium carbonate beneath insoluble monolayers: Suitable models of mineral-matrix interactions in biomineralization? Top Curr Chem 2007;270:1-41.

[90] Saleuddi.As, Wilbur KM. Shell Regeneration in Helix Pomatia. Can J Zoolog 1969;47:51-&.

[91] Fritz M, Radmacher M, Gaub HE. Granula Motion and Membrane Spreading during Activation of Human Platelets Imaged by Atomic-Force Microscopy. Biophysical Journal 1994;66:1328-34.

[92] Nakahara H. An electron microscope stru of the growing surface of nacre in two gastropod species, Turbo cornutus and Tegula pfeifferi. Venus Jpn J Malac 1979;38:205-11.

[93] Wise SW. Microarchitecture and Deposition of Gastropod Nacre. Science 1970;167:1486-&.

[94] Uozumi S, Togo Y. Formation of the nacreous and th[e innermost prismatic layer in Omphalius rusticus (gmelin) (gastropoda). Jour Fac Sci, Hokkaido Univ, Ser IV 1975;17:153-72.

[95] Watabe N. Crystal-Growth of Calcium-Carbonate in the Invertebrates. Prog Cryst Growth Ch 1981;4:99-147.

[96] Morse DE, Cariolou MA, Stucky GD, Zaremba CM, Hansma PK. Genetic coding in biomineralization of microlaminate composites. Materials Research Society Symposium1993. p. 59-67.

[97] Mutvei H. On the internal structures of the nacreous systems tablets in molluscan shells. Scanning Electron Microsc 1979;2:457-62.

[98] Wada K. Nucleation and growth of aragonite crystals in the nacre of bivalve molluscs. Biomineralization 1972;6:141-59.

[99] Westbroek P, De Jong EW. Biomineralization and biological metal accumulation : biological and geological perspectives : papers presented at the fourth International Symposium on Biomineralization, Renesse, the Netherlands, June 2-5, 1982. Dordrecht,

Holland ; Boston Hingham, MA: D. Reidel Pub. ; Sold and distributed in the U.S.A. and Canada by Kluwer Boston Inc.; 1983.

[100] Nakahara H, Bevelander G, Kakei M. Electron microscopic and amino acid studies on the outer and inner shell layers of *Haliotis rufescens*. Venus (Jap J Malac) 1982;41:33-46.

[101] Dastjerdi AK, Rabiei R, Barthelat F. The weak interfaces within tough natural composites: experiments on three types of nacre. J Mech Behav Biomed 2012;19:50-60.

[102] Lapota D, Rosen G, Chock J, Liu CH. Red and green abalone seed growout for reseeding activities off Point Loma, California. J Shellfish Res 2000;19:431-8.

[103] Jackson AP, Vincent JFV, Turner RM. The Mechanical Design of Nacre. P Roy Soc B-Biol Sci 1988;234:415-+.

[104] Weibull W. A Statistical Distribution Function of Wide Applicability. J Appl Mech-T Asme 1951;18:293-7.

[105] Leung HM, Sinha SK. Scratch and indentation tests on seashells. Tribol Int 2009;42:40-9.

[106] Denkena B, Koehler J, Moral A. Ductile and brittle material removal mechanisms in natural nacre-A model for novel implant materials. J Mater Process Tech 2010;210:1827-37.

[107] Fischer A, Bobzin K. Friction, wear and wear protection : International Symposium on Friction, Wear and Wear Protection 2008, Aachen, Germany. Weinheim, Germany: Wiley-VCH; 2009.

[108] Wang RZ, Suo Z, Evans AG, Yao N, Aksay IA. Deformation mechanisms in nacre. J Mater Res 2001;16:2485-93.

[109] Barthelat F, Espinosa HD. Mechanical properties of nacre constituents: an inverse method approach. MRS Proceedings2004.

[110] Huang ZW, Li XD. Nanoscale structural and mechanical characterization of heat treated nacre. Mat Sci Eng C-Mater 2009;29:1803-7.

[111] Mohanty B, Katti KS, Katti DR. Experimental investigation of nanomechanics of the mineral-protein interface in nacre. Mech Res Commun 2008;35:17-23.

[112] Sumitomo T, Kakisawa H, Owaki Y, Kagawa Y. In situ transmission electron microscopy observation of reversible deformation in nacre organic matrix. J Mater Res 2008;23:1466-71.

[113] Smith BL, Schaffer TE, Viani M, Thompson JB, Frederick NA, Kindt J. Molecular mechanistic origin of the toughness of natural adhesives, fibres and composites. Nature 1999;399:761-3.

[114] Velazquez-Castillo RR, Reyes-Gasga J, Garcia-Gutierrez DI, Jose-Yacaman M. Crystal structure characterization of nautilus shell at different length scales. Biomaterials 2006;27:4508-17.

[115] Ji BH, Gao HJ. Mechanical properties of nanostructure of biological materials. J Mech Phys Solids 2004;52:1963-90.

[116] Fratzl P. Biomimetic materials research: what can we really learn from nature's structural materials? J R Soc Interface 2007;4:637-42.

[117] Fratzl P, Weinkamer R. Nature's hierarchical materials. Prog Mater Sci 2007;52:1263-334.

[118] Katti KS, Katti DR, Pradhan SM, Bhosle A. Platelet interlocks are the key to toughness and strength in nacre. J Mater Res 2005;20:1097-100.

[119] Barthelat F, Espinosa HD. Elastic properties of nacre aragonite tablets. Proc Annual Conference and Exposition on Experimental and Applied Mechanics paper2003.

[120] Bruet BJF, Qi HJ, Boyce MC, Panas R, Tai K, Frick L. Nanoscale morphology and indentation of individual nacre tablets from the gastropod mollusc Trochus niloticus (vol 20, pg 2400, 2005). J Mater Res 2005;20:3157-.

[121] Ghosh P, Mohanty B, Verma D, Katti KS, Katti DR. Machanical Properties of Biological nanocomposite nacre: Multiscale modeling and experiments on nacre from red abalone. MRS Symposium2006.

[122] Kearney C, Zhao Z, Bruet BJF, Radovitzky R, Boyce MC, Ortiz C. Nanoscale anisotropic plastic deformation in single crystal aragonite. Physical Review Letters 2006;96.

[123] Mohanty B, Verma D, Katti KS, Katti DR. Time dependent nanomechanical response on nacre. Mater Res Soc2007.

[124] Barthelat F, Espinosa HD. Mechanical properties of nacre constituents: An inverse method approach. Mater Res Soc Symp P 2005;844:67-78.

[125] Perzyna A. Thermodynamic Theory of Viscoplasticity. Advances in Applied Mechanics 1971;11:313-54.

[126] Knoll M. Charge potential and secondary emissions of electron irradiated bodies. Phys Z 1935;36:861-9.

[127] Goldstein J, Newbury DE, Joy DC, Lyman CE, Echlin P, Lifshin E. Scanning Electron Microscopy and X-ray Microanalysis. 3 ed: Springer; 2003.

[128] Steinarsson A, Imsland AK. Size dependent variation in optimum growth temperature of red abalone (Haliotis rufescens). Aquaculture 2003;224:353-62.

[129] Weiner S, Traub W. Macromolecules in Mollusk Shells and Their Functions in Biomineralization. Philos T Roy Soc B 1984;304:425-&.

[130] Wainwright PC. Biomechanical Limits to Ecological Performance - Mollusk-Crushing by the Caribbean Hogfish, Lachnolaimus-Maximus (Labridae). J Zool 1987;213:283-97.

[131] Kniprath E. Formation and Structure of Periostracum in Lymnaea-Stagnalis. Calc Tiss Res 1972;9:260-&.

[132] Kniprath E. Ultrastructure and Growth of Sea-Urchin Tooth. Calc Tiss Res 1974;14:211-28.

[133] Kniprath E. Mantle Growth in Lymnaea Stagnalis. Cytobiologie 1975;10:260-7.

[134] Kniprath E. Ontogeny of Shell Field in Lymnaea-Stagnalis. Roux Arch Dev Biol 1977;181:11-30.

[135] Kniprath E. Growth of Shell-Field in Mytilus (Bivalvia). Zool Scr 1978;7:119-20.

[136] Kniprath E. Functional-Morphology of the Embryonic Shell-Gland in the Conchiferous Mollusks. Malacologia 1979;18:549-52.

[137] Kniprath E. On the Shell-Gland in Helix-Aspersa (Gastropoda). Arch Zool Exp Gen 1980;121:207-+.

[138] Kniprath E. Larval Development of the Shell and the Shell Gland in Mytilus (Bivalvia). Roux Arch Dev Biol 1980;188:201-4.

[139] Kniprath E. Ontogenetic Plate and Plate Field Development in 2 Chitons, Middendorffia and Ischnochiton. Roux Arch Dev Biol 1980;189:97-106.

[140] Kniprath E. Ontogeny of the Molluscan Shell Field - a Review. Zool Scr 1981;10:61-79.

[141] Timmermans LPM. Studies on shell formation in molluscs. Neth J Zool 1969;19:417-523.

[142] Saleuddin ASM. Ultrastructural Studies on Formation of Periostracum in Helix-Aspersa (Mollusca). Calc Tiss Res 1976;22:49-65.

[143] Saleuddin ASM, Dillaman RM. Direct Innervation of Mantle Edge Gland by Neurosecretory Axons in Helisoma-Duryi (Mollusca-Pulmonata). Cell Tissue Res 1976;171:397-401.

[144] Saleuddin ASM, Jones GM. Actin-Like Filaments in Neurosecretory Cells of Helisoma-Duryi (Gastropoda, Pulmonata). Can J Zool 1976;54:2001-10.

[145] Nudelman F, Gotliv BA, Addadi L, Weiner S. Mollusk shell formation: Mapping the distribution of organic matrix components underlying a single aragonitic tablet in nacre. J Struct Biol 2006;153:176-87.

[146] Jolly C, Berland S, Milet C, Borzeix S, Lopez E, Doumenc D. Zonal Localization of Shell Matrix Proteins in Mantle of Haliotis tuberculata (Mollusca, Gastropoda). Mar Biotechnol 2005;6:541-51.

[147] De Waele A. Memoires Academie Royale de Belgique, classe des Sciences, 1931:31-51.

[148] Thompson JB, Paloczi GT, Kindt JH, Michenfelder M, Smith BL, Stucky G. Direct observation of the transition from calcite to aragonite growth as induced by abalone shell proteins. Biophysical Journal 2000;79:3307-12.

[149] Gotliv BA, Addadi L, Weiner S. Mollusk shell acidic proteins: In search of individual functions. Chembiochem 2003;4:522-9.

[150] Brusca RC, Brusca GJ. Invertebrates. 2nd ed. Sunderland, Mass.: Sinauer Associates; 2003.

[151] A. Bubel. Epidermal Cells. In: J. Bereiter-Hahn AGM, and K. S. Richard, editor. Biology of the Integument. Berlin, Germany: Springer; 1984. p. pp. 400– 77.

[152] Simkiss K. The Mollusca: Form and Function. In: Clarke ERTaR, editor. London, UK: Academic Press; 1988. p. pp. 11–35.

[153] Mutvei H, Dauphin Y, Cuif JP. Observations sur l'organisation de la couche externe du test des Haliotis (Gastropoda): un cas exceptionnel de la variabilite´ mine´ralogique et microstructurale. Bull Mus Nat Hist Nat Paris Ser 1985;4 7:73-91.

[154] Dauphin CY, Mutvei H, Denis A. Mineralogy, chemistry and ultrastructure of the external shell-layer in ten species of Haliotis with reference to Haliotis tuberculata (Mollusca: Archaeogastropoda). Bull Geol Inst Univ Uppsala NS 1989;15:7-38.

[155] Hawkes GP, Day RW, Wallace MW, Nugent KW, Bettiol AA, Jamieson DN. Analyzing the growth and form of mollusc shell layers, in situ, by cathodoluminescence microscopy and Raman spectroscopy. J Shellfish Res 1996;15:659-66.

[156] Voltzow J. Gastropoda: Prosobranchia. In: Kohn FWHaAJ, editor. Microscopic Anatomy of Invertebrates. New York, NY, USA: Wiley-Liss; 1994. p. pp. 111–252.

[157] Grenon JF, Walker G. Histology and Histochemistry of Pedal Glandular System of 2 Limpets, Patella-Vulgata and Acmaea-Tessulata (Gastropoda-Prosobranchia). J Mar Biol Assoc Uk 1978;58:803-&.

[158] Shirbhate R, Cook A. Pedal and Opercular Secretory Glands of Pomatias, Bithynia and Littorina. J Mollus Stud 1987;53:79-96.

[159] Crenshaw M, Ristedt H. Role of Organic Matrix in Molluscan Shell Formation. J Dent Res 1976;55:B75-B.

[160] Weiner S, Traub W. X-Ray-Diffraction Study of the Insoluble Organic Matrix of Mollusk Shells. Febs Lett 1980;111:311-6.

[161] Barthelat F. Biomimetics for next generation materials. Philos T R Soc A 2007;365:2907-19.

[162] Shaw GA, Prorok B, Starman LA. MEMS and nanotechnology. Volume 6. New York ; London: Springer; 2012.

[163] Barthelat F, Zhu DJ. A novel biomimetic material duplicating the structure and mechanics of natural nacre. J Mater Res 2011;26:1203-15.

[164] Espinosa HD, Juster AL, Latourte FJ, Loh OY, Gregoire D, Zavattieri PD. Tablet-level origin of toughening in abalone shells and translation to synthetic composite materials. Nat Commun 2011;2.

[165] Lopez MI, Chen PY, McKittrick J, Meyers MA. Growth of nacre in abalone: Seasonal and feeding effects. Mat Sci Eng C-Mater 2011;31:238-45.

[166] Song F, Soh AK, Bai YL. Structural and mechanical properties of the organic matrix layers of nacre. Biomaterials 2003;24:3623-31.

[167] Gries K, Kroger R, Kubel C, Fritz M, Rosenauer A. Investigations of voids in the aragonite platelets of nacre. Acta Biomater 2009;5:3038-44.

[168] Checa AG, Cartwright JH, Willinger MG. Mineral bridges in nacre. J Struct Biol 2011;176:330-9.

[169] Bardenhagen SG, Stout MG, Gray GT. Three-dimensional, finite deformation, viscoplastic constitutive models for polymeric materials. Mech Mater 1997;25:235-53.

[170] Khan A, Zhang HY. Finite deformation of a polymer: experiments and modeling. Int J Plasticity 2001;17:1167-88.

[171] Khan AS, Lopez-Pamies O, Kazmi R. Thermo-mechanical large deformation response and constitutive modeling of viscoelastic polymers over a wide range of strain rates and temperatures. Int J Plasticity 2006;22:581-601.

[172] Plaseied A, Fatemi A. Deformation response and constitutive modeling of vinyl ester polymer including strain rate and temperature effects. J Mater Sci 2008;43:1191-9.

[173] Lopez MI, Meza Martinez PE, Meyers MA. Organic interlamellar layers, mesolayers and mineral nanobridges: Contribution to strength in abalone (Haliotis rufescence) nacre. Acta Biomater 2014;10:2056-64.

[174] Belcher AM, Gooch EE. In: Bäuerlein E, editor. Biomineralization: From Biology to Biotechnology and Medical Application: Wiley-Interscience; 2000. p. 221.

[175] Rivlin RS, Thomas AG. Large Elastic Deformations of Isotropic Materials .8. Strain Distribution around a Hole in a Sheet. Philos Tr R Soc S-A 1951;243:289-98.

[176] Lubarda VA. Constitutive analysis of thin biological membranes with application to radial stretching of a hollow circular membrane. J Mech Phys Solids 2010;58:860-73.

[177] Vecchio KS, Zhang X, Massie JB, Wang M, Kim CW. Conversion of bulk seashells to biocompatible hydroxyapatite for bone implants. Acta Biomater 2007;3:910-8.

[178] Guo YP, Zhou Y. Transformation of nacre coatings into apatite coatings in phosphate buffer solution at low temperature. Journal of Biomedical Materials Research Part A 2008;86A:510-21.

[179] Zhu LQ, Wang HM, Xu JH, Wei D, Zhao WQ, Wang XX. Effects of titanium implant surface coated with natural nacre on MC3T3E1 cell line in vitro. Prog Biochem Biophys 2008;35:671-5.

[180] Oaki Y, Kotachi A, Miura T, Imai H. Bridged nanocrystals in biominerals and their biomimetics: Classical yet modern crystal growth on the nanoscale. Adv Funct Mater 2006;16:1633-9.

[181] Katti KS, Katti DR, Dash R. Synthesis and characterization of a novel chitosan/montmorillonite/hydroxyapatite nanocomposite for bone tissue engineering. Biomed Mater 2008;3.

[182] Launey ME, Munch E, Alsem DH, Saiz E, Tomsia AP, Ritchie RO. A novel biomimetic approach to the design of high-performance ceramic-metal composites. J R Soc Interface 2010;7:741-53.

[183] Chen P-Y, Sun C-Y, Chan Y-C, Lee J-W, Duh J-G. Structural Characterization and Mechanical Evaluations of Abalone Nacre-inspired Multilayer Coatings Synthesized by RF Sputtering and Pulsed Laser Deposition. The Minerals, Metals, and Materials Society 142nd Annual Meeting & Exhibition Orlando, Florida2013.

[184] Hirata GA, Diaz SP, Chen P-Y, Meyers MA, McKittrick J. Bioinspired inorganic/polymer thin films. Materials Research Society Symposium Proceedings2010. p. 8.